



HAL
open science

Modelling solar radiation for PV optimisation

Lea Al Asmar

► **To cite this version:**

Lea Al Asmar. Modelling solar radiation for PV optimisation. Environmental Engineering. École des Ponts ParisTech, 2021. English. NNT : 2021ENPC0034 . tel-03636889

HAL Id: tel-03636889

<https://pastel.hal.science/tel-03636889>

Submitted on 11 Apr 2022

HAL is a multi-disciplinary open access archive for the deposit and dissemination of scientific research documents, whether they are published or not. The documents may come from teaching and research institutions in France or abroad, or from public or private research centers.

L'archive ouverte pluridisciplinaire **HAL**, est destinée au dépôt et à la diffusion de documents scientifiques de niveau recherche, publiés ou non, émanant des établissements d'enseignement et de recherche français ou étrangers, des laboratoires publics ou privés.



ÉCOLE DES PONTS PARISTECH

DOCTORATE SCHOOL: SCIENCE, ENGINEERING AND
ENVIRONMENT

PHD THESIS

MODELLING SOLAR RADIATION FOR PV OPTIMISATION

LÉA AL ASMAR

DEFENDED ON: 16/12/2021

Jury:

- **Annica Ekman** Prof., University of Stockholm, Sweden - *Reporter*
- **Philippe Blanc** Prof., Ecole des Mines ParisTech, France - *Reporter*
- **Isabelle Chiapello** HDR, Laboratoire d'optique atmosphérique, France - *Examinator*
- **Jean-Charles Dupont** PhD, Laboratoire de Météorologie dynamique (LMD), France - *Examinator*
- **Jean-Louis Dufresne** Prof., Laboratoire de Météorologie dynamique (LMD), France - *President of the jury*
- **Karine Sartelet** HDR, CEREa, Ecole des Ponts ParisTech, France - *PhD supervisor*
- **Eric Dupont** PhD, CEREa, EDF R& D, France - *Co-Supervisor*
- **Luc Musson-Genon** PhD, CEREa, EDF R& D, France - *Guest*

Acknowledgments

First and foremost, I would like to thank the whole jury for their interest and availability and notably the two reporters, Prof. Annica Eckman and Prof. Philippe Blanc, for reviewing this manuscript.

Next, I would like to thank the CEREAL laboratory and EDF R&D for financing this thesis and letting me prepare it in a pleasant working environment. In particular, I thank my supervisors Karine Sartelet and Eric Dupont who followed my work closely and provided valuable comments and corrections throughout the last three years.

I owe my deepest gratitude to Luc Musson-Genon with whom I had utmost pleasure working. Thank you for the multiple hours we spent on the phone and for transmitting your curiosity and passion to science, and most importantly, thank you for being such a good professor, I am very happy that I got the opportunity to meet you and learn from you.

I also would like to thank Martin Ferrand, for all the help on `code_saturne` and all the time passed trying to fix the 3-D module, as well as Pietro Bernaradara, for the support, the guidance and for everything you provided. Along with, I thank Laurent, Yassine and Oume for their help and interesting discussions on my work. Moreover, I thank the whole CEREAL team, from both sides EDF and Ecole des Ponts, for being such great co-workers, notably Jeoffery, Palmira, Cedric, Yannick, Rafael, Rayna, Konstantin, Youngesob, Clémentine. In particular, I thank Lya and Hector, with whom I shared my office, coffee, maté, lunches, *obrigada por tudo*, for the help, the various advises, the support and for becoming such good friends.

Furthermore, I would like to thank the SIRTAL for providing the data for the work of this thesis and special thanks to Jean-Charles Dupont for your interest in my work and for the discussions. Additionally, I thank the IZNE institute of the Bonn-Rhein-Sieg University, and especially James Barry and Prof. Stefanie Meilinger, for inviting me to your institute and for the nice visit.

Considering the pandemic situation and various quarantines, I am very grateful of having such amazing flatmates, Sandra, Pauline and Popo, who have also been my co-workers, and have always provided me with a peaceful place to work in and amazing life support. I would also like to thank, all the passengers of Bobillot: Gabriel, Catarina, Magali, Giulia, Nono for all the good times and nice memories.

I would also like to particularly thank my capoeira team and specially professor Rasta, Navalha, Valentao, Pantera Negra, Lua, Caxixi, Bambu, Perguntinha, Chinela, Tia, Bruna, Rose, Aymeric, for providing me with a lot of *Axé*; it gave me so much effort and courage to continue and go on with this thesis.

This section wouldn't be complete without thanking my amazing friends from Cité universitaire, university curriculum (CMI), red cross team, childhood friends for the support, the trips,

the fun times and the company. Special thanks to Lucila, Davide, Fabricio, Antonios, Martin, Christina, Nicole, Marianna, Antonio, Hugo, Junior, Carlos, Pablo, Wilhelm, Axel, Eric, Fouad, Ameer, Bassem, Adrien, Cecile and Charlotte. Special thanks to Gaurav, always showing me the right way, for providing some corrections of this manuscript and to my special friend Morgana, who has been here all along the way, giving me strength and motivation to continue, even while living so far away.

Last but not least, I would like to thank all my family in France as well as those living in Lebanon and specially my cousins Gaele, Alexia, Christopher, Yann and Marc. Thank you for being here despite everything happening. My heartfelt appreciation to my parents and to my sister, Fadi, Jennifer and Ray, for their warm support; this achievement is also yours. I would also like to dedicate this work to my late grandpa, Ibrahim Kazan, whose love and support I have always felt through music, and who has always pushed me and encouraged me to continue studying.



Figure 1: Photo taken by the sky imager during my visit at the Bonn-Rhein-Sieg University

ABSTRACT

A strong development of the solar energy sector is expected for the coming years in France and around the world. An accurate prediction of the amount of solar irradiance reaching the ground is necessary to optimize the performance of [photovoltaic \(PV\)](#) farms and to forecast the production at different time scales. However, the amount of solar irradiance reaching the ground is influenced by different geographical, meteorological and atmospheric parameters, including the characteristics of clouds and aerosols. The objective of this thesis is to improve the modelling of solar radiation, by focusing on the impact of clouds and aerosols.

Improvements have been made to the standalone [1D](#) irradiance model of the [CFD](#) software code `_saturne`. The model now estimates the total solar irradiance and its direct and diffuse components, taking into account clouds, aerosols and absorption by minor gases. Simulations are conducted and compared to measurements at the French [SIRTA](#) observatory (instrumental site for atmospheric remote sensing research), located in Palaiseau, Île-de-France. Satisfactory results are obtained during clear-sky days when considering the impact of aerosols, which optical properties are estimated by coupling our model to the Polyphemus platform. Clouds have a strong influence on the amount of solar irradiance reaching the ground, they have large spatio-temporal variations and are difficult to model. The estimation of irradiance during cloudy-sky days is improved by coupling the model to on-site measurements of cloud parameters (cloud optical thickness, cloud fraction) from the [SIRTA](#) observatory. A sensitivity analysis on the cloud parameters is performed in order to better understand and quantify the influence of these parameters on the simulated irradiance (global and direct), and to identify the data sources that minimize the prediction error. Moreover, hourly values of solar fluxes are analysed to determine and physically understand the causes of the largest errors between model and measurements when measured cloud parameters are used.

The second part of the thesis consisted in applying and validating the model on a well-documented case of a radiative fog at the [SIRTA](#) (ParisFog campaign), where the fog evolves into a low stratus cloud. Special attention is given to the impact of aerosols concentration and of the presence of black carbon in cloud droplets on the dissipation of the fog as well as the hypothesis used for the cloud fraction.

In the third part, further improvements are implemented in the [3D](#) irradiation scheme in order to take into account the aerosols and clouds and for its application to [PV](#) farms. In a first step, this [3D](#) model is applied to this case of radiative fog, and results are compared to those obtained with the [1D](#) scheme.

RÉSUMÉ

Un fort développement de la filière énergie solaire est prévu pour les prochaines années en France et dans le monde. Une modélisation précise du rayonnement solaire est nécessaire pour minimiser les incertitudes sur l'estimation du productible de futures fermes et optimiser leur conception. Cependant, le rayonnement solaire au sol est fortement influencé par plusieurs paramètres géographiques, météorologiques et atmosphériques, dont notamment les caractéristiques des nuages, et celles des aérosols. L'objectif de cette thèse est d'améliorer la modélisation du rayonnement solaire, en mettant l'accent sur celles dues à la présence de nuages et d'aérosols.

Des améliorations ont d'abord été apportées au modèle de rayonnement 1D du logiciel CFD code_saturne. Ce modèle estime dorénavant le rayonnement global, direct et diffus, en prenant en compte l'impact des gaz atmosphériques, des aérosols et des nuages. Les simulations sont effectuées au SIRTA, observatoire atmosphérique en Ile-de-France, et comparées aux mesures de rayonnement effectuées dans cet observatoire. Une bonne estimation du rayonnement en ciel clair est obtenue en prenant en compte la présence d'aérosols dont les propriétés optiques sont estimées grâce à un chaînage avec la plateforme Polyphemus. Les nuages conduisent notamment à une forte atténuation du rayonnement et ils sont très complexes à modéliser en raison notamment de leur forte variabilité spatio-temporelle. Afin d'améliorer la modélisation en ciel nuageux, le modèle est couplé aux mesures sur site pour déterminer les propriétés optiques des nuages (épaisseur optique, fraction nuageuse). Différents tests de sensibilité sont conduits afin de mieux comprendre l'impact de ces propriétés et les instruments utilisables pour les mesurer. L'analyse de la comparaison entre rayonnement mesuré et calculé (réalisée pour le rayonnement global et sa composante directe) est basée à la fois sur des scores statistiques globaux et sur une étude détaillée des causes possibles des erreurs les plus importantes. Un second axe de la thèse a consisté à appliquer et valider ce modèle de rayonnement sur à un cas bien documenté de brouillard radiatif au SIRTA (campagne ParisFog) évoluant en stratus bas après sa dissipation. L'accent est porté sur la prise en compte des aérosols et notamment du carbone suie dans la composition des gouttelettes lors de la phase de dissipation, ainsi que sur l'hypothèse considérée pour la fraction nuageuse.

Dans un troisième axe, des améliorations sont apportées au modèle de rayonnement 3D de code_saturne pour la prise en compte des aérosols et nuages et en vue de son application à la modélisation d'une ferme PV. Une vérification du comportement du modèle est faite sur ce cas de brouillard radiatif, avec des comparaisons entre les résultats des modèles 1D et 3D.

Acronyms

1D one dimensional. [i](#), [ii](#), [xii](#), [xiv](#), [3](#), [4](#), [28](#), [29](#), [32](#), [33](#), [35](#), [40](#), [43](#), [44](#), [46–96](#), [119–127](#), [130–134](#), [163](#), [164](#)

2D two dimensional. [43](#), [47](#), [60](#), [161](#)

3D three dimensional. [i](#), [ii](#), [xii–xiv](#), [3](#), [4](#), [28](#), [29](#), [32](#), [33](#), [35](#), [40](#), [42](#), [43](#), [46–48](#), [60](#), [119–121](#), [123–127](#), [130–134](#), [163](#), [164](#)

AER Atmospheric and Environmental Research. [44](#)

ANN Artificial Neural Network. [31](#)

AOD Aerosol Optical Depth. [19](#), [56](#), [57](#), [63](#), [65](#), [137](#), [161](#), [165](#)

AOPs Aerosol Optical Properties. [32](#), [50](#), [53](#), [54](#), [56](#)

ARIMA Auto-Regressive Integrated Moving Average. [30](#)

ARMA Auto-Regressive Moving Average. [29](#), [30](#)

ART Atmospheric Research Team. [44](#)

BC Black Carbon. [22](#), [56](#), [96](#), [118](#), [119](#), [122](#)

CCN Cloud Condensation Nuclei. [17](#)

CDF Cumulative Distribution Function. [29](#)

CEREA Centre d’Enseignement et de Recherche en Environnement Atmosphérique. [3](#), [56](#)

CFD Computational Fluid Dynamics. [i](#), [ii](#), [3](#), [28](#), [47](#), [60](#), [121](#), [122](#)

COD Cloud Optical Depth. [xiii](#), [19](#), [21–23](#), [50](#), [52](#), [59](#), [60](#), [65–73](#), [75–81](#), [86](#), [87](#), [90](#), [91](#), [93](#), [121](#), [122](#), [138](#), [161](#), [162](#), [165](#)

COPs Cloud Optical Properties. [xi](#), [20](#), [49](#), [50](#), [52–54](#), [66](#), [68](#), [122](#), [161](#)

DHI Diffuse Horizontal Irradiance. [2](#), [24](#)

DISORT Discrete Ordinate Method for Radiative Transfer. [42](#), [44](#), [45](#), [59](#), [123](#), [125](#), [127](#), [132](#)

DNI Direct Normal Irradiance. [2](#), [24](#), [25](#), [45](#), [59](#)

Acronyms

- ECMWF** European Centre for Medium Range Weather Forecasts. [31](#), [56](#)
- EDF** Électricité De France. [1](#), [3](#), [47](#)
- EGU** European Geosciences Union. [4](#), [5](#)
- EMS** European Meteorological Society. [5](#)
- FARMS** Fast All-sky Radiative Model for Solar application. [43–46](#)
- GFDL** Geophysical Fluid Dynamics Laboratory. [32](#)
- GHI** Global Horizontal Irradiance. [2](#), [24](#), [25](#), [32](#), [59](#)
- GOES** Geostationary Operational Environmental Satellite. [46](#)
- GTI** Global Tilted Irradiance. [2](#)
- IFS** Integrated Forecasting System. [31](#), [44](#)
- IR** infrared. [7](#), [120](#), [123](#), [127](#), [130](#)
- Iwc** Ice water content. [22](#)
- IWP** Ice Water Path. [22](#)
- KS18** [Sartelet et al. \[2018a\]](#). [3](#), [47](#), [49–56](#), [59–63](#), [72](#), [161](#)
- LA21** [Al Asmar et al. \[2021a\]](#). [5](#), [49](#), [50](#), [52](#), [53](#), [56](#), [86](#), [87](#), [90](#), [91](#)
- LA21-2** [Al Asmar et al. \[2021b\]](#). [5](#), [21](#), [96](#), [118](#), [119](#)
- LCOE** Levelized Cost Of Energy. [3](#)
- LH74** [Lacis and Hansen \[1974\]](#). [32](#), [44](#), [47](#), [50](#), [52](#), [61](#), [82–84](#), [127](#)
- LIDAR** Light Detection and Ranging. [23](#), [65](#), [66](#), [71](#), [74](#), [80](#), [90](#), [93](#), [121](#)
- LLBRTM** Line by Line Radiative Transfer Model. [44](#)
- LW** longwave. [26](#)
- Lwc** Liquid water content. [21](#), [138](#)
- LWP** Liquid Water Path. [xiii](#), [21](#), [22](#), [52](#), [61](#), [65](#), [67–70](#), [73](#), [75](#), [76](#), [79–81](#), [87](#), [90](#), [91](#), [93](#), [94](#), [121](#), [122](#), [161](#), [162](#), [165](#)
- MBE** Mean Absolute Error. [91](#)
- MBE** Mean Bias Error. [63](#), [71–75](#), [78–80](#), [85](#), [89](#), [162](#), [165](#)

Acronyms

- MC** Monte-Carlo. [42](#), [46](#), [47](#), [123](#)
- MFBE** Mean Fractional Bias Error. [56](#), [57](#), [63](#), [85](#)
- MFE** Mean Fractional Error. [57](#)
- MRM** Meteorological Radiation Model. [43](#), [44](#)
- NCAR** National Centre for Atmospheric Research. [32](#)
- NMB** Normal Mean Bias. [72–74](#), [76](#), [78](#), [85](#), [162](#)
- NOA** National Observatory of Athens. [44](#)
- NOAA** National Oceanic and Atmospheric Administration. [32](#)
- NREL** National Renewable Energy Laboratory. [45](#)
- NWP** Numerical Weather Prediction. [xi](#), [28](#), [29](#), [31](#), [32](#), [35](#), [44](#), [59](#), [60](#), [73](#)
- PV** photovoltaic. [i](#), [ii](#), [xi](#), [1–4](#), [45](#), [58](#), [120](#), [122](#), [123](#), [134](#)
- PYR** Pyranometers/Pyrheliometer. [24](#), [65–67](#), [69–71](#), [73–75](#), [80](#), [86](#), [87](#), [90](#), [93](#), [161](#), [165](#)
- R&D** Research and Development. [3](#), [47](#)
- RADAR** Radio Detection and Ranging. [24](#)
- REF** Ground-reflected radiation. [2](#)
- RMSE** Root Mean Square Error. [50](#), [57](#), [67](#), [69](#), [71–76](#), [85](#), [86](#), [89](#), [90](#), [162](#)
- RRTM** Rapid Radiative Transfer Model. [32](#), [43](#), [44](#), [59](#)
- RTE** Radiative Transfer Equation. [xii](#), [xiii](#), [28](#), [29](#), [32](#), [33](#), [35](#), [40](#), [42–44](#), [120](#), [121](#), [123–127](#), [132](#), [163](#)
- SHDOM** Spherical Harmonics Discrete Ordinate Method. [46](#)
- SIR** solar infrared. [xiv](#), [14](#), [43](#), [50](#), [52](#), [56](#), [96](#), [120–122](#), [124–126](#), [128–131](#), [133–135](#), [137–141](#), [144](#), [163–165](#)
- SIRTA** Site Instrumental de Recherche par Télédétection Atmosphérique. [i](#), [ii](#), [xii](#), [6](#), [23](#), [24](#), [26](#), [27](#), [49–58](#), [60](#), [61](#), [63–73](#), [75–81](#), [87–92](#), [94](#), [96](#), [160–162](#), [165](#)
- SRRL** Solar Radiation Research Laboratory. [45](#)
- SSA** Single Scattering Albedo. [20](#), [22](#), [40](#), [52](#), [81](#), [118](#), [138](#), [139](#)
- SW** shortwave. [26](#)

Acronyms

UV ultraviolet. [7](#), [13](#), [120](#)

UV-vis ultraviolet-visible. [xiv](#), [43](#), [50](#), [52](#), [56](#), [96](#), [121](#), [122](#), [124–126](#), [128–135](#), [137–141](#), [144](#), [163–165](#)

WRF Weather Research Forecast. [xii](#), [32](#), [44](#), [49–54](#), [56](#), [60–63](#), [66](#), [68](#), [71](#), [73–78](#), [81](#), [82](#), [161](#), [162](#)

XZ14 [Zhang et al. \[2014\]](#). [96](#), [118](#), [119](#), [165](#)

Nomenclature

I_{wc}	Ice water content
L_{wc}	Liquid water content
\bar{R}_r	Albedo due to Rayleigh scattering
\bar{T}	Temperature
β_d	Scattering coefficient
β_e	Extinction coefficient
ϵ_λ	Emittance of the atmosphere
κ	Hygroscopicity of aerosols
λ	Wavelength
μ	Cosinus of the zenith angle
μ_0	Cosinus of the Solar zenith angle
ν_d	BC volume fraction
Ω	Solid angle
ω	Single scattering albedo
ω	Single scattering co-albedo
ω_a	Aerosol single scattering albedo
ω_c	Cloud single scattering albedo
ϕ	Azimuth angle
ϕ_0	Solar azimuth angle
ρ	Density
ρ_a	Air density
ρ_i	Ice density
ρ_l	Liquid water density

Nomenclature

σ_d	Standard deviation of the radius distribution
σ_B	Stefan-Boltzmann constant
τ	Optical depth
τ_a	Aerosol optical depth
τ_c	Cloud optical depth
τ_s	Scattering optical depth
τ_{abs}	Absorption optical depth
Θ	Angle between the incident light direction and the scattered light direction
θ	Zenith angle
θ_0	Solar zenith angle
A^G	Absorption function
c	Velocity of light
C_P	Specific heat at constant pressure
D	Total Transmission function
d_o	Cloud droplet diameter
D_P	Particle diameter
ds	Thickness
E	Radiance energy
E_λ	Emission of a real body
F	Total flux density of radiant energy or irradiance
$F \downarrow$	Downward fluxes
$F \uparrow$	Upward fluxes
F_0	Solar flux density
F_λ	Monochromatic flux density or monochromatic irradiance
F_C	Cloud Fraction
g	Asymmetry factor
g_a	Aerosol asymmetry factor

Nomenclature

g_c	Cloud asymmetry factor
I_λ	Monochromatic intensity or Radiance
J_λ	Source function
j_λ	Source function coefficient
k_λ	Absorption coefficient
k_T	Clearness index
L	Maximum ice crystal length
m	Optical air mass
$n(L)$	Ice crystal distribution
$n(r)$	Droplet size distribution
n	Cloud index
n_λ	Refractive index
N_d	Total number droplet
$P(\theta)$	Scattering phase function
Q_{ext}	Efficiency factor
R	Reflection function
r	Radius
r_0	Earth-sun mean distance
R_a	Dry radius
R_c	Cloud albedo
r_e	Mean effective cloud radius
R_g	Ground albedo
R_p	Planetary albedo
R_{wa}	Dry radius
RH	Relative humidity
S	Solar constant
S_{rad}	Heating rate

Nomenclature

T	Transmission function
T_{mg}	Transmission function for minor gases
U	Total Reflection function
V	Volume
x	Size parameter
z	Vertical height
z_{1D}	Altitude of the 1D domain
z_{3D}	Altitude of the 3D domain
z_{aero}	Altitude of the highest aerosol layer

Contents

1	General introduction	1
1.1	The energy transition and the expansion of photovoltaic (PV) power	1
1.2	PV power and solar irradiance	1
1.3	Thesis objectives	3
1.4	Thesis outline	4
2	Solar radiation: a general description	6
2.1	Introduction	6
2.2	Solar radiation: basic concepts and interaction with matter	7
2.2.1	Concepts and definitions	7
2.2.2	The depletion of radiation	10
2.2.2.1	Scattering	10
2.2.2.2	Absorption	11
2.2.2.3	Extinction	11
2.2.2.4	Emission	11
2.3	Solar radiation: from the top of the atmosphere to the ground	11
2.3.1	Composition and structure of the Earth's Atmosphere	12
2.3.1.1	Atmospheric absorption	13
2.3.2	Aerosols and clouds	14
2.3.2.1	Aerosols	14
2.3.2.2	Clouds and Fogs	17
2.3.2.3	Parametrization	19
2.3.2.4	Cloud Optical Properties (COPs)	20
2.3.3	Ground albedo	23
2.4	Solar radiation and atmospheric monitoring	23
2.4.1	Remote sensing techniques	23
2.4.2	In-situ measurements	24
2.4.2.1	Radiation monitoring instruments	24
2.4.3	Site Instrumental de Recherche par Télédétection Atmosphérique (SIRTA)	26
3	Solar radiation: numerical modeling	28
3.1	Introduction	28
3.2	An overview	29
3.2.1	Statistical models	29
3.2.2	Cloud imagery and satellite based models	30
3.2.3	Hybrid models	31
3.2.4	Numerical Weather Prediction (NWP) models	31

Contents

3.3	Radiative Transfer Equation (RTE)	32
3.3.1	The general equation of radiative transfer	33
3.3.2	Application to a plane parallel atmosphere	33
3.3.2.1	The RTE	33
3.3.2.2	Analytical resolution of the RTE	35
3.3.3	Application to a three dimensional (3D) medium	40
3.3.3.1	The RTE	40
3.3.3.2	Analytical resolution of the RTE	42
3.4	Radiative transfer numerical models	43
3.4.1	1D radiative models	43
3.4.1.1	1D integral models	43
3.4.1.2	1D multi-layered models	44
3.4.2	Modelling of solar irradiance in a cloudy atmosphere	45
3.4.3	3D radiative models	46
3.5	code_saturne solar radiation model	47
3.5.1	General description	47
4	The 1D integral radiative scheme of code_saturne	49
4.1	Introduction	49
4.2	Preamble: previous work and preparation of input data	50
4.2.1	Previous work and improvement of the solar radiative scheme	50
4.2.2	Preparation of input data	53
4.2.2.1	Simulations using WRF model	53
4.2.2.2	Simulations using the Polyphemos model	56
4.3	Article: Al Asmar et al. (2021): Improvement of solar irradiance modelling during cloudy-sky days using measurements	58
4.3.1	Abstract	58
4.3.2	Introduction	58
4.3.3	Methodology	60
4.3.3.1	The solar irradiance scheme of code_saturne	60
4.3.3.2	Input data	61
4.3.3.3	Simulated meteorological data	62
4.3.3.4	Simulated aerosol concentrations	63
4.3.3.5	Observational data at SIRTA	64
4.3.3.6	Determination of cloud properties	66
4.3.3.7	Cloud fraction	66
4.3.3.8	Cloud Optical Depth	67
4.3.3.9	Separation between clear-sky and cloudy-sky days	69
4.3.4	Model evaluation	71
4.3.4.1	Irradiance on clear-sky days	71
4.3.4.2	Irradiance on cloudy-sky days	72
4.3.5	Improvement of irradiance modelling on cloudy-sky days	73
4.3.5.1	Cloud Fraction	73
4.3.5.2	Cloud fraction equals to 1	73

Contents

4.3.5.3	Cloud Fraction extracted from measurements	73
4.3.5.4	Cloud optical depth	75
4.3.5.5	Satellite measurements	75
4.3.5.6	Estimation from LWP	75
4.3.6	Discussion	76
4.3.7	Conclusion	80
4.3.8	Appendix	81
4.3.8.1	Calculation of cloud optical properties	81
4.3.8.2	The irradiance model - integral method	82
4.3.8.3	Statistical indicators	85
4.4	Complementary works	86
4.4.1	Comparison with HelioSat models	86
4.4.2	Discussion on the parametrization developed for the COD	87
4.4.3	Supplement on the error discrepancies analysis	90
4.5	Summary	93
5	The multi-layered radiative scheme of code_saturne	96
5.1	Introduction	96
5.2	Article 2: Al Asmar et al. (2021): Modeling the contribution of aerosols to fog evolution through their influence on solar radiation	98
5.2.1	Abstract	98
5.2.2	Introduction	98
5.2.3	The layer-dependent scheme for solar radiation in code_saturne	100
5.2.4	The ParisFog experiment	101
5.2.4.1	Observations and simulation conditions	101
5.2.4.2	Fog-event simulation	103
5.2.4.3	Sensitivity tests	105
5.2.4.4	Sensitivity tests on the fog evolution	106
5.2.5	Conclusion	110
5.2.6	Appendix	111
5.2.6.1	Optical characteristics of aerosols and clouds	111
5.2.6.2	Estimation of solar radiation	112
5.3	Complementary notes	118
5.3.1	The domain of the simulation	118
5.3.2	Calculation of the Black Carbon Fraction in cloud droplets	118
5.4	Summary	119
6	General conclusion	120
6.1	Overview on the chapters	120
6.2	Future prospects	122
6.3	Implementation of a 3D radiative scheme in code_saturne	123
6.3.1	Introduction	123
6.3.2	Resolution of the RTE in code_saturne 3D radiative model	124

Contents

6.3.3	Calculation of the absorption coefficients from the 1D model	127
6.3.3.1	Estimations during clear-sky days of the equivalent absorption coefficient	128
6.3.3.2	Estimations during cloudy-sky days of the equivalent absorption coefficient	129
6.3.4	Comparison 1D/3D	130
6.3.4.1	Clear sky - without aerosols	130
6.3.5	Work in progress	130
6.3.6	Conclusion	132
A	Supporting Material	135
A.1	The 1D radiative scheme	135
A.1.1	Solar radiation at the upper limit of the atmosphere	135
A.1.2	Atmospheric parameters	136
A.1.2.1	Meshes	136
A.1.3	Clouds and aerosol optical properties	136
A.1.3.1	Parameterization of aerosols	137
A.1.3.2	Parameterization of clouds	138
A.1.4	Solar radiation modelling	139
A.1.4.1	UV-vis band (Absorption by ozone)	141
A.1.4.2	SIR band (Absorption by water vapor)	144
A.1.5	Total absorption and fluxes	145
	Bibliography	146
	List of Figures	159
	List of Tables	164

Chapter 1

General introduction

Contents

1.1 The energy transition and the expansion of photovoltaic (PV) power	1
1.2 PV power and solar irradiance	1
1.3 Thesis objectives	3
1.4 Thesis outline	4

1.1 The energy transition and the expansion of **photovoltaic (PV) power**

The energy transition is a pathway towards the decarbonization of the energy sector, which is vital to mitigate the effects of global climate change. Renewable energies are cornerstones of this energy transition, since they reduce carbon dependency. In the last years, the expansion of renewable energies has seen tremendous growth: at the end of 2020, global renewable generation capacity was equal to 2799 GW which represented 37 % of total electricity generation capacity. Solar energy accounted for 26 % of the global total, with a capacity of 733 GW (IRENA, figure 1.1). Global solar energy capacity addition in 2020 reached 125 GW and is expected to keep increasing. The forecast is dependent on the different country policies, speed of implementation, administration challenges, ... that are resumed in IEA [2020] but, in the accelerated case, global solar annual PV additions are expected to reach almost 165 GW during 2022-2035 [IEA, 2020].

Within this framework, the French electricity company **Électricité De France (EDF)** wants to install 30 GW of new solar capacity in France between 2020 and 2035 and this plan is part of the CAP2030 strategy of the group.

1.2 **PV power and solar irradiance**

PV generators convert the electromagnetic energy of solar radiation to electrical energy. Consequently, the production of electricity highly depends on the amount of solar irradiance arriving at its surface. Therefore, an accurate prediction of the amount of solar irradiance reaching the ground is necessary to reduce the uncertainty on **PV** energy-yield assessment, to optimize

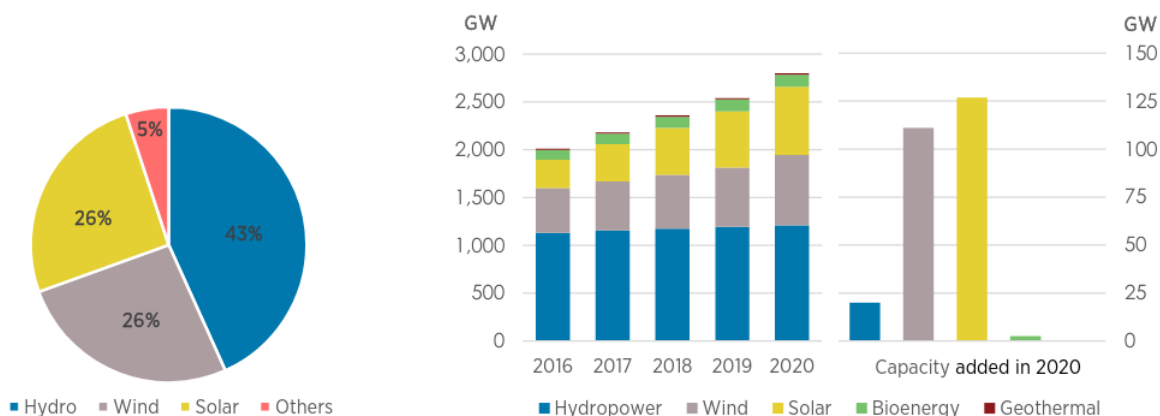


Figure 1.1: Global renewable generation capacity by energy source (left panel) and power capacity growth (right panel) by IRENA.

the performance of PV modules and to forecast the production at different time scales. Solar irradiance or the radiant flux density of sunlight (SI unit of W m^{-2}) can be separated into different components represented in figure 1.2:

- **Direct Normal Irradiance (DNI)**: the light that comes directly from the sun without any deviation in trajectory. It is measured on a surface perpendicular to the sun.
- **Diffuse Horizontal Irradiance (DHI)**: the solar irradiance measured on a horizontal surface. It comes from multiple diffusion and reflection by clouds, aerosols and molecules in the atmosphere. It also includes the part of radiation that has been reflected by the ground and which is scattered by the atmosphere back towards the horizontal plane.
- **Global Horizontal Irradiance (GHI)**: the total downward solar irradiance received by a surface horizontal to the ground

They are related by the following equation,

$$GHI = \cos\theta_0 DNI + DHI \quad (1.1)$$

where θ_0 is the zenith angle, the angle between the zenith and the centre of the Sun's disc. If a tilted surface is considered, it will also receive a small amount of **Ground-reflected radiation (REF)** that will be added to the diffuse sky radiation seen by the tilted plane (DTI) for the calculations of the **Global Tilted Irradiance (GTI)**, a crucial variable for PV assessment [Myers, 2017]. Thus, $GTI = \cos \theta_0 DNI + DTI + REF$.

The amount of solar irradiance reaching the ground is influenced by different geographical, meteorological and atmospheric parameters such as aerosols, atmospheric gases and clouds which significantly reduce solar irradiance at ground level. Those parameters have important spatio-temporal variations, leading to difficulties to accurately model solar irradiance. Various numerical models have been developed to calculate the surface solar irradiance, including the

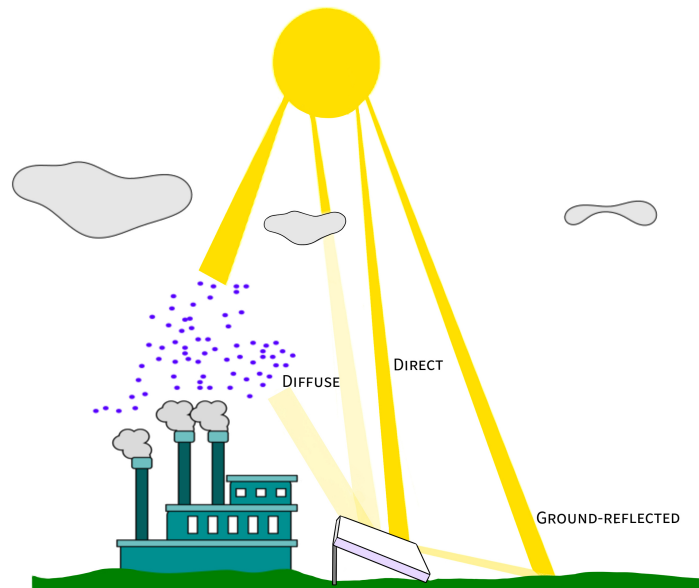


Figure 1.2: Schematic representation of the direct, diffuse and ground-reflected irradiance.

radiation model of the CFD software `code_saturne` developed by EDF R&D that has been used in its **one dimensional (1D)** version in Sartelet et al. [2018a] (referred to as **KS18**) to estimate solar irradiance in Palaiseau, Île-de-France and in Carpentras, Provence in France. The model has so far successfully estimated solar irradiance during clear-sky days in August 2009, but overestimated it during cloudy-sky days. However, clouds strongly influence the solar fluxes at the surface, as they cover more than 70% of the globe Stubenrauch et al. [2012]. They also occur frequently in some parts of the world, an example being the Paris region. Furthermore, the production of **PV** power could also be affected by shading and **PV** module temperature. More specifically, the performance of a **PV** farm can be negatively impacted by the shading of surrounding obstacles or of the **PV** modules which constitutes the farm. For such application, it is necessary to have a **three dimensional (3D)** estimation of radiation on the **PV** panel. EDF R&D performs different research activities aiming at reducing the **Levelized Cost Of Energy (LCOE)** of **PV** energy and increasing the operational performance of solar farms. This thesis was undertaken in the framework of this program, especially to improve the solar resource estimation. It carried out at the **CEREA** laboratory (Atmospheric Environment Research and Teaching centre). It is a joint laboratory between EDF R&D and the French engineering school Ecole des Ponts ParisTech that is strongly involved in the research activities related to sustainable development and renewable energies' development.

1.3 Thesis objectives

Considering the diverse problematic raised above, the scientific questions that we want to address in this thesis are: how can we improve the solar irradiance modelling in cloudy or foggy

atmospheres? What **1D** model (*integral* or *multi-layered* model ¹) is more appropriate for the estimation of surface solar fluxes using code_saturne? How can we consider the shadow effect in a **PV** farm with code_saturne?

In order to attempt answering the scientific questions and to provide industrial solutions, the workload provided for this thesis followed three main objectives:

Objective 1: *Improvement of the 1D integral radiation model in a cloudy atmosphere using measurements and verification of its robustness on a long period.*

Objective 2: *Modelling the vertical profile of flux divergence using the 1D multi-layered model and taking into account the contribution of aerosols to a fog evolution through their influence on solar radiation*

Objective 3: *Development of the 3D model and comparison to the 1D model in horizontal homogeneous conditions*

Hence, this thesis deals with the estimation of solar irradiance using code_saturne and the improvement of the radiation model during cloudy-sky day, as well as its validation using its **1D** and **3D** modules. The industrial objectives consist in disposing a new solar radiative scheme in code_saturne, in its **1D** and **3D** versions, and to prepare this new module for its application to the conception phase of a **PV** farm.

1.4 Thesis outline

The thesis is structured as follows:

- **Chapter 2** gives a general description of solar radiation and its propagation through the atmosphere. Remote sensing and in-situ measurement techniques are also presented.
- **Chapter 3** presents a review on the numerical modelling of solar irradiance, the radiative transfer equation and its resolution as well as the code_saturne radiation scheme.
- **Chapter 4** details the improvements introduced in code_saturne radiation scheme (*integral* model) for the calculations of solar downward fluxes at the earth's surface, its validation on a long period particularly for cloudy sky days.
- **Chapter 5** presents the ability of the model to calculate the vertical profile of flux divergence and the validation of the *multi-layered* model on a case of a fog. Moreover, sensitivity tests are conducted to model the contribution of aerosols in solar radiation on fog dissipation.
- **Chapter 6** summarizes the work done for this thesis and provides conclusions. Future perspectives are also given, and the first works done for the implementation of the **3D** radiation scheme of code_saturne and comparison to the results obtained with the **1D** scheme are provided.

In the framework of this thesis, two articles were written which constitute parts of the manuscript and two papers were presented to the two conferences [European Geosciences](#)

¹The concept of integral and multi-layered model is introduced in section [3.3.2](#)

Union (EGU) and European Meteorological Society (EMS):

Journal articles:

Al Asmar L., Musson-Genon L., Dupont E., Dupont J-C.& Sartelet K. (2021): Improvement of solar irradiance modelling during cloudy-sky days using in-situ measurements, *Solar Energy* (referred to as [LA21](#)).

Al Asmar L., Musson-Genon L., Dupont E., Ferrand M. & Sartelet K.: Modelling the contribution of aerosols to fog evolution through their influence to solar radiation *Submitted to MDPI Climate journal* (referred to as [LA21-2](#)).

Conference communication:

Al Asmar L., Musson-Genon L., Dupont E.& Sartelet K. (2021): Improvement of solar irradiance modelling during cloudy-sky days using in-situ and satellite measurements. [EGU](#) General Assembly 2021, online, 19–30 Apr 2021, EGU21-3007, <https://doi.org/10.5194/egusphere-egu21-3007>, 2021.

Al Asmar, L., Musson-Genon, L., Dupont, E., and Sartelet, K. (2021): Study on the role of Black Carbon aerosols in cloud droplets during the dissipation of a fog., [EMS](#) Annual Meeting 2021, online, 6–10 Sep 2021, EMS2021-72, <https://doi.org/10.5194/ems2021-72>, 2021

Chapter 2

Solar radiation: a general description

2.1 Introduction

The sun is a star with a radius of 696 105 km and a surface temperature of 5800 K. It produces a huge amount of energy and emits it at a rate of $6.7 \times 10^7 \text{ W m}^{-2}$, which makes it the Earth's primary natural source of energy [Liou, 2002]. As soon as solar irradiance gets closer to the Earth's surface, it interacts with different atmospheric components like gas, molecules, aerosols and clouds, which vary with the season and geographic location on Earth. This thesis focuses on upgrading the solar irradiance model of code_saturne that considers the different interactions of light with the atmosphere to calculate the total amount of radiation that reaches the Earth's surface at a specific location. Moreover, it focuses on the interaction of radiation with clouds or fogs. The numerical simulations that are conducted require different meteorological measurements for the description of atmospheric parameters and for comparison purposes. On that account, for a better understanding of the radiation model of code_saturne and the studies that were conducted in this thesis, this chapter presents the fundamental radiative processes that form the physical basis of radiative transfer in the earth's atmosphere as well as the methods used to measure the radiation and related parameters. Consequently, section 2.2 introduces the basic concepts and definitions and section 2.3 describes the composition of the atmosphere and focuses on aerosols, clouds and fogs. The remote sensing techniques and in-situ measurements, and the SIRTA site, are briefly introduced in section 2.4.

Contents

2.1 Introduction	6
2.2 Solar radiation: basic concepts and interaction with matter	7
2.2.1 Concepts and definitions	7
2.2.2 The depletion of radiation	10
2.3 Solar radiation: from the top of the atmosphere to the ground	11
2.3.1 Composition and structure of the Earth's Atmosphere	12
2.3.2 Aerosols and clouds	14
2.3.3 Ground albedo	23
2.4 Solar radiation and atmospheric monitoring	23
2.4.1 Remote sensing techniques	23
2.4.2 In-situ measurements	24

2.2 Solar radiation: basic concepts and interaction with matter

This section aims at defining the basic parameters used to define solar radiation. Moreover, it describes the attenuation of radiation that occurs when it propagates in a medium.

2.2.1 Concepts and definitions

Solar radiation The electromagnetic radiation spectrum, shown in figure 2.1, represents the complete range of wavelengths of electromagnetic radiation: from the longest radio waves through visible light and all the way to the shortest gamma rays.

Due to its extremely high temperature and the energy it radiates, the sun emits short wave radiation. Once it reaches the Earth's atmosphere, it gets absorbed by clouds and the surface. The ground heats up and re-emits energy. The earth being cooler than the sun, it emits long wave radiation in the form of infrared rays.

In contrast to long wave radiation, short wave radiation has shorter wavelength and therefore higher frequency and energy. When it enters our atmosphere, it gets absorbed by numerous atmospheric components and the solar energy that reaches the ground is in the range $[0.3 - 4]\mu\text{m}$ and lies partly in the **ultraviolet (UV)** range, visible range and **infrared (IR)** range.

Solar constant S The solar constant S is the amount of total solar energy reaching the top of the atmosphere. It is defined as the flux of solar energy at the mean distance between the sun and the earth across a surface of unit area normal to the solar beam.

The solar constant is computed using an energy conservation principle [Liou, 2002]:

$$S = F_0 \left(\frac{r}{r_0}\right)^2 \quad (2.1)$$

where r_0 is the earth-sun mean distance, F_0 is the solar flux density, in W m^{-2} , at the top of the atmosphere when the instantaneous distance between the earth and the sun is r . A mean value of the solar constant is 1365 W m^{-2} .

Solid angle The solid angle Ω is defined as the ratio of the area σ of a spherical surface intercepted by a cone to the square of its radius r :

$$\Omega = \sigma/r^2 \quad (2.2)$$

Thus, the differential solid angle in polar coordinates is:

$$d\Omega = d\sigma/r^2 = \sin\theta d\theta d\phi \quad (2.3)$$

where θ and ϕ are the zenith and azimuthal (or azimuth) angles respectively (figure 2.2). For an observer on earth, the sun describes a course in the sky, from east to west, which is

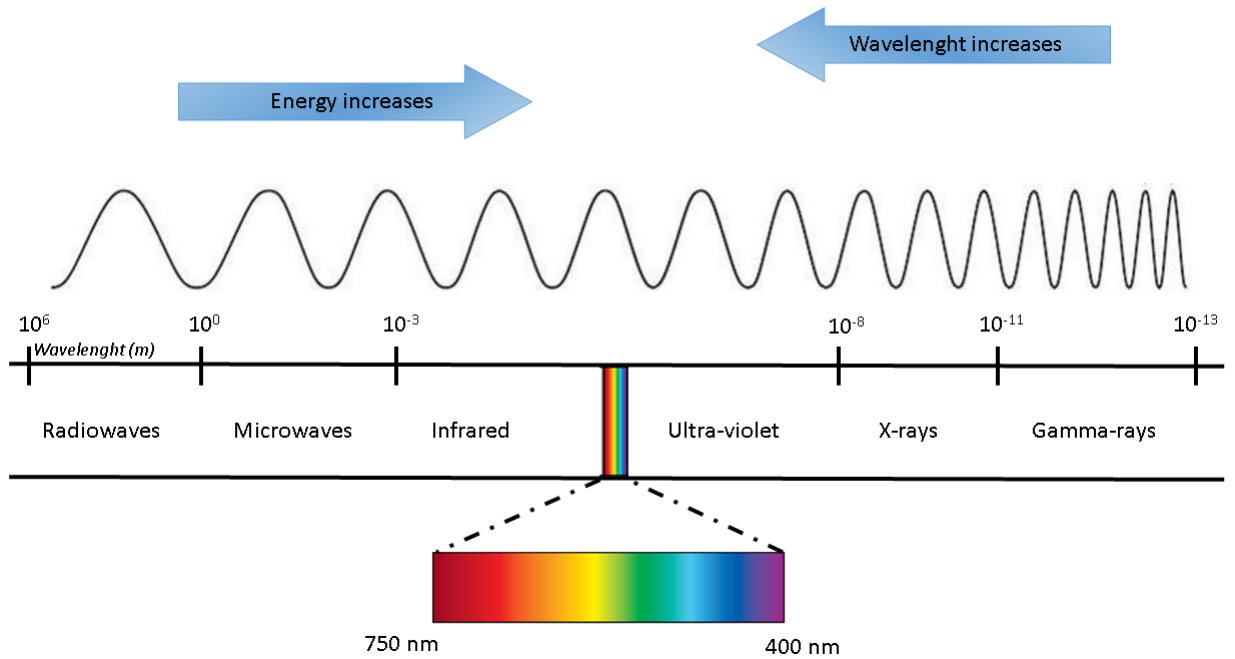


Figure 2.1: Electromagnetic radiation spectrum

described by the solar zenith angle and the solar azimuth. The solar azimuth ϕ_0 is defined as the angle between the projection of the direction of the sun on the horizontal plane and the north, and increasing clockwise. The solar zenith angle θ_0 is the angle formed by the direction of the sun and the local vertical (zenith) (figure. 2.3).

Radiance The monochromatic intensity or radiance I_λ is the differential amount of radiant energy dE_λ in a time interval dt and in a specified wavelength interval $[\lambda, \lambda + d\lambda]$ which crosses an element of area dA in directions confined to a differential solid angle $d\Omega$ (the area considered is defined as perpendicular to the propagation direction represented by the zenith and azimuth angles (θ, ϕ) ; $\cos \theta dA$ then represents the projection of dA perpendicular to the propagation direction) [Liou, 2002]:

$$I_\lambda = \frac{dE_\lambda}{\cos \theta d\Omega d\lambda dt dA} \quad (2.4)$$

It can be expressed in W/m^3 and is also known as the brightness or luminance. The luminance is then the radiant energy per area per time per frequency and per steradian, and therefore it is a function of direction.

Irradiance The monochromatic flux density or the monochromatic irradiance is defined by the normal component of I_λ integrated over the entire hemispheric solid angle and can be

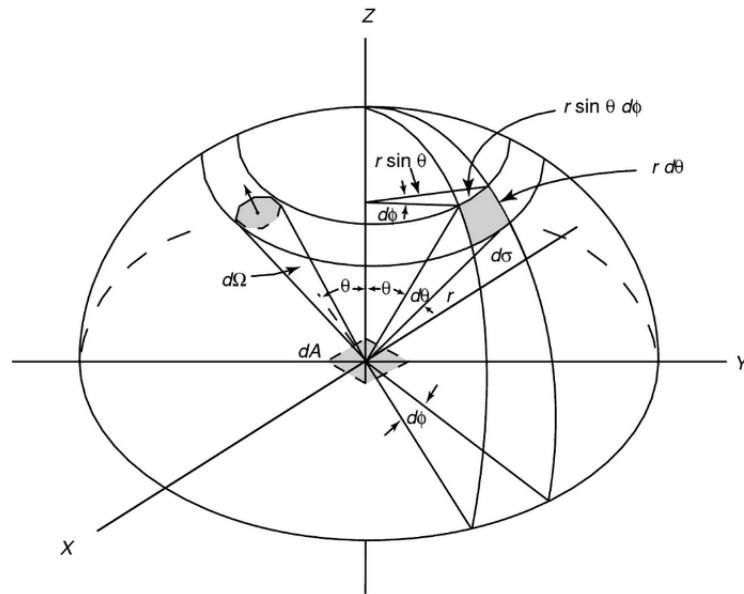


Figure 2.2: Illustration of the differential solid angle $d\Omega$ in polar coordinates and the zenith θ and azimuthal ϕ angles. [Liou, 2002]

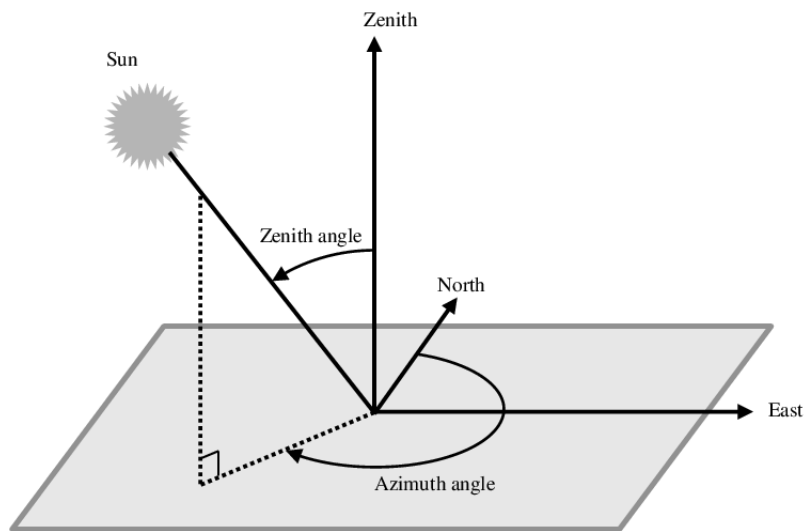


Figure 2.3: Illustration of the solar zenith θ_0 and azimuthal ϕ_0 angles. [Nou et al., 2016]

expressed as [Liou, 2002]:

$$F_{\lambda} = \int_{\Omega} I_{\lambda} \cos\theta d\Omega \quad (2.5)$$

The total flux density of radiant energy, or irradiance, F is the integration over all wavelengths of the monochromatic irradiance and is expressed in W/m^2 . It is the energy flux onto a flat surface. It usually refers to the energy per unit time and unit area on a horizontally oriented flat surface. It is the quantity which describes the flux on a specific receiver.

2.2.2 The depletion of radiation

When radiation is propagated in a medium, it gets attenuated by the particles and gases composing the medium. The processes affecting the radiation are: the scattering, absorption, extinction and emission phenomena which are described in the following subsection.

2.2.2.1 Scattering

Most of the light that reaches our eyes does not come directly from its source, but indirectly through the process of scattering: land and water surfaces and the objects surrounding us are visible through the light that they scatter.

Scattering is a physical process associated with light and its interaction with matter. It occurs at all wavelengths. A particle or molecule in the path of incoming light deflects the incident wave and re radiates that energy in all directions. In the atmosphere, the particles responsible for scattering range in size from gas molecules ($\sim 10^{-4} \mu\text{m}$) to aerosols ($\sim 1 \mu\text{m}$), water droplets ($\sim 10 \mu\text{m}$) and ice crystals ($\sim 100 \mu\text{m}$) [Liou, 2002].

The atmosphere contains many particles and molecules, thus a particle or molecule can scatter the light that has already been scattered by other particles or molecules. This process is called *multiple scattering*.

The effect of particle size on scattering depends on the size parameter x defined as the ratio of the particle circumference to the incident wavelength λ : $x = \frac{2\pi r}{\lambda}$, where r is the particle radius:

- The scattering can be described by Rayleigh's law when particles are much smaller than the incident wavelength ($x \ll 1$). This law states that the amount of scattering is inversely proportional to the fourth power of the wavelength: $I \propto \frac{1}{\lambda^4}$. It is used for the interaction of radiation with **gas molecules**.

It implies that the long wavelengths are much less scattered by the particles than the smaller ones.

- The scattering is described by Mie's law [Mie, 1908] for particles whose size is comparable to or slightly greater than the wavelength ($x \gtrsim 1$); it is known as Mie's scattering. It is used to describe interactions of light with **aerosols**.
- The geometric scattering without Mie calculation is applied when particles are much larger than the wavelength ($x \gg 1$). It is applied when light interacts with **water drops**. In this case, scattering is no longer dependent on the wavelength.

2.2.2.2 Absorption

Scattering is often accompanied by absorption. The energy absorbed by molecules at a given wavelength is converted into another form of energy and is no longer present in the light. It only occurs at specific wavelengths. The Beer-Lambert law estimates the attenuation of a monochromatic light I_λ :

$$\frac{dI_\lambda}{ds} = -k_\lambda(s)I_\lambda \quad (2.6)$$

where k_λ is the absorption coefficient at a wavelength λ , it depends on the medium light is travelling through.

2.2.2.3 Extinction

Both scattering and absorption remove energy from the light traversing the atmosphere. The radiation is attenuated, and this phenomenon is the extinction. Thus, extinction is a result of scattering and absorption, and it is also wavelength dependent. For particles whose size is comparable to or slightly greater than the wavelength ($x \gtrsim 1$), Mie's law can be applied.

2.2.2.4 Emission

The absorption of energy by particles and molecules leads to emission. In fact, as the atmosphere has its own temperature, it emits energy inside its own spectral domain. The Stefan-Boltzmann law states that the total energy emitted by a black body is proportional to the fourth power of its absolute temperature \bar{T} :

$$B(\bar{T}) = \int_0^\infty B_\lambda(\bar{T})d\lambda = \sigma_B \bar{T}^4 \quad (2.7)$$

where σ_B is the Stefan-Boltzmann constant. The atmosphere doesn't, however, behave as a black body. The emittance of the atmosphere $\epsilon_\lambda(\bar{T})$ need to be added to the formula. The emission of a real body is described as:

$$E_\lambda(\bar{T}) = \epsilon_\lambda(\bar{T})B_\lambda(\bar{T}) \quad (2.8)$$

$\epsilon_\lambda(\bar{T})$ is the ratio of the flux emitted by a body to the flux emitted by a black body at the same temperature [Cotton and Anthes, 1992]. In a cloudy atmosphere, it varies with the liquid water content and particle spectra in clouds (see section 2.3.2.2).

2.3 Solar radiation: from the top of the atmosphere to the ground

Due to the different physical processes presented in section 2.2.2, when solar radiation makes its way from the top of the atmosphere to the ground, it gets diminished as soon as it interacts with the atmosphere. As a consequence, on average, less than half of extra terrestrial radiation reaches ground level (figure 2.4). Afterwards, some of it gets reflected by the ground. A deeper understanding of the atmosphere and its constituents is useful for the comprehension of these

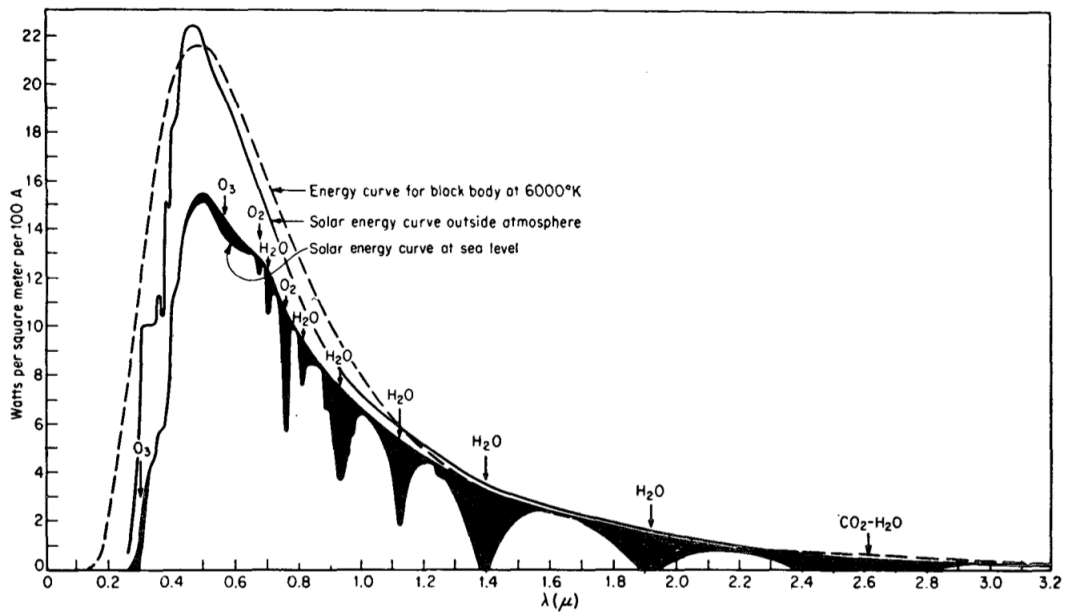


Figure 2.4: Spectral energy curve outside the atmosphere and at sea level. The darkened areas represent gaseous absorption in the atmosphere (Lacis and Hansen [1974] (referred to as LH74)).

phenomena. Therefore, the composition and structure of the Earth's atmosphere is provided in the following subsection. Moreover, as aerosols and clouds have an important impact upon radiative transfer, a detailed presentation is provided before introducing the surface reflectivity or ground albedo.

2.3.1 Composition and structure of the Earth's Atmosphere

For a better description of the interactions of the atmosphere with solar radiation, it is necessary to understand the atmosphere's composition and structure. The atmosphere is divided into four distinct layers as it can be seen in figure 2.5 which represents the vertical temperature profile for the standard atmosphere:

- The troposphere (lower atmosphere) which is characterized by a decrease of temperature.
- The stratosphere (middle atmosphere) which is characterized by an isothermal layer and then an increase of temperature. Ozone is present in this layer.
- The mesosphere (middle atmosphere) where temperature decreases.
- The thermosphere (upper atmosphere) where temperature is constant.

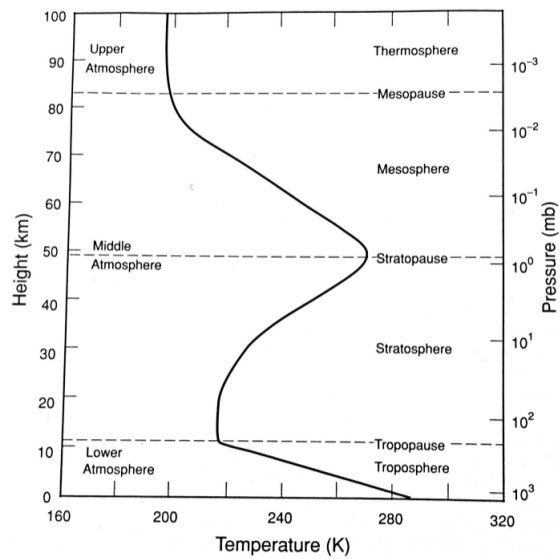


Figure 2.5: Vertical temperature profile [Liou, 2002]

The Earth's atmosphere is mainly composed of two groups of gas: those with nearly steady concentrations and those with variable concentrations. Table, in figure, 2.6 lists the chemical formulas and volume ratios for the concentrations of permanent and variable gases present in the atmosphere.

Nitrogen, oxygen and argon account for more than 99.96 % of the atmosphere. Variable gases are extremely important in the radiation budget of the atmosphere, even if their concentration is small. Water vapour is the major radiative and dynamic element. It is followed by ozone. Stratospheric ozone at altitude going from 15 to 30 km is responsible for the absorption of ultraviolet radiation, it is essential to life on earth.

The atmosphere also contains various kinds of precipitation, aerosols and clouds, which are known to be highly variable in space and time. Aerosols are solid or liquid particles in a surrounding gas and can be produced by natural processes as well as human activities Titos Vela [2014]. They modify the stability of the troposphere, the amount of solar radiation reaching Earth's surface and the formation of clouds. Clouds which micro-physical composition depends on the cloud type cover more than 70 % of the sky and may generate precipitation. Aerosols and clouds are further detailed in section 2.3.2.

2.3.1.1 Atmospheric absorption

Absorption of short wave radiation in the atmosphere (in the range $[0.3 - 4]\mu\text{m}$) occurs in a series of wavelength bands. The gaseous absorption is represented in figure 2.4. The primary gaseous absorbers are ozone and water vapour. The absorption of solar flux in the UV and visible ($0.3-0.7 \mu\text{m}$) band is dominated by the absorption by ozone. It takes place in the thermosphere and in the mesosphere. There is also weak absorption by ozone in the visible and

Permanent constituents		Variable constituents	
Constituent	% by volume	Constituent	% by volume
Nitrogen (N ₂)	78.084	Water vapor (H ₂ O)	0–0.04
Oxygen (O ₂)	20.948	Ozone (O ₃)	0–12 × 10 ⁻⁴
Argon (Ar)	0.934	Sulfur dioxide (SO ₂) ^b	0.001 × 10 ⁻⁴
Carbon dioxide (CO ₂)	0.036	Nitrogen dioxide (NO ₂) ^b	0.001 × 10 ⁻⁴
Neon (Ne)	18.18 × 10 ⁻⁴	Ammonia (NH ₃) ^b	0.004 × 10 ⁻⁴
Helium (He)	5.24 × 10 ⁻⁴	Nitric oxide (NO) ^b	0.0005 × 10 ⁻⁴
Krypton (Kr)	1.14 × 10 ⁻⁴	Hydrogen sulfide (H ₂ S) ^b	0.00005 × 10 ⁻⁴
Xenon (Xe)	0.089 × 10 ⁻⁴	Nitric acid vapor (HNO ₃)	Trace
Hydrogen (H ₂)	0.5 × 10 ⁻⁴	Chlorofluorocarbons	Trace
Methane (CH ₄)	1.7 × 10 ⁻⁴	(CFCl ₃ , CF ₂ Cl ₂)	
Nitrous oxide (N ₂ O) ^b	0.3 × 10 ⁻⁴	CH ₃ CCl ₃ , CCl ₄ , etc.)	
Carbon monoxide (CO) ^b	0.08 × 10 ⁻⁴		

^a After the U.S. Standard Atmosphere (1976) with modifications.

^b Concentration near the earth's surface.

Figure 2.6: Concentrations of permanent and variable gases in the atmosphere [Liou, 2002].

near infrared (SIR) bands. Rayleigh scattering of short wave radiation back to space occurs mainly at wavelength of less than 0.8 μm and depletes the available flux. In the SIR band (0.7–4 μm), water vapour absorbs a significant amount of solar flux in the lower atmosphere. The carbon dioxide CO₂ molecules absorb in different wavelengths of the SIR band. Its strongest absorption occurs at 2.7 μm , and it overlaps with H₂O absorption and contributes to solar flux absorption in the lower stratosphere. Oxygen O₂ and nitrogen N₂ main absorption occurs at wavelength shorter than 0.3 μm , where nearly all incoming radiation in the upper atmosphere gets absorbed. Other minor gases, like Nitric oxide NO, Nitrogen dioxide N₂O, Carbon monoxide CO, Methane CH₄ absorb relatively little energy from the sun either because they occur in too small quantities or because they are dissociated at high levels. However, they have been measured and parametrized by numerous researchers like Psiloglou et al. [1997, 2000].

2.3.2 Aerosols and clouds

First aerosols, then clouds and fogs, are defined here. Later on, the parametrization of their optical properties are detailed, and special attention is given to the optical properties of cloud.

2.3.2.1 Aerosols

Definition An aerosol can be defined as a suspension of liquid or solid particles in a gas [Seinfeld and Pandis, 1998]. Figure 2.7 represents the different types of atmospheric aerosols. Principal modes, sources, particle formation and removal mechanism are also indicated. Aerosols can originate from different sources: they can either exist naturally in the atmosphere and are issued from the erosion of rocks, volcanic eruption, sea salt emitted from the oceans, mineral desert dust... or they can have anthropogenic origins and come from road traffic, energy production by coal factories etc. Aerosols are removed from the atmosphere by different mecha-

nism: incorporation into cloud droplets and rain out or by sedimentation or mechanical action from the wind. Their lifetime can span from a few hours to a few weeks, even longer if they are present in the stratosphere (like after the eruption of Mount Pinatubo in 1991). Their size is also variable: it ranges from a few nanometres to several hundreds of micrometers. The most common way to present particle size distribution for atmospheric aerosols is in terms of the three modes [Titos Vela, 2014]:

- The Aitken or Nuclei mode: it includes particles that are emitted from combustion processes or formed in the atmosphere by gas-to-particle conversion. They are transformed through coagulation and condensation into particles of the accumulation mode and cloud processing ($D_P < 0.1 \mu\text{m}$; where D_P is the particle diameter). Nuclei particles have relatively short lifetimes in the atmosphere.
- The accumulation mode ($0.1 < D_P < 2.5 \mu\text{m}$): it includes combustion, smog and coagulated nuclei-mode particles. Particles in this mode are small, but they coagulate too slowly to reach the coarse-particle mode. Hence, they have a relatively long lifetime in the atmosphere, and they account for most of the visibility effects of atmospheric aerosols. Rain-out (e.g. cloud droplets formation) or washout (collision of rain droplets or snowflakes) are the main removal mechanism. The nuclei and accumulation modes together constitute “fine” particles.
- Coarse mode ($2.5 < D_P < 10 \mu\text{m}$): they consist of windblown dust, large salt particles and mechanically generated anthropogenic particles. They have a lifetime in the atmosphere of only a few hours and are removed from it through sedimentation in addition to rain out or washout.

Moreover, particles with a diameter smaller than $2.5 \mu\text{m}$ are known as $\text{PM}_{2.5}$ and those with a diameter smaller than $10 \mu\text{m}$ are known as PM_{10} .

Effect of aerosols Aerosol particles with anthropogenic origins affect the environment and are linked with visibility degradation Titos Vela [2014]. Aerosols can also affect human health by entering the human respiratory and cardiovascular system and damaging cells and organs. In contrast to PM_{10} particles that are not absorbed by the human respiratory system, the particles $\text{PM}_{2.5}$ are responsible for the worst effect for human health.

In addition, aerosols perturb earth’s energy and influence the climate in two different ways: directly and indirectly. The direct effect is the mechanism of scattering and absorption of solar radiation by particles (as detailed in section 2.2.2). The indirect effect is related to cloud condensation nuclei: an increase in the concentration of aerosols increases the cloud condensation nuclei, that leads to more cloud droplet with smaller radii for a constant liquid water content. Atmospheric aerosols affect the cloud formation processes in different way, like modifying the cloud albedo, the cloud radiative forcing (CRF) or precipitation patterns. [Seinfeld and Pandis, 2016, Sarangi et al., 2018].

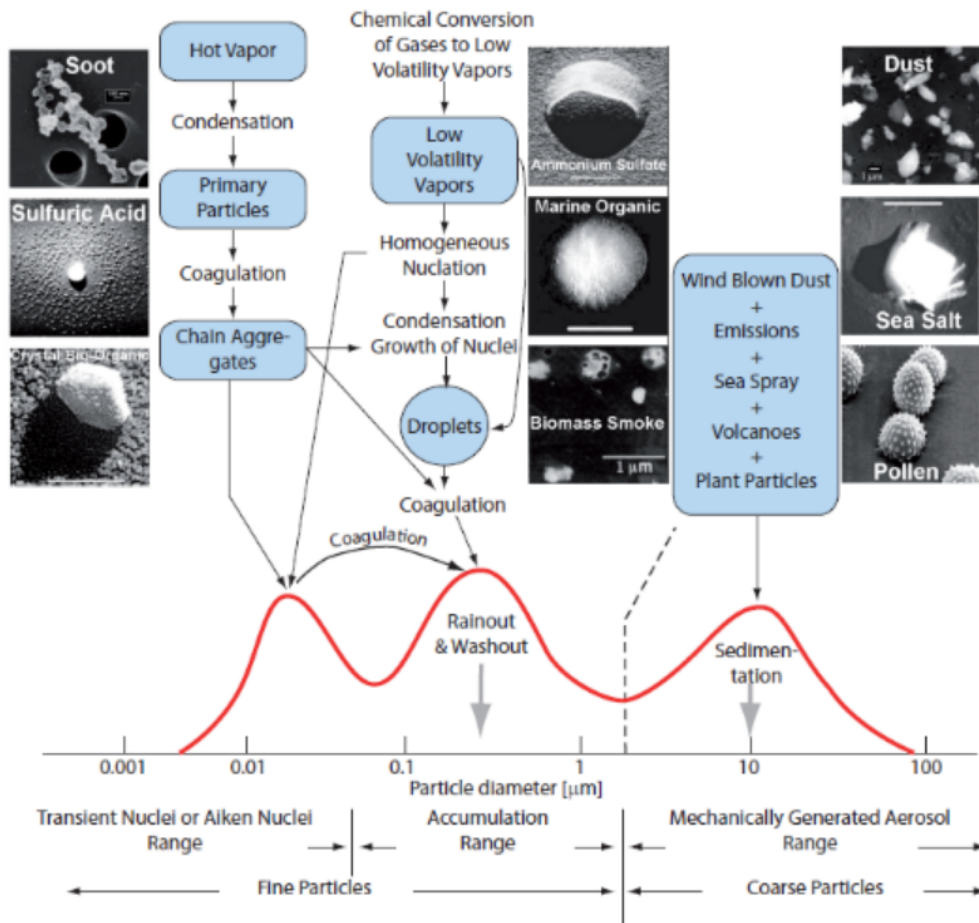


Figure 2.7: Schematic representation of the distribution of an atmospheric aerosol. Principal modes, sources, and particle formation and removal mechanisms are indicated [Seinfeld and Pandis, 1998]

2.3.2.2 Clouds and Fogs

Clouds are any visible mass suspended in the air and composed of water droplets, ice crystals, or a mixture of both. They cover more than 70 % of the planet earth and are the most important regulators of the radiation budget of the earth atmosphere system [Liou, 2002]. Particle concentration, size distribution and shape, and cloud thickness and geometry influence the transfer of radiation. Fogs can be defined as clouds close to the surface. The formation, classification, and parametrization of clouds and fogs are detailed here.

Cloud formation and cloud types Clouds are formed in rising cool air - or sufficiently humid air - that allows the activation of aerosol particles, that serves as **Cloud Condensation Nuclei (CCN)**, into cloud droplets in supersaturated air. The nucleated cloud particles are initially very small, but they grow by vapour deposition and collision-coalescence. The size distribution, the chemical composition and the number of particles have a great influence on **CCN** activation and consequently on chemical composition, size distribution and number of cloud droplets.

Clouds exist in the troposphere, stratosphere and mesosphere and can be categorized in different groups (represented in figure 2.8). There are two main types which define the suffixes of their given names:

- '*Cumulus*': it includes clouds formed by air rising due to positive or negative buoyancy. They are puffy with vertical development.
- '*Stratus*': clouds that are formed from a forced lifting of air. They are layered clouds with no vertical development.

Depending on the altitude level they are found in, there are:

- High level clouds *Cirro* (at 5-13 km of altitude) - *Cirrus*, *cirrocumulus* and *cirrostratus* - includes clouds composed of ice crystal. Technically, these clouds produce precipitation, but it never reaches the ground. Instead, it re-evaporates, creating virga clouds.
- Mid-level clouds *Alto* (at 2-7 km of altitude) - *Altostratus* and *Altostratus*
- Low clouds *strato* (at 0-2 km of altitude) *stratus*, *stratocumulus*, and *Nimbostratus* - stratus and stratocumulus clouds do not produce precipitation while nimbostratus clouds are often associated with heavy rain
- Multi-level Clouds- *cumulus*, *cumulonimbus* - are clouds that have a large vertical build-up. They can spread through the lower, middle, and upper cloud levels.

Fog Similar to clouds, a fog is a humid air mass containing microscopic, activated water droplets (or, in cold areas, ice crystals) but it is in direct contact with the Earth's surface. The American Meteorology Society, 2021 defines clouds as the reduction of visibility to below 1 km due to the presence of suspended water droplets in the vicinity of the Earth's surface. Because visibility is reduced during a fog event, it is associated with increased hazards in

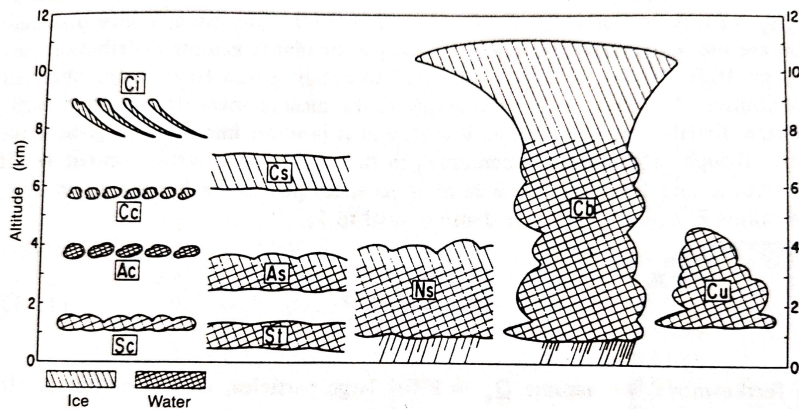


Figure 2.8: Schematic representation of various clouds. Ci: cirrus, cc: cirrocumulus, Ac: altostratus, Sc: stratocumulus, Cs: cirrostratus, At: altostratus, St: stratus, Ns: nimbostratus, Cb: cumulonimbus, Cu: cumulus. [Lenoble, 1993]

road, maritime and air traffic. Fog may also contribute in reducing air pollution because the wet deposition of pollutants is more efficient through fog than rain due to the larger droplet surface area and the longer residence time near the surface [Wærsted, 2018]. When the air near the surface becomes supersaturated with water vapour, droplets grow to micrometer sizes, which forms a fog. The increase of water vapour content, the reduction of air temperature or a combination of both can lead to the supersaturation of the air and therefore to the formation of fogs. Therefore, we can define different fog types depending on the meteorological conditions that resulted in the fog formation; for e.g. advection fog, precipitation fog, ice fog, radiation fog, ... In the present work, we are interested in radiation fogs. It forms when the air just above the surface is supersaturated due to the cooling of the earth's surface through the emission of long wave radiation, it usually occurs during the night in clear-sky situations. [Haeffelin et al., 2010]. It is associated with anticyclones above land. The formation of radiation fog is highly dependent on the wind. Due to turbulent mixing, strong winds dilute the cooling and moistening in a too thick layer that block the occurrence of supersaturation, whereas, too low wind leads to dew deposition instead of a fog [Wærsted, 2018]. Three evolutionary stages have been identified for the life cycle of a radiation fog, and some of the physical processes that impact the liquid water of the fog are schematically represented in figure 2.9 [Wærsted, 2018] :

- Formation phase: it consists of the formation of small cloud droplets that will form the fog. It often starts by a thin layer just above the cold surface, but it can also form at a few tens of metres of altitude that is rapidly thickened downward to the surface
- Development phase: it represents the thickening of the fog. The thin layer of fog develops vertically, and it will have a significant emissivity so that the radiative cooling gets transferred from the surface to the top of the fog. This cooling at the top will make the initially stable fog layer neutrally stratified, which enhances vertical mixing.

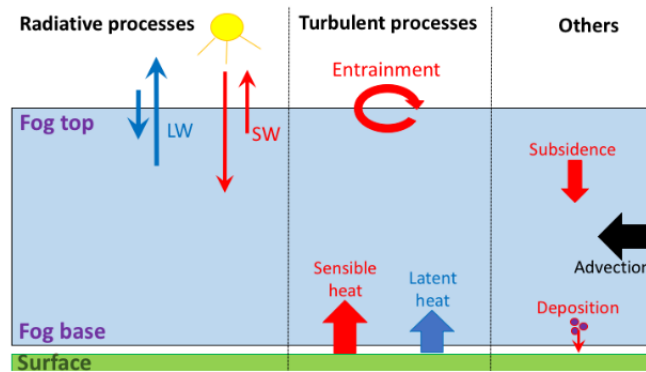


Figure 2.9: The physical processes which impact the liquid water of the fog layer by producing water (marked in blue) or reducing it (marked in red) [Wærsted, 2018]

- Dissipation phase: As the sun rises, the surface gets heated by solar radiation. Therefore, turbulence through buoyancy is generated by the cooling from above and heating from below the fog. It promotes mixing between the fog and the unsaturated air above the top of the fog, which leads to the evaporation of fog droplets. Evaporation of fog droplets also occur as they approach the heated surface below due to apparition of sun radiation, or alternatively, an increase in wind speed. Thus, dissipation of radiation fog usually occurs in the morning. This phase is characterized by a reduction of the liquid water content and droplet size near the surface and, therefore, an increase in visibility.

2.3.2.3 Parametrization

Various parameters exist to describe aerosol and cloud particles. In this thesis, we focus on three main parameters important for solar radiation: the optical depth, the single scattering albedo and the asymmetry factor that are presented in this paragraph. As the major part of this thesis focuses on cloudy or foggy atmospheres, cloud parametrization is further detailed. Note that, clouds and fogs are represented using the same parameters. Hence, both will be referred to as clouds.

Optical depth The optical depth indicates the degree to which aerosols or clouds prevent the transmission of light in the atmosphere. It is defined by Liou [2002]:

$$\tau(\lambda) = \int_{\delta z} \beta_e(\lambda, z) dz \quad (2.9)$$

where β_e is the extinction coefficient. In this thesis, τ_a and τ_c represent the **Aerosol Optical Depth (AOD)** and **Cloud Optical Depth (COD)** respectively.

Asymmetry factor The asymmetry factor g reflects the scattering energy distribution and is defined as follows: [Liou, 2002]

$$g = \frac{1}{2} \int_0^\pi \cos\Theta P(\Theta) \sin(\Theta) d\Theta \quad (2.10)$$

Θ is the angle between the incident light direction and the scattered light direction, $P(\Theta)$ is the normalized scattering phase function which characterizes the angular distribution of the scattered radiation field and, for Rayleigh scattering for incident unpolarized sunlight, it is given by: $P(\cos \Theta) = \frac{3}{4} (1 + \cos^2 \Theta)$. It can be expanded as a series of associated Legendre functions.

The asymmetry factor represents the preferred scattering direction (forward or backward) during the attenuation of irradiance and varies from -1 for complete back-scatter to 0 for isotropic (or symmetric) scatter (e.g. Rayleigh scattering) and to +1 for forward scatter. In this thesis, g_a and g_c represent the asymmetry factory for aerosols and clouds, respectively.

Single Scattering Albedo (SSA) Clouds and aerosols deplete radiation on one hand and reflect radiation on the other hand. Therefore, we may define the **Single Scattering Albedo (SSA)** as the ratio of the scattering coefficient (β_s) to the extinction coefficient (β_e) in the form:

$$\omega = \frac{\beta_s}{\beta_e} \quad (2.11)$$

The **SSA** quantifies the importance of scattering. It represents the percentage of a light beam that undergoes the scattering event. For non-absorbing particles, the **SSA** is close to 1. It depends on the wavelength, the size of particles and their chemical composition. In this thesis, ω_a and ω_c represent the **SSA** for aerosols and clouds, respectively.

2.3.2.4 Cloud Optical Properties (COPs)

Looking out the window, one can observe the complicated shapes of clouds. However, considering that their finite geometries are quite complex, in 1D models we assume them as being horizontally homogeneous and therefore short wave radiation that enters a cloud through the top is more likely to be reflected back to space, however, cloud particles that are typically larger than the wavelength of radiation, scatter light predominately in the forward direction which leads to radiation escaping from the side of a cloud. It will more likely be directed toward the surface [Hogan and Shonk, 2013]. This effect is quite important as it can increase the solar radiation at the earth's surface specially when cumulus clouds are present, due to their complex geometry the ratio of the area of cloud side to the total cloud cover is significant. The 3D representation of clouds is then useful to overcome this problem.

Additionally, some **COPs** depend on the constitution of clouds, hence we present them in this section and distinguish them for clouds made of water droplets or ice crystals.

Cloud fraction One of the main requirements to model radiative effects is a good representation of the cloud fraction at the ground, which requires information on the overlapping between cloud layers. A total cloud fraction ($F_C = 1$) for all cloudy-sky situations is sometimes used in modelling [Nielsen et al., 2014]. Otherwise, different formulas exist in literature to take into account the several cloud layers that may overlap. For example, we can mention the

cloud fractions corresponding to the maximum, minimum, and random overlap assumption or a combination of these classical cloud fraction formulas which are detailed in [Oreopoulos and Khairoutdinov, 2003, Räisänen, 1998] and briefly in LA21-2.

Water clouds (~ 0-5 km of altitude) The scattered light from clouds depends on their droplet size distribution, $n(r)$, which can be defined by some measure of the mean size [Liou, 1992]. The amount of light scattered by spherical droplets is proportional to their cross-sectional area, therefore we can define the mean effective radius as:

$$r_e = \frac{\int_0^\infty n(r)r^3 dr}{\int_0^\infty n(r)r^2 dr} \quad (2.12)$$

The **Liquid Water Path (LWP)** (in g m^{-2}) is a measure of the total amount of liquid water present between two points in the atmosphere, it is the vertically integrated **Liquid water content (Lwc)** (kg m^{-3}) defined as:

$$LWP = \int_0^{\Delta z} (Lwc) dz \quad (2.13)$$

If the cloud is assumed to be vertically uniform with respect to the droplets size distribution, the total vertical **LWP** is then $LWP = Lwc \Delta z$.

Otherwise, it can be related to the mean effective radius as:

$$LWP = \Delta z \frac{4\pi}{3} \rho_l \int_0^\infty n(r)r^3 dr \quad (2.14)$$

where ρ_l is the liquid water density. The optical depth for a given droplet size distribution is defined by:

$$\tau_C = \Delta z \int_0^\infty n(r) Q_{ext} \pi r^2 dr \quad (2.15)$$

where Q_{ext} is the efficiency factor which depends on the droplet radius, wavelength and refractive index. For solar visible wavelength: $Q_{ext} \approx 2$ for cloud droplets (for spherical cloud droplets, it can be evaluated from Mie's theory and is a function of the size parameter x (defined in section 2.2.2) and the refractive index of the particle n_λ . x is large for short wave radiation and typical cloud droplet distribution which makes Q_{ext} approach an almost constant value of 2) [Liou, 1992, Cotton and Anthes, 1992]. Therefore, the **COD** can be expressed as:

$$\tau_C \approx \frac{3}{2} LWP / r_e \quad (2.16)$$

where r_e is in micrometers.

It is a very important parameter needed to describe the radiative properties of clouds. It characterizes the strength of depletion and doesn't have any dimension. When it is equal to 0, it means that there is no extinction. For typical terrestrial clouds, it is usually larger than 1. A rough range is $5 < \tau_C < 500$ [Stephens, 1978a] depending on the type of cloud and the size of the water droplets. The change of optical depth of a cloud layer changes the amount of

reflected radiation and thereby alters the energy reaching the earth's surface and atmosphere below the layer. Therefore, the greater the COD, the greater the reflection and absorption of solar energy.

To determine the COD, one needs to calculate the LWP and the effective radius. The cloud droplet radii depends on the cloud type, and calculations of local values of r_e could be used. Considering log-normal distribution of droplet sizes, the mean effective radius r_e may be calculated as in code_saturne [Zhang et al., 2014] by:

$$r_e = \left(\frac{3\rho_a Lwc}{4\rho_l N_d \pi} \right)^{1/3} \exp(\sigma_d^2) \quad (2.17)$$

where N_d is the total droplet number concentration, ρ_a the air density, σ_d the standard deviation of the radius distribution (refer to Zhang et al. [2014] for the detailed equations).

As mentioned earlier, the other important parameters for cloud description are the asymmetry factor and the clouds SSA.

As more energy is scattered forward, the asymmetry factor of clouds increases toward unity. For a typical terrestrial cloud, the range for the asymmetry factor is $0.75 < g < 0.9$. [Stephens, 1984].

In addition, clouds are essentially diffusive with a small absorption by cloud droplets and other particles present in clouds, thus, values of SSA should be close to 1. However, it varies strongly with wavelength and droplet size. Different parameterization have been derived, an overview can be found in Cotton and Anthes [1992], Stephens [1984].

Nielsen et al. [2014] defined different parametrization of the SSA and asymmetry factor for different spectral bands. This parametrization depend only on the equivalent cloud droplet's radius r_e . Moreover, Black Carbon (BC) particles (or soot) are emitted during the combustion of various types of fuel and non-exhaust traffic-related processes. They are distinguished by their ability to lower the SSA and absorb solar irradiance but are often neglected in the calculation of the SSA. Consequently, Chuang et al. [2002] developed a parametrization for the SSA of clouds as a function of r_e and volume fraction of black carbon inside the drop for each wavelength of the short wave radiation. In our study, we used the parametrization of Nielsen et al. [2014] for both SSA and asymmetry factor of clouds. However, as we also got interested in the presence of BC in cloud droplets, we also considered the parametrization of Chuang et al. [2002]. The equations used are detailed in appendix A.1.

Ice clouds (~ 5-12 km of altitude) The optical proprieties of ice clouds are complicated due to the geometries of ice particles, the uncertainties related to their concentration and size spectra. The lwc for a given ice crystal distribution $n(L)$ may be defined by:

$$Iwc = \int V \rho_i n(L) dL \quad (2.18)$$

where ρ_i is the density of ice in g m^{-3} , V is the volume of an individual ice crystal in m^3 and L is the maximum crystal dimension (or the length) in μm . lwc is in units of g m^{-3} , $n(L)$ in $\text{m}^{-3} \mu\text{m}^{-1}$. The Ice Water Path (IWP) for a cloud with a thickness Δz is then $IWP = \Delta z \text{ lwc}$

and the COD for ice clouds may be defined by the following empirical relation [Liou, 1992]:

$$\tau_c \cong IWP(c + b/D_e) \quad (2.19)$$

where D_e is the mean effective ice crystal size, $c \cong -6.656 \times 10^{-3}$ and $b \cong 3.686$ for ice columns. For the sake of simplicity and because it is a CFD code dedicated to atmospheric boundary layer, in code_saturne, we make the hypothesis that cloud cover is dominated by liquid water clouds, thus all clouds are parametrized using the equations for water clouds. However, interested readers may find more details about the parametrization of ice clouds in Qiang [1996], Liou [1992].

2.3.3 Ground albedo

The surface reflectance or albedo R_g represents the amount of incoming radiation which is reflected from the earth. It is a measure of the diffuse reflection of solar radiation out of the total solar radiation and represents the capacity of a surface to reflect radiation. R_g mainly depends on the properties of the surface itself (moisture and colour) but also on the solar zenith angle and on the wavelength of solar radiation [Meng, 2020]. These factors vary with the geographic location and time. However, in radiation models, it is often taken as a constant that depends on land use coverage and can go from 0 for a black body to 1 for a body that reflects all incident radiation.

2.4 Solar radiation and atmospheric monitoring

The atmosphere can be monitored using different types of methods, such as in situ measurements and remote sensing observations. The following section briefly discusses some active and passive remote sensing and in-situ instruments that are useful for the detection of molecules, aerosols, clouds and meteorological parameters and for radiation monitoring, which are more detailed in Lenoble [1993]. Furthermore, the [Site Instrumental de Recherche par Télédétection Atmosphérique \(SIRTA\)](#) site that provided the different measurements used in this thesis is introduced.

2.4.1 Remote sensing techniques

The term remote sensing covers all measurements made at a distance from the object to be observed. The information between the “observed” and the “observer” is carried out by waves. We focus in our study on the carrying of electromagnetic waves. One speaks of “active remote sensing” when the electromagnetic wave is produced by a man-made emitter, and of “passive remote sensing” when the solar radiation or the long wave radiation emitted by the earth is used.

A popular active remote sensing instrument is the [Light Detection and Ranging \(LIDAR\)](#) instrument. It uses the light of a laser beam back-scattered toward a detector by molecules, aerosols and clouds. Different kinds of LIDAR exist. Here we are interested in the backscattering LIDAR which uses backscatter and extinction coefficient vertical profiles can be derived from the backscattering signal. It can be used to estimate the boundary layer height, the cloud

base height and the cloud fraction.

In the microwaves' wavelength, the [Radio Detection and Ranging \(RADAR\)](#) is operationally used for meteorological purposes. Different types of [RADAR](#) exist depending on the wavelength range they operate at. More particularly, the cloud and precipitation [RADAR](#) (centimetre wavelength for precipitation and millimetre wavelength for non-raining clouds) can capture clouds and provide short timescale prediction of precipitation. More specifically, in the millimetre wavelength range, Doppler cloud Radar is used to provide vertical profiles of reflectivity, for instance, and could characterize cloud and fog properties. BASTA is a Doppler cloud radar developed by the French laboratory LATMOS and is used by the [SIRTA](#) observatory (presented below), it was developed with the aim of reducing the instrument cost while providing accurate results [[Delanoë et al., 2016](#)].

Microwave radiometer is also a common instrument for such purposes. It measures energy emitted at microwave frequencies by gases, particles, solid or liquids, ... Furthermore, various parameters (like the vertical profile of temperature and humidity, liquid water path, aerosol optical depth or cloud fraction) may be retrieved from the signal measured.

Remote sensing can be performed from ground-based stations, air-borne or space-borne instruments. Ground based observations are limited to a few geographical points, but have the advantage of providing continuous time series. Sun radiation is generally measured from the ground. Airborne remote sensing can be performed from balloons or aircraft flying at a certain level of the atmosphere. However, they lack in continuity both in time and geographic coverage. Satellite remote sensing allow a more or less global coverage of the planet earth and years of observations, but the sampling rate is very low for mobile orbit satellites. The artificial satellites are placed at a certain orbit around earth, in particular, geostationary satellites are placed at earth's equatorial plane such that their rotation period is exactly equal to the period of the earth's rotation around the axis. Meteosat is one of the geostationary satellite, launched by the European Space Agency.

All geostationary satellites provide images in the visible and infrared spectral bands. Infrared images can provide information on the cloud's top temperature or cloud fraction (used in this thesis). Visible imagery can provide the cloud albedo. Moreover, sky images can be retrieved from All Sky Imager placed on the ground to capture the atmospheric state by taking pictures.

2.4.2 In-situ measurements

In-situ measurements regroup instruments that are located directly at the point of interest and in contact with the subject of interest. They allow, for example, the measurement of temperature, humidity, wind speed and radiation. The latter will be further discussed in the following section.

2.4.2.1 Radiation monitoring instruments

The measurements of solar direct, global and diffuse irradiance are performed regularly at many meteorological stations. The most common instruments are called pyrheliometers (for the direct [DNI](#)) and pyranometers (for the global [GHI](#) and diffuse [DHI](#)) (in this thesis, they are often referred to as [PYR](#)). They are schematically represented in figure [2.10](#).

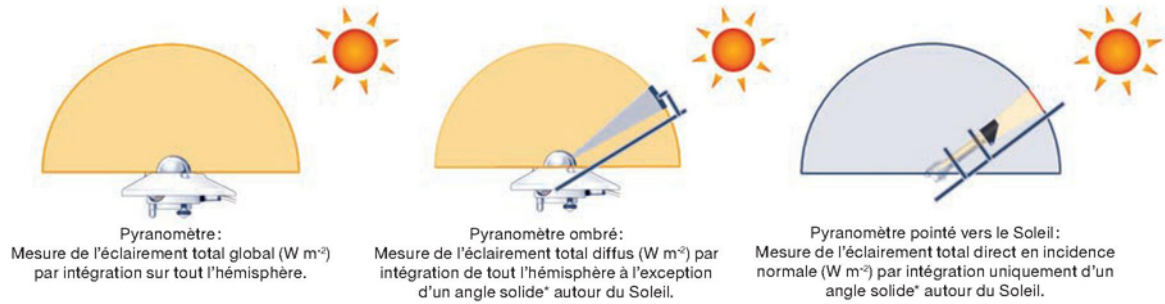


Figure 2.10: Schematic representation of a pyranometer (left panel) for the measurement of the total global irradiance by integrating over all the directions of the hemisphere, a pyranometer with a shadow ring (middle panel) for the measurement of the total diffuse irradiance by integrating over all the directions of the hemisphere except a solid angle around the sun, a pyrhelimeter (right panel) for the measurement of the direct normal incident irradiance by integrating only over the solid angle around the sun [Blanc et al., 2017].

Pyranometers are used to measure the global irradiance received on a horizontal surface. They are mounted on a horizontal platform. The detector is a thermopile protected by glass hemispheres. Thus, incoming radiation gets absorbed by a horizontal blackened surface and the increase of temperature gets measured by thermocouples. Irradiance gets measured by quantifying the photocurrent generated. Its response is independent on the incidence direction and depends only on the received irradiance. It can be used to measure the diffuse radiation when shadowed from the direct solar beam. To do so, a small opaque disk or a shadow ring can be mounted to follow the movement of the sun by a clock driven mechanism.

The direct solar irradiance can be measured by pyrhelimeter, where the detector is always mounted in the bottom of a tube oriented toward the sun. The field of view is larger than the sun's apparent diameter. The principle is similar: sunlight enters the instrument through a window and is directed onto a thermopile, which converts heat to an electrical signal that can be recorded.

The direct irradiance is crucial for the economic and energy evaluations of different solar energy applications, like solar concentrating and flat plate systems [Padovan et al., 2014]. However, the measurement of direct irradiance with the pyrhelimeter is very expensive and thereby less common on solar stations. It makes its estimation quite complex and decomposition models based on observations are sometimes used to separate the measurements of DNI from GHI [Padovan et al., 2014, Bertrand et al., 2015] or simple methods for correcting the satellite derived DNI data have been developed [Polo et al., 2015].

Sun photometers are instruments that can also measure direct solar irradiance. Their objective is to retrieve the atmosphere optical depth. The measurements are made in wavelength intervals free of gas absorption, and the molecular and ozone contributions are deduced to obtain the aerosol optical depth. It consists of a photoelectric detector in a collimating tube with band filters.

2.4.3 Site Instrumental de Recherche par Télédétection Atmosphérique (SIRTA)

Site Instrumental de Recherche par Télédétection Atmosphérique (SIRTA) is a French national observatory dedicated to the observation of the atmosphere. It is located in the semi-urban area at Ecole Polytechnique, Palaiseau, 20 km southwest of Paris, France (48, 71 °N, 2.2 °E). It has been collecting data since 2002 from active and passive remote sensing and from in-situ measurements at the surface. From the multitude of instruments located at the SIRTA, we can cite standard meteorological measurements such as 2-m temperature and humidity, 10-m wind speed and surface pressure that are recorded continuously. In addition, a 30-m mast allows the measurements at six different levels of temperature and humidity. Sonic anemometers provide wind speed measurements at 10 m and 30 m. Visibility is measured at screen level (3 or 4 m) and at 20 m. Two pairs of pyranometers and pyrhemometers measure global upwelling and downwelling *shortwave* (SW) and *longwave* (LW) radiative flux. The instruments from which data are used in this thesis are installed in zone 1 and 2 shown in figure 2.11 and further detailed in sections 4.3 and 5.2. For the first study of this thesis (chapter 4), meteorological data sets were extracted from the SIRTA Re-OBS project whose goal is to synthesize, analyse and homogenize all SIRTA observations hourly averaged in a single NetCDF file from 2003 to now [Chiriaco et al., 2018]. It has been developed in order to study regional climate variability, for the particular case of Paris area. For the second study of the thesis (chapter 5), meteorological data sets were extracted from the ParisFog campaign. It is a field experiment that covered more than 100 fog and near-fog situations in October 2006–March 2007. The experimental setup monitored on a routine basis surface conditions, large and small-scale dynamics, radiation, turbulence, precipitation, droplet and aerosol micro-physics, and aerosol chemistry, combining in situ and remote sensing instruments on a long-term basis deployed at the SIRTA site.

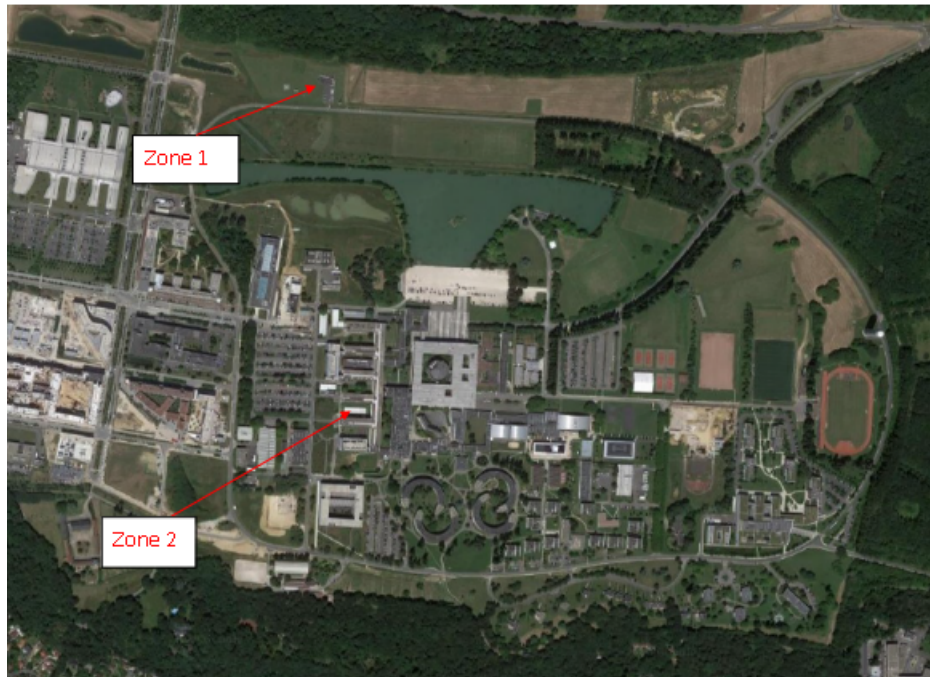


Figure 2.11: Satellite image of the Ecole Polytechnique campus, where the [SIRTA](#) observatory is situated. The two zones where instruments from which data are used in this thesis are shown.

Chapter 3

Solar radiation: numerical modeling

3.1 Introduction

An accurate knowledge of solar radiation at the ground is one of the most essential step for the design of solar power systems. As it can't be directly measured everywhere on earth and over long enough periods, numerical models are often used. A number of numerical models have been developed to improve the solar resource estimation, including the CFD software code_saturne. The different numerical models may be classified depending on whether or not they solve the Radiative Transfer Equation (RTE) which is the mathematical description of the propagation of radiation through a medium. Some models follow the statistical behaviour of solar radiation or are based on satellite images and others, like code_saturne, solve the RTE by making simplifying assumptions, for example by considering a plane-parallel atmosphere (1D calculations) rather than a 3D medium. In code_saturne 1D radiative scheme, there is a distinction between two models depending on the assumption taken for the vertical discretization of the atmosphere: the *integral* model assumes that the atmosphere is made of one homogeneous layer; the *multi-layered* model assumes that the atmosphere is divided into several layers.

Subsequently, this chapter aims at presenting an overview of some various numerical models that exist in the literature to estimate the solar irradiance available at the Earth's surface. We focus on a few models only that are useful or similar to the work done in this thesis before introducing the code_saturne radiation model. This chapter is structured as follows: section 3.2 describes an overview of different types of models. Section 3.3 presents the general form of the RTE, its application to a plane parallel atmosphere (1D model) as well as a 3D medium. The methods to solve the RTE are also detailed. Section 3.4 presents the numerical models based on radiative transfer resolution for a plane-parallel atmosphere (following the integral or multi-layered methods) and for 3D mediums. Finally, in section 3.5, a general description of the code_saturne radiative model is provided.

Contents

3.1 Introduction	28
3.2 An overview	29
3.2.1 Statistical models	29
3.2.2 Cloud imagery and satellite based models	30
3.2.3 Hybrid models	31
3.2.4 Numerical Weather Prediction (NWP) models	31
3.3 Radiative Transfer Equation (RTE)	32
3.3.1 The general equation of radiative transfer	33

3.3.2	Application to a plane parallel atmosphere	33
3.3.3	Application to a three dimensional (3D) medium	40
3.4	Radiative transfer numerical models	43
3.4.1	1D radiative models	43
3.4.2	Modelling of solar irradiance in a cloudy atmosphere	45
3.4.3	3D radiative models	46
3.5	code_saturne solar radiation model	47
3.5.1	General description	47

3.2 An overview

A detailed review of numerical models used for the estimation of solar radiation can be found in [Ineichen \[2006\]](#), [Badescu \[2008\]](#), [Lorenz and Heinemann \[2012\]](#), [Diagne et al. \[2013\]](#) of which a few are presented in the following section. A number of methods are based on the statistical behaviour of solar radiation or on satellite images and do not depend on the radiative transfer modelling. The forecasting timescales are often short and go from a few minutes to a few hours. Hybrid models have been introduced to overcome deficiencies, combining individual models to use the best of each. Some radiation models based on the solving of the RTE are included in [Numerical Weather Prediction \(NWP\)](#) models that are useful for long forecasting times (longer than few hours). A brief description of statistical, hybrid, satellite based and [NWP](#) models is provided in the following sections.

3.2.1 Statistical models

Many studies have been conducted on the statistical behaviour of solar radiation. Some of the works that have produced important advances are presented here.

[Angstrom \[1924, 1956\]](#) derived regression expressions for the different components of the daily solar radiation based on the sunshine duration. The work of [Liu and Jordan \[1960\]](#) has been used by several researchers and led to the development of different methodologies as well as different types of equations to model the solar radiation variability. They emitted a hypothesis of a universal character of the [Cumulative Distribution Function \(CDF\)](#)¹ curve of the daily clearness index. The clearness index is the ratio of the horizontal global radiation on the ground to that initially available at the top of the atmosphere: it represents the transparency of the atmosphere and provides information of the actual state of the atmosphere and on the availability of solar energy at a given place.

Another statistical method is the [Auto-Regressive Moving Average \(ARMA\)](#) model. It is often applied to auto-correlated time series data. It is a statistical analysis model that uses time series data to either better understand the data set or to predict future trends. [ARMA](#) is based on two parts: autoregressive (AR) part and moving average (MA) part. AR models make forecasts using a linear combination of past values, while MA models try to capture unexpected

¹A CDF describes the probability distribution of a real random variable. A more detailed definition and expression can be found in the book of [Badescu \[2008\]](#)(chapter 3)

events. This method can also be referred to as **ARMA** (p,q) where p, the lag order and q, the moving average are the order of AR and MA respectively. This makes **ARMA** models very flexible, as they can represent several types of time series by using different orders. It should be noted that for this model, time series must be stationary (see [Hamilton \[1994\]](#)). The stationarity of a distribution is defined in [Hamilton \[1994\]](#) as a non-time dependence of neither the mean of the distribution nor the autocovariance (probability limit of an ensemble average). For non-stationary series, the **Auto-Regressive Integrated Moving Average (ARIMA)** technique has been developed. It starts by removing trends, then uses stochastic methods to couple the autoregressive component (AR) to the moving average component (MA).

3.2.2 Cloud imagery and satellite based models

Several algorithms and models have been developed to estimate the solar irradiance at the earth surface from satellite images, they can be used where no ground measurement data exists. Although, the availability of ground database is growing up through different measuring networks, they often have a low spatial density which makes satellite-derived models useful for quantifying the solar radiance at ground level for a large area. The Heliosat model is briefly presented here.

The Heliosat model was originally proposed by [Cano et al. \[1986\]](#) and later it has been modified and improved through different versions. Moreover, Centre O.I.E. (Observation, Impacts, Energie) of MINES ParisTech uses the Heliosat model to create and update databases of solar radiation called HelioClim.

Heliosat-1 was a pure empirical model. It consists in a linear relationship between the cloud index n and the clearness index k_T : $k_T = an + b$; a and b parameters have to be fitted with ground data. The cloud index is a normalized parameter describing the cloudiness. It is defined from the irradiance measurements of the satellite radiometer and mathematically expressed as [[Badescu, 2008](#)]:

$$n = \frac{R_p - R_g}{R_c - R_g} \quad (3.1)$$

R_p being the planetary albedo ², R_c the cloud albedo, R_g the ground albedo. The clearness index k_T is defined as the global hourly irradiance normalized by the extraterrestrial irradiance. In order to deal with atmospheric and cloud extinction separately, this version was further developed to Heliosat-2. It incorporates physical atmospheric parameters such as the Linke turbidity factor, [[Rigollier et al., 2000](#)] which describes the optical thickness of the atmosphere and summarizes the attenuation of the direct beam by representing the absorption by water vapour and absorption and scattering by aerosols [[Angles et al., 1999](#)]. Heliosat-2 is one of the most widely validated methods developed for estimating solar radiation from satellite images. It is an open-source method that can be applied worldwide: it has been validated in oceanic, Mediterranean, desert and semi-arid climate regions [[Dagestad, 2004](#), [Lefèvre et al., 2007](#), [Moradi et al., 2009](#), [Wahab et al., 2010](#), [Al-Jumaily et al., 2010](#), [Blanc et al., 2011](#)], Mozam-

²The fraction of incident solar radiation that is reflected by the Earth-atmosphere system and returned to space

bique [Wald and Blanc, 2011], Zimbabwe [Blanc et al., 2011] and French Guiana [Isabelle et al., 2013]. Heliosat model was then improved towards a more physical model. In Heliosat-3 version, aerosols and other atmospheric absorbers parameters were added. It is based on SOLIS scheme [Müller et al., 2004] for radiative transfer modelling. It doesn't rely on the Linke turbidity factor, the attenuation depends on the atmospheric parameters. It then evolved into Heliosat-4 which provides a better estimation of the direct and diffuse components. The radiative equation is approximated by the product of clear-sky irradiance and a term describing the cloud extinction [Oumbe et al., 2009]. Thus, it is composed of two abacus-based models: McClear for the irradiance under clear-sky and McCloud for the irradiance extinction due to clouds. The McClear model estimates the radiation that should be received during clear-sky conditions anywhere in the world since 2004, and it includes absorption by aerosols, water vapour and ozone. The Heliosat-4 method showed satisfactory results for global irradiance and a noticeable better quality than the previous versions of Heliosat for the direct irradiance. [Qu, 2013, Lefèvre et al., 2013]

3.2.3 Hybrid models

Hybrid models have been introduced to overcome the deficiency in using individual models and use the best of each method. Many researchers proposed combining different methods to improve the forecasting accuracy [Cao and Cao, 2005, 2006, Cao and Lin, 2008, Reikard, 2009]. For example, Cao and Cao [2006] combined Artificial Neural Network (ANN) with wavelet analysis for forecasting total solar daily irradiance. An ANN is an interconnected structure of simple processing units, whose functionality can graphically be shown to resemble that of the biological processing elements. The processing capabilities of this artificial network assembly are determined by the strength of the connections between the processing units, the specific architecture pattern followed during the construction of the network and some special set of parameters adopted during the training of the network. In Moncada et al. [2018], an artificial intelligence method is combined to sky imager data to forecast irradiance.

3.2.4 Numerical Weather Prediction (NWP) models

NWP models are used for long-term prediction (1-2 weeks). They solve differential equations which describe the weather evolution. The non-linear equations are discretized and resolved using numerical algorithms. They provide a temporal and spatial distribution of the meteorological parameters (global solar irradiance, temperature, pressure, humidity, wind and clouds) and therefore are well suited to estimate solar irradiance. NWP models are divided into two categories: global NWP and mesoscale models.

On one hand, global NWP have coarse space resolution, in the range of 9-50 km depending on the model. For instance, the Integrated Forecasting System (IFS) from the ECMWF (European Centre for Medium Range Weather Forecasts) provides weather forecast up to 10 days ahead at a horizontal resolution of 9 km, including solar surface irradiance and different cloud parameters. On the other hand, mesoscale models cover a smaller part of Earth but with a higher spatial resolution [Diagne et al., 2013]. They require input data from global NWP models for initialization and boundary conditions. One example is the fifth generation mesoscale

model MM5 that has been developed at Pennsylvania State University and at the [National Centre for Atmospheric Research \(NCAR\)](#). It used a terrain following coordinate, a time split scheme to solve finite difference equations and has multiple nesting capabilities [[Grell et al., 2005](#)]. [Weather Research Forecast \(WRF\)](#) is another example that can be seen as a follow-up model to MM5: it is an open source mesoscale model with continuous development and integrates features from the other models. It includes numerical methods with higher order of accuracy [[Skamarock et al., 2008](#)]. WRF was developed by the [National Oceanic and Atmospheric Administration \(NOAA\)](#), [NCAR](#) and more than 150 research centres in meteorology. It has been designed for both atmospheric research and operational forecasting applications. The model is based on two modules: one dynamic module that gives the spatial and temporal evolution of atmospheric parameters (ex, wind, pressure temperature and humidity) and one physical module that represents the physical interactions between those variables. The atmospheric radiation models of WRF are detailed in [Skamarock et al. \[2008\]](#), they include the [Rapid Radiative Transfer Model \(RRTM\)](#) model, the Eta [Geophysical Fluid Dynamics Laboratory \(GFDL\)](#) model for short wave and long wave radiation (which is a version of the [Lacis and Hansen \[1974\]](#) (referred to as [LH74](#)) parametrization), the MM5 radiative model for short wave. All radiation models are 1D schemes and calculations are made on different spectral bands: from 1 (for the MM5 model) up to 16 (for [RRTM](#)) bands. The effect of cloud, water vapour, carbon dioxide and ozone is considered in all models except for the MM5 model which only considers the effect of clouds.

The WRF-Solar [[Jimenez et al., 2016b](#)] is a configuration of WRF intended for solar energy applications. It computes separately the direct and diffuse components and takes into account the aerosols effect and the feedbacks between aerosols, solar irradiance and clouds.

One of the limitation of NWP models is their ability to estimate radiation on cloudy days. Several NWP-based GHI forecasts in Europe have been evaluated and compared by [Lorenz et al. \[2009\]](#). They showed that the estimation of radiation of the model were very satisfactory in clear-sky condition, but not for cloudy conditions. Moreover, the impact of aerosols, clouds, water vapour and other gases on the estimation of solar energy is large [[Gueymard, 2008](#), [Breitkreuz et al., 2009](#)]. However, NWPs do not usually model aerosol concentrations. In some cases, they do not consider aerosols [[Gueymard and Ruiz-Arias, 2015](#)]. In others, a simple parametrization of aerosol effects is used, by assuming [Aerosol Optical Properties \(AOPs\)](#) to be constant with space and time or using climatological values [[Morcrette et al., 2008](#), [Jimenez et al., 2016b](#)]. Moreover, measured optical properties can be used in [Kambezidis et al. \[2016\]](#) but they can also be derived from chemical transport models [[Breitkreuz et al., 2009](#), [Sartelet et al., 2018a](#)].

3.3 Radiative Transfer Equation (RTE)

Numerous numerical models are based on the resolution of the RTE or simplified formulations. Prior to presenting them, the theoretical basis of the RTE is elaborated here. The RTE mathematically describes the propagation of radiation through a medium. Firstly, the general form is provided. Secondly, it is applied to a plane parallel atmosphere and thirdly to a 3D

medium. In addition, the “exact” methods and approximate solutions are presented for each application.

3.3.1 The general equation of radiative transfer

A pencil of radiation going through a medium will be attenuated by its interaction with matter. Let’s consider an intensity of radiation I_λ . After traversing a thickness ds (in the direction of its propagation), it will become $I_\lambda + dI_\lambda$ [Liou, 2002]. Thus,

$$dI_\lambda = -k_\lambda \rho I_\lambda ds \quad (3.2)$$

where ρ is the density of the material, k_λ the mass extinction cross-section for radiation of wavelength λ . One may define the source function coefficient j_λ in order to consider the emission from the matter as well as the multiple scattering from all other directions into the pencil (at the same wavelength):

$$dI_\lambda = j_\lambda \rho ds \quad (3.3)$$

When combining equations 3.2 and 3.3, we obtain:

$$dI_\lambda = -k_\lambda \rho I_\lambda ds + j_\lambda \rho ds \quad (3.4)$$

If we define the source function J_λ such that $J_\lambda \equiv j_\lambda/k_\lambda$, then we obtain the general radiative transfer equation without any coordinate system imposed [Liou, 2002]:

$$\frac{dI_\lambda}{k_\lambda \rho ds} = -I_\lambda + J_\lambda \quad (3.5)$$

A common simplification is the 1D or plane-parallel atmosphere approximation that assumes that the optical properties vary with height z only and not in the horizontal directions. Even in cloudy atmosphere, 1D models are able to give reasonable results. However, despite their expensive computational cost, 3D approximations are more accurate as they can provide a better description of cloud effects (like reflection of radiation on the edges). Analytical and numerical solutions are now detailed.

3.3.2 Application to a plane parallel atmosphere

3.3.2.1 The RTE

For many atmospheric radiative transfer applications, it is physically appropriate to consider that, in localized portions, the atmosphere is plane-parallel and that variations of temperature and gaseous profiles occur only in the vertical direction. Thus, the linear distances are measured normal to the plane of stratification and denoted by z (figure 3.1). The sun is considered as a point light source. The transfer problem can be divided into two parts, for the direct and diffuse components. The direct component is associated with the exponential attenuation of unscattered solar radiation. The diffuse component results from the multiple scattering processes undergone by a light beam. The polar coordinate is considered with (μ', ϕ') the incoming and (μ, ϕ) the outgoing light beam. ($\mu = \cos \theta$ the cosine of the zenith angle; ϕ the azimuth

angle - refer to section 2.2.1 and μ and $-\mu$ the upward and downward directions associated with the light beam). The general equation representing the transfer of diffuse solar energy is [Liou, 1992, 2002] (here we omit the subscript λ on some radiative quantities):

$$\mu \frac{dI(z; \mu, \phi)}{k\rho dz} = -I(z; \mu, \phi) + J(z; \mu, \phi) \quad (3.6)$$

where I is the intensity of radiation and J the source function. By injecting the normal optical depth:

$$\tau = \int_z^\infty k\rho dz' \quad (3.7)$$

we obtain the basic equation of radiative transfer in plane-parallel atmospheres:

$$\mu \frac{dI(\tau; \mu, \phi)}{d\tau} = I(\tau; \mu, \phi) - J(\tau; \mu, \phi) \quad (3.8)$$

The downward and upward diffuse fluxes at a given optical depth level, τ , are defined by [Liou, 1992]:

$$F_{diff}^{\uparrow\downarrow}(\tau) = 2\pi \int_0^{\pm 1} I(\tau, \mu) \mu d\mu \quad (3.9)$$

where \uparrow and \downarrow represent the upward and downward fluxes, respectively. The direct downward flux at τ is given by the exponential attenuation of the effective solar flux at the top of the atmosphere ($\mu_0 F_0$):

$$F_{dir}^\downarrow(\tau) = \mu_0 F_0 e^{-\tau/\mu_0} \quad (3.10)$$

The total upward and downward fluxes are:

$$F^\uparrow(z) = \int_0^\infty F_{diff}^\uparrow(\tau) d\lambda \quad (3.11)$$

$$F^\downarrow(z) = \int_0^\infty (F_{diff}^\downarrow + F_{dir}^\downarrow) d\lambda \quad (3.12)$$

and the net flux:

$$F_s(z) = F^\downarrow(z) - F^\uparrow(z) \quad (3.13)$$

The heating rate due to the absorption of solar flux in the atmosphere is produced by the divergence of the net solar flux:

$$\left(\frac{\delta T}{\delta t}\right)_s = \frac{1}{\rho C_p} \frac{dF_s(z)}{dz} \quad (3.14)$$

where ρ is the air density and C_p the specific heat at constant pressure.

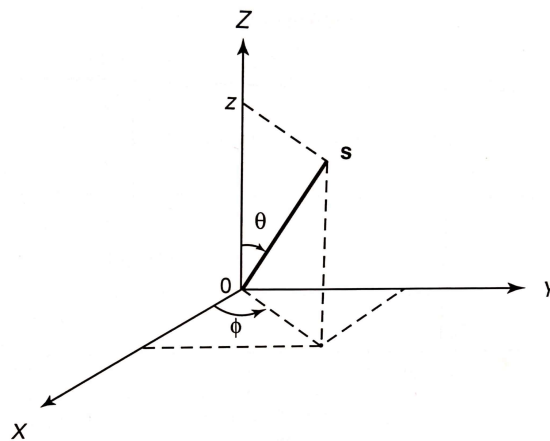


Figure 3.1: Geometry of a plane parallel atmosphere where θ and ϕ are the solar zenith and azimuthal angles and s represents the sun [Liou, 2002].

3.3.2.2 Analytical resolution of the RTE

Numerous methods have now been elaborated to solve the 1D equation of the RTE (equation 3.8) and the analytical treatment is generally followed by numerical calculations. The computer time depends on the complexity of the physical problem and the desired accuracy. Simplified problems allow us to pursue the development of analytical equations to call the method “exact”. In complement and to avoid going through long procedures for computing and integrating irradiance, approximate solutions were developed to obtain the upward and downward fluxes. One “exact” solution is the discrete ordinate method that transforms the RTE in a system of linear differential equations by a Fourier and Legendre decomposition of its individual terms and the integral is approximated by a sum over discrete angles (for different directions). In contrast, the adding method is another “exact” solution which considers radiation in two directions only: upward and downward. If radiance is required for a number of wavelengths or integrated over the solar spectrum, radiance may be calculated separately for all wavelengths. The adding method is very common and employed in many climate and NWP models and is able to provide accurate results in little computation time.

We first discuss the “exact” solutions for radiative transfer in a plane-parallel atmosphere, more specifically the adding method because it is used in code_saturne 1D model. Subsequently, we present two-streams approximations for radiative transfer as well as the delta function for adjustments. The discrete ordinate method will be presented in the 3D modelling section, as it may also be applied to a 3D medium, which is the case in code_saturne 3D radiative model.

The adding method The adding method for radiative transfer has been demonstrated to be a powerful tool for multiple scattering calculations [Liou, 2002]. It was first stated by Stokes [1862] after its development by Peebles and Plesset [1951] in gamma-ray transfer, then by

De Hulst [1980], Hansen [1971]. It consists in dividing the atmosphere into a number of homogeneous layers, each having its own optical depth τ , and defining a reflection (R) and a transmission (T) function for each layer. The reflection and transmission of the entire atmosphere may be obtained by calculating the successive transmissions and reflections between the layers.

In order to introduce the adding method, we may start by considering one of the layers: it is uniformly illuminated from above and from below by a parallel beam of radiation with flux $\mu_0 F_0$ per unit area perpendicular to the incident beam (figure 3.2). The total radiation reflected by the two layer atmosphere is the sum of terms corresponding to radiation which has crossed the boundary between the two layers n times going upward ($n= 0, \infty$). The same is true for the diffusely transmitted radiation. The intensity of radiation diffusely reflected I_r and transmitted I_t by one layer in terms of the reflection R and transmission T functions are given by the following expression (illuminated from above):

$$\pi I_r(\mu) = \mu_0 R(\mu, \mu_0) F_0 \quad (3.15)$$

$$\pi I_t(\mu) = \mu_0 T(\mu, \mu_0) F_0 \quad (3.16)$$

when the layer is illuminated from below, the reflection R^* and transmission T^* functions are given by:

$$\pi I_r^*(\mu) = \mu_0 R^*(\mu, \mu_0) F_0 \quad (3.17)$$

$$\pi I_t^*(\mu) = \mu_0 T^*(\mu, \mu_0) F_0 \quad (3.18)$$

If we consider the two layers on top of each other, we can define the reflection and total (direct and diffuse) transmission functions by R_1 and \tilde{T}_1 , and R_2 and \tilde{T}_2 for the top and bottom layers. The combined total reflection and transmission between the two layers is defined by U and, \tilde{D} respectively. In reference to figure 3.2 and accounting for the multiple reflections of the light beam in the two layers we can define:

$$R_{12} = R_1 + \tilde{T}_1^* R_2 \tilde{T}_1 + \tilde{T}_1^* R_2 R_1^* R_2 \tilde{T}_1 + \tilde{T}_1^* R_2 R_1^* R_2 R_1^* R_2 \tilde{T}_1 + \dots \quad (3.19)$$

$$= R_1 + \tilde{T}_1^* R_2 \tilde{T}_1 [1 + R_1^* R_2 + (R_1^* R_2)^2] \quad (3.20)$$

$$= R_1 + \tilde{T}_1 R_2 \tilde{T}_1^* / (1 - R_1^* R_2) \quad (3.21)$$

Similarly,

$$\tilde{T}_{12} = \tilde{T}_1 \tilde{T}_2 / (1 - R_1^* R_2) \quad (3.22)$$

$$U = R_2 \tilde{T}_1 / (1 - R_1^* R_2) \quad (3.23)$$

$$\tilde{D} = \tilde{T}_1 / (1 - R_1^* R_2) \quad (3.24)$$

By defining the operator S as:

$$S = R_1^* R_2 / (1 - R_1^* R_2) \quad (3.25)$$

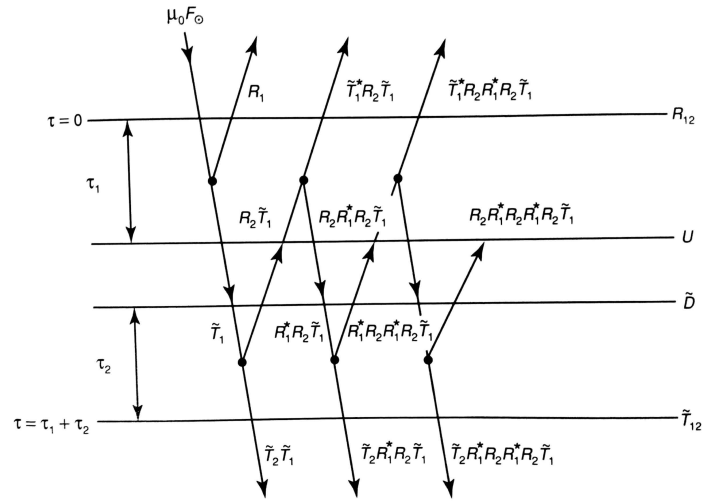


Figure 3.2: Configuration of the adding method. For convenient illustration, the two layers (of optical depth τ_1 and τ_2) are illustrated like if they were physically separated. [Liou, 2002]

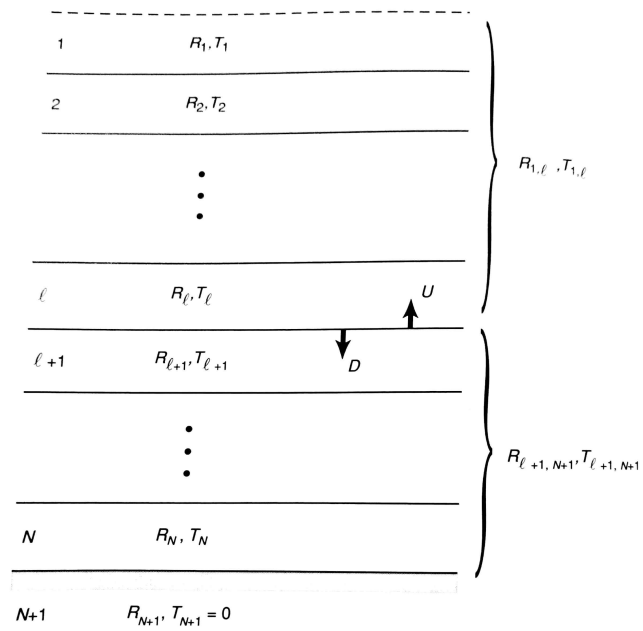


Figure 3.3: Illustrated diagram of the adding method for the computation of internal intensities U and D (defined in section 3.3.2.2) [Liou, 2002]

so that,

$$1 + S = (1 - R_1^* R_2)^{-1} \quad (3.26)$$

we can write,

$$R_{12} = R_1 + \tilde{T}_1^* U \quad (3.27)$$

$$\tilde{T}_{12} = \tilde{T}_2 \tilde{D} \quad (3.28)$$

$$U = R_2 \tilde{D} \quad (3.29)$$

We now separate the direct and diffuse components of the total transmission function:

$$\tilde{T} = T + e^{-\tau/\mu'} \quad (3.30)$$

where $\mu' = \mu_0$ when transmission is associated with the incident solar beam and $\mu' = \mu$ when it is associated with the emergent light beam in the direction μ . Therefore,

$$\tilde{D} = D + e^{-\tau_1/\mu_0} = (1 + S)T_1 + S e^{-\tau_1/\mu_0} + e^{-\tau_1/\mu_0} \quad (3.31)$$

$$\tilde{T}_{12} = e^{-\tau_2/\mu} D + T_2 e^{-\tau_1/\mu_0} + T_2 D + \exp\left[-\left(\frac{\tau_1}{\mu_0} + \frac{\tau_2}{\mu}\right)\right] \delta(\mu - \mu_0) \quad (3.32)$$

D , T_1 and T_2 are the diffuse components only. The δ function shows that the direct transmission function is a function of μ_0 only.

The set of iterative equations for the computation of diffuse transmission and reflection for two layers are:

$$Q = R_1^* R_2 \quad (3.33)$$

$$S = Q/(1 - Q) \quad (3.34)$$

$$D = T_1 + S T_1 + S e^{-\tau/\mu_0} \quad (3.35)$$

$$U = R_2 D + R_2 e^{-\tau_1/\mu_0} \quad (3.36)$$

$$R_{12} = R_1 + e^{-\tau_1/\mu} + T_1^* U \quad (3.37)$$

$$T_{12} = e^{-\tau_2/\mu} D + T_2 e^{-\tau_1/\mu_0} + T_2 D \quad (3.38)$$

Similarly, an analogous scheme can be defined for the radiation emergent from below, R_{12}^* and T_{12}^* :

$$Q = R_2 R_1^* \quad (3.39)$$

$$S = Q/(1 - Q) \quad (3.40)$$

$$U = T_2^* + S T_2^* + S e^{-\tau_2/\mu'} \quad (3.41)$$

$$D = R_1^* U + R_1^* e^{-\tau_2/\mu'} \quad (3.42)$$

$$R_{12}^* = R_2^* + e^{-\tau_2/\mu} + T_2 D \quad (3.43)$$

$$T_{12}^* = e^{-\tau_1/\mu} U + T_1^* e^{-\tau_2/\mu'} + T_1^* D \quad (3.44)$$

Method	γ_1	γ_2	γ_3
Quadrature two-stream	$[1-\omega(1+g)/2]\mu_1$	$\omega(1-g)/2\mu_1$	$(1-3g\mu_1\mu_0)/2$
Eddington	$[7-(4+3g)\omega]/4$	$-[1-(4-3g)\omega]/4$	$(2-3g\mu_0)/4$

Table 3.1: Coefficients in two-stream approximations (ω is the single scattering albedo, g the asymmetry factor, $\mu_0=\cos\theta_0$, θ_0 the solar zenith angle, $\mu_1 = 1/\sqrt{3}$)

Two streams approximations: the Eddington and two-stream quadrature approximations With the aim of simplifying the computation of upward and downward fluxes, approximate equations were developed and can be obtained by various approaches. They yield closed-form analytical results that may be easily interpreted and adequately represent important features of multiple scattering processes. Numerous methods have been developed and can be found in Meador and Weaver [1980] but only the two stream quadrature and Eddington approximations are presented here because both are used in the work done for this thesis. However, they are all derived from the equations of upward and downward fluxes intensity (derived from equ. 3.6) and from the phase function (or single-particle scattering law for scattered radiation) which is the first moment of the asymmetry factor (equ. 2.10). They result in a system of two differential equations which can be written in the following form:

$$\frac{dF \uparrow(\tau)}{d\tau} = \gamma_1 F \uparrow(\tau) - \gamma_2 F \downarrow(\tau) - \gamma_3 \omega F_0 e^{-\tau/\mu_0} \quad (3.45)$$

$$\frac{dF \downarrow(\tau)}{d\tau} = \gamma_2 F \uparrow(\tau) - \gamma_1 F \downarrow(\tau) + (1 - \gamma_3) \omega F_0 e^{-\tau/\mu_0} \quad (3.46)$$

The γ_i coefficients represent various choices of coefficients, they depend on the manner in which the intensity and phase functions are approximated and are gathered in table 3.1 for the Eddington and two stream quadrature approximations. The third term on the right-hand side may be dropped, in this case $F \downarrow$ stands for the total (diffuse plus direct) downward flux. The difference between the two-stream quadrature and Eddington approximation is that, in the quadrature two-stream approximation, there are only the upward and downward intensities in the direction μ_1 and $-\mu_1$ given by the Gauss quadrature formula and the phase function is expanded in two terms of Legendre polynomials. In Eddington's approximation, both intensity and phase function are expanded in two polynomial terms. (More details can be found in Liou [2002], Meador and Weaver [1980]).

The delta function adjustment The two stream or Eddington approximations are often used in general circulation and climate models because they can achieve efficient radiative computation. However, they have been shown to be good approximations only for optically thick layers and not for optical thin layers or when significant absorption is involved, because the scattering by atmospheric particulates is highly peaked in the forward directions. Therefore, a delta function adjustment can be incorporated to those models in order to adjust the absorption and scattering of the atmosphere. It has shown satisfactory results and Schaller [1979] illustrated that the δ -Eddington and δ -two-stream (quadrature) have similar accuracy. It consists in removing the fraction of scattered energy residing in the forward peak, f , from

the scattering parameters: optical depth τ , SSA ω and asymmetry factor g . The primes indicate the adjusted parameters. The optical (extinction) depth can be expressed as the sum of the scattering (τ_s) and absorption (τ_{abs}) optical depth, we can write:

$$\tau' = \tau'_s + \tau'_{abs} = (1 - f)\tau_s + \tau_{abs} = \tau(1 - f\omega) \quad (3.47)$$

Thus, the adjusted SSA is:

$$\omega' = \frac{\tau'_s}{\tau'} = \frac{(1 - f)\omega}{1 - f\omega} \quad (3.48)$$

and the asymmetry factor:

$$g' = \frac{g - f}{1 - f} \quad (3.49)$$

Joseph and Wiscombe [1976] expressed the forward fraction of the scattered light in function of the asymmetry factor: $f=g^2$ which gives:

$$g' = \frac{g}{1 + g} \quad (3.50)$$

$$\tau' = (1 - \omega g^2)\tau \quad (3.51)$$

$$\omega' = \frac{(1 - g^2)\omega}{1 - \omega g^2} \quad (3.52)$$

Integral and multi-layered assumptions In this thesis, the adding method is used for 1D calculations. However, two different assumptions were made and referred to as the “*integral method*” and the proper adding method, referred to as the “*multi-layered method*”. They are represented in figure 3.4: in the integral method, the atmosphere is assumed to be one homogeneous layer with optical properties of atmospheric components integrated over the vertical axis. The fluxes are estimated at the ground through reflection and transmission factors. In the second method, the atmosphere is divided into a number of layers and reflection and transmission factors are calculated in each layer in function of the optical properties of this layer.

3.3.3 Application to a three dimensional (3D) medium

If one wishes to consider, for example, a spherical geometry, clouds in a finite dimension and/or inhomogeneity in the horizontal direction, the plane-parallel assumption is not applicable. 3D modelling of radiative transfer is then necessary.

3.3.3.1 The RTE

From equation 3.5 and considering an inhomogeneous medium and the extinction coefficient $\beta_e = k_\lambda \rho$ we have: (the subscript λ is omitted for simplicity):

$$-\frac{dI}{\beta_e ds} = I - J \quad (3.53)$$

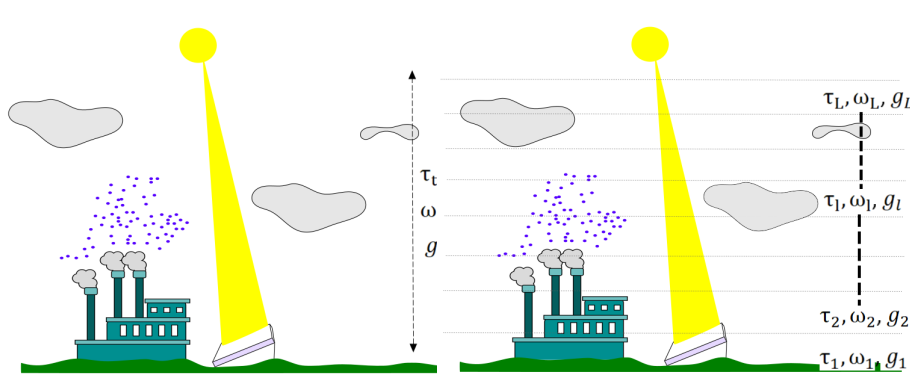


Figure 3.4: Schematic representation of the integral method (left) and multi-layered method (right) of the 1D solar radiation scheme of code_saturne.

The differential operator is defined in time and space as:

$$\frac{d}{ds} = \frac{1}{c} \frac{\delta}{\delta t} + \Omega \cdot \nabla \quad (3.54)$$

where c is the velocity of light, Ω the unit vector for the direction of scattering through a position vector s , t is time. In a steady state condition, we have:

$$-\frac{1}{\beta_e(s)} (\Omega \cdot \nabla) I(s, \Omega) = I(s, \Omega) - J(s, \Omega) \quad (3.55)$$

where J can be produced by the single scattering of the direct solar beam, multiple scattering of diffuse intensity and emission of the medium. If we assume that the medium is vertically and horizontally homogeneous, It is given in any coordinate systems by:

$$J(s, \Omega) = \frac{\omega(s)}{4\pi} \int_{4\pi} P(s, \Omega, \Omega') I(s, \Omega') d\Omega' + \frac{\omega(s)}{4\pi} P(s, \Omega, \Omega_0) F_0 e^{\frac{-\tau}{\mu_0}} + (1 - \omega(s)) B(T(s)) \quad (3.56)$$

where Ω' is the direction of a pencil of radiation that got increased by multiple scattering from the direction Ω , $-\Omega_0$ is the direction of the direct solar radiation (the minus sign denotes that it is always downward), $P(\Omega, -\Omega_0)$ is the non-dimensional phase function that denotes the redirection of the incoming intensity defined by $-\Omega_0$ to the outgoing intensity defined by Ω (and is defined in section 2.3.2.3) and $B(T(s))$ is the emission defined in section 2.2.2.4.

If we assume the medium to be absorbent, non-scattering and non-emitting, and homogeneous with respect to its single scattering proprieties including the extinction coefficient, then the equations get simplified to:

$$\frac{dI}{ds} = (\Omega \cdot \nabla) I(s, \Omega) = -k(s) I(s, \Omega) \quad (3.57)$$

with:

$$I(s, \Omega) = \int_{\lambda_1}^{\lambda_2} I_\lambda(s, \Omega) d\lambda \quad (3.58)$$

$$k(s) = \int_{\lambda_1}^{\lambda_2} k_{\lambda}(s) I_{\lambda}(s, \Omega) d\lambda / \int_{\lambda_1}^{\lambda_2} I_{\lambda}(s, \Omega) d\lambda \quad (3.59)$$

3.3.3.2 Analytical resolution of the RTE

Various methods for angular discretization exist, one example is the spherical harmonics (P_N) method that discretizes the angular variable of the RTE into spherical harmonics. It gives a set of coupled partial differential equations, called the P_N equations (N refers to the spherical harmonics truncation order) [Koerner et al., 2018]. Another way is stochastic methods, such as Monte-Carlo (MC) method that involves releasing and tracing photons from a source through a medium divided into a number of cubic cells. The absorption and scattering of photons may be considered as stochastic processes in which the scattering phase function is assimilated to a transformation probability function that redistributes the photons in different directions [Liou, 2002, Mayer, 2009]. A third method is the discrete ordinates' method, which solves the RTE on a fixed angular grid to remove the angular dependence and is further detailed because it is used in code_saturne 3D radiative model.

The Discrete Ordinates method for Radiative Transfer The Discrete Ordinates Method for Radiative Transfer, also known as DISORT, has been developed by Chandrasekhar [1950]. It is an exact method to solve the RTE and is similar to the adding method in terms of numerical calculations.

Liou [1973] demonstrated the utility and power of this method to compute the radiation fluxes in cloudy and aerosol atmospheres. It involves the discretization of the basic RTE and a solution of a set of first order differential equations. The method was found to be efficient and accurate [Stamnes and Swanson, 1981, Stamnes and Dale, 1981]. A numerical stable algorithm in multiple scattering and emitting layered media applicable from the UV to the radar region of the electromagnetic spectrum was proposed by Stamnes et al. [1988] and has been used in several radiative models (see section 3.4).

In the discrete ordinate method, the full solid angle 4π is divided into a finite set of discrete angular intervals and the direction variation μ is discretized in N_{DOM} directions μ_k , as represented in figure 3.5 for $N_{DOM}=8$, and consists of approximating an integral term by a finite summation. For a given function f , it becomes:

$$\int_0^{4\pi} f(\mu) d\Omega = \sum_{k=1}^{k=N_{DOM}} f(\mu_k) \omega_k \quad (3.60)$$

ω_k is the weight associated to each direction μ_k . The RTE becomes a system of $2N_{DOM}$ linear differential equations for the $2N_{DOM}$ unknown functions. Makké [2015] details various quadrature models used for the discrete ordinate method. We focus on the S_N method because it is used in code_saturne radiation model. It consists of defining a finite number of direction N_{DOM} as: $N_{DOM}=N \times (N+2)$, N being the order of the quadrature. Each subdomain follows the invariance principle around the angle. The different propagation directions and weights are then calculated on one subdomain and deduced by symmetry on the others.

Noting that only a finite number of directions are imposed, the results suffer from the so-called

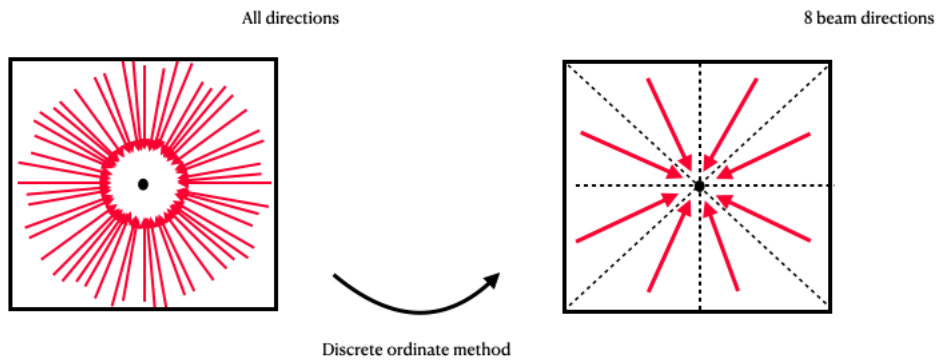


Figure 3.5: Illustrated diagram of the discrete ordinate method for $N_{DOM}=8$, it is represented in 2D for simplification purposes.

ray effect or unphysical spatial distortion. Specifically, the distribution function is solved in a limited number of discrete angular directions, which allows the information to propagate only along some specific directions. A solution would be to increase the number of ordinates, which also increases the computational time [Zhu et al., 2020].

3.4 Radiative transfer numerical models

Various models consider the plane-parallel assumption and neglect the horizontal variations in the atmosphere. They consider clouds as being homogeneous and plane parallel, which is not true in nature, but this assumption allows solving the RTE in a small amount of computer time. The RTE may then be solved using the two stream or the discrete ordinate methods. From the various empirical models of literature we will present the Meteorological Radiation Model (MRM) model that is based on the integral method, the RRTM and the Fast All-sky Radiative Model for Solar application (FARMS) that consider different layers of the atmosphere. However, for realistic studies on the interaction of radiation and clouds, 3D models are necessary, and some techniques are detailed in the following section. Prior to introducing 3D models, we will elaborate some complements related to the modelling of solar radiation in a cloudy atmosphere.

3.4.1 1D radiative models

3.4.1.1 1D integral models

As the name indicates, integral models refer to radiative transfer models based on the integral assumption for the resolution of fluxes at the surface: it is based on the two stream method by considering the atmosphere as being made of one homogeneous layer. The spectral band may be divided in several sub-bands: two sub-bands (UV-vis and SIR) in code_saturne, but not necessarily, like in MRM presented below that considers one spectral band only.

Meteorological Radiation Model (MRM) MRM was initially developed by the Atmospheric Research Team (ART) at the National Observatory of Athens (NOA) [Kambezidis et al., 1997]. MRM is a code which estimates solar irradiance on a horizontal surface. Its main advantage is that it requires only meteorological parameters measured by classical meteorological stations as input: air temperature, relative humidity, barometric pressure and sunshine duration. It uses these common meteorological data for estimating solar radiation through transmission functions, some taken from LH74's parametrization.

Different version of the code were elaborated: the original form of MRM (MRM v1) worked efficiently only under clear-sky conditions. MRM v2 introduced new analytical transmittance equations that made it more efficient. However, this version still worked well under clear-sky conditions only. Therefore, to overcome these deficiencies, a third version was developed, MRM (MRM v3). A further development of the MRM was achieved, MRM v4, providing further improvement in relation with partly cloudy and overcast skies. However, severe errors in the transmittance and solar geometry equations were discovered and then corrected in a new version of MRM (MRM v5). It was used to simulate radiation during the solar eclipse of the 29 March 2006 [Psiloglou and Kambezidis, 2007] where it showed satisfactory results, and it performed better than previous versions in both global and diffuse radiation components during tests conducted in Athens, Greece, and Eilat and Bed-Dagan, Israel. Equations describing the different versions of, MRM as well as results, can be found in Badescu [2008].

3.4.1.2 1D multi-layered models

Multi-layered models refer to a type of model that solve the RTE using the adding method and by dividing the atmosphere in different homogeneous layers. Several models exist in literature, we present here the RRTM model that is implemented in several general circulation or NWP models, and FARMS that is a recent and efficient model.

Rapid Radiative Transfer Model (RRTM) The RRTM, developed by AER, calculates short wave and long wave fluxes as well as cooling rates. It can be applied to general studies of atmospheric radiative transfer and for implementation into general circulation models (like IFS, WRF, MM5). The RRTM model includes calculations in clear-sky and cloudy-sky, with a parametrization of the radiative effect of water and ice clouds. It is divided into 16 bands in the long wave spectrum (referred to as RRTM_LW) and 14 bands in the short wave (referred to as RRTM_SW). The RRTM_SW model v2.4 is based on the DISORT algorithm and modelled sources of extinction including water vapour, carbon dioxide, ozone, methane, oxygen, aerosols, and Rayleigh scattering. Validation against the LLBRTM model are done and justify the accuracy of the model [Clough et al., 2005]. In more recent versions, the two-stream method is used instead of DISORT.

Fast All-sky Radiative Model for Solar application (FARMS) With the aim of developing an efficient and fast radiative transfer model, the FARMS has been developed. It uses a simplified clear-sky radiative transfer model, REST2, and simulated cloud transmittances and reflectances from RRTM with a sixteen-stream DISORT method. It is known for being

faster than regularly used solar resource assessment and forecasting models, with an accuracy in computing cloud transmittance and solar irradiance that is comparable or better than two-stream models [Xie et al., 2016]. The FARMS-NIT (Narrow-band Irradiances for Tilted surface) directly solves spectral radiances from the radiative transfer equation, which profoundly increases the accuracy in surface irradiances, especially over inclined PV panels [Xie and Sengupta, 2018]. It computes irradiance by considering three possible paths of photon transmission in a cloud-free atmosphere. For each path, the scattering by aerosols is simulated using the single scattering phase function and a two stream approach and the radiative transfer equation of downward irradiance is analytically solved. The accuracy of the model was evaluated by the clear-sky observations at the National Renewable Energy Laboratory (NREL)'s Solar Radiation Research Laboratory (SRRL) and various radiative transfer models [Xie and Sengupta, 2018]. It is enhanced for cloudy sky conditions by retrieving the cloud transmittance and reflectance are efficiently retrieved from a comprehensive look-up table pre-computed by a 32-stream DISORT algorithm [Xie et al., 2019]. With the aim of reducing the uncertainty in estimating the DNI, FARMS models were extended to compute the DNI. They are based on inputs from the atmospheric and land surface retrievals and a finite-surface integration algorithm. It estimates solar radiation at different solid angles, thus efficiently inferring its contribution to a surface perpendicular to the sun direction [Xie et al., 2020].

3.4.2 Modelling of solar irradiance in a cloudy atmosphere

The attenuation of solar radiation by clouds is oversimplified in various solar energy models. Numerous models consider clear-sky conditions only in the computation of solar irradiance at the Earth's surface (Müller et al. [2004], Gueymard [2008], Lefèvre et al. [2013], Ineichen [2008]). However, solar irradiance is highly attenuated by clouds, and it is important to consider them. Moreover, noting their role in the state of the atmospheric system, information on all cloud types and fogs are important from regional weather to global climate models.

To model radiative transfer processes in cloudy atmospheres, the interaction between the micro physical and macro physical structure of clouds and the radiation should be modelled and radiative transfer equations should be simplified. Therefore, the description of clouds' optical properties are needed (detailed in section 2.3.2.3 and in Cotton and Anthes [1992]). Though, for several reasons, it is quite challenging to properly integrate cloud properties or assimilate clouds in satellite models. In fact, moist processes are non-linear and difficult to take into account. Water appears in all phases (vapour, liquid, mixed phase or iced) in the cloudy atmosphere which complicates the radiative transfer equations and may increase the computational requirements and/or lead to numerical instabilities as in Polkinghorne and Vukicevic [2011]. Plus, clouds and precipitation are highly variable in time and space. Furthermore, clouds location errors are possible in satellite data assimilation [Polkinghorne et al., 2010, Kostka et al., 2014, Kurzrock, 2019].

Recent studies have approached the above-mentioned problems. A common method is the use of quantitative observations obtained by remote sensing measurements and especially geostationary satellite observations (as in the Heliosat v-4 model or in Kurzrock et al. [2018] and Gregow et al. [2020]). In Kostka et al. [2014], meteosat observations are used. They are smoothed horizontally, and a correction is applied to account for the slant satellite viewing

angle through the atmosphere. The brightness measurements from the [Geostationary Operational Environmental Satellite \(GOES\)](#) satellite images have been used to derive the bulk effect of clouds, the cloud albedo and absorption [[Gautier et al., 1980](#)]. [Polkinghorne et al. \[2010\]](#) use [GOES](#) measurements and introduce a simple cloud mask to distinguish between clear-sky observations and those with either low or high clouds. It is done in the aim of reducing cloud location errors. However, a poor agreement is obtained between observations and the model because of imperfections in the representation of the cloud situation. Nevertheless, these methods are severely restricted by data availability and the climate of the regions. Moreover, to overcome the long computational requirements, a solution would be the pre-computation of cloud extinction reflection and emission using rigorous radiative transfer models as it is done for [FARMS](#) model [[Xie et al., 2019](#)]. In the latter, the pre-computed transmittance of radiance is done by considering various scenarios for all the possible absorption and scattering events in the layers of the atmosphere. However, as discussed in chapter 2, in [1D](#) calculations we miss many effects related to cloud geometry like the transport of radiation through cloud side. However, this effect is quite important as it can increase the solar radiation at the earth's surface. [3D](#) radiative transfer model are then useful to overcome this problem. [Hogan and Shonk \[2013\]](#), for instance, presented a model to represent the effects of horizontal radiation transport through cloud sides in two-stream radiation schemes. They quantify the [3D](#) effect by studying the difference on the Top-of-atmosphere cloud radiative forcing using a [1D](#) and [3D](#) model. They showed that the [3D](#) effect on short wave cloud radiative forcing varies between around 25% and around 100%, depending on solar zenith angle. Furthermore, the [3D](#) cloud effects become particularly important for a certain type of clouds like cumulus clouds [Hogan and Shonk \[2013\]](#) and when the model resolution is on the order of or higher than the altitude of clouds [[Wissmeier et al., 2013](#)].

3.4.3 [3D](#) radiative models

[3D](#) model to solve the radiative transfer equation are useful for a better representation of cloud effects discussed earlier. As there is no simple closed numerical solution of the [3D](#) radiative transfer equation, iterative solutions are applied, like the [Spherical Harmonics Discrete Ordinate Method \(SHDOM\)](#). Another popular technique is the [Monte-Carlo \(MC\)](#) method that allows to consider all relevant atmospheric and surface processes without simplifying assumptions and the solution of radiative transfer in nearly arbitrarily complex [3D](#) media. Both techniques are now briefly presented.

[Spherical Harmonics Discrete Ordinate Method \(SHDOM\)](#) The algorithm and computer program [SHDOM](#) of [Evans \[1998\]](#) is used to model [3D](#) atmospheric radiative transfer. It uses a spherical harmonic angular representation useful for reducing memory use and time computing, and the radiative transfer source function is computed on a discrete spatial grid. Cloud [3D](#) effect is tested, and accurate results are obtained for simple geometries and realistic simulated clouds.

[Monte-Carlo \(MC\)](#) Despite its high computer cost, [MC](#) method are popular [3D](#) radiative models. [O'Hirok and Gautier \[1998\]](#) developed a model based on this method and includes

the important atmospheric and surface radiative constituents, Rayleigh scattering, absorption and scattering by both cloud droplets and aerosols, and absorption by the major atmospheric gases. They demonstrated that if cloud field is taken from satellite images, atmospheric absorption may be underestimated using plane-parallel (1D) assumptions compared to 3D computations. Note that the realistic cloud field representation was extracted from satellite visible and infrared imagery and that only water-based clouds were considered. They also showed the importance of the morphology of the cloud factor and the vertical stratification of water vapour. The MC method is used in the MYSTIC model [Mayer, 2009], which is part of the radiative transfer package known as “libRadtran” [Mayer and Kylling, 2005]. It has also been used for comparison purposes for the evaluation of the paNTICA model, a Fast 3D Radiative Transfer Scheme to Calculate Surface Solar Irradiance [Wissmeier et al., 2013]. In the latter, they showed that considering the 3D effects is necessary if higher model resolutions are used in the future and proposed ways to consider them and, thus, to reduce the errors made with 1D radiative transfer solvers.

3.5 code_saturne solar radiation model

The work for this thesis is based on the radiation model included in the CFD code code_saturne in its 1D and 3D versions. This section aims at introducing the module, the 1D equations are detailed in appendix A.1 and the 3D equations in chapter 6.3.

3.5.1 General description

code_saturne is an open-source CFD software developed by EDF R&D. It can solve the Navier-Stokes equations for 2D, 2D-axisymmetric and 3D flows. It can handle either incompressible or compressible flows, with or without heat transfer and turbulence. Several modules exist for specific physics like radiative heat transfer, combustion (gas, coal, heavy fuel oil, ...), magneto-hydrodynamics, compressible flows, two-phase flows (Euler-Lagrange approach with two-way coupling), atmospheric flows.

In this thesis, we have improved and used the 1D and 3D radiative scheme of code_saturne. On the basis of previous works, Milliez [2006] worked on the radiative effects in an urban canopy for the case of a transparent atmosphere. In Zhang [2010]’s thesis, the radiative fog was simulated using the standalone 1D model. Makké [2015] developed the 3D module for the infrared radiation in an absorbing medium, which was later adapted by Yassine Manaane for solar radiation and KS18 added the possibility to take into account the absorption and diffusive properties of aerosols.

In the standalone 1D scheme, the calculation of the global, direct and diffuse irradiances depend on the optical properties of clouds and aerosols, absorption of atmospheric gases and ground albedo. The model is based on the LH74 parameterization. It is based on the adding method presented in section 3.3.2.2 and a parametrization of the absorption of solar radiation by ozone, water vapour and earth’s surface. Two different assumptions are made for the modelling of 1D -irradiance inspired by LH74 : the integral method, used in the study of chapter 4 and the multiple-layered method used in the study of chapter 5. These two methods have been used for this thesis, however, in the official version of code_saturne, only the multiple-layered

method was added because both methods provide very close results for downward surface solar irradiance and the vertical flux divergence is useful information for various applications of code_saturne.

The 1D radiative scheme is included in the 3D scheme. In fact, the 3D scheme calculates irradiance up to 2000 m, then it uses the calculations of the 1D scheme. Moreover, the 1D fluxes are used as the top boundary condition for the 3D scheme. Equations and details can be found in section 6.3.

Chapter 4

The 1D integral radiative scheme of code_saturne

4.1 Introduction

This chapter aims at developing the first objective of this thesis:

Objective 1: *Improvement of the 1D integral radiation model in a cloudy atmosphere using measurements and verification of its robustness on a long period.*

As a matter of fact, the 1D radiation scheme of code_saturne presented in chapter 3.5 was evaluated, in its previous version, in KS18 where it performed well for clear-sky days but poorly for cloudy-sky days during August 2009 at the SIRTA Observatory in Île-de-France. Indeed, clouds strongly influence solar radiation and are difficult to model. In this chapter, the model is used in order to conduct simulations for August 2009 as in KS18 but also for a longer period of time for the whole year 2014 in order to test the model on different seasons of the year. In-situ and remote sensing measurements play an important role in this chapter. They first allow us to improve the model and find adequate equations for the description of radiative fluxes and optical properties. Then, measurements of cloud optical properties (COPs) are used as input to the code and sensitivity tests are conducted on the different extracted measurements and compared to those simulated using WRF . Through this study, the model improved, specially under a cloudy atmosphere and a new version of the 1D integral radiation scheme is developed. Satisfactory results are obtained under all sky situations and validated using observations and the HelioClim model. However, some discrepancies between simulations and observations existed and are analysed in order to understand their causes.

Part of the following study is presented in a paper that will soon be published by the Solar Energy journal ("Improvement of solar irradiance modelling during cloudy-sky days" by Al Asmar et al. 2021 referred to as LA21) and constitutes an important part of this chapter. Therefore, this chapter is structured as follows: in section 4.2, we detail the previous work as well as the one that was done for the improvement of the radiation model and the preparation of some input data to the radiative scheme. In section 4.3, the article LA21 is presented. Before concluding this chapter, complementary works are detailed in section 4.4.

Contents

4.1 Introduction	49
4.2 Preamble: previous work and preparation of input data	50
4.2.1 Previous work and improvement of the solar radiative scheme	50
4.2.2 Preparation of input data	53

4.3 Article: Al Asmar et al. (2021): Improvement of solar irradiance modelling during cloudy-sky days using measurements	58
4.3.1 Abstract	58
4.3.2 Introduction	58
4.3.3 Methodology	60
4.3.4 Model evaluation	71
4.3.5 Improvement of irradiance modelling on cloudy-sky days	73
4.3.6 Discussion	76
4.3.7 Conclusion	80
4.3.8 Appendix	81
4.4 Complementary works	86
4.4.1 Comparison with HelioSat models	86
4.4.2 Discussion on the parametrization developed for the COD	87
4.4.3 Supplement on the error discrepancies analysis	90
4.5 Summary	93

4.2 Preamble: previous work and preparation of input data

4.2.1 Previous work and improvement of the solar radiative scheme

In [KS18](#), the 1D radiation scheme was used to estimate irradiance fluxes at the surface in August 2009 at the [SIRTA](#) and Carpentras (south of France). The study focused on the effect of aerosols on the direct and global irradiances. Note that, in chapters 4 and 5 the direct irradiance refers to the horizontal direct irradiance which is the component measured on a horizontal surface (and not the DNI which is more common). [AOPs](#) were calculated using the air quality modelling platform *Polyphemus* (refer to section 4.2.2.2) and the meteorological and ground data and [COPs](#) were estimated using the [WRF](#) model (refer to section 4.2.2.1). As it can be seen in figures 4.1 and 4.2 representing the diurnal cycles of the global and direct surface fluxes, satisfactory results were obtained during clear-sky days (with [RMSE](#) score of 24 W m^{-2} for the global component and 33 W m^{-2} for the direct component) and simulations overestimated observations during cloudy-sky days and important biases and [RMSE](#) scores of 140 W m^{-2} and 198 W m^{-2} for the global and direct components respectively.

Consequently, for a better description of cloud effects, the radiation scheme was revised and modified. Prior to developing the different improvements that were added to the model, it is important to understand the model's calculation chain, presented in figure 1 of [LA21](#). As explained in [LA21](#), the model needs several data as input ([AOPs](#), [COPs](#), meteorological and ground data). The model is based on the [LH74](#) parametrization: the irradiance is computed by considering two spectral bands: [UV-vis](#) band (300-700 nm) and [SIR](#) band (700-3000 nm). The transmission and reflective functions for clouds and aerosols are calculated with the δ -quadrature two-stream approximation, including [Joseph and Wiscombe \[1976\]](#) correction (refer to section 3.3.2.2). The absorption and transmission functions for gases (ozone and water

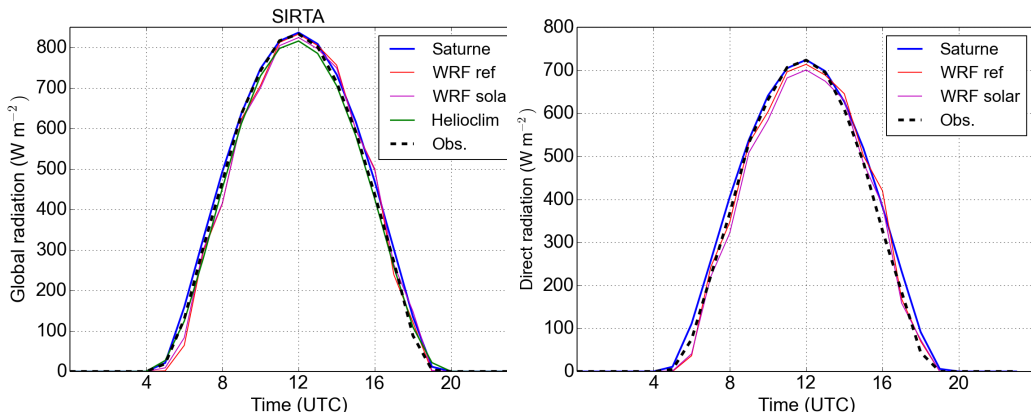


Figure 4.1: Diurnal cycle of global (left panel) and direct (right panel) irradiances measured at the **SIRTA** during clear-sky days in August 2009 (- - -) and compared to simulated values computed with Helioclim (—), code_saturne (—), **WRF solar** (—), **WRF -ref** (—) from **KS18**.

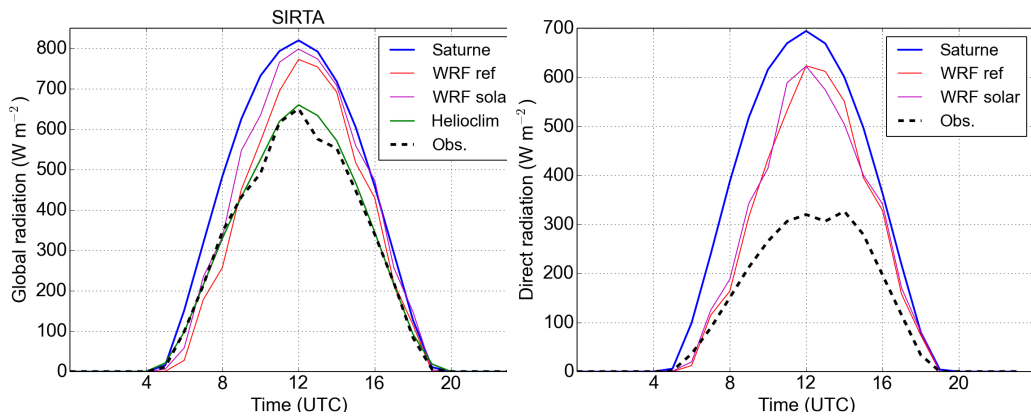


Figure 4.2: Diurnal cycle of global (left panel) and direct (right panel) irradiances measured at the **SIRTA** during cloudy-sky days in August 2009 (- - -) and compared to simulated values computed with Helioclim (—), code_saturne (—), **WRF solar** (—), **WRF -ref** (—) from **KS18**.

vapour) are taken from LH74. Irradiance fluxes are calculated at the ground only and compared to ground measurements.

This study was conducted as a follow-up to KS18. First, investigations were conducted in order to understand the problem during cloudy-sky days simulations. The main problem was that the cloud liquid water path as well as the cloud fraction estimated using WRF model were very low and close to 0 for most layers and at all time in August 2009 which may be due to the large spatial resolution of WRF during that period. Therefore, results obtained for cloudy-sky days were similar to those during clear-sky days. In consequence, we focused on the calculations over the SIRTA site, not only because it is a cloudy region, but also because it has high-quality measurements of surface radiative fluxes and remote sensing instruments which provide various COPs (cloud fraction, LWP, cloud base height, ...). Cloud fraction and COD from the SIRTA ReObs deduced from satellite measurements were used as input to the code and simulations ran for August 2009. Having the right parameters as input to the model, we were able to improve it and choose adequate equations for the description of COPs and radiative fluxes.

The cloud fraction in KS18 that was weighted depending on the transmittance of the cloud and to the COD (equ. 1.4 of KS18) is no longer used. After testing the different parametrization of cloud fraction of Oreopoulos and Khairoutdinov [2003], we decided to use for this study the maximum overlapping assumption if the cloud fraction in the different layers is provided as input. From the individual layer cloud fractions, the combined cloud fraction at the ground is equal to the maximal value of cloud fraction when using the maximum overlapping assumption. This choice was made because the values cloud fraction from WRF (the only one available for each layer for this study) are low and underestimated. Additionally, the SSA and asymmetry factor for clouds are now calculated separately for the UV-vis and SIR spectral band and are not integrated over the whole spectrum as in KS18 for more precise results. The equations of Nielsen et al. [2014] are used as detailed in section 4.3.8.1.

Furthermore, another main difference with KS18 radiation scheme concerns the direct radiation estimation. Previously, it was calculated using Psiloglou et al. [2000]'s expression (refer to KS18), but we had noticed that for specific cases the value of the direct irradiance was higher than the one for the global irradiance. In order to avoid having unphysical results and to be more coherent with the estimation of global fluxes, we chose to calculate it using an expression inspired by LH74 parametrization (refer to section 4.3.8.2). Additionally, the radiation scheme was modified in order to consider the absorption of minor gases through the transmission function for minor gases (Tmg-equ.A.6 Psiloglou et al. [2000]). Figure 4.3 shows the diurnal cycle of global and direct irradiances during cloudy-sky days before and after the model's improvement and coupling with satellite measurements for the COPs. The estimation of radiation fluxes in a cloudy atmosphere has clearly improved, as we can see in figure 4.3 and the metrics of comparison provided in LA21.

The model was also validated on a longer period (for the year 2014) in order to test it during different seasons of the year. However, compared to August 2009, fewer measurements were available for the year 2014. In particular the COD was not available, and it was interesting to see how it is possible to retrieve such an important parameter from existing measurements (microwave radiometric measurements of LWP).

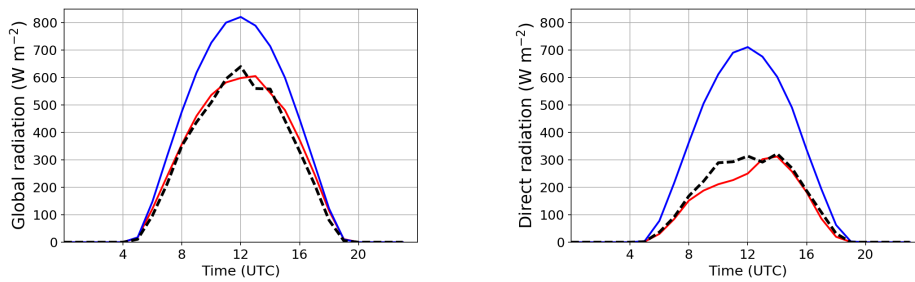


Figure 4.3: Diurnal cycle of global (left panel) and direct (right panel) irradiances measured at the [SIRTA](#) during cloudy-sky days in August 2009 (- - -) and compared to simulated values computed with `code_saturne` as in [KS18](#) (—) after improving the model and coupling it with satellite measurements for the [COPs](#) (—)

4.2.2 Preparation of input data

Two periods are simulated in [LA21](#): August 2009 and year 2014. Input data for the description of meteorological, ground data, [AOPs](#) and [COPs](#) were taken from [KS18](#) for the simulations in August 2009. Meteorological and [COPs](#) from [WRF](#) simulations as well as emissions and concentrations from Polyphemus simulations were obtained from [Sartelet et al. \[2018b\]](#) for the period of 08/01/2014-30/10/2014. However, the ground albedo had to be extracted and the [AOPs](#) had to be computed, as detailed in the sections [4.2.2.1](#) and [4.2.2.2](#) respectively.

4.2.2.1 Simulations using [WRF](#) model

[WRF](#) model has been presented in section [3.2.4](#) and the irradiance fluxes estimated by [WRF](#)-solar model were used in [KS18](#) for comparison purposes. [WRF](#) simulations were conducted in order to estimate [COPs](#) (cloud fraction, liquid water content), water vapour, temperature and pressure vertical profiles as well as ground albedo. Simulations for August 2009 were retrieved from the study of [KS18](#) and from [Sartelet et al. \[2018b\]](#) for the year 2014 except for the ground albedo that had to be extracted. The following subsection briefly describes the parameters used for the simulation and the validation for the albedo of the year 2014.

Configuration The detailed configuration and parametrization scheme for August 2009 can be found in [KS18](#) and for the year 2014 in [LA21](#). The three different domains simulated by [WRF](#) are represented in figure [4.5](#):

- The coarser domain (W01: 70×70 grid points): Western Europe with a spatial resolution of $40 \times 40 \text{ km}^2$
- The intermediate domain (W02: 65×61 grid points): France with a $20 \times 20 \text{ km}^2$ resolution

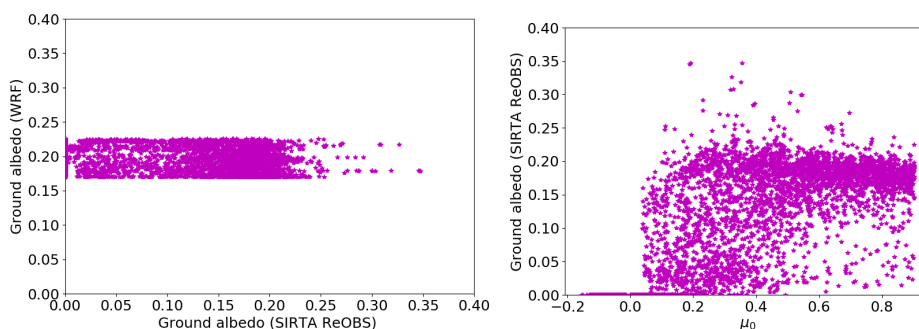


Figure 4.4: Ground albedo from WRF versus the one measured at SIRTA (left panel). Estimated ground albedo at SIRTA versus μ_0 (cosinus of the solar zenith angle) (right panel) during the period 08/01/2014-30/10/2014.

- The inner domain (W03: 41×41 grid points): greater Paris (Île-de-France) with a 5×5 km² resolution.

The vertical resolution is made of 40 levels from the surface up to 50 hPa. Simulations for year 2014 were conducted on the inner domain, and the one used for August 2009 were conducted on the intermediate domain (resolution of 20×20 km²) which partially explains the misrepresentation of clouds in KS18. The inner domain could have been used for August 2009 for a better description of COPs but AOPs were estimated with Polyphemus only for the inner and coarser domains, and we should have the same domains for both Polyphemus and WRF simulations.

Validation for the ground albedo The averaged ground albedo extracted from WRF for the period "year 2014" at the SIRTA is equal to 0.2 with a low standard deviation of 0.02. Considering that the SIRTA site is a mix of bare soil/small grass and that the grass albedo varies between 0.21 and 0.27 [Gul et al., 2018] and dark bare soil lower the albedo to 0.17 [Markvart et al., 2003], we may conclude that the value used in WRF is a good estimation. Moreover, the albedo was estimated from the ratio of the upward to downward fluxes measured at the SIRTA. The averaged measured albedo is equal to 0.13 with a standard deviation of 0.08. The comparison between the simulated and measured albedo is represented in figure 4.4. The higher standard deviation of the measured albedo can be observed in this figure, it is related to the dependence of the albedo to the zenith angle. In fact, contrarily to simulated values, the measured albedo depends on the zenith angle which explains the values close to 0 or to 0.35. This is represented in figure 4.4 (right panel). However, for values for which irradiance is the strongest during the day, the albedo from WRF compares well to measurements. It explains why similar metric scores comparing the simulated and measured irradiances were obtained when the simulation ran using the measured albedo instead of WRF's albedo.

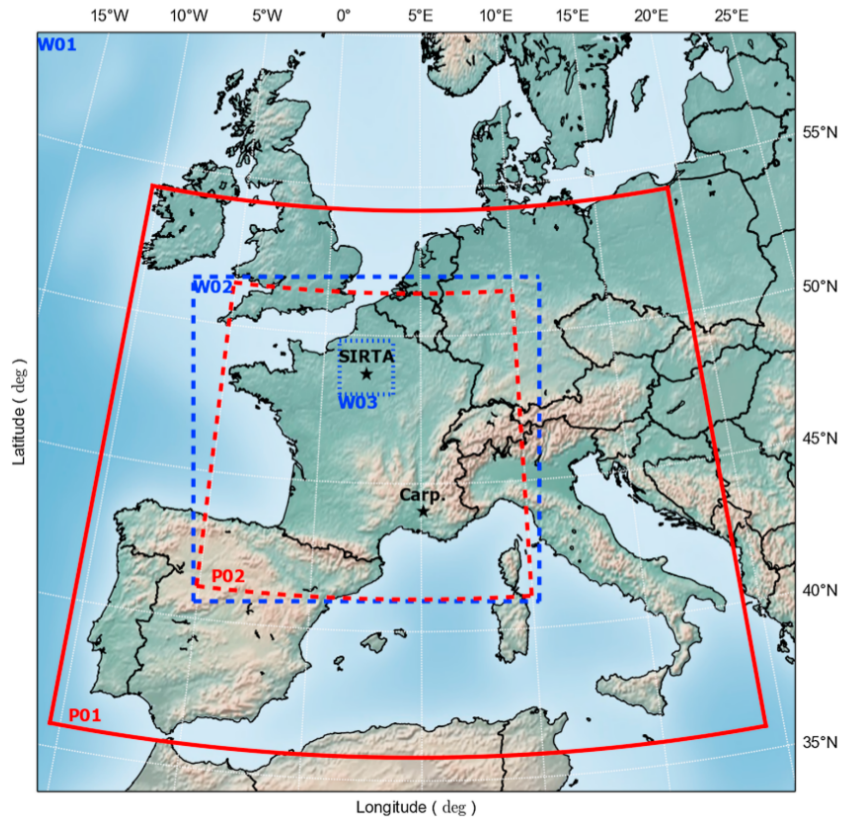


Figure 4.5: Topographic map of the main domain (W01 = Western Europe) showing the location of the two nested domains (W02 = France and W03 = Île-de-France). The SIRTA and Carpentras sites are located by a star. The domains simulated with Polyphemus/Polair3D are represented by the red quadrilaterals (P01 = Europe and P02 = France). (KS18)

4.2.2.2 Simulations using the Polyphemus model

The validation of AOD in the UV-vis domain for the year 2014 is provided in LA21. However, a more detailed presentation of the model and the validation in the SIR domain is given here.

Description The air quality simulation has been done using the chemistry transport model Polair3D of the Polyphemus platform developed at the CERE laboratory [Mallet et al., 2007]. Polyphemus is an open-source platform that gathers several dispersion models (Gaussian, Eulerian, ...), advanced methods in particular for data assimilation and miscellaneous tools (mainly for data processing). It can support different dispersion models, consider different spatio-temporal scales and treat different types of pollutants. It was initially developed around the chemistry-transport model Polair3D which has since been rewritten for further integration in Polyphemus.

In this study, we use the dispersion model Polair3D which includes a gas chemistry model and a size resolved model for aerosols. Among particle compounds we have:

- primary compounds (mineral dust, Black Carbon (BC) and 3 primary organic of intermediate, semi and low volatility)
- inorganic compounds (ammonium, sulfate, nitrate, chloride and sodium)
- secondary organic compounds

It is a bin model where aerosols are internally mixed and the size distribution goes from 0.01 to 10 μm . The model takes as input the meteorological data of WRF or ECMWF. The particles concentrations and corresponding AOPs were computed with Polyphemus following a method described in detail in KS18 .

Configuration For the year 2014, the simulations are performed on the W03 domain using the simulation of WRF on the same domain. Configuration is detailed in LA21 .

Validation for AOPs for the year 2014 Simulated AOD is compared to observed AOD extracted from the SIRTA ReObs project. They are compared using the metrics in table 4.1 and in figure 4.6. Following LA21 and the criterion defined by Boylan and Russell [2006], we may conclude that the AOD is well estimated. However, as seen in figure 4.6 (and MFBE scores) the simulated AOD tends to overestimate observation. However, as AOD measurements aren't available for the whole period, the simulated values are used. It explains the poorer estimation of direct irradiance in 2014 compared to 2009 during clear-sky days (refer to LA21).

λ	500 nm	1000 nm
Mean Obs.(AOD)	0.056	0.156
Mean Sim.(AOD)	0.07	0.18
RMSE	0.058	0.12
MFE (%)	48	57
MFBE (%)	+ 19	+32

Table 4.1: Comparison between simulated AOD from Polyphemus and observed AOD from SIRTA ReObs at SIRTA in 2014.

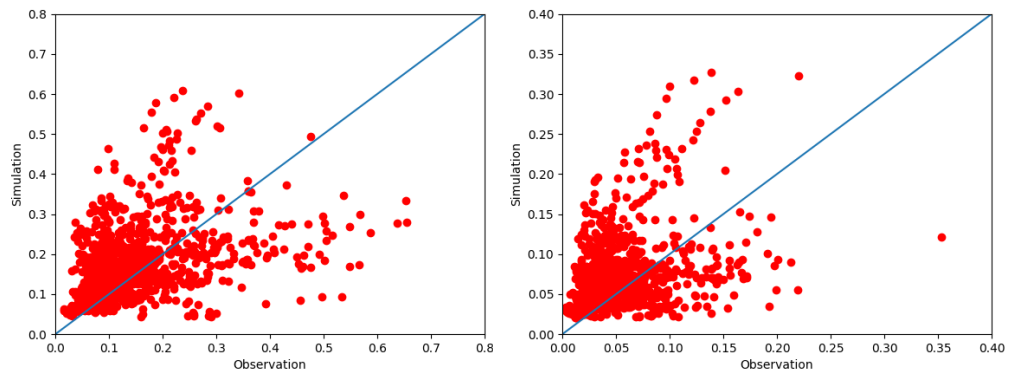


Figure 4.6: Simulated versus observed AOD in 2014 at $\lambda=500$ nm (left panel) and $\lambda=1000$ nm (right panel)

4.3 Article: Al Asmar et al. (2021): Improvement of solar irradiance modelling during cloudy-sky days using measurements

4.3.1 Abstract

Clouds have a strong influence on the amount of solar irradiance reaching the ground. However, they have large spatio-temporal variations and are difficult to model. The 1D irradiance model of code_saturne is used to estimate the global and direct solar irradiances at the ground, taking into account the impact of atmospheric gas, clouds and aerosols. Simulations are conducted and compared to measurements at the French SIRTAs observatory (instrumental site for atmospheric remote sensing research), located in Palaiseau, Île-de-France in August 2009 and in the year 2014. Although irradiance is very well modelled during clear-sky days, it is over-estimated during cloud-sky days. The estimation of irradiance during cloudy-sky days is improved by coupling the model to on-site measurements of cloud parameters from the SIRTAs. RMSEs around 59 W m^{-2} and 50 W m^{-2} and MBEs around $+17 \text{ W m}^{-2}$ and -18 W m^{-2} are obtained, respectively, for global and direct irradiances during cloudy-sky days using pyranometer measurements for cloud fraction and microwave radiometric measurements for liquid water path. A sensitivity analysis on the cloud parameters that may lead to the best improvement of simulated irradiance is performed. The cloud optical depth is the most important one, followed by the cloud fraction. The different instruments used for the determination of these parameters are examined. Moreover, hourly values of solar fluxes are analysed to determine and physically understand persistent errors between model and measurements when measured cloud parameters are used.

4.3.2 Introduction

The energy transition is a pathway toward the decarbonisation of the energy sector. It is necessary to reduce energy-related CO_2 emissions to limit climate change. To do so, energy-efficiency measures and renewable energies are set up. Thus, the expansion of solar energies is an important cornerstone of the energy transition. Solar irradiance is the input power source of photo-voltaic (PV) generators. An accurate prediction of the amount of solar irradiance reaching the ground is necessary to reduce the uncertainty on PV energy-yield assessment, to optimize the performance of PV farms, and to forecast the production at different time scales. The amount of solar irradiance reaching the ground is influenced by different geographical, meteorological and atmospheric parameters. Those parameters have important spatio-temporal variations, leading to difficulties to accurately model solar irradiance. Depending on the forecast needs, different models have been developed to represent irradiance fluxes at the surface of the Earth [Lorenz and Heinemann, 2012, Diagne et al., 2013]. They can be categorized according to the forecasting timescales: for very short time scales (from minutes to few hours), statistical models combined to on-site measured irradiance data can be used [Reikard, 2009]. Satellite or cloud-imagery based models are used to derive irradiance forecasts [Lorenz and Heinemann, 2012], but they highly depend on the data availability, which depends for example on the passage of the satellite over the studied area. For longer

forecasting times (longer than some hours), Numerical Weather Prediction (NWP) models are the most suitable choice. NWP models are based on the modelling of physical phenomena. They predict the atmospheric variables based on current weather condition by solving the differential equations describing the evolution of these variables, which are required to estimate solar irradiance. Hybrid models have also been developed. They merge different approaches and derive an optimized forecast depending on the forecast horizon that integrates different kinds of input data [Cao and Cao, 2005].

NWP and hybrid models represent the diffuse, direct and global solar irradiances with different levels of complexity: from empirical models [Rigollier et al., 2000] or physics-based models [Xie et al., 2016] to radiative transfer based calculations [Müller et al., 2004] as presented in the overview of [Ineichen, 2006]. An example of an intermediate complexity representation is the two-stream approximation, which solves the transfer of irradiance through a plane parallel atmosphere and integrates irradiance over the zenith angle. Transmission and reflection functions are estimated using two or more spectral bands, and integrated over the vertical, like the rapid radiative transfer model (RRTM) [Clough et al., 2005] that uses the Discrete Ordinate method for Radiative Transfer (DISORT) algorithm [Stamnes et al., 1988] to solve the radiative transfer equation using multiple scattering. In the physics-based model of [Xie et al., 2016], the cloud transmittance and reflectance is estimated using plain exponential functions of solar zenith angle, cloud optical thickness and effective particle size. The description of the state of the atmosphere is required as an input of these solar-irradiance models. Atmospheric parameters include the optical properties of aerosols (AOP), clouds, water vapour and other gases. Although meteorological parameters may be derived from NWP, this is not always the case for AOPs, which may be derived from chemical transport models [Breitkreuz et al., 2009, Sartelet et al., 2018a].

The direct irradiance is crucial for the economic and energy evaluations of different solar energy applications, like solar concentrating and flat plate systems [Padovan et al., 2014]. It can be estimated from the transmission functions in the intermediate complexity models presented above. In empirical models, its estimation can be quite complex and decomposition models based on observations are sometimes used to separate the direct normal irradiance (DNI) from global horizontal irradiance (GHI) [Padovan et al., 2014, Bertrand et al., 2015] or simple methods for correcting the satellite derived DNI data [Polo et al., 2015].

Clear-sky irradiance is often accurately modelled [Psiloglou and Kambezidis, 2007, Blanc et al., 2011, Lefèvre et al., 2013, Kambezidis et al., 2016, Sartelet et al., 2018a], especially when the influence of aerosols is taken into account. Sartelet et al. [2018a] (referred to as KS18) showed that irradiance fluxes at the surface are strongly improved during clear-sky days when AOP are estimated from the aerosol concentrations simulated by a chemistry-transport model.

However, the modelling of irradiance during cloudy-sky days is a common problem for the various numerical models [Morcrette, 1991, Morcrette et al., 2008, Lorenz and Heinemann, 2012, Diagne et al., 2013], KS18. Clouds have a strong influence on solar irradiance at the surface, but they are extremely variable in space and time. The parameterization of clouds requires the determination of the cloud fraction at the ground, which requires the knowledge of the overlapping of the different vertical cloud layers [Räisänen, 1998], as well as cloud optical properties such as cloud optical depth (COD), single scattering albedo, and asymmetry factor [Stephens, 1978a, 1984, Nielsen et al., 2014]. In particular, low clouds are found in nearly

all types of convecting systems and are misrepresented in climate models [Naud et al., 15 Jun. 2010, Haynes et al., 2011, Gregow et al., 2020]. Satellite measurements have been used to improve the representation of cloud properties and irradiance. For example, geostationary satellite-derived cloud properties have been used to derive surface solar irradiance under cloudy sky [Schillings et al., 2004]. The brightness measurements from GOES satellite images have been used to derive the bulk effect of clouds, the cloud albedo and absorption [Gautier et al., 1980]. To better forecast irradiance, different methods are used. The description of clouds and irradiance in NWP models may be improved using satellite and/or in-situ measurements and data assimilation, as detailed in [Kurzrock et al., 2018] and [Gregow et al., 2020]: as satellite irradiances contain information on clouds, they may be directly assimilated; or retrieved cloud properties may be used to adjust the initial state of the NWP model. Other methods exist in literature. For example, in [Roy et al., 2001], a neural network approach is used to derive cloud coverage in the sky. In [Moncada et al., 2018], an artificial intelligence method is combined to sky imager data to forecast irradiance.

The goal of the current study is to improve the estimation of irradiance during cloudy-sky days by coupling a solar-irradiance model with on-site measurements, and to compare the added-value of different measurements. Because irradiance on cloudy-sky days is strongly influenced by the cloud fraction and the cloud optical depth (COD) [Lorenz and Heinemann, 2012], their representation using different parameterizations and measurements will be compared to determine the most efficient ones.

The 1D irradiance model included in the 3D CFD (Computational Fluids Dynamics) model code_saturne¹, described in KS18, is used in this study to represent the global and direct solar irradiances. Meteorological data from the WRF model and aerosol's concentrations from the air-quality modelling platform *Polyphemus* are used as input data [Sartelet et al., 2018b, André et al., 2020]. The measurements of cloud properties are obtained from different instruments of the French observatory SIRTa [Haeffelin et al., 2005], located in the southern suburbs of Paris. The article is structured as follows: first, the methodology and configuration of the simulation are detailed. Second, the modelling of irradiance during clear-sky days and cloudy days is briefly evaluated. Third, the impact of using different measured parameters to improve the modelling during cloudy days is estimated. Finally, an analysis of errors conforming to cloud properties is presented.

4.3.3 Methodology

4.3.3.1 The solar irradiance scheme of code_saturne

code_saturne is an open-source CFD software. It solves the Navier-Stokes equations for 2D, 2D-axisymmetric and 3D flows. In this study, the standalone 1D irradiance model of code_saturne is used to estimate, every hour, the total solar irradiance and its direct and diffuse horizontal components at the surface of the Earth (KS18).

This model parameterizes the attenuation of irradiance from gas, aerosol and clouds present in the atmosphere above the location studied. The solar irradiance flux is computed by consid-

¹<https://www.code-saturne.org/cms/>

ering irradiance from two spectral bands: the ultraviolet–visible (UV–vis) band (300–700 nm) and the solar infrared (SIR) band (700–3000 nm). In these two spectral bands, the solar irradiance is influenced by different processes:

- In the UV-vis band, solar irradiance is absorbed by ozone in the stratosphere and is scattered by air molecules (Rayleigh scattering), aerosols and clouds in the troposphere.
- In the SIR band, the absorption by water vapour dominates the ozone absorption in the troposphere.

The calculation of the irradiance is done at the ground surface by calculating the attenuation in the column above the surface. For the global and direct irradiance, this attenuation absorption is estimated through reflection and transmission factors defined by the multiple-scattering theory using the two-stream approximation (LH74 [Lacis and Hansen, 1974]). The atmosphere is assumed to have horizontally homogeneous optical properties and gas concentrations. The reflection and transmission factors of LH74 are used with the optical properties of atmospheric components integrated over the vertical axis. The original LH74 scheme has been modified to introduce the cloud fraction and differentiate the calculation during cloudy and clear-sky days, to compute both the direct and diffuse components of solar irradiance, and to take into account the aerosol contribution.

The description of the equations used here are similar to those of KS18, and are described in the appendix. The difference between KS18 and the present study lies in the calculation of the direct irradiance : in KS18, the parameterization of [Psiloglou and Kambezidis, 2007] is used, while the current study uses a formula that we derived and that is more consistent with the global irradiance model developed by LH74.

4.3.3.2 Input data

The solar irradiance scheme needs several inputs to be specified, such as the ground albedo and the vertical distribution of:

- Meteorological variables: temperature, pressure, relative humidity.
- Aerosol and cloud optical properties (optical depth, liquid water path (LWP), cloud cover fraction, single scattering albedo and asymmetry factor).

The simulations of direct, global and diffuse solar irradiances are performed and compared to measurements at the French SIRTA observatory, located at Palaiseau, in the southern suburbs of Paris [Haefelin et al., 2005]. The SIRTA observatory hosts the BSRN station of Palaiseau. Two periods are simulated: the period of 'August 2009', from 04/08/2009 to 28/08/2009, as in KS18, and the 'year 2014', from 08/01/2014 to 28/10/2014. The model's chain used is represented in Figure 4.7:

The input meteorological data (temperature, pressure, relative humidity) and ground albedo are obtained from WRF simulations. The cloud optical properties (cloud cover fraction, liquid water content) are derived from WRF outputs or from measurements. The air-quality platform Polyphemus provided the aerosol concentration data for the year 2014, as presented in

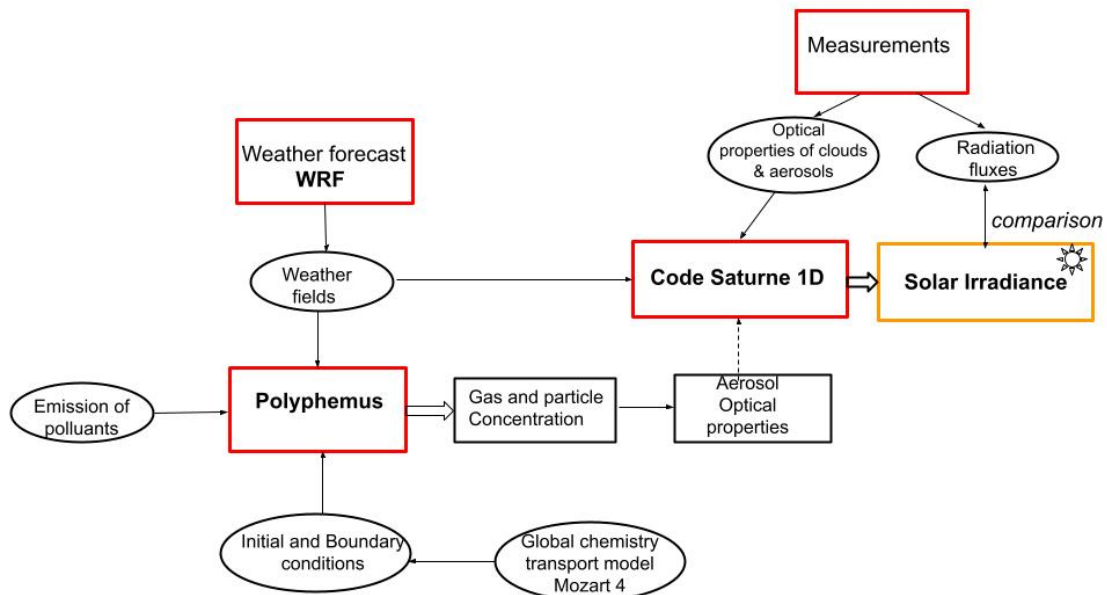


Figure 4.7: Scheme representing the models chain used for our cases of studies of August 2009 and the year 2014.

the following section. The aerosol optical properties are extracted from measurements for the period of August 2009. The configuration of the simulation used to generate the data is now briefly summarized, as well as the observational data used as input of the irradiance scheme to improve the cloudy-sky irradiance simulations.

4.3.3.3 Simulated meteorological data

The input meteorological fields are obtained from simulations with the [WRF](#) model. [WRF](#) is an open-source mesoscale model that solves the compressible and non-hydro-static Navier-Stokes equations [[Skamarock et al., 2008](#)].

For August 2009, as detailed in [KS18](#), the [WRF](#) model ran from 10 July to 30 August 2009 with hourly outputs. [WRF](#) simulations were initialized at 0000 UTC every 7 days with a 24 hours spin up. The simulation over the French domain was used for the current study. It has a spatial resolution of $20 \times 20 \text{ km}^2$ (65 x 61 grid points), see Figure 1 of [KS18](#). The vertical resolution goes from the surface up to 50 hPa. It is made of 40 terrain-following levels. The [WRF](#) "single moment 6 classes" scheme was used for the microphysics, combined with the Kain-Fritsch cumulus scheme ([[Kain and Fritsch, 1993](#)]).

For the year 2014, the set-up of the WRF simulation is detailed in [Sartelet et al., 2018b]. WRF simulations ran from 02 January to 28 October 2014 with hourly outputs. They were initialized at 0000 UTC every 6, 3 or 2 days depending on the period. The simulation over the greater Paris (Île-de-France) domain is used in the current study. Its spatial resolution is $5 \times 5 \text{ km}^2$ resolution (41×41 grid points). The vertical resolution goes up to 100hPa and is made of 28 vertical levels refined near the surface. For microphysics, Kessler scheme [Kessler, 1995] is used combined with the cumulus Grell-Freitas ensemble scheme [Grell and Devenyi, 2002].

Evaluation of the simulated ground albedo The ground albedo is obtained from WRF simulations. For the period 'year 2014', the averaged simulated albedo is equal to 0.2 with a standard deviation of 0.02. The averaged measured albedo is equal to 0.13 with a standard deviation of 0.08. The use of measured albedo instead of simulated values in code_saturne doesn't impact solar irradiance calculations. Contrary to simulated values, the measured albedo depends on the zenith angle μ_0 . For values of μ_0 for which irradiance is the strongest during the day, simulated albedo is similar to measurements.

4.3.3.4 Simulated aerosol concentrations

Aerosol optical data are computed using the air-quality modelling platform *Polyphemus* as detailed in KS18. The aerosol concentrations are computed with the chemistry-transport model Polair3D of the platform Polyphemus, which also determined the size and the composition of particles. The meteorological data needed as input of Polair3D/Polyphemus were obtained by interpolating the WRF simulations detailed in the previous section on the Polair3D/Polyphemus grid. The set-up of the simulations is detailed in KS18 for August 2009 and in [Sartelet et al., 2018b] for the year 2014. For August 2009, the simulations were performed from 15 July to 29 August 2009 over the France domain, with a spatial resolution of $0.2249^\circ \times 0.2249^\circ$ ranging from latitude 41.2°N to 51.32°N and from longitude 5°W to 9.84°E . The vertical was discretized with 8 levels of interfaces: 0, 50, 150, 300, 800, 1500, 2500, 4000, 6000 m. For the year 2014, the simulations were performed from 08/01/2014 to 30/12/2014 on the Île-de-France domain: spatial resolution of $0.02^\circ \times 0.02^\circ$ ranging from latitude 48°N to 49.5°N and from longitude 1.35°E to 3.55°E . The vertical was discretized with 14 levels of interfaces: 0, 30, 60, 100, 150, 200, 300, 500, 750, 1000, 1500, 2400, 3500, 6000, 12000 m.

Evaluation of the simulated AOD For August 2009, as detailed in KS18: at 500 nm, the measured and simulated mean AODs are respectively 0.18 and 0.14 with a mean fractional error (MBE) of 43% and a mean fractional bias (MFBE) of -28%. For the year 2014, at 500 nm, the measured AODs from the SARTA ReOBS [Chiriaco et al., 2018] and simulated mean values are respectively 0.056 and 0.07 with a MBE of 48% and a MFBE of +19%. To evaluate simulations of particle concentrations, [Boylan and Russell, 2006] defined the following criteria: the MBE should be lower than 50% and the MFBE should be between -30% and +30%, which are well satisfied here. The AODs simulated by Polyphemus compare well to measurements.

4.3.3.5 Observational data at SIRT

SIRT is a French observatory dedicated to the observation of the atmosphere. It has been collecting data for more than 15 years from active and passive remote sensing instruments and in-situ measurements. It is located in a semi-urban area, 20 km south of Paris, France (48,71 N, 2.2 E). SIRT Re-OBS is a project whose goal is to synthesize, analyse, homogenize, all SIRT observations hourly averaged in a single NetCDF file from 2003 to now [Chiriaco et al., 2018].

Instruments and parameters

The instruments used and the parameters extracted from SIRT Re-Obs are resumed in table 4.2.

Instrument	Variables	Uncertainty	Native Resolution	Availability	Reference
Multi-wavelength sun-photometer (CIMEL CE-318)	AOD by Sun and sky scanning	0.01	–	in 2009 and 2014	[Holben et al., 1998]
Pyranometers and Pyrhemeliometers (PYR)	Surface downwelling short wave irradiance (global, direct and diffuse components); cloud fraction	-5 W m^{-2}	1s	in 2009 and 2014	[Long et al., 2006]
Sky imager	Cloud fraction	$\sim 5\%$; depends on cloudy situation	1min	in 2009 and 2014	[Long and DeLuisi, 1998]
LIDAR	Cloud fraction (by integration over time); cloud base height	$\sim 5\%$	1h	in 2009	[Morille et al., 2007]
Meteosat Second Generation satellite	Cloud fraction (using the percentage of cloudy pixels over 15x15 pixels images); COD (in an iterative manner, by simultaneously comparing satellite-observed reflectances at visible and near-infrared wavelengths to lookup tables (LUTs) of simulated reflectances); LWP (from the retrieved COD and droplet effective radius)	–	3 km	in 2009	[Roebeling et al., 2006]
Microwave radiometer HATPRO	LWP	$\pm 20 \text{ g m}^2$	5s	in 2014	[Rose et al., 2005]
Celiometer	Cloud base height	15 m	30 s	in 2014	[Haeffelin et al., 2005]
Rain gauge R3070	Precipitation	0.1 mm	5s	in 2009 and 2014	[Haeffelin et al., 2005]

Table 4.2: Instruments and parameters extracted from SIRTA ReObs.

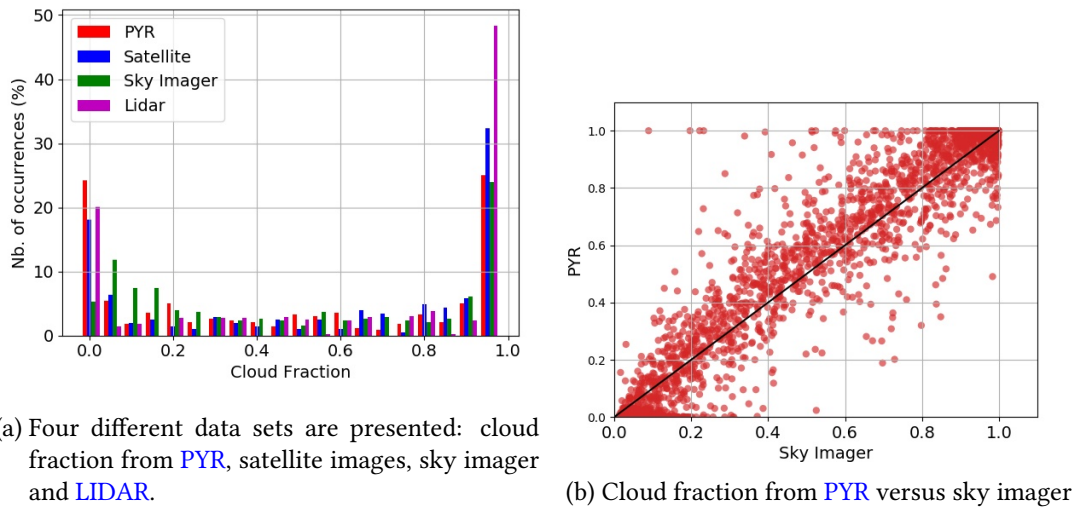


Figure 4.8: Distribution of cloud fraction during August 2009 (a) and the comparison between the two available cloud fractions for year 2014 (b) at **Sirta**.

4.3.3.6 Determination of cloud properties

In order to represent clouds in the model, the cloud fraction and different cloud optical parameters (**COPs**) are used: **COD**, which is presented in the following section, single scattering albedo, asymmetry factor, and cloud droplets effective radii, described in the appendix.

4.3.3.7 Cloud fraction

From WRF simulations The simulated cloud fraction is known at each vertical level of the model. It is difficult to estimate the cloud fraction seen from the ground because the overlapping between cloud layers is not known. Here a maximum overlapping is assumed.

Comparisons of cloud fraction from satellite, **PYR, sky imager and **LIDAR** in August 2009** The measured cloud fraction is integrated over the vertical. Cloud fractions issued from Meteosat Second Generation satellite data using the percentage of cloudy pixels are of great interest, because of their global coverage. However, data are only available when the satellite is passing above the studied location. Thus, the data extracted from satellite images is the one with the most invalid data ($\sim 28\%$ of invalid values during the day). This percentage of invalid data is $\sim 10\%$ for the cloud fraction measured with a **LIDAR**, $\sim 7\%$ for **PYR**, and 0% for the sky imager. The cloud fraction distribution in August 2009 obtained with these instruments is represented in the histogram of Figure 4.8a. In the set of values extracted from **PYR** and from satellite images there are respectively: $\sim 25\%$ and $\sim 32\%$ of cloudy sky ($F_C > 0.95$), $\sim 25\%$ and $\sim 18\%$ of clear-sky situations ($F_C < 0.05$) and $\sim 50\%$ of partially cloudy-sky situations for both data sets. The data extracted from the sky imager does not contain values exactly equal to 0 or 1, but it contains, respectively, $\sim 5\%$ and $\sim 24\%$ of clear and cloudy sky situations.

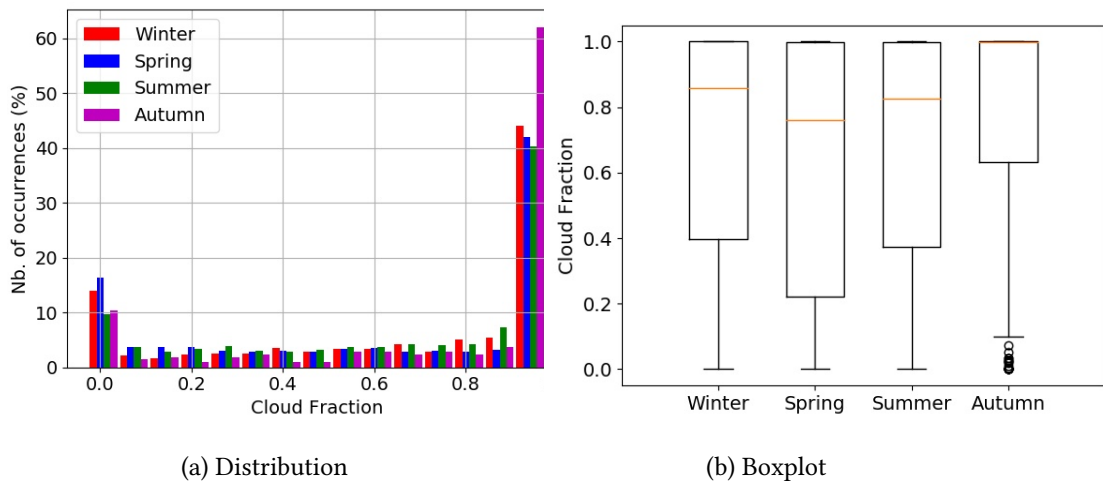


Figure 4.9: The cloud fraction (PYR) at SIRT A during the four seasons of 2014.

Comparisons of cloud fraction from PYR and sky imager in 2014 For the year 2014, only the cloud fraction from PYR and from sky imager are available: the two set of data are quite similar with a RMSE score of 0.168, they are represented in figure 4.8b. The distribution of cloud fraction from PYR for the year 2014 is represented in Figure 4.9a and the box diagram for each season in Figure 4.9b. It should be noticed that in Autumn (October), 50% of the values of cloud fraction are equal to 1 and the other 50% are between 0.1 and 1. For the other seasons the median is around 0.85 in winter, 0.75 in spring, 0.82 in summer. Figure 4.9a represents the distribution of cloud fraction for each season, normalized by the number of valid values for each season. Over the whole year, fully cloudy situations (cloud fraction of 1) are the most frequent. The other values are in the range [0,0.99] with a higher density around 0. Therefore, there are only a few clear-sky situations and the distribution of cloud fraction is quite similar throughout the different seasons.

4.3.3.8 Cloud Optical Depth

The COD (τ_C) is an adimensional parameter that characterizes the strength of attenuation by clouds. When it is equal to 0, there is no extinction of irradiance due to clouds. τ_C depends on the type of cloud and the size of the water drops or ice crystals. For water clouds, it can be approximated by [Stephens, 1978a]:

$$\tau_C = \frac{3}{2} \frac{LWP}{\rho r_e} \quad (4.1)$$

where LWP is the liquid water path (g m^{-2}), ρ the density of water (g m^{-3}) and r_e the effective diameter in m.

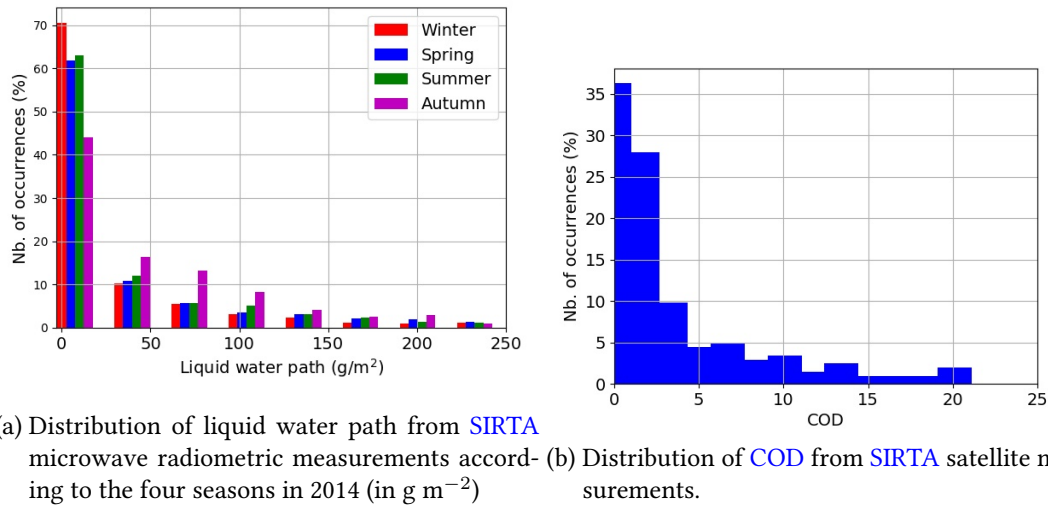


Figure 4.10: Distribution of COPs in August 2009 and year 2014.

From WRF simulations When WRF simulations are used to estimate τ_C , it is calculated using equation (4.1) with LWP calculated with WRF and a constant value of r_e ($14 \mu\text{m}$ [Stubenrauch, 2013]).

Satellite measurements of COD They are available in the SIRTA ReObs database for year 2009. The COD distribution is represented in the histogram of Figure 4.10b. The values range between 0 and 109 with a majority in the range [0,4]. Therefore, most of the clouds present at SIRTA are low density clouds [Stephens, 1984].

Microwave radiometer measurements of LWP They are available for the year 2014 and their distribution is represented in Figure 4.10a. It can be seen that the LWP distribution is similar for the different seasons with most of the values lower than 25g m^{-2} . The differences observed for autumn can be explained at least in part by the fact that autumn includes only October in this study. The variations of the LWP span a wider range of values when the cloud fraction is higher than 0.5 (Figure 4.11 shows the LWP versus cloud fraction in March and June, the evolution during these two months is well representative of the year). These high variations might be caused by the simultaneous occurrence of multiple cloud layers. Furthermore, the LWP increases with the cloud fraction.

Improvement of the estimation of COD from LWP Because no estimation of COD and cloud droplet radii was available in 2014, the COD is calculated from the LWP data obtained from microwave radiometric measurements. To determine the relation between COD and LWP at SIRTA, satellite data from 2005 to 2010 are used. These data include values of COD and of LWP (which is derived from COD and from an estimation of the effective radius r_e following [Roebeling et al., 2006]). A first approach consisted in computing an averaged value of the effective radius over the whole period 2005-2010 ($12 \mu\text{m}$), and then to derive the COD for

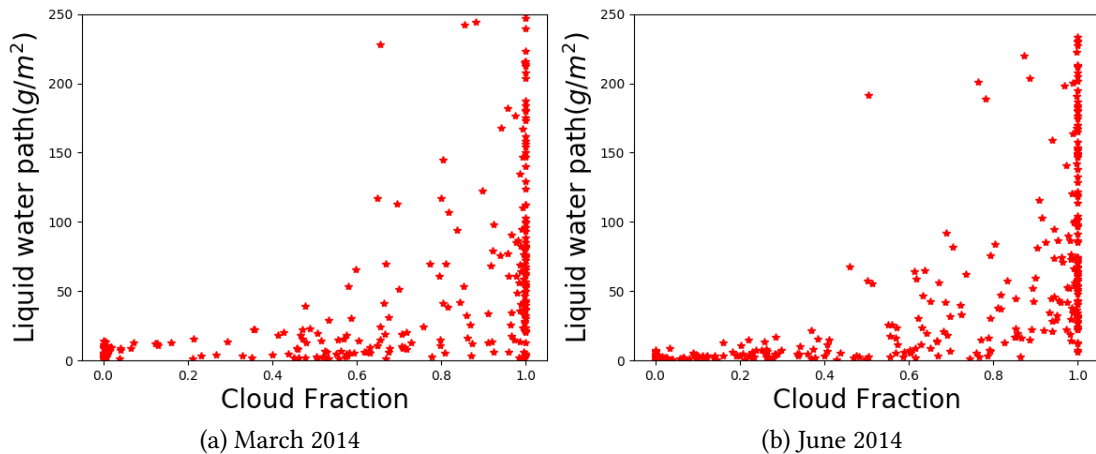


Figure 4.11: Distribution of LWP versus cloud fraction from PYR

2014 from the LWP measurements with equation 4.1 using this mean effective radius. As the effective radius varies in time, a second approach is to determine a statistical relation between COD and LWP using the satellite data from the period 2005-2010.

The relation between COD and LWP is fitted using two different equations, depending on the value of LWP:

1. A linear fit for values of the LWP lower than 14 g m^{-2} : $\tau_c = 0.181LWP - 0.001$ when $LWP \leq 14 \text{ g m}^{-2}$
2. A logarithmic fit for values of LWP higher than 14 g m^{-2} : $\log_{10}(\tau_c) = 1.7095 \ln(\log_{10}(LWP)) + 0.2633$. This equation was inspired from the fitted equation of [Stephens, 1978b] for conservative scattering because purely scattering is a good approximation for clouds for solar irradiance.

The scattering plot of COD versus LWP and the fitted models are represented in Figure 4.12a. The RMSE between the estimated COD and the measured one is calculated to compare the different models over the period 2005-2010. A RMSE of 8.18 is obtained with equation 4.1 and 7.6 with the relation established in this paper, which is the best approximation of COD for our specific case. The distribution of LWP for the period 2005-2010 shows that the majority of points are in a range of LWP going from 5 to 100 g m^{-2} (Figure 4.12b). The fitted model is then pushed by those values of LWP, it coincides well for our case: in 2014, the majority of LWP falls into the same range (Figure 4.10a).

4.3.3.9 Separation between clear-sky and cloudy-sky days

Due to the difficulties linked to the modelling of clouds, the model is evaluated separately for clear-sky days and cloudy-sky days. At the SIRTA, the separation between clear-sky days and cloudy-sky days is done using the measured cloud fraction from a radiometric station (for

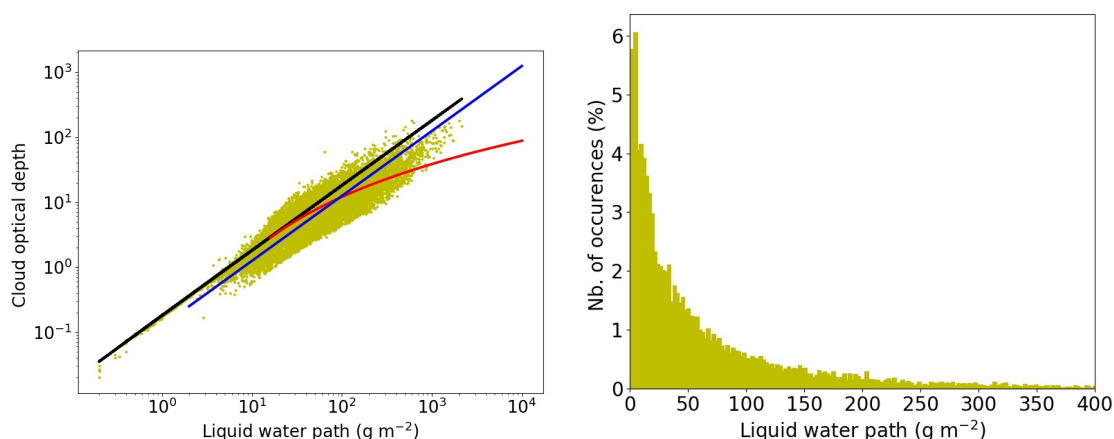


Figure 4.12: COD versus LWP from 2005 to 2010 at SIRTA (*), the approximation of COD using the fitted model (linear model — + logarithmic model — and equation 4.1 with $r_e=12\mu\text{m}$ —).

August 2009) or PYR (for year 2014). A day is classified as clear sky, when the average of the hourly cloud fraction short wave is lower than 5% between 9 UTC and 15 UTC [Sartelet et al., 2018a]. The other days are considered as cloudy-sky days, and they include overcast skies (cloud fraction higher than 0.95). For every day, only the hours for which all measurements are available are considered. For the case of August 2009, 5 clear-sky days are identified: 6, 12, 15, 16, 23 of August, it is the equivalent of 60 hours, and 20 cloudy-sky days (195 hours). Table 4.3 shows the number of hours of clear-skies and cloudy-skies for each month of the year 2014. Because only 6 days (75 hours) can be classified as clear sky, the statistical scores are less significant than for cloudy-sky days.

Month of year 2014	Nb. of clear-sky hours	Nb. of cloudy-sky hours
January	0	147
February	0	204
March	23	284
April	14	287
May	15	229
June	16	332
July	16	307
August	0	398
September	0	316
October	0	275

Table 4.3: Number of clear-sky and cloudy-sky hours for each month of 2014 following the availability of cloud fraction from PYR and LWP from radiometric measurements.

Period	Case	Fc	COD
August 2009	Sim09.0	WRF	WRF
	Sim09.1	WRF	Satellite
	Sim09.2	1	Satellite
	Sim09.3	PYR	Satellite
	Sim09.4	Sky imager	Satellite
	Sim09.5	LIDAR	Satellite
	Sim09.6	Satellite	Satellite
	Sim09.7	PYR	WRF
Year 2014	Sim14.0	WRF	WRF
	Sim14.1	WRF	Fitted model
	Sim14.2	1	Fitted model
	Sim14.3	PYR	Fitted model
	Sim14.4	Sky imager	Fitted model
	Sim14.5	PYR	Equation 4.1
	Sim14.6	PYR	WRF

Table 4.4: Cloud parameters defining the different cases studied. F_C : cloud fraction; COD: cloud optical depth.

4.3.4 Model evaluation

For model evaluation, the computed global and direct irradiances are compared to those measured at the SIRTA site using PYR (see section 4.3.3.5). The definition of the different statistical indicators used to evaluate our model can be found in appendix C. The different simulations discussed in this paper are reported in Table 4.4. In the reference simulations used in this section and noted sim09.0 for August 2009 and sim14.0 for the year 2014, the WRF meteorological simulations are used to estimate the COD and the cloud fraction.

4.3.4.1 Irradiance on clear-sky days

The model is first evaluated for clear-sky days, which are less numerous than cloudy-sky days, but also easier to model. For August 2009, the daily global and direct solar irradiances on clear-sky days at SIRTA in August 2009 (Sim09.0) are shown respectively in Figures 4.13a and 4.13b. The daily cycle and amplitude are well modelled for both global and direct irradiances. Statistics show a RMSE around 22 W m^{-2} for global irradiance with a MBE of 5 W m^{-2} and a RMSE around 19 W m^{-2} for direct irradiance with a MBE of 5 W m^{-2} .

For the year 2014, the model performs well for global fluxes, although it slightly underestimates the measurements. The RMSE ranges between 12 and 29 W m^{-2} depending on the month, with an average of 19 W m^{-2} and a MBE of 5 W m^{-2} on average. For direct fluxes, the model underestimates the measurements with an averaged MBE of -7 W m^{-2} and the RMSE ranges between 15 and 28 W m^{-2} depending on the month, with an average of 21 W m^{-2} . The estimation of the direct component is less good in 2014 than in August 2009, because

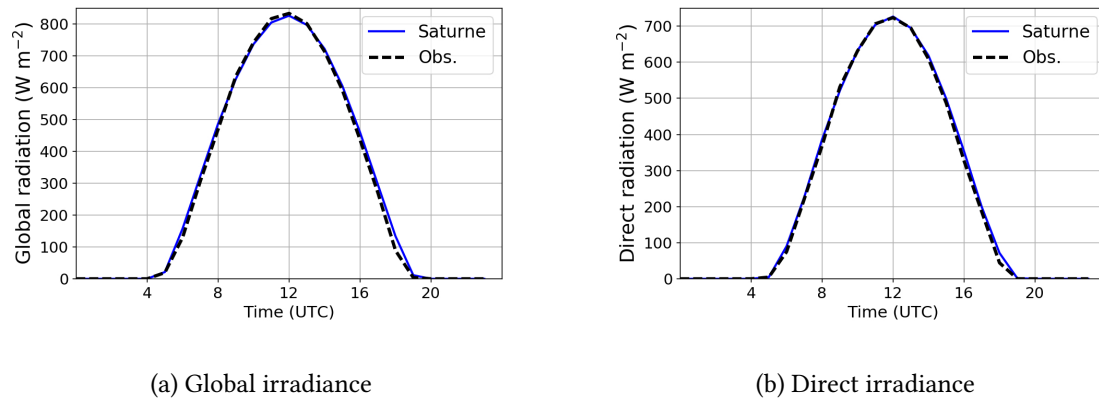


Figure 4.13: Diurnal cycle of solar irradiances at [SIRTA](#) on clear-sky days in August 2009 (in W m^{-2})

aerosol optical depths were estimated from the measurements for August 2009 and from the modelling for the year 2014.

These scores can be compared to the [RMSE](#) scores obtained at the BSRN station of Palaiseau using the McClear model, an irradiance model developed for clear-sky conditions [[Lefèvre et al., 2013](#)] or to the HelioClim-3v3 database [[Blanc et al., 2011](#), [Espinar et al., 2012](#)], which is derived from images of the Meteosat series of satellites. For the period 2005-2007, the McClear model leads to a [RMSE](#) of 25 W m^{-2} for global irradiance and of 37 W m^{-2} for direct normal irradiance [[Lefèvre et al., 2013](#)]; for the HelioClim-3v3 database, the [RMSE](#) is equal to 62 W m^{-2} for global irradiance and to 79 W m^{-2} for direct normal irradiance [[Espinar et al., 2012](#)].

Although the number of cases, the period and the time averaging period of our simulation and measurement are not the same as those of Mc Clear/Helioclim-3v3, the scores obtained with code_saturne demonstrate the quality of the model.

4.3.4.2 Irradiance on cloudy-sky days

The comparison between observations and simulations during cloudy-sky days in August 2009 is provided in [Table 4.5](#). As in [KS18](#), Sim09.0 strongly overestimate observations with a [RMSE](#) of 149 W m^{-2} and 220 W m^{-2} for global and direct irradiance respectively. The overestimation is larger for the direct than for the global irradiances ([MBE](#)= $+108 \text{ W m}^{-2}$ and [NMB](#) of $+99\%$ versus $+65 \text{ W m}^{-2}$ and $+31\%$).

As for August 2009, the modelled global and direct irradiances are strongly overestimated during the year 2014 ([Table 4.5](#); Sim14.0). For global irradiance, the [RMSE](#) averaged over the whole year 2014 is 146 W m^{-2} with an averaged [MBE](#) of 26 W m^{-2} and a [NMB](#) that reaches its maximum of $+49\%$ in January and its minimum of -7% in June. For direct irradiance, the averaged [RMSE](#) is equal to 157 W m^{-2} with a [MBE](#) of 23 W m^{-2} and a [NMB](#) ranging from $+134\%$ (in January) to $+11\%$ (in July). For both periods, these large errors may come from a bad estimation of cloud fraction and [COD](#). However, statistical scores are slightly better for

2014 than for August 2009, probably because of the lower resolution of WRF simulations in 2009.

4.3.5 Improvement of irradiance modelling on cloudy-sky days

In the aim of improving irradiance modelling on cloudy-sky days, different simulations are conducted using observed data for the cloud optical depth and/or the cloud fraction. The simulations are summarized in Table 4.4.

4.3.5.1 Cloud Fraction

The different measurements of cloud fraction (section 4.3.3.5) and the simple value of 1, sometimes used in modelling [Nielsen et al., 2014], are used as input to the code. They are compared to the cloud fraction extracted from the WRF simulations. In the cases presented here, the COD is taken from satellite measurements for August 2009 and from the fitted model for the year 2014 using radiometric measurements of LWP.

4.3.5.2 Cloud fraction equals to 1

The modification of cloud fraction (Sim09.2) has an important impact on the estimation of irradiance for August 2009 and especially for the direct irradiance. Taking the cloud fraction equal to 1 leads to an under-estimation of the measurements: the RMSE is equal to 204 W m^{-2} , the MBE to -101 W m^{-2} and the NMB to -67% (against 203 W m^{-2} , $+94 \text{ W m}^{-2}$ and $+78\%$ respectively for direct irradiance using WRF for the cloud fraction - Sim 09.1- Table 4.5). A similar behaviour is seen for the year 2014 (Sim14.2). The RMSEs, MBEs and NMBes are reported for every month in Figures 4.14, 4.15 and 4.16 and the averages over the year for RMSEs and MBEs are in Table 4.5. Direct fluxes are highly under-estimated for every month (the NMB varies from -99% (January) to -60% (May), with an averaged MBE of -63 W m^{-2}) and values of RMSE range from 33 to 184 W m^{-2} with an average of 131 W m^{-2} .

For the two simulated periods, the MBEs are high and negative. Due to a significant number of partially cloudy days at SIRTa, taking a cloud fraction of 1 for the whole period leads to a large under-prediction of the direct irradiance. However, it leads to satisfactory results for global irradiance (RMSE= 65 W m^{-2} , MBE= $+12 \text{ W m}^{-2}$, NMB of $+45 \%$ in January and $+8 \%$ in May and August), partially justifying its utility in NWP models.

4.3.5.3 Cloud Fraction extracted from measurements

The computation of irradiances, using measurements for the cloud fraction, improved especially for the direct irradiance. Clouds mainly transform direct irradiance in diffuse irradiance, and consequently their impact is lower for global irradiance than for direct irradiance. Statistical scores for August 2009 are reported in Table 4.5. For the direct irradiance, the best RMSE is obtained using the cloud fraction from PYR (Sim09.3: RMSE of 87 W m^{-2} and NMB of -17% against 203 W m^{-2} and $+79\%$ when the cloud fraction is from WRF simulation - Sim09.1). The estimation of direct irradiance using the cloud fraction from sky imager also leads to similar results, with a RMSE of 99 W m^{-2} and a NMB of -27% . However, the direct irradiance is highly

under-estimated when the cloud fraction is extracted from the LIDAR (Sim09.5) and satellite images (Sim09.6), with a MBE score equals, respectively, to -53 W m^{-2} and -40 W m^{-2} , NMB equals, respectively to -50% and -33% and RMSE equals, respectively, to 135 W m^{-2} and 112 W m^{-2} .

For the year 2014, the statistical scores using the cloud fraction from PYR and sky imager are represented in Figures 4.14, 4.15 and 4.16. With a cloud fraction from PYR (Sim14.3), the RMSEs for global irradiance range between 37 and 69 W m^{-2} , depending on the month, with an average of 59 W m^{-2} and an average MBE of $+17 \text{ W m}^{-2}$. The NMB scores range between $+4\%$ and $+47\%$. Global fluxes are always over-estimated. For direct irradiance, the model underestimates the measurements with an averaged MBE of -18 W m^{-2} , a NMB between -22% and -45% and the RMSE ranges between 16 and 88 W m^{-2} depending on the month, with an average of 50 W m^{-2} . Simulations with the cloud fraction extracted from the sky imager (Sim14.4) lead to similar statistics for global radiation and slightly poorer for direct irradiance: the RMSEs range from 17 to 81 W m^{-2} with an average of 60 W m^{-2} , an averaged MBE of -18 W m^{-2} and a NMB between -1.5% and -39% . These statistics are much better than those obtained in the simulations with a cloud fraction from WRF (Sim14.1), which lead to an averaged RMSE for global irradiance of 93 W m^{-2} and of 130 W m^{-2} for direct irradiance. For all conducted tests, acceptable results are obtained for global fluxes, but the change of cloud fraction values highly impacts the direct irradiance. However, the direct component is important for different application of solar energy systems, such as concentrating and flat-plate solar systems [Padovan et al., 2014]. Hence, a good representation of cloud fraction is crucial. In our case, the best results are obtained with a cloud fraction extracted from PYR or a sky imager.

	Direct		Global	
Case	RMSE (W m^{-2})	MBE (W m^{-2})	RMSE (W m^{-2})	MBE (W m^{-2})
Sim09.0	220	+108	149	+65
Sim09.1	203	+94	131	+48
Sim09.2	204	-101	103	-32
Sim09.3	87	-22	87	-13
Sim09.4	99	-33	87	-14
Sim09.5	135	-53	94	-23
Sim09.6	112	-40	88	-18
Sim09.7	198	+82	156	+82
Sim14.0	157	+23	146	+26
Sim14.1	130	-6	93	+33
Sim14.2	131	-63	65	+12
Sim14.3	50	-18	59	+17
Sim14.4	60	-18	60	+19
Sim14.5	49	-16	66	+17
Sim14.6	125	+22	131	+25

Table 4.5: Comparison of simulated and measured direct and global solar irradiances at [SIRTA](#) during cloudy days for the different cases studied. The RMSEs and MBEs are expressed in W m^{-2} .

4.3.5.4 Cloud optical depth

In this section, different estimations of the [COD](#) are used for August 2009 and year 2014 and are compared to the [COD](#) calculated by [WRF](#). The cloud fraction is extracted from [PYR](#).

4.3.5.5 Satellite measurements

For August 2009, simulations using the [COD](#) measured by satellite (Sim09.3) lead to satisfactory results for both global and direct irradiances. Statistics are reported in Table 4.5. The [RMSE](#) is around 87 W m^{-2} for both global and direct irradiance and the [MBE](#) scores are respectively equal to -13 W m^{-2} and -22 W m^{-2} . It shows that simulated fluxes under-estimate measurements. Compared to a [COD](#) taken from [WRF](#) (Sim09.7), it represents a huge improvement.

4.3.5.6 Estimation from LWP

For the year 2014, the [COD](#) can be computed from microwave radiometric measurements of [LWP](#) using 2 models (fitted model (Sim14.3) or equation 4.1 (Sim14.5)), as described in section 4.3.3.8. RMSEs, MBEs and NMBes are respectively reported in Figures 4.14, 4.15 and 4.16. The RMSEs are higher in summer than in winter, because irradiance fluxes are higher. In fact, as it can be seen in Figure 4.16, relative errors are more important in the winter than in summer

(for Sim 14.3: for global irradiance, $NMB = +47\%$ in January and $NMB = +4\%$ in June and for direct irradiance, $NMB = -45\%$ in January and $NMB = -22\%$ in June).

The direct irradiance estimated using the COD of the fitted model is mainly described by the linear equation (defined for values of LWP lower than 14 g m^{-2}). This is due to the fact that values of LWP greater than 14 g m^{-2} lead to COD greater than 2.5, and clouds with COD greater than 2.5 are thick enough to lead to very small direct irradiance. The scores are very similar, but slightly better when the COD is estimated using equation 4.1 with a fixed effective radius than using the fitted model.

In opposite to the direct irradiance, which becomes almost zero if clouds have a LWP higher than 14 g m^{-2} , the global irradiance decreases as the COD increases, but it does not cancel out because of diffuse irradiance. Therefore, the global irradiance is impacted by the whole range of values of COD . Similar statistical scores are obtained with the fitted model and using Equation 1 but slightly better scores are obtained with the fitted model (Sim 14.3). For Sim 14.3, the lowest $RMSE$ scores, for global irradiance, is equal to 37 W m^{-2} and is obtained in January, and the highest is around 69 W m^{-2} , it is obtained in May. The averaged $RMSE$ is 59 W m^{-2} . For direct irradiance, $RMSEs$ are in the range $[16, 88] \text{ W m}^{-2}$, with an average of 50 W m^{-2} . Therefore, for this case, code_saturne overestimates global irradiance and underestimates direct irradiance for every month of the year 2014.

The results are satisfactory and a big improvement compared to the case when COD is taken from WRF measurements (Sim 14.6: the averaged $RMSE$ for global irradiance is about 131 W m^{-2} and for direct irradiance, the $RMSE$ is about 125 W m^{-2}).

This study shows the importance of COD in the estimation of irradiance fluxes during cloudy sky days. It can be well estimated from LWP data (in this case extracted from radiometric measurements) or empirical relations to improve the estimation of irradiance during cloudy-sky days. It also shows the stronger importance of COD compared to the cloud fraction for the estimation of global irradiance.

4.3.6 Discussion

The calculation of irradiance fluxes by code_saturne is done hourly. For the majority of simulated hours, code_saturne approximates well the observations. However, it is not always the case. Thus, an analysis of the results is conducted in order to understand why the quality of the estimation of the irradiance varies. The analysis is done for August 2009 (Sim 09.3) and for the year 2014 (Sim 14.3). One first explanation of the gap between observation and simulation is that code_saturne calculates the irradiance fluxes at each hour while the observational data are averaged. In fact, for each variable taken from the $SIRTA$ ReObs file, the hourly mean values are calculated from the native resolution data (5 s to 1 min) by averaging all the data available within ± 30 min around the full hour [Chiriaco et al., 2018].

For August 2009, the cases when the absolute difference on global or direct irradiance is higher than 200 W m^{-2} are analysed: 20 hours in 2009 were detected. Among these cases of large differences between simulated and observed direct irradiance, 63% correspond to partially cloudy days and 32% to fully cloudy days. There was no precipitation for any case. In most of the cases, 58%, were obtained when a low cloud was present. 32% of cases were ob-

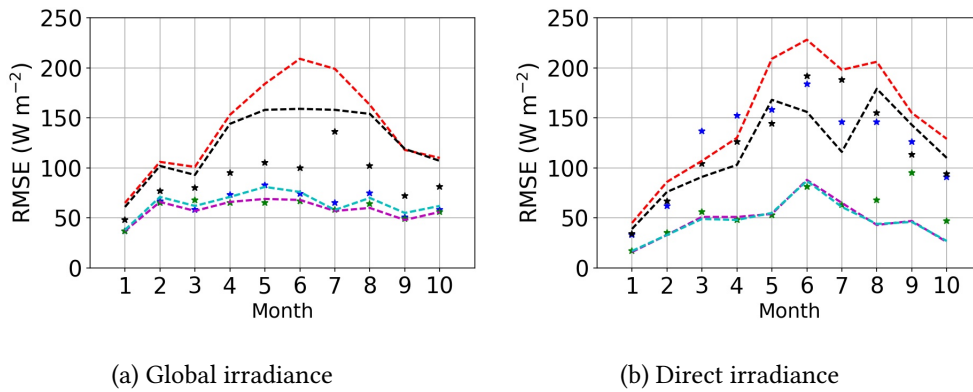


Figure 4.14: RMSEs (in W m^{-2}) between simulated and measured global (a) and direct (b) solar irradiances at [SIRTA](#) during cloudy-sky days in 2014. WRF evaluation: --- Sim14.0. Sensitivity to cloud fraction/COD: * Sim14.1; * Sim14.2; * Sim14.4; - - - Sim14.3; - - - Sim14.5; - - - Sim14.6.

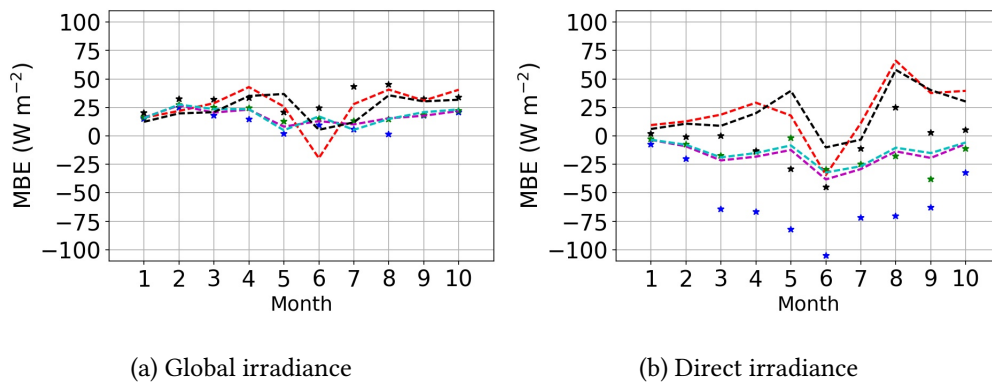


Figure 4.15: MBEs (in W m^{-2}) between simulated and measured global (a) and direct (b) solar irradiances at [SIRTA](#) during cloudy-sky days in 2014. WRF evaluation: --- Sim14.0. Sensitivity to cloud fraction/COD: * Sim14.1; * Sim14.2; * Sim14.4; - - - Sim14.3; - - - Sim14.5; - - - Sim14.6.

tained during a transition period of COD: the hour after a minima or maxima of COD.

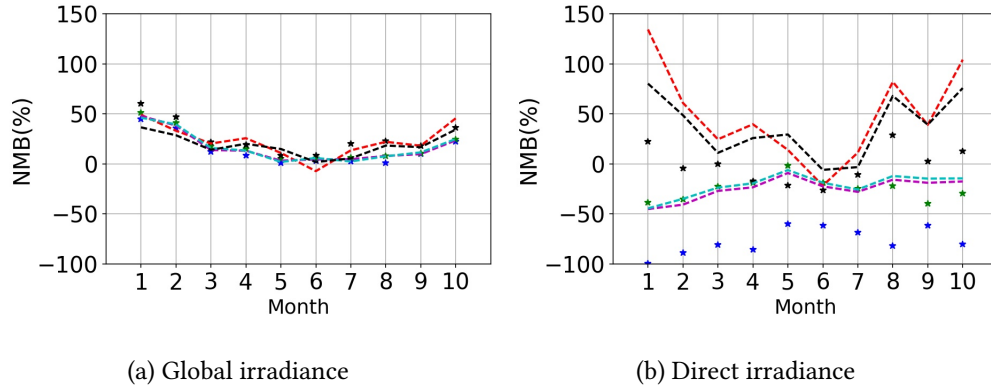


Figure 4.16: NMB scores (in %) between simulated and measured global (a) and direct (b) solar irradiances at SIRTA during cloudy-sky days in 2014. WRF evaluation: --- Sim14.0. Sensitivity to cloud fraction/COD: * Sim14.1; * Sim14.2; * Sim14.4; - - - Sim14.3; - - - Sim14.5; - - - Sim14.6.

	MBE(G)	MBE(D)
$\sigma(G_{obs}) > 100$	68	73
$\sigma(G_{obs}) < 100$	25	13
$\sigma(LWP) > 30$	39	16
$\sigma(LWP) < 30$	29	24
$\sigma(F_C) > 0.2$	62	64
$\sigma(F_C) < 0.2$	30	19

Table 4.6: MBE of global (G) /direct (D) irradiance fluxes (in $W m^{-2}$) for different ranges of standard variation of measured global irradiance G_{obs} (in $W m^{-2}$)/liquid water path LWP in ($g m^{-2}$) / cloud fraction F_C in 2014.

	$G_{CS} - G_{obs} < 0$	$G_{CS} - G_{obs} > 0$
$\bar{\sigma}(G_{obs})$	88	32
$\bar{\sigma}(LWP)$	78	41
$\bar{\sigma}(F_C)$	0.086	0.06

Table 4.7: Averaged standard variation of measured global irradiance G_{obs} (in $W m^{-2}$)/liquid water path LWP (in $g m^{-2}$) / cloud fraction F_C when measured global irradiance is underestimated or overestimated by code_saturne in 2014.

Condition	$F_c > 0.95$	$0.50 < F_c < 0.75$	$0.25 < F_c < 0.50$
MBE (G)	83	62	43
\bar{G}_{obs}	178	452	458
MBE(G)/ \bar{G}_{obs}	0.46	0.14	0.09
MBE (D)	12	81	75
\bar{D}_{obs}	13	239	305
MBE(D)/ \bar{D}_{obs}	0.92	0.34	0.25

Table 4.8: Mean absolute error (MBE) of global (G) and direct (D) irradiances and the ratio MBE over the averaged measured fluxes for different conditions on the cloud fraction (F_c) in 2014 (in $W m^{-2}$).

The analysis is now conducted for the entire simulation of year 2014. The standard deviation of the measured global irradiance, LWP and cloud fraction are extracted from the SIRTa ReObs file. Table 4.6 shows the MBE of global and direct irradiances for different conditions on the measured global irradiance, LWP and cloud fraction. A better estimation of global irradiance is obtained for lower fluctuations of measured global irradiance, LWP and cloud fraction. A similar tendency is obtained for direct irradiance except when the standard deviation of LWP is higher than $30 g m^{-2}$. It is normal considering that direct irradiance is attenuated for values of LWP higher than $14 g m^{-2}$. Therefore, the quality of the estimation is linked to the quick changes within an hour in the measurements.

Table 4.7 shows the standard variation of measured global irradiance fluxes/ LWP and cloud fraction when measured global irradiance is over-estimated and under-estimated. When code_saturne under-estimates observations, the averaged standard deviation of observed global irradiance, LWP and cloud fraction are higher than when code_saturne overestimates observations. It can be related to the fact that averaging of measurements pushes them towards higher values.

The mean absolute error (MBE) is calculated for the global and direct irradiances for different ranges of cloud fraction in 2014 (table 4.8). The MBE increases with the cloud fraction. The ratio MBE-mean measured irradiance is higher for the direct irradiance. For overcast situations, diffuse irradiance is dominant. The few high values of simulated direct irradiance during overcast sky are obtained when the COD is low, they might be due to a poorly coordination between measured LWP and cloud fraction or to a low density cloud blocking the sun.

The type of clouds does not contribute significantly to the difference. Cirrus clouds optical depth is usually described by another formula than used here (for ice clouds, the definition of cloud optical properties can be found in [Qiang, 1996, Baum et al., 2014]). A study was done on hours during which cirrus clouds were the only type of cloud present. It was shown that they are well represented in code_saturne and hourly differences of irradiance fluxes are not linked to their presence.

4.3.7 Conclusion

The 1D irradiance model of the atmospheric module of code_saturne aimed at improving irradiance fluxes at SIRTAs in Palaiseau, Île-de-France. This study aimed to improve the estimation of irradiance during cloudy-sky days. Therefore, the model was evaluated hourly and with the presence of clouds during two periods: August 2009 and year 2014. Cloud properties, such as the cloud fraction and COD, are used as input. Because the mesoscale meteorological model has difficulties to estimate them, measurements done at the SIRTAs site were used. The cloud fraction was extracted from satellite images, LIDAR, short wave measurements (PYR) and sky imager. The liquid water path (LWP)/COD were extracted from radiometric and satellite measurements. The main conclusions are:

- A good representation of the COD is crucial for modelling solar irradiance during cloudy-sky days. The cloud fraction may improve solar irradiance modelling if the estimation of COD is correct, especially for direct irradiance.
- Assuming the sky completely cloudy but with an accurate representation of COD leads to simulated global irradiance that may be more accurate than using an estimation of cloud fraction from numerical models. However, it is not the case for the direct irradiance.
- The simulated irradiance obtained using a cloud fraction extracted from PYR or from sky imager is more accurate than those obtained using LIDAR or satellite measurements.
- A fitted model was developed to estimate COD from LWP measurements. Satellite and radiometric measurements of LWP lead to satisfactory simulations of irradiances, although satellite data are not always available. This shows that the link that exists between COD and LWP is well established, and that LWP may be used as a proxy of COD in irradiance modelling.

Moreover, hourly values of solar fluxes were examined to determine the reasons for the few discrepancies between measurements and simulated irradiances. The main source of errors that were detected are:

- code_saturne calculates fluxes every hour, while observational data are averaged within 30 mins around the full hour.
- The hourly bias is higher when the fluctuations within the hour of global irradiance/LWP/cloud fraction measurements are high.
- There was no particular type of clouds that impacted the results. However, in August 2009, during more than 50% of the cases leading to a large discrepancy between measurements and observations, a low cloud was present.
- The MBE on irradiance fluxes increases with the cloud fraction and its impact is more important for the direct component.

Overall, we showed that code_saturne performs well at SIRTAs during clear-sky and cloudy-sky days, when measurements of cloud fraction and LWP are used. All components of irradiance are well modeled and especially the direct fluxes (with RMSEs around 21 W m^{-2} during clear-sky days and 50 W m^{-2} during cloudy sky-days) which is mandatory for some applications such as concentrating and flat-plate solar systems.

Acknowledgment: The authors would like to acknowledge SIRTAs for providing the data used in this study. The work of L. Al Asmar was supported by CEREA, a member of the Pierre-Simon Laplace Institute (IPSL) and by ANRT through an EDF-CIFRE contract (Grant number: 2018/1415).

4.3.8 Appendix

4.3.8.1 Calculation of cloud optical properties

The cloud fraction, COD and LWP were extracted from SIRTAs Re-Obs data file or WRF simulation. The cloud droplet radii, single scattering albedo (SSA) and asymmetry factor had to be calculated in the code.

Cloud droplet radii It is calculated following equation 4.1.

Cloud single scattering albedo (SSA) and the cloud asymmetry factor The calculations are made separately in the UV-vis band and in the SIR band.

They are approximated following the formulations of [Nielsen et al., 2014]. They depend only on the equivalent cloud droplets radius r_e , and are defined for different spectral bands: 250-440; 440-690 nm in the UV-visible domain and 690-1190; 1190-2380 nm in near IR domain. The integration over the wavelength is made by weighting each formulation with the irradiance energy contained in each band. The single scattering albedo (SSA) in the UV-visible and SIR bands (ω_0^{UV-Vis} and ω_0^{SIR}) are calculated with the following formulas:

$$\omega_0^{UV-Vis} = \omega_{0-1} \times 0.24 + \omega_{0-2} \times 0.76 \quad (4.2)$$

$$\omega_{0-1} = 1 - 3.3 \times 10^{-8} r_e \quad (4.3)$$

$$\omega_{0-2} = 1 - 10^{-7} r_e \quad (4.4)$$

In the SIR band,

$$\omega_0^{SIR} = \omega_{0-3} \times 0.60 + \omega_{0-4} \times 0.40 \quad (4.5)$$

$$\omega_{0-3} = 0.99 - 1.49 \times 10^{-5} r_e \quad (4.6)$$

$$\omega_{0-4} = 0.9985 - 9.210^{-4} r_e \quad (4.7)$$

In the UV-Vis band, the cloud asymmetry, g_0^{UV-Vis} , is calculated with the following formula:

$$g_0^{UV-Vis} = \omega_{0-1} \times 0.24 \times g_1 + \omega_{0-2} \times 0.76 \times g_2 \quad (4.8)$$

$$g_{0-1} = 0.868 + 1.4 \times 10^{-4}re - 6.1 \times 10^{-3}e^{-0.25re} \quad (4.9)$$

$$g_{0-2} = 0.868 + 2.5 \times 10^{-4}re - 6.3 \times 10^{-3}e^{-0.25re} \quad (4.10)$$

In the SIR band, the cloud asymmetry, g_0^{SIR} , is calculated with the following formula:

$$g_0^{SIR} = \omega_{0-3} \times 0.60 \times g_3 + \omega_{0-4} \times 0.40 \times g_4 \quad (4.11)$$

$$g_{0-3} = 0.867 + 3.1 \times 10^{-4}re - 7.8 \times 10^{-3}e^{-0.195re} \quad (4.12)$$

$$g_{0-4} = 0.864 + 5.4 \times 10^{-4}re - 0.133e^{-0.194re} \quad (4.13)$$

4.3.8.2 The irradiance model - integral method

Global Irradiance

UV-Vis band The most significant source of heating in the stratosphere comes from the absorption of solar irradiance by ozone. Rayleigh diffusion through multiple-scattering is taken into account with a simple albedo and the global irradiance G_{UV-VIS} , is expressed as follows:

$$G_{UV-VIS} = F_C G_{1,UV-VIS} + (1 - F_C) G_{2,UV-VIS} \quad (4.14)$$

where F_C is the cloud fraction, $G_{1,UV-VIS}$ and $G_{2,UV-VIS}$ the global irradiance for cloudy-sky and clear-sky with aerosols respectively. They are expressed as:

$$G_{1,UV-VIS} = \mu_0 F_0 (0.647 - \bar{R}_r(\mu_0) - A_{UV-VIS}^G) \frac{T_{c,UV-VIS}^G}{1 - R_{c,UV-VIS}^G R_g} T_{mg} \quad (4.15)$$

$$G_{2,UV-VIS} = \mu_0 F_0 (0.647 - \bar{R}_r(\mu_0) - A_{UV-VIS}^G) \frac{T_{a,UV-VIS}^G}{1 - R_{a,UV-VIS}^G R_g} T_{mg} \quad (4.16)$$

- μ_0 the cosine of the zenith angle
- F_0 the irradiance flux incident at the top of the Earth atmosphere. It is calculated using the formula of [Paltridge and Platt, 1976] : $F_0 = 1365 \text{ W m}^{-2}$
- \bar{R}_r the albedo due to Rayleigh scattering (as in LH74)
- R_g the ground albedo (calculated by WRF)
- A_{UV-VIS}^G is the irradiance absorption function in the UV-VIS band by O_3 (as in LH74)

- $T_{c,UV-VIS}^G$ and $R_{c,UV-VIS}^G$ the transmission and reflective functions for clouds
- $T_{a,UV-VIS}^G$ and $R_{a,UV-VIS}^G$ the transmission and reflective functions for clear-sky for aerosols
- T_{mg} is the general transmittance function for seven main atmospheric gases (H_2O , O_3 , CO_2 , CO , N_2O , CH_4 and O_2). It is expressed following [Psiloglou et al., 1997], it depends on 'm', the air mass, given by [Kasten and Young, 1989].

SIR band The most important source of heating in the low atmosphere is due to water vapour absorption. As reported by LH74, parametrizing water vapour absorption is more complicated than for ozone absorption. In the SIR band spectrum, G_{SIR} , is expressed as follows:

$$G_{SIR} = F_C G_{1,SIR} + (1 - F_C) G_{2,SIR} \quad (4.17)$$

where F_C is the cloud fraction; the global irradiance for cloudy-sky $G_{1,SIR}$ and clear-sky with aerosols $G_{2,SIR}$ are expressed as:

$$G_{1,SIR} = \mu_0 F_0 (0.353 - A_{SIR}^G) \frac{T_{c,SIR}^G}{1 - R_{c,SIR}^G R_g} T_{mg} \quad (4.18)$$

$$G_{2,SIR} = \mu_0 F_0 (0.353 - A_{SIR}^G) \frac{T_{a,SIR}^G}{1 - R_{a,SIR}^G R_g} T_{mg} \quad (4.19)$$

- A_{SIR}^G represents the absorption by water vapour (as in LH74)
- $T_{c,SIR}^G$ and $R_{c,SIR}^G$ the transmission and reflective functions for clouds
- $T_{a,SIR}^G$ and $R_{a,SIR}^G$ the transmission and reflective functions for clear-sky for aerosols

The transmission and reflective functions The transmission and reflective functions for cloudy-sky, T_c^G and R_c^G and for clear-sky T_a^G and R_a^G are described by the following formulas of [Meador and Weaver, 1980]:

$$T^G = \frac{2k}{(k + \gamma_1)e^{k\tau'} + (k - \gamma_1)e^{-k\tau'}} \quad (4.20)$$

$$R^G = \frac{\gamma_2[e^{k\tau'} - e^{-k\tau'}]}{(k + \gamma_1)e^{k\tau'} + (k - \gamma_1)e^{-k\tau'}} \quad (4.21)$$

where

$$k = (\gamma_1^2 - \gamma_2^2)^{1/2} \quad (4.22)$$

$$\gamma_1 = \frac{\sqrt{3}}{2} [2 - \omega'_0(1 + g')] \quad (4.23)$$

$$\gamma_2 = \frac{\sqrt{3}\omega'_0}{2}(1 - g') \quad (4.24)$$

where τ' , g' and ω'_0 are the scaled optical depths, single scattering albedo and asymmetry factor. They are introduced by [Joseph and Wiscombe, 1976] in order to take into account the highly forward scattering for water clouds and aerosols [Stephens, 1984]. This correction is often called δ two-stream [Liou, 2002]:

$$\tau' = \tau(1 - \omega_0 * g^2) \quad (4.25)$$

$$\omega'_0 = \frac{\omega_0(1 - g^2)}{1 - g^2\omega_0} \quad (4.26)$$

$$g' = \frac{(g - g^2)}{(1 - g^2)} \quad (4.27)$$

The coefficients τ , g and ω_0 change depending if we are on clear-sky or on cloudy-sky conditions:

For clear-sky:

- $\tau = \tau_a$
- $\omega_0 = \omega_a$
- $g = g_a$

For cloudy-sky:

- $\tau = \tau_a + \tau_C$
- $\omega_0 = (\omega_a\tau_a + \omega_C\tau_C)/\tau$
- $g = (g_a\omega_a\tau_a + g_C\omega_C\tau_C)/\tau\omega_0$

Direct Irradiance In order to calculate the direct irradiance, a model inspired by LH74 was developed. It is similar to the one developed for global irradiance, and it is based on the same principles.

UV-vis band

$$I_{1,UV-VIS} = \mu_0 F_0 (0.647 - \bar{R}_r - A_{UV-VIS}^G) T_{mg} T_C^D \quad (4.28)$$

$$I_{2,UV-VIS} = \mu_0 F_0 (0.647 - \bar{R}_r - A_{UV-VIS}^G) T_{mg} T_{a,UV-VIS}^D \quad (4.29)$$

SIR band

$$I_{1,SIR} = \mu_0 F_0 (0.353 - A_{SIR}^G) T_{mg} T_C^D \quad (4.30)$$

$$I_{2,SIR} = \mu_0 F_0 (0.353 - A_{SIR}^G) T_{mg} T_{a,SIR}^D \quad (4.31)$$

where $\mu_0, F_0, \bar{R}_r, A^G$ have been defined in the previous paragraphs. T^D is given by:

$$T^D = e^{-m\tau} \quad (4.32)$$

4.3.8.3 Statistical indicators

Different statistical indicators are calculated in this study, they are defined in the following section. o_i and c_i are the observed and the simulated concentrations at time and location i , respectively. n is the number of data.

The Root Mean Square Error (RMSE)

$$RMSE = \sqrt{\frac{1}{n} \sum_{i=1}^n (c_i - o_i)^2} \quad (4.33)$$

The Mean Fractional Bias Error (MFBE)

$$MFBE = \frac{1}{n} \sum_{i=1}^n \frac{c_i - o_i}{(c_i + o_i)/2} \quad (4.34)$$

The Mean Bias Error (MBE)

$$MBE = \frac{1}{n} \sum_{i=1}^n (c_i - o_i) \quad (4.35)$$

The Mean Fractional Error (MBE)

$$MBE = \frac{1}{n} \sum_{i=1}^n \frac{|c_i - o_i|}{(c_i + o_i)/2} \quad (4.36)$$

The Mean Absolute Error (MAE)

$$MAE = \frac{1}{n} \sum_{i=1}^n |c_i - o_i| \quad (4.37)$$

The Normalized Mean Bias (NMB)

$$NMB = \frac{\sum_{i=1}^n (c_i - o_i)}{\sum_{i=1}^n o_i} \quad (4.38)$$

4.4 Complementary works

4.4.1 Comparison with HelioSat models

The HelioSat model (which provides the HelioClim database) presented in section 3.2.2 is one of the most widely validated model. The CAMS Radiation service also provides irradiance fluxes, they are estimated by the HelioSat v4 model with clear-sky model-based parameters (aerosols, water vapour and ozone) and satellite-based cloud information. In order to evaluate the code_saturne model and the usefulness of using in-situ cloud data, the global and direct irradiances are computed using code_saturne (with measurements of COPs as input - Sim 14.3). They are compared to HelioSat v3 and CAMS radiation data for the year 2014 (hourly averaged) and to HelioSat-v2 for August 2009 and to on-site radiation measurements at SIRTA. We first compare statistical scores then diurnal cycles of irradiance.

The statistical scores are calculated on hourly irradiances, as in LA21, using only the time stamps for which measurements are available. For the global component in August 2009, comparing the measured irradiance to the simulated one with HelioSat, the RMSE is equal to 68 W m^{-2} (KS18) and with code_saturne, it is equal to 87 W m^{-2} for Sim09.3. For year 2014, MBE and RMSE scores are represented in figures 4.20 and 4.21. The global flux is overestimated by the three models, as it can be seen in figure 4.20 (left panel). MBE scores obtained using the HelioSat and CAMS models shows similar statistics (ranging between $+3$ and $+14 \text{ W m}^{-2}$ with an average of 8 W m^{-2} using CAMS and 7 W m^{-2} using HelioSat), RMSE scores are also similar (averaged RMSE equal to 42 W m^{-2} with HelioSat and 45 W m^{-2} with CAMS). The estimation of the global flux using code_saturne fluctuates, it is always poorer than HelioSat and CAMS except in July when it performs slightly better than CAMS. Averaged MBE and RMSE scores are, respectively, equal to $+17$ and 59 W m^{-2} . The direct irradiance is overestimated by both HelioSat and CAMS. However, code_saturne always underestimates it (figure 4.20 (right panel)). HelioSat and CAMS have averaged RMSE scores of 51 W m^{-2} using CAMS and 58 W m^{-2} using HelioSat, but CAMS MBE scores are better (average of 12 W m^{-2} using CAMS and 21 W m^{-2} using HelioSat). The RMSE scores show that code_saturne performs better than HelioSat for every month except in June, when the best estimation was obtained using HelioSat. In comparison to CAMS, it fluctuates, for some month a better RMSE is obtained using code_saturne and other with CAMS and the averaged RMSE is similar (averaged RMSE using code_saturne of 50 W m^{-2} and MBE of -17 W m^{-2}). We may conclude that HelioSat and CAMS radiation models perform better than code_saturne (when measurements are used as input) for the estimation of the global component and for the direct component, CAMS and code_saturne performs better than HelioSat. However, CAMS overestimates irradiance and code_saturne underestimates it. It demonstrates the quality of code_saturne radiative model when it is coupled to on-site measurements, especially for the direct component.

Measurements are sometimes missing, which makes it impossible to plot diurnal cycles over a certain period. In order to overcome this problem, missing data are replaced by linear interpolation. If there are more than 5 missing data in a day, the entire day is not considered in the diurnal cycle of irradiance. Thus, diurnal cycles for cloudy days are plotted for Sim 09.03 (cloud fraction from PYR and COD from satellite) of August 2009 (figure 4.17) and Sim 14.6 of

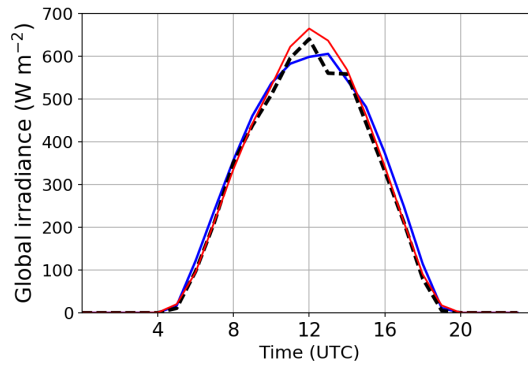


Figure 4.17: Diurnal cycle of global irradiances measured at SIRTA during cloudy-sky days in August 2009 (---) and computed with HelioSat (—), code_saturne-Sim.09.3 (—)

May and January 2014 (cloud fraction from PYR and COD from logarithmic model) (figures 4.18 and 4.19) and compared to measurements from the SIRTA and HelioSat simulations. For August 2009, the HelioSat irradiances are derived from the HelioSat-2 model and for 2014 from the HelioSat-3 model (refer to section 3.2.2 for the description of HelioSat and HelioClim).

As it can be seen in those figures, when the right parameters are used as input for the description of clouds as in Sim 09.3 or Sim 14.6, code_saturne compares well to measurements for both global and direct components with a slight under estimation of the direct irradiance. The form of the curves and the different peaks that confirm the presence of clouds are well represented as it can be observed in figure 4.18 right. For the year 2014, the diurnal cycles are presented in figures 4.18 and 4.19 for cloudy sky days of May and January 2014 respectively (those months were chosen as they represent two different seasons). These scores demonstrate the quality of code_saturne radiative model when it is coupled to on site measurements, especially for the direct component. It should be noted that we would have had a better comparison to HelioSat in 2014 if satellite measurements of COD were available for that year.

4.4.2 Discussion on the parametrization developed for the COD

As detailed in LA21, COD measurements were not available in 2014 and a model is developed to estimate the COD from microwave radiometric measurements of LWP and is referenced as the fitted model. It is inspired from Stephens [1978b]. They plotted, for different cloud types, the broadband optical thickness of the clouds for two spectral domains as a function of LWP. Points were determined from Mie Theory and the least-squares-fitted lines to these points were derived both for conservative scattering ($\omega_0 = 1$, $0.3\mu\text{m} \leq \lambda \leq 0.75\mu\text{m}$) and for non-conservative scattering ($\omega_0 \leq 1$, $0.75\mu\text{m} \leq \lambda \leq 4\mu\text{m}$). Because purely scattering is a good approximation for clouds for solar radiation, we chose to use the equation for conservative scattering for LWP higher than $14 \text{ g}\cdot\text{m}^{-2}$ and combined it to a linear fit based on the observations from 2005 to 2010 for LWP lower than $14 \text{ g}\cdot\text{m}^{-2}$. We showed in LA21 that the

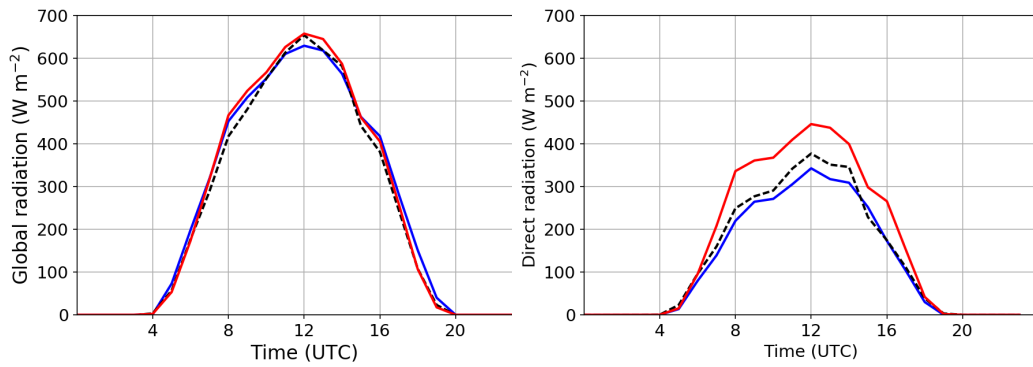


Figure 4.18: Diurnal cycle of global (left panel) and direct (right panel) irradiances during cloudy sky days in May 2014 measured at SIRTA (- - -) and computed with HelioSat (—) and code_saturne-Sim.14.6 (—)

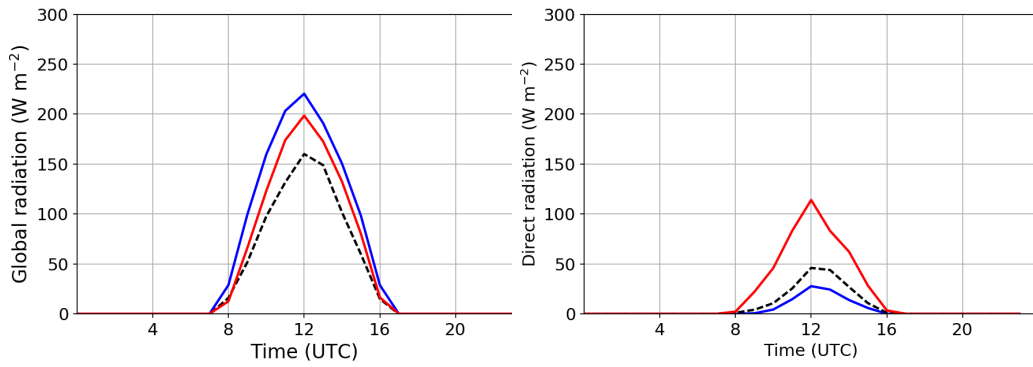


Figure 4.19: Diurnal cycle of global (left panel) and direct (right panel) irradiances during cloudy sky days in January 2014 measured at SIRTA (- - -) and computed with HelioSat (—) and code_saturne-Sim.14.6 (—)

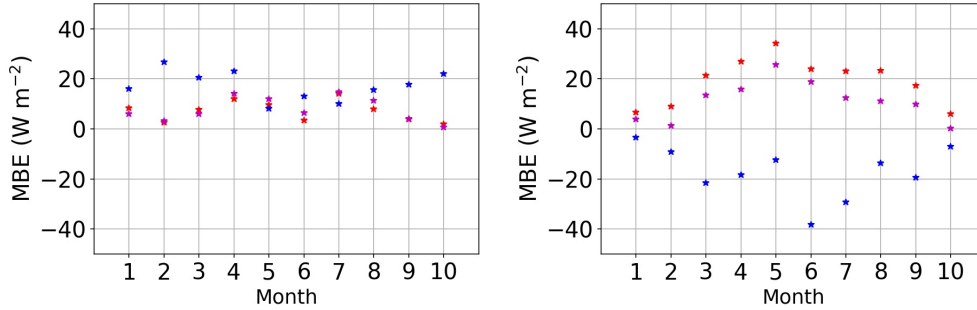


Figure 4.20: MBE (in $W m^{-2}$) between SIRTA measurements of global (left panel) and direct (right panel) irradiances and simulations using HelioSat-v3 (*) and code_saturne-Sim.14.6 (*) for every month of year 2014.

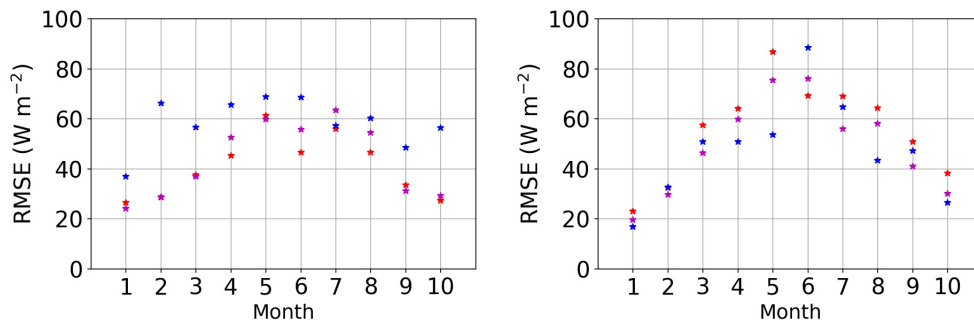


Figure 4.21: RMSE (in $W m^{-2}$) between SIRTA measurements of global (left panel) and direct (right panel) irradiances and simulations using HelioSat-v3 (*) and code_saturne-Sim.14.6 (*) for every month of year 2014.

fitted model was a good approximation of the COD.

Another model for the estimation of the COD was tested but not presented in LA21: the linear fit was extended for the whole range of LWP, it is referenced as "the linear model". The COD versus liquid water path and the different fitted models are represented in figure 4.22. The hourly measured COD (using satellite) between 2005 and 2010 is represented by the green scatter plot. The different trend lines for the estimation of the COD are represented: in black for the linear model, in red for Stephen's equation, in dark blue for the fitted model, in light blue for the estimation using equation 1 of LA21. The fitted model doesn't go through the scatter plot for high values of LWP, because, as seen in figure 6b of LA21, the highest density of points is in the range of LWP of 5-100 g m⁻². The RMSE between the estimated COD from LWP measurements from 2005 to 2010 and the satellite measurements are calculated and equal to: 16.3 W.m⁻² using Stephen's model, 14.4 W.m⁻² using the linear fit, 8.18 W.m⁻² using equation 1 and 7.6 W.m⁻² using the fitted model which makes it the closest to the measurements of the period 2005-2010.

Simulations were conducted using the "linear fit" for the estimation of COD. For the direct irradiance, similar results are obtained using the linear and fitted models because the COD is described by the same equation when LWP is lower than 14 g m⁻² and for LWP greater than 14 g m⁻², values of direct irradiance are very low. For the global component, results were better using the fitted models presented in LA21 except in January, February, March and October when the linear model performed slightly better. Taking into account, that the linear fit calculates higher values of COD than the logarithmic model, and that the type of clouds is dependent on the geographic place and time of the year a possible explanation during these months, clouds at the SIRTA had different optical properties and needed to be described by the linear fit.

To sum up, this small study conducted for the linear fit rethink the methodology followed for the development of the 'fitted model'. Thereby, for a more precise estimation of the COD, we could eventually have different analytical models for different seasons of the year or for different intervals of LWP.

4.4.3 Supplement on the error discrepancies analysis

A follow-up of the discussion part of LA21 is presented.

As it was mentioned in LA21, better results were obtained when cloud fraction was extracted from PYR or sky imager compared to LIDAR and satellite measurements. One possible explanation is that irradiance observations and cloud fraction are both extracted from PYR, it is then coherent to have good results with this type of data. Compared to LIDAR and satellite measurements, sky imager measure cloud fraction in a more direct way and consider multiple direction (in contrarily to LIDAR that measures in only one direction).

As seen in figure 4.23 representing the measured irradiance versus the simulated one, code_saturne compares well to measurements and slightly underestimates the direct component. However, there are few cases of strong discrepancy, they are analysed in LA21 (discussion). While analysing them, we were first searching for a link with the cloud type. As it can be seen in figure 4.24, there are low (0-2000 m), middle (2000-5000 m) and high (5000-7000 m) clouds at the SIRTA Observatory every month during the "year 2014" measured using the ceilometer. High

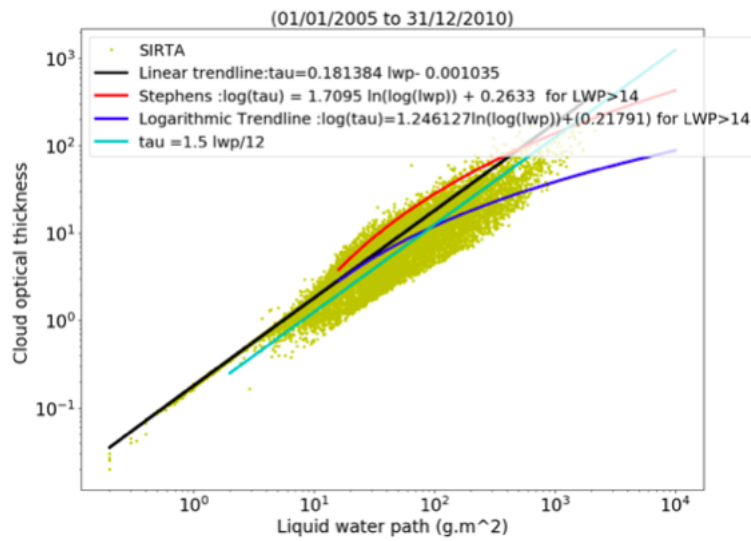


Figure 4.22: COD versus LWP from 2005 to 2010 at SIRTA (*), the approximation of COD using the fitted model (linear model — + logarithmic model —) and equation 4.1 with $r_e=12\mu\text{m}$ —) and Stephens [1978b] parametrization —.

clouds are the least present, contrarily to low clouds. In May there are very few high clouds (less than 5%) and a high proportion of low clouds (around 90 %). As mentioned earlier, clouds are represented in code_saturne following the parametrization of water clouds. Therefore, an analysis was conducted for the hours when only a high cloud (supposed to be made of ice) was presented. However, there was no direct relation between ice clouds and discrepancies between simulated and observed irradiances. Moreover, it is complicated to find a relation between the type of cloud and the discrepancies due to the overlapping of clouds that occurs most of the time (as it can be seen in figure 4.24).

The discrepancies could be correlated with the fluctuations (at time scales lower than 1 hour) of the measurements (that are documented in SIRTA ReObs file with their standard deviation) and with the values of LWP and cloud fraction as detailed in LA21. In particular, we found that a correlation exists between the cloud fraction and the MBE of global and direct irradiances. During overcast sky, there are few cases for which there are high values of simulated direct irradiance when measured direct irradiance was close to 0. In fact for those cases, the COD was low, and in LA21 we had stated that it might be due to a poorly coordination between measured LWP and cloud fraction or to a low density cloud blocking the sun. One example occurred on the 09/08/2014 at 16 h when the error (MBE) on direct irradiance is equal to -250 W m^{-2} and at 17 h when the error on direct irradiance is equal to -121 W m^{-2} . Figure 4.25 shows the time evolution of LWP, cloud fraction, precipitation and cloud base height on the 09/08/2014. Simulated direct irradiance compares well to measurements until 16 h. Low clouds are present until 17 h and high clouds are present after 13 h. In addition, there is no precipitation the whole day, which may indicate the presence of cirrus and stratocumulus clouds.

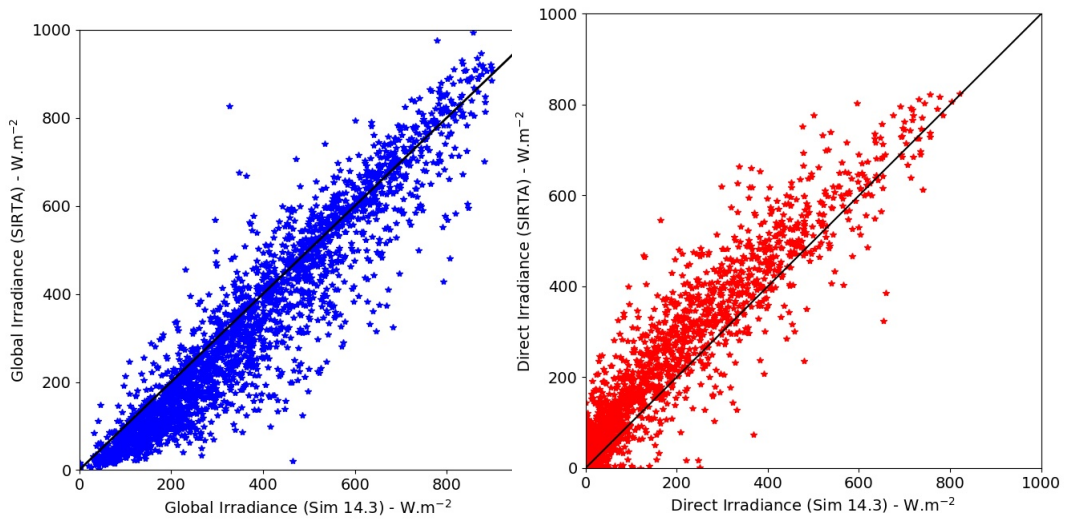


Figure 4.23: Global (left panel) and direct (right panel) irradiances measured at the SIRTA and compared to simulated values computed with code_saturne (Sim. 14.3).

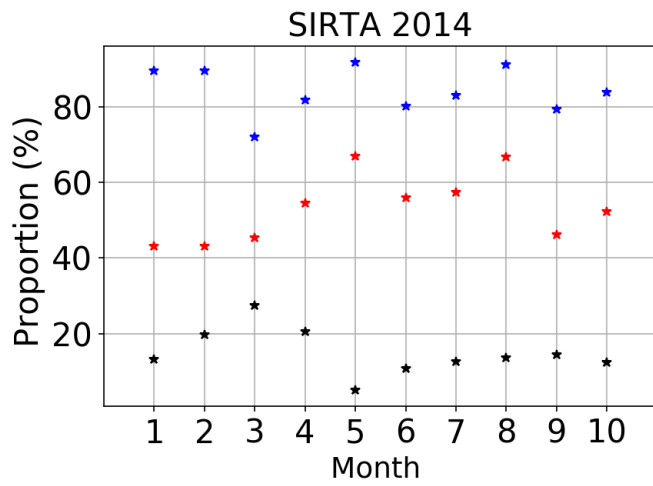


Figure 4.24: The proportion of low (blue), middle (red) and high (black) clouds at the SIRTA Observatory from 08/01/2014 to 30/10/2014 from ceilometer measurements.

However, the error doesn't seem to be correlated to the type of cloud. The strong disagreement between simulated and measured values coincides well with the drop of LWP that is close to 0 after 16h while the cloud fraction is still equal to 1. In this figure that is representative of other similar cases, there might be an incoherence between the LWP and cloud fraction. Indeed, after 16 h, there is a cloud fraction equal to 1 which will lead to resolving the cloudy-sky equations, but as the LWP is equal to 0, the simulated irradiance value will be high and similar to the one obtained during clear-sky situation. As the cloud fraction (equal to 1) is taken from PYR in this case, it is directly related to the measured irradiance at the surface, which is then very low. Hence, it explains the difference obtained between measurements and simulated values. One possible explanation is that the problem comes from the measurements and another is that is due to treatment of ice clouds either by code_saturne or by the microwave radiometer. It also shows that the performance of our model is directly linked to the accuracy and coherence of the input data.

Note: the cloud base height is retrieved from LIDAR measurements every 5 min and provide information on the cloud height for up to 3 levels. In order to have the cloud base height every hour, a histogram gathering all LIDAR measurements of cloud height in the 30 mins around the full hour was plotted and then the peaks for each category (low, middle and high clouds) were reported. That way, it is possible to have the altitude of the most probable cloud layer for each of the three cloud categories.

The precipitation is retrieved every 5s at 2 m height and then accumulated over 1 min to provide information of precipitation in mm/min every minute. As we needed the precipitation for every hour, the accumulated precipitation over each hour is calculated.

4.5 Summary

The standalone 1D radiation model of code_saturne was evaluated for the two periods: August 2009 and the year 2014. We focus on the estimation of fluxes in a cloudy atmosphere by coupling the model with on-site and satellite measurements. A sensitivity analysis on the cloud parameters was conducted, which showed the importance of the COD for the estimation of global irradiance. Moreover, a model was developed to estimate the COD from Liquid water path measurements only and showed to be a good approximation. code_saturne radiation model was validated and compared to on site measurements and to the HelioSat model. Finally, hourly values of solar fluxes were analysed to physically understand the cases of large errors between modelled and measured solar radiation.

In this chapter, solar fluxes were calculated at the surface using the *integral method*, which considers the atmosphere as being one homogeneous layer. However, it is also possible to estimate solar fluxes using the *multi-layered method*, which divides the atmosphere in multiple layers. It is a more precise method that requires higher, but still short, computer time and allows calculating the heating and fluxes for the different vertical layers. The *multi-layered method* was tested for the year 2014 and similar results were obtained at the ground using both methods. For solar applications, for instance, we are only interested in getting the fluxes at the ground, the integral method is then sufficient. For other type of studies, the information on the vertical profile of divergence flux is important and a multi-layered method is then

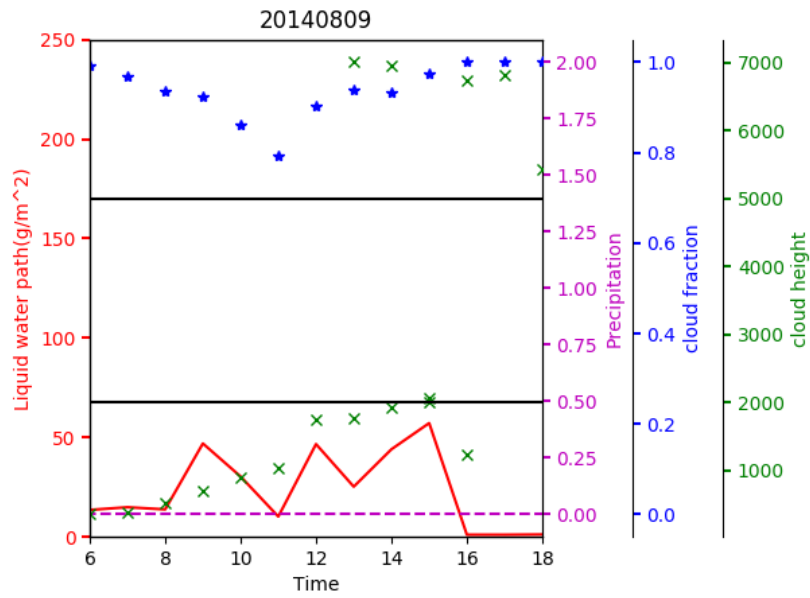


Figure 4.25: Diagram showing the time evolution of LWP (in red, in g m^{-2}), Precipitation (in purple, in mm/hr), cloud fraction (in blue) and cloud base height (in green, in m) on the 08/09/2014 at the SIRTA Observatory. The horizontal black lines mark the separation between the low, middle and high clouds.

necessary. The application of this method is furthermore discussed in chapter 5.

Chapter 5

The multi-layered radiative scheme of code_saturne

5.1 Introduction

In this chapter, we focus on the second objective of this thesis:

Objective 2: *Modelling the vertical profile of flux divergence using the 1D multi-layered model and taking into account the contribution of aerosols to a fog evolution through their influence on solar radiation.*

Further to the work carried up in chapter 4, the adjustments brought to the 1D radiation scheme of code_saturne as well as the different sensitivity tests conducted led to the development of a new version of the existing scheme. These adjustments were introduced in the 7.0 version of code_saturne. The radiative model introduced uses the *multi-layered* method in both spectral band (UV-vis and SIR). Therefore, the vertical profiles of downward and upward fluxes and heating rates are calculated as well as the direct, global and diffuse components at the surface. Following the estimation of surface radiative fluxes presented in the previous chapter, the 1D radiation scheme of code_saturne has been applied to a case in which the flux divergence in the atmosphere layers has been accounted for : a fog episode documented at SIRTA during the campaign ParisFog. As seen in chapter Black Carbon (BC) particles in cloud droplets and their interaction with the fog. We also tested different configuration such as considering interstitial aerosols or a constant cloud droplet radius or even a simpler parametrization for the modelling of irradiance fluxes at the surface. The ParisFog campaign is introduced in section 2.4.3; we are here interested in a fog event that occurred the 18-19/02/2007, on the 18th there was a clear sky day followed by the appearance of a fog in the early morning of the 19th that later evolved into a low stratus cloud. This chapter may be seen as the follow-up of Zhang et al. [2014] (XZ14). The studies conducted are the object of a paper submitted to the Journal of Geophysical Research - Atmosphere, referenced as LA21-2, that represents an important part of this chapter.

We start by developing the simulation of the fog and the different sensitivity tests conducted in section 5.2 (or paper LA21-2); then, section 5.3 provides additional information for a better comprehension of the work conducted.

Contents

5.1	Introduction	96
5.2	Article 2: Al Asmar et al. (2021): Modeling the contribution of aerosols to fog evolution through their influence on solar radiation	98
5.2.1	Abstract	98

Chapter 5 The multi-layered radiative scheme of code_saturne

5.2.2	Introduction	98
5.2.3	The layer-dependent scheme for solar radiation in code_saturne	100
5.2.4	The ParisFog experiment	101
5.2.5	Conclusion	110
5.2.6	Appendix	111
5.3	Complementary notes	118
5.3.1	The domain of the simulation	118
5.3.2	Calculation of the Black Carbon Fraction in cloud droplets	118
5.4	Summary	119

5.2 Article 2: Al Asmar et al. (2021): Modeling the contribution of aerosols to fog evolution through their influence on solar radiation

5.2.1 Abstract

Aerosols and in particular their black carbon (BC) content influence the atmospheric heating rate and fog dissipation. Substantial improvements have been introduced to the solar scheme of the computational fluid dynamic model code_saturne to estimate fluxes and heating rates in the atmosphere. This solar scheme is applied to a well-documented case of a fog that evolves into a low stratus cloud. Different sensitivity tests are conducted. They show that aerosols have a major effect with an overestimation of the direct solar fluxes by 150 W m^{-2} when aerosols are not considered, and a reduction of the heating of the layers. Aerosols lead to an increase of the heating rate by as much as 55 % in the solar infra-red (SIR) band and 100% in the Ultra-Violet visible (UV-vis) band. Taking into account the fraction of BC in cloud droplets also accentuates the heating in the layers at the top of the fog layer where water liquid content is maximum. When the BC fraction in cloud droplets is equal to $8.6 \cdot 10^{-6}$, there is an increase of approximately $7.3 \text{ }^\circ\text{C/day}$ in the layers. Increasing the BC fraction leads to an increase of this heating in the layer, especially in the UV-vis band.

5.2.2 Introduction

Aerosols play a major role in the atmosphere, both for air quality and meteorology. They have multiple interactions with atmospheric processes, mostly through the formation of clouds and their impact on solar irradiance.

Cloud droplets are formed by heterogeneous nucleation where aerosols serve as cloud condensation nuclei (CCN). The size distribution, the chemical composition and the number of particles have a large influence on CCN activation and consequently on chemical composition, size distribution and number of cloud droplets. Those affect the cloud optical properties and the radiation balance (aerosol indirect effect) [Rap et al., 2013, Sartelet et al., 2018a]. Consequently, the parameterization of CCN activation is a very active field of research (e.g., Cohard et al. [1998], Nenes and Seinfeld [2003], Cheng et al. [2007], Abdul-Razzak et al. [1998]). In clear-sky conditions, aerosols interact directly with solar irradiance through irradiance absorption and scattering, depending on aerosols properties (aerosol direct effect). The interactions of aerosols with solar irradiance are largely studied because of their importance in climate change [Kawahara et al., 2002] and climate engineering [Ming et al., 2014]. In addition, the accurate estimation of solar irradiance at the earth surface is essential for estimating the photovoltaic production.

In numerical weather models (NWP), the impact of aerosols on solar irradiance is not always accurately modelled [Gueymard and Ruiz-Arias, 2015]. Aerosols are often parametrized in a simple way, for example, by assuming constant optical properties in space and time [Psiloglou et al., 2000] or using measured or climatological values as in the Weather Research Forecast Solar model [Jimenez et al., 2016a]. Aerosol optical properties can also be provided by an off-line Chemical Transport Model [Sartelet et al., 2007] or directly estimated by NWP models,

including more simple aerosol modelling [Morcrette et al., 2009]. In previous works, using the solar radiation scheme of the open-source Computational Fluid Dynamic (CFD) model code_saturne ¹, the influence of aerosols on irradiance at the ground was represented by vertically integrating the optical properties of aerosols [Sartelet et al., 2018a, Al Asmar et al., 2021a]. However, aerosols also influence the downward and upward radiative flux of the different vertical layers of the atmosphere, leading to local heating [Liou, 2002], which affects the formation of fog and clouds. This influence of aerosols on solar radiation can be modelled by their optical properties (optical depth, single scattering albedo and asymmetry factor), which depend on their size distribution and chemical composition [Hess et al., 1998]. For example, black carbon (BC) strongly contributes to the atmospheric heating rate [Lu et al., 2020]. Cloud droplet nucleation depends on the composition of aerosols and their hygroscopicity [Abdul-Razzak and Ghan, 2000]. In particular, the presence of black carbon (BC) in cloud droplets modifies the single scattering albedos of clouds, leading to an increase of solar heating in the cloud layers [Ch yle et al., 1996, Chuang et al., 2002, Sandu et al., 2005, Motos et al., 2019]. Because NWP and CFD models do not describe the full complexity of clouds, their effects on solar radiation are difficult to model and linked to uncertainties [Jimenez et al., 2016a, Al Asmar et al., 2021a]. Because the atmosphere is discretized (in time but also spatially with a model mesh size), partial cloudiness has to be introduced to the modelling of solar radiation. Partial cloudiness is usually treated by mainly two hypothesis that consider either maximum or random overlapping of the clouds in the different vertical layers. A mix of these two hypothesis is often used in global climate models [Morcrette and Jakob, 2000, Ritter and Geleyn, 1992, Hogan and Bozzo, 2016]. Tridimensional nephanalysis of cloud coverage, Tian and Curry [1989] shows that the maximum overlap assumption is more justified if there is no clear interstice between adjacent cloud layers. Random overlap is a better approximation in the other cases when different types of cloud co-exist in the vertical with no correlation between their horizontal structures.

To illustrate the influence of aerosols on solar radiation and their interactions with clouds, the solar radiative scheme of code_saturne is improved to include aerosols with a detailed description of their optical properties in the different vertical layers of the atmosphere. One-dimensional (vertical) simulations are performed during a well-documented case of a fog that evolves into a low stratus cloud [Zhang et al., 2014] during the campaign ParisFog [Haeffelin et al., 2010] at Palaiseau in the south of Paris area. Because the constraints of computational cost are predominant for both climate and CFD modelling at very fine scales, a simple solar radiative scheme is used: it is based on the two-stream method using two spectral bands (Lacis and Hansen [1974] (LH74)). This scheme represents well the direct and global irradiances at the ground during clear-sky days when aerosol optical properties are well modelled [Sartelet et al., 2018a, Al Asmar et al., 2021a]. It is now extended, similarly to Zhang et al. [2014], to describe scattering and absorption processes in the vertical atmospheric layers to calculate the heating and the downward radiation fluxes at the soil-atmosphere interface. The scattering and absorption by particles (aerosols and cloud droplets) and gases are explicitly described in the vertical.

¹<https://www.code-saturne.org/cms/>

This paper presents the improvements made in the solar radiative scheme of code_saturne, to be used at atmospheric fine scales. It is applied to a case of fog evolution during the campaign ParisFog to understand the role of BC in cloud droplets in fog dissipation and the influence of the modelled cloud fraction. This paper is organized as follows:

1. In section 2, the solar radiative model is briefly presented and equations are given in the appendices.
2. In section 3 the solar scheme is used and compared to the LH74 scheme for a one-dimensional simulation of a fog event during the ParisFog campaign at SIRTa. The role of aerosols on the heating of atmospheric layers is investigated for clear sky and foggy sky.
3. In section 4 sensitivity tests are conducted in order to evaluate the impact of different parametrizations including the presence of aerosols before fog formation, BC in cloud droplets and cloud fraction during and after fog development.

5.2.3 The layer-dependent scheme for solar radiation in code_saturne

The solar radiation scheme proposed by LH74 has been largely used in numerical weather prediction (NWP) for climate modelling and in limited area models (weather research forecast (WRF), [Skamarock et al., 2008, Zhang et al., 2014, Sartelet et al., 2018a, Al Asmar et al., 2021a]) because of its efficiency and its low computer cost. The solar spectrum is divided into two bands: the UltraViolet-visible (UV-vis) band (0.2-0.7 μm) where absorption by ozone occurs in the upper layers of the atmosphere, and the Solar Infrared (SIR) domain (0.7-5 μm) where absorption by water is dominant in the lower part of the atmosphere. The solar radiation scheme of code_saturne is inspired by the LH74 scheme, it has been modified by Sartelet et al. [2018a] and Al Asmar et al. [2021a] to accurately consider aerosols and cloud fraction in the simulation of direct and global solar radiation at the ground. It has also been used by Zhang et al. [2014] (XZ14) to model the solar radiation for the different vertical layers of the atmosphere, using a previous version of the solar radiation scheme and making the approximation that aerosols are purely scattering particles.

Here, the solar radiation scheme of code_saturne is modified to model the solar radiation for the different vertical layers of the atmosphere, taking into account the absorbing and scattering properties of particles. They are characterized by their optical properties: aerosol optical depth (AOD), single scattering albedo (SSA) and asymmetry factor. Furthermore, compared to XZ14, maximum and random overlap parameterizations for cloud fraction have been introduced, the adding method for scattering has been added in the UV-vis band, and, following Al Asmar et al. [2021a], other improvements have been made: the optical air mass, the absorption by minor gases, the Rayleigh diffusion, the choice of the δ two-stream approximation and the estimation of direct radiation that could be important for photovoltaic applications. The equations are detailed in the appendix (appendix 5.2.6.1 for the cloud and aerosol optical

properties and appendix 5.2.6.2 for the calculation of irradiance fluxes).

At the earth surface, this solar radiative model (part of code_saturneV7.0) has been validated in [Al Asmar et al., 2021a] when considering the atmosphere as being made of one single homogeneous layer, by comparison with irradiance measurements at SIRTa during the year 2014. The results were satisfactory with respectively a RMSE of 19 W m^{-2} (global) with a bias of 5 W m^{-2} and 21 W m^{-2} (direct) with a bias of -7 W m^{-2} for clear-sky situations and RMSE of 59 W m^{-2} (global) with a bias of 17 W m^{-2} and 50 W m^{-2} (direct) with a bias of -18 W m^{-2} for cloudy-sky situations.

In order to evaluate the heating of atmospheric layers by solar radiation, a simulation of a fog event is performed in this study using the CFD software code_saturne V7.0 (which includes this solar radiative scheme) during one of the Intensive Observation Periods (IOP) of the ParisFog campaign [Haeffelin et al., 2010].

5.2.4 The ParisFog experiment

5.2.4.1 Observations and simulation conditions

Data and simulations used in this study are those of the (IOP)13 of the campaign ParisFog which took place at SIRTa observatory (Palaiseau, France) the 18th and 19th February 2007. During this IOP, different instruments have been deployed:

- Vertical profiles of wind, temperature and humidity by radiosondes at 12, 21 (UTC) on the 18th of February and 0000, 0300, 0600, 1000 (UTC) the 19th of February.
- Near surface measurements on a 30-m mast of: temperature, humidity, wind and turbulence by sonic anemometers, long wave and solar radiative fluxes.
- Surface measurements at 2 m of: temperature, humidity, visibility, radiative fluxes
- Fog droplet number with an optical particle counter (OPC) Pallas Wallas 2000
- Ceilometer measurements to estimate the fog/stratus layer depth/elevation
- Aerosols size distribution with a Scanning Mobility Particle Size (SMPS), and an optical particle counter (OPC Grimm 1.109), and filter sampling to determine their chemical composition.

The fog event is simulated here with the one-dimensional atmospheric module of code_saturne described in the previous section, using the same configuration as XZ14. In code_saturne, the prognostic variables evolving in time and on the vertical are: the liquid potential temperature, the horizontal wind components, the total water content (liquid and vapour) and the cloud droplet number concentration. The surface temperature and humidity are imposed at the earth surface. They are computed by an extrapolation method based on the Monin Obukhov similarity theory, where surface temperature and humidity are estimated from their measurement at 2 m and 10 m [Musson-Genon et al., 2007]. The size distribution of fog droplet is described by a log-normal law and the nucleation scheme of Abdul-Razzak and Ghan [2000]

is used. The liquid water content and the partial cloudiness are estimated by using a sub-grid condensation scheme, depending on the sub-grid distribution law for total water content and liquid potential temperature fluctuations [Bouzereau et al., 2007].

There are several differences compared to the simulations performed by XZ14. First, we use here a more recent version (V7.0) of code_saturne, in which some improvements have been made concerning the turbulent closure of the code. The first order turbulence closure using a mixing length depending on Richardson number [Musson-Genon, 1995] is replaced by the $k-\epsilon$ model of the version 7.0 [Guimet and Laurence, 2002]. Second, the solar scheme described in the previous section is used, and the influence on the fog evolution of different options related to solar radiations is studied. The total aerosol optical depth (AOD) and asymmetry factor are computed in both the UV-vis and SIR bands using the AERONET data. The integration over frequency is made following Sartelet et al. [2018a] with measurement at 500, 700 and 1400 nm by means of the Angström coefficient due to a lake in experimental knowledge. Aerosols are distributed homogeneously on the vertical into two layers: a first layer of 1000 m depth where 90% of the total AOD is considered and a second layer between 1000 and 3000 m for residual AOD (10% of the total AOD). These altitudes have been chosen in regard to the evolution of the height of the boundary layer during the IOP13 deduced from the vertical profiles of humidity and temperature. The aerosol asymmetry factor and single scattering albedo are integrated on the vertical and considered to be constant in time for the duration of the simulation, they are respectively equal to 0.6638 and 0.963 in the UV-vis band and to 0.6486 and 0.964 in the SIR band.

The nucleation scheme of Abdul-Razzak and Ghan [2000], which is used in XZ14, assumes that the aerosol size distribution is made of three lognormal modes, and takes into account the aerosol chemical composition including the BC fraction. The parameters of these log-normal modes have been deduced from SMPS and OPC measurements by Rangognio [2009] and are used in XZ14. They are shown in table 5.1. The chemical composition inferred the critical supersaturation for each mode through an hygroscopicity parameter, which depends on the osmotic coefficient, the fraction of soluble substance, the number of ions produced by dissociation of a salt molecule in water and the molecular weight of the aerosol material. BC is considered as insoluble with an osmotic coefficient of 1. Knowing that cloud condensation nuclei are essentially formed by the accumulation mode (mode 3 - table 5.1), it is possible to estimate the volume fraction ν_d of BC in cloud droplets. As BC in aerosols is determined by filter sampling and chemical analysis, it is necessary to determine the mean wet diameter of the mode 3. By using the simple formulation of Zieger et al. [2010] for the ratio d_{wet}/d_{dry} and with a humidity of 95%, we obtain a BC volume fraction of ν_d of $8.6 \cdot 10^{-6}$ for a concentration of BC of 16% (XZ14) of the dry-aerosol mass in the mode 3. This percentage is considered to be constant for the three modes. Then the maximum possible value is obtained by considering $d_{wet}/d_{dry} = 1$, that leads to $\nu_d = 1.6 \cdot 10^{-4}$.

In the XZ14 simulations using the LH74 scheme, the single scattering albedo and the asymmetry factor for clouds were constant in time and on the vertical. They are now dependent on the equivalent radius of fog droplet, which is variable in time and on the vertical and different in the UV-vis and SIR bands.

In section 5.2.4.2, the fog evolution is simulated with these new conditions with surface tem-

	Mode 1	Mode 2	Mode 3
$N_a(\text{cm}^{-3})$	8700	8300	1000
$R_a (\mu\text{m})$	0.0165	0.055	0.4
σ_a	1.57	1.59	1.3

Table 5.1: Aerosol size distribution characteristics at 2100 (UTC) during IOP 13 used in the control simulation. N_a is the number of particles, R_a their dry radius and σ_a the standard deviation of the log-normal distribution.

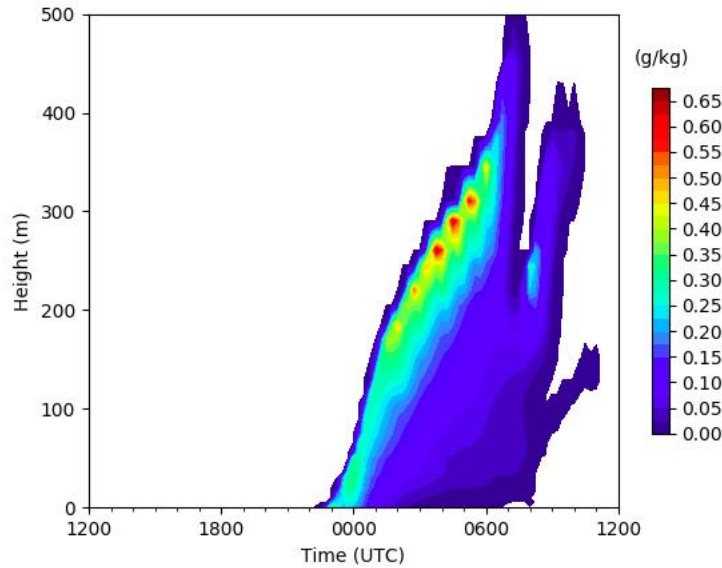


Figure 5.1: Temporal evolution of the simulated liquid water content in g kg^{-1} with the solar scheme when surface parameters are deduced from observations.

perature and humidity deduced from observation, with random overlap for partial cloudiness and without taking into account BC in cloud droplets (simulation referred to as the 'base case' or control simulation).

5.2.4.2 Fog-event simulation

During the IOP13, the fog appears on the 18th of February at 2230 (UTC) after a clear-sky afternoon and dissipates in a low stratus in the morning of the 19th of February at sunrise around 0700 (UTC). This is well represented in the simulation as seen in figure 5.1). Further details about the conditions of this IOP are given in XZ14. Here, we essentially focus on solar radiation effects during the clear-sky phase and the dissipation phase. On the 18th afternoon, the sky is slightly covered with high clouds at 1200 (UTC). It becomes clear in the afternoon as shown in figure 5.2, which represents the global and direct irradiances at the earth's surface.

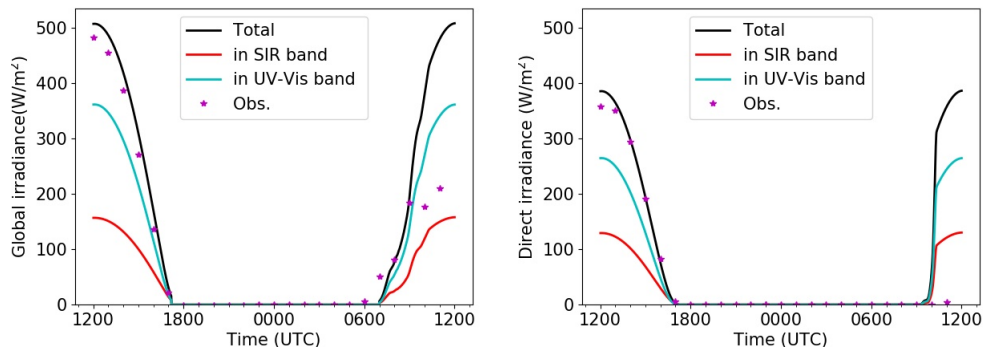


Figure 5.2: Comparisons, at the earth surface, between observations and simulation of global solar (left) and direct solar (right) irradiances.

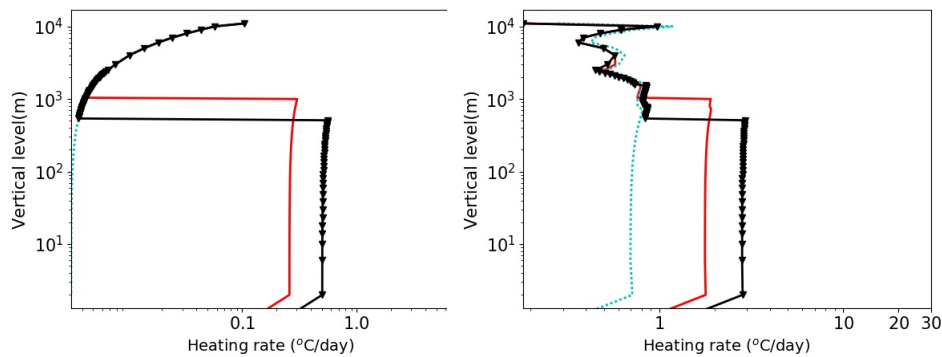


Figure 5.3: Heating rate in the atmospheric layers on 18/02/2007 at 1500 (UTC) for the UV-vis band (left) and for the SIR band (right) (in $^{\circ}\text{C}/\text{day}$) — base case; - - - no aerosols in the modelling of irradiance fluxes; -v- aerosol boundary layer of 500 m.

Except from 1200 (UTC) to 1300 (UTC) where high clouds are probably present but not simulated, the global and direct surface irradiances are well estimated by the simulation during the afternoon preceding the fog appearance. Although the influence of aerosols on downward and upward fluxes is taken into account for both UV-vis and SIR bands, the heating rate in clear sky is largely dominated by the SIR band (figure 5.3).

During the dissipation phase in the morning of the 19th February, the simulated global irradiance at the surface (figure 5.2) compares well to observations between 0600 (UTC) and 0900 (UTC). The stratus disappearance is too fast in the simulation, leading to a large overestimation of both the direct and global irradiances between 1000 (UTC) and 1200 (UTC). Note that, during the elevation phase (0600-0900 (UTC)), the stratus is sufficiently deep to totally extinct the observed direct radiation.

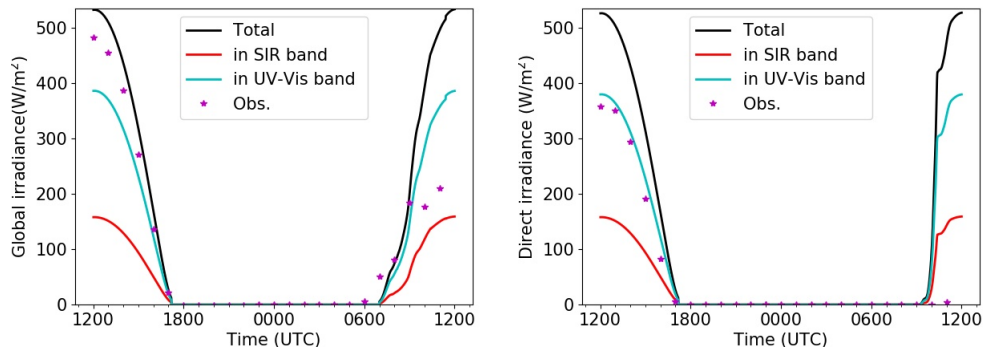


Figure 5.4: Same as figure 5.2 but for a simulation without aerosols in the modelling of irradiance fluxes.

5.2.4.3 Sensitivity tests

Sensitivity tests on aerosols The fog evolution is impacted by aerosols in different ways: first aerosols directly impact the irradiance fluxes and the heating rates, but also they impact the nucleation into cloud droplets and the chemical composition of the droplets. Here, their influence on the fog evolution through the irradiance fluxes is studied, by performing a simulation without taking into account aerosols in the modelling of the irradiance fluxes. This impact is presented in figure 5.4 for the irradiance fluxes at the earth surface and in figure 5.3 for the vertical distribution of the heating in the atmospheric layers at 1500 (UTC). The temporal evolution of the simulated liquid water content is similar to the one of the base case (figure 5.1). Therefore, the dissipation of the fog is not much affected by considering aerosols in the modelling of solar radiation fluxes here. In fact, as surface temperature and humidity are forced to observations in all the simulations of this paper, the contribution of aerosols is only taken into account in the heating rate of the atmospheric layers that is insufficient to significantly modify the evolution of the fog layer in the dissipation phase. Nevertheless, the surface solar irradiances (figure 5.4), as expected, are largely overestimated if aerosols are not considered. The gap at 1200 (UTC) is around 30 W m^{-2} for the global and 150 W m^{-2} for the direct. The larger overestimation of the direct component is linked to the scattering of aerosols, which transform direct irradiation to diffuse irradiation. Note the very weak differences between global and direct irradiances for the simulation without aerosols. This is due to Rayleigh diffusion, which is only parameterized in the UV-vis band by means of the factor $1/(1 - \bar{R}_a^* R_g)$ as in LH74. Compared to the control simulation, the heating in the layers is very low in the UV-vis band (corresponding to ozone absorption) if aerosols are not considered in the modelling of the irradiances; in the SIR band, it decreases of approximately $0.9 \text{ }^\circ\text{C/day}$.

Because the exact distribution of aerosols on the vertical is unknown due to the time variability of the boundary layer height during the IOP13, it is interesting to estimate the effect of a more concentrated aerosol layer in the lower part of the atmosphere which is equivalent to a lower boundary layer height. This could represent a pollution event as it often appears during winter anticyclones which are favourable to radiation fogs. The heating rate for a sim-

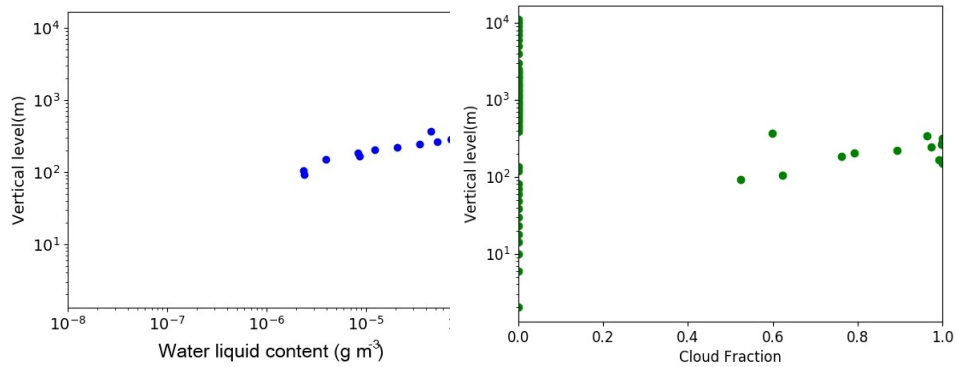


Figure 5.5: Vertical profile of the liquid water content (in g m^3) (left) and cloud fraction (right) at 0900 (UTC) on the 19th February for the base case.

ulation with a depth of 500 m for the first aerosol layer close to the ground instead of 1000 m is presented in figure 5.3. The heating rates increase strongly from 1.8 °C/day to 2.8 °C/day in the SIR band and from 0.25 to 0.5 °C/day in the UV-vis band. In that case, the contribution of UV-vis band to heating rate is not negligible compared to that of the SIR band.

Note that aerosol properties are estimated from AERONET data. The role of BC concentration in aerosol particle as studies in Lu et al. [2020] is not investigated in this paper, which rather focuses on the influence of the fraction of BC in cloud droplets on the fog evolution.

5.2.4.4 Sensitivity tests on the fog evolution

Sensitivity tests are conducted in order to evaluate the impact of a better description of cloud optical properties in the solar irradiance scheme. Here we are specifically interested in the solar heating in the cloud layers. In this paragraph, the results are presented at 0900 (UTC) before the disappearance of the stratus and when solar heating is significant. The vertical profile of liquid water content and cloud fraction are presented in figure 5.5 for the base case. Firstly, each sensitivity simulation is performed by modifying a particular variable, such as the cloud optical depth. The same vertical profiles of liquid water content and cloud fraction as in the base case are used. They are shown in figure 5.5. This set of sensitivity simulations are referred to as the ‘stationary’ tests. Then, the impact of the modification of the variable on the simulated fog is evaluated, by letting the liquid water path and cloud fraction evolve accordingly to this change. This set of sensitivity simulations are referred to as the ‘evolving’ tests. The ‘evolving’ tests help understand the impact of the modified variables on the liquid water field and how it affects the results of simulations and the dissipation of the fog.

Sensitivity to interstitial aerosols Interstitial aerosol particles are particles that are too small to be activated to cloud droplets. However, for rigorous calculations, they should be considered during cloudy-sky situation. This is done by adding the AOD to the COD during cloudy-sky situations in equations 5.10, 5.11 and 5.12 and in the estimation of the direct irra-

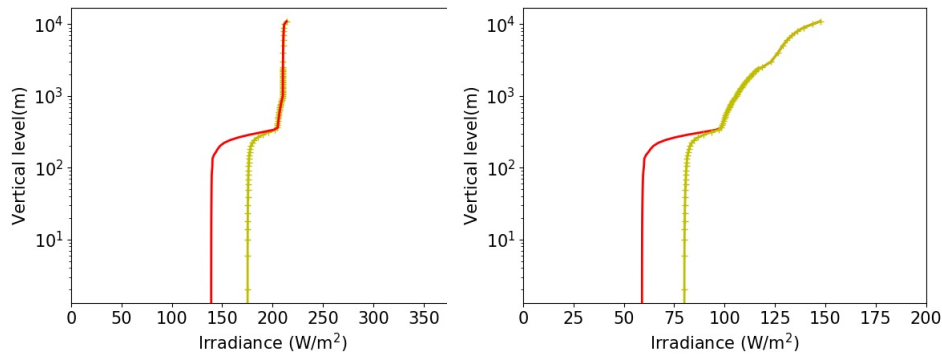


Figure 5.6: Downward global fluxes in the atmospheric layers at 0900 (UTC) on the 19th of February for UV-vis band (left) and for SIR band (right) (— base case; +- constant cloud droplet's effective radius of 10 μ m).

diance for the base case. However, not taking into account interstitial aerosols in the cloud layer of our simulation has a very low impact both on the heating rate and fluxes. For the 'stationary' test, the heating rate at the top of the cloud layer decreases by less than 0.3 °C/day in the UV-vis band and 0.2 °C/day in the SIR band. Similarly, the downward global and direct surface irradiances are slightly impacted, with an increase lower than 1.4 W m⁻² in the UV-vis band and 0.35 W m⁻² in the SIR band. Interstitial aerosols do not impact the evolution of the cloud layer during its dissipation phase.

Sensitivity to effective radius of cloud droplet The effective radius of cloud droplets is used for the calculation of the SSA and asymmetry factor (equations in appendix 5.2.6.1). It is variable in time and space and the average radius is equal to 2.7 μ m (the average has been calculated for all cloudy layers, in time and on the vertical). Taking the constant value of 2.7 μ m in the model has a very low impact both on the heating rate (less than 0.5 °C/day) and irradiance fluxes (less than 1 W. m⁻²) However, a constant effective radius of 10 μ m, often used as climatological value for low clouds, increases both the global and direct irradiances. Compared to the base case in the stationary case at 0900 (UTC), the heating rate is mainly impacted in the SIR band with an increase of 1.9 °C/day. The downward surface irradiance is strongly impacted, it is higher by approximately 36 W m⁻² in the UV-vis band and 22 W m⁻² in the SIR band (figure 5.6). An overestimation of the droplet radius reduces the value of the cloud optical depth, which increases the downward fluxes under the cloud. In the UV-vis band, the scattering to space is now lower, in the SIR band, the absorption in the cloud layer is lower. As the impact on the heating rate is relatively low and as the earth surface temperature is forced to observation in our simulations, the dissipation of the fog is not impacted by these variations of the effective radius of cloud droplet.

Sensitivity to BC concentration In the base case, the influence of the BC concentration in the cloud droplet on the heating rate is not considered. However, BC absorbs solar irradiation and increases the heating rate in the atmospheric layers. The BC concentration can be taken

into account in the calculation of the SSA of clouds following [Chuang et al. \[2002\]](#) (refer to appendix 5.2.6.1 for equations). We do not have direct measurements of the BC fraction in the fog droplet and large uncertainty on aerosol wet diameter, therefore we consider two possible BC fraction in cloud droplets: $V_{fBC} = 8.6 \cdot 10^{-6}$ and the maximum value of $V_{fBC} = 1.6 \cdot 10^{-4}$, as detailed in section 5.2.4.1.

The introduction of BC with $V_{fBC} = 8.6 \cdot 10^{-6}$ in cloud droplets impacts the heating rate (figure 5.7) and fluxes at the ground. In the ‘stationary’ test, as expected, the heating rate is accentuated at the top of the cloud layer where the liquid water content is maximum. There is an increase of the heating rate of approximately $7 \text{ }^\circ\text{C/day}$ in the SIR band and $0.3 \text{ }^\circ\text{C/day}$ in the UV-vis band at 0900 (UTC). In that case, the contribution of the UV-vis band to the heating rate becomes significant. As absorption of irradiance is more important in the cloud layers, the global and direct irradiances at the earth’s surface are directly impacted by taking into account BC concentration in the cloud droplet. However, this impact is weak: at 0900 (UTC), compared to the base case, the global irradiance is lower than -1.45 W m^{-2} in the SIR band and -0.22 W m^{-2} in the UV-vis band. In the ‘evolving’ test, the total heating rate is higher (by $3.2 \text{ }^\circ\text{C/day}$) when the BC fraction in cloud droplets is taken into account, and the global irradiances at the earth’s surface increase by 9.2 W m^{-2} in the SIR band and 18.4 W m^{-2} in the UV-vis band at 0900(UTC) compared to the base case (figures not presented here).

When V_{fBC} is equal to $1.6 \cdot 10^{-4}$, as expected, the heating in the layers increases even more: compared to the base case, there is an increase of approximately $5.5 \text{ }^\circ\text{C/day}$ in the UV-vis band and $10.3 \text{ }^\circ\text{C/day}$ in the SIR band for the ‘stationary case’ (figure 5.7). That leads to a decrease of the global irradiance at the earth surface of -2 W m^{-2} in the SIR band and -4 W m^{-2} in UV-vis band, compared to the base case. For the ‘evolving’ test, the water liquid content is impacted and is reduced (by around 0.05 g/kg) during and after the dissipation of the fog compared to the base case. The fog elevates from the ground earlier (around 0600 (UTC) instead of 0700 (UTC)) and the stratus cloud dissipates faster (the stratus now is completely dissipated around 0930(UTC) instead of 1100 (UTC)). That corresponds to a significant increase of the surface irradiances, at 0900 (UTC) for global irradiance ($+16. \text{ W m}^{-2}$ in the SIR band, $+28.8 \text{ W m}^{-2}$ in the UV-vis band) and at 1000 (UTC) for direct irradiance ($+39.4 \text{ W m}^{-2}$ in the SIR band, $+77.4 \text{ W m}^{-2}$ in the UV-vis band).

Sensitivity to the treatment of partial cloudiness In this study, the evolution of a fog layer that elevates in a stratus at the end of the morning is simulated. For these conditions, as mentioned by Tian and Curry (1989), it seems more appropriate to assume maximum overlapping instead of random overlapping for the partial cloudiness. Even though the heating rate does not change significantly when assuming random overlapping ($+1.1 \text{ }^\circ\text{C/day}$ in the SIR band), the upward and downward fluxes are impacted both in the UV-vis and SIR bands leading to a slight decrease of solar irradiances at the earth’s surface (-3.3 W m^{-2} in the SIR band, -5.6 W m^{-2} in the UV-vis band). The evolution of the fog layer is not modified, the cloud fraction being equal to 1 in the cloud layer from 0600 (UTC) to 0800 (UTC). The cloud fraction only differs from 1 in the dissipation phase after 0900 (UTC) when the liquid water content in

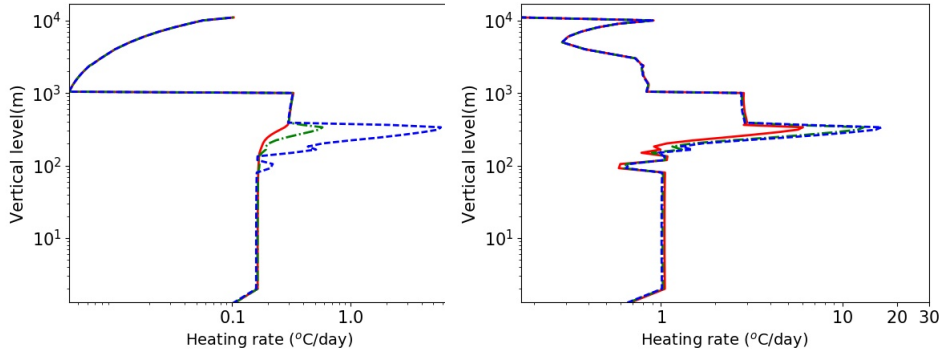


Figure 5.7: Heating rate in the atmospheric layers at 0900 (UTC) on the 19th of February for UV-vis band (left) and for SIR band (right) (for 'stationary case') (— base case, i.e. without BC; - - $V_{fBC} = 8.6 \cdot 10^{-6}$; - - - $V_{fBC} = 1.6 \cdot 10^{-4}$).

the cloud layer is very low.

Simplified parametrization As shown in the sensitivity study, the solar heating in the lower part of the atmosphere is low in the UV-vis band compared to the SIR band. In fact, ozone absorption is only efficient in the upper layer of the atmosphere and overlap correction between gas and particles can be neglected in the troposphere. In addition, the spatial and time variability of effective radius is not very important if a correct averaged value is used for the cloud droplet. Here, a simpler parameterization of solar heating in the UV-vis band is designed in order to save computer cost. In addition, for many applications only the global and direct solar fluxes at the earth's surface are necessary and the vertical distribution of fluxes is not useful. Considering the integral cloud and aerosol optical properties, as in [Sartelet et al. \[2018a\]](#) and [Al Asmar et al. \[2021a\]](#), the downward fluxes at the ground surface in the UV-vis band can be written as:

$$F \downarrow_g^{UV-vis,nc} = \mu_0 F (0.647 - A_{o3}(x) - \bar{R}_r(\mu_0)) T_{mg} T_a / (1. - R_a^* R_g) \quad (5.1)$$

$$F \downarrow_g^{UV-vis,c} = \mu_0 F (0.647 - A_{o3}(x) - \bar{R}_r(\mu_0)) T_{mg} T_c / (1. - R_c^* R_g) \quad (5.2)$$

$$F \downarrow_d^{UV-vis,nc} = \mu_0 F (0.647 - A_{o3}(x) - \bar{R}_r(\mu_0)) T_{mg} e^{-m\tau_a^{tot}} \quad (5.3)$$

$$F \downarrow_d^{UV-vis,c} = \mu_0 F (0.647 - A_{o3}(x) - \bar{R}_r(\mu_0)) T_{mg} e^{-m\tau_c^{tot}} \quad (5.4)$$

With $x = \mu_{O3}(\infty, 0)$, T_a , R_a^* , T_c , R_c^* are calculated as equations 5.16 and 5.17 but for the total optical depth of cloud τ_c^{tot} and aerosol τ_a^{tot} ; the different variables are defined in appendix 5.2.6.2.

The heating rate in the layers is computed as in LH74 with equations (5.37), (5.38), (5.39) and (5.47). The simplification of the parameterization consists in neglecting absorption in

the aerosol and cloud layers that are considered as purely scattering in the UV-vis band. In the stationary test at 0900 (UTC), the difference with the base case is low, 0.22 °C/day in the SIR band and -0.32 °C/day in the UV-vis band where there is no heating rate due to aerosols. The results of this simpler parameterization for the surface irradiances at 0900 (UTC) for the UV-vis band (compared to the base case, the difference for the global: 1.3 W m⁻²; direct: 0.07 W m⁻²) and SIR band (compared to the base case, the difference for the global: -0.19 W m⁻²; direct 0.0 W m⁻²) are quite similar to the base case. For the 'evolving' test, as the total heating rate (sum of UV-vis band and SIR band contributions) is very close to that of the base case, the liquid water content in the fog/stratus layer is similar and the differences for surface irradiances are low: for example at 0900 (UTC), in the UV-vis band, the actual version differs of the base case by +1.23 W m⁻² for the surface global irradiance and of +0.05 W m⁻² for the surface direct irradiance; in the SIR band the differences are equal to +0.4 W m⁻² for surface global irradiance and 0 W m⁻² for surface direct irradiance. The dissipation of the fog is not affected. Calculations are simpler, which shows the advantage of using such a method that is a good first approximation. Note that, if Joseph et al. (1976) corrections are omitted when using this simplified method, code_saturne results are not impacted for this specific case.

5.2.5 Conclusion

A simple solar radiation scheme has been developed in order to introduce the aerosols in the two-stream parameterization of Lacis and Hansen, (1974). Two spectral bands are considered: the UV-vis band (0.2- 0.7 μm) where ozone absorption is predominant in the stratosphere and the SIR band (0.7-5 μm) where absorption and diffusion by water vapour, clouds, aerosols and Rayleigh scattering are the major processes in the troposphere.

Substantial improvements have been introduced to the original version.

The optical properties of clouds (optical depth, single scattering albedo and asymmetry factor) are now taken into account in both spectral bands, and they are estimated as functions of the effective radius of the cloud droplet. The optical properties of aerosols are also differentiated for each band. In order to include clouds and aerosols effects in the UV-vis band, the adding method is introduced to calculate transmission and reflection functions for clouds and aerosols layers as for the SIR band but by neglecting the overlapping with ozone in the lower atmosphere. The two-stream method has been modified to take into account highly forward scattering due to cloud droplets and aerosols following Joseph et al. (1976) for both quadrature and standard Eddington approximations with a re-actualized optical air mass formulation. The cloud fraction has been introduced in the solar scheme, giving us the possibility to use random or maximum overlapping for the different cloud layers. For photovoltaic application, the downward direct solar irradiance is now computed and absorption by minor atmospheric gases like CO₂, CO, N₂O, CH₄, O₂ has been added in the global and direct vertical fluxes. This solar scheme has been used to simulate a case of fog event during the ParisFog campaign. The effect of the main improvements has been illustrated. The main conclusions are:

As expected, before the fog formation (clear-sky conditions), aerosols play a major role in the estimation of radiation and heating rates. When they are not considered, the fluxes at the surface are highly overestimated (especially the direct flux that increases of 150 W.m⁻²) and the heating in the layers is strongly underestimated both in the UV-vis and SIR bands (decrease

of 0.9 °C/day in the SIR band), compared to the base case in which a 1000 m deep aerosol layer is introduced. For lower aerosol boundary layer (higher concentration of aerosols in the low atmosphere), as a representation of a pollution event in winter time, the heating in this layer increases, especially in the UV-vis band: it increases of 55% in the SIR band and 100% in the UV-Vis band. The aerosol absorption becomes significant compared to the SIR band: the heating rate in the UV-vis band is now approximately 30% of the heating rate in the SIR band. During the fog dissipation, considering the BC concentration in the cloud droplets modifies sensitively the distribution of heating rate in the vertical. The total heating rate increases at the top of the cloud layer of 7.3 °C/day for BC volume fraction in cloud droplets of $8.6 \cdot 10^{-6}$ and of 15.8 °C/day for a BC volume fraction in cloud droplets of $1.6 \cdot 10^{-4}$. Even if this effect is rather low with a BC concentration fraction in cloud droplets of $8.6 \cdot 10^{-6}$, it might be major for more persistent clouds or fog in low atmosphere. Concerning the impact of the cloud microphysics on solar heating, it seems that a constant value for the effective radii of the cloud droplet is a good approximation if the mean value retained is well adapted for the type of cloud simulated. In our simulations, taking the maximum overlapping instead of the random overlapping assumption for cloud fraction has a very low impact, the cloud fraction being close to 1 when the fog/stratus water content is significant. In that case, the random overlapping assumption has the advantage to be more economic in computer cost. Lastly, in order to save computational cost in solar radiation calculations, neglecting the solar heating in the UV-vis band in the lower part of the atmosphere is indeed a good first approximation as underlined by the work of LH74 if aerosols and clouds are correctly considered in the estimation of downward solar fluxes at the ground surface.

5.2.6 Appendix

5.2.6.1 Optical characteristics of aerosols and clouds

Both cloud droplets and aerosols induce scattering. They are characterized by their optical properties, their optical thicknesses τ_c and τ_a , their SSA ω_c and ω_a and their asymmetry factor g_c and g_a .

For clouds, the optical parameters τ_c , ω_c , g_c depend on the equivalent cloud droplet's radius r_e (in μm) following Stephens [1984]:

$$\tau_c = \frac{3 Lwc}{2 r_e} \quad (5.5)$$

where Lwc is the liquid water content in g m^{-2} .

Following Nielsen et al. [2014], the expression of ω_c and g_c are wavelength dependent. They are defined for the SIR band and for the UV-vis band separately. The integration over wavelengths for the UV-vis and SIR bands is done by weighting each wavelength band $\Delta\lambda_i$ with the radiance energy $E_{(\Delta\lambda_i)}$ in the band following Tsay et al. [1989], Chou [1992], Al Asmar et al. [2021a]:

$$\omega_c = \frac{\sum_{i=1}^{\alpha} \omega_{\Delta\lambda_i} E_{(\Delta\lambda_i)}}{\sum_{i=1}^{\alpha} E_{(\Delta\lambda_i)}} \quad (5.6)$$

$$g_c = \frac{\sum_{i=1}^{\alpha} \omega_{\Delta\lambda_i} g_{\Delta\lambda_i} E_{(\Delta\lambda_i)}}{\sum_{i=1}^{\alpha} \omega_{\Delta\lambda_i} E_{(\Delta\lambda_i)}} \quad (5.7)$$

where $\Delta\lambda$ represents the wavelength difference of each spectral band of the UV-vis or the SIR domain. The UV-vis domain is divided into $\alpha = 2$ spectral bands: 250-440 nm; 440-690 nm (represented by the indicator 'i'). The near SIR domain is also divided into $\alpha = 2$ spectral bands: 690-1190 nm; 1190-2380 nm (represented by the indicator 'i').

The SSA ω_c as calculated above is used in the case where BC concentration is neglected in the cloud droplet (volume fraction of BC in cloud droplet is lower than 1.10^{-8}). In the other case, BC concentration is taken into account following [Chuang et al. \[2002\]](#). They developed a parametrization to calculate the SSA in function of the mean cloud droplet diameter and the volume fraction of BC in the cloud droplet. It is defined for different spectral bands by the following expression:

$$\bar{\omega}(\nu_d, d_o) = \bar{\omega}_c + \beta_1(1 - e^{-\beta_3(\nu_d - \nu_o)}) + \beta_2(1 - e^{-\beta_4(\nu_d - \nu_o)}) \quad (5.8)$$

For a cloud droplet diameter $d_o = 20 \mu\text{m}$, the droplet volume BC fraction ν_d is $\nu_o = 10^{-8}$ and $\bar{\omega}_c = 1 - \omega_c$, the single scattering co-albedo without BC. β_i coefficients and $\bar{\omega}_c$ are given in [Chuang et al. \[2002\]](#) for different spectral bands. The dependence on droplet diameter d is approximated by:

$$\bar{\omega}(\nu_d, d) = \frac{\frac{d}{d_o} \bar{\omega}(\nu_d, d_o)}{1 + 1.8 \bar{\omega}(\nu_d, d_o) \left(\frac{d}{d_o} - 1\right)} \quad (5.9)$$

The integration over both UV-vis and SIR bands is made by weighting the resulting SSA with the radiance energy contained in each band.

For aerosols, the AOD, SSA and asymmetry factors given at a specific wavelength are integrated over the UV-vis and SIR bands. For this specific case, they are constant in time and taken from the AERONET database.

5.2.6.2 Estimation of solar radiation

Solar radiation in the SIR band For water droplets, the multiple diffusion processes are directly modelled using the adding method with a k-distribution method for overlapping between liquid and vapour water absorption (LH74).

For each cloud layer l in the frequency interval n , the optical thickness $\tau_{l,n}$, the single scattering albedo $\omega_{l,n}$ and the asymmetry factor g are:

$$\tau'_{l,n} = \tau_c + \tau_a + k_n u_{wv} \quad (5.10)$$

$$\omega'_{l,n} = (\omega_c \tau_c + \omega_a \tau_a) / \tau'_{l,n} \quad (5.11)$$

$$g' = (\omega_c \tau_c g_c + \omega_a \tau_a g_a) / (\omega'_{l,n} \tau'_{l,n}) \quad (5.12)$$

where $u_{wv}(z, z') = \int_{z'}^z \rho_{h2o}(z'') \left(\frac{P(z'')}{P_0} \right) \sqrt{\frac{T_0}{T(z'')}}^m dz''$ with $m=1$ as suggested by LH74.

Joseph and Wiscombe [1976] corrections are used in order to describe highly forward scattering for cloud droplets and aerosols.

That gives with $f=g'^2$ [Stephens, 1984]:

$$\tau_{l,n} = \tau'_{l,n}(1 - f\omega'_{l,n}) \quad (5.13)$$

$$\omega_{l,n} = \omega'_{l,n}(1 - f)/(1 - f\omega'_{l,n}) \quad (5.14)$$

$$g = (g' - f)/(1 - f) \quad (5.15)$$

The transmission and reflection functions used in the adding method for the two-stream approximation for the solar global radiation are described by Meador and Weaver [1980].

$$R_l = \frac{\gamma_2(e^{k\tau} - e^{-k\tau})}{(k + \gamma_1)e^{k\tau} + (k - \gamma_1)e^{-k\tau}} \quad (5.16)$$

$$T_l = \frac{2k}{(k + \gamma_1)e^{k\tau} + (k - \gamma_1)e^{-k\tau}} \quad (5.17)$$

with $\tau = \tau_{l,n}$ and $k = (\gamma_1^2 - \gamma_2^2)^{1/2}$. The values γ_1 and γ_2 depend on the two-stream approximation used:

Standard Eddington approximation (SEA, [Eddington, 1916, Meador and Weaver, 1980])

$$\gamma_1 = 1/4(7 - \omega_{l,n}(4 + 3g)) \quad (5.18)$$

$$\gamma_2 = -1/4(1 - \omega_{l,n}(4 - 3g)) \quad (5.19)$$

Two-stream quadrature approximation [Meador and Weaver, 1980]

$$\gamma_1 = 3^{1/2}(1 - \omega_{l,n}(1 + g)/2) \quad (5.20)$$

$$\gamma_2 = 3^{1/2}\omega_{l,n}(1 - g)/2 \quad (5.21)$$

With the corrections of Joseph and Wiscombe [1976] these approximations are often called δ two-stream or δ -Eddington [?]. The transmission function for direct solar radiation is $T_l = \exp(-m(\tau_a + k_n u_{wv}))$ for the clear-sky layers and for the cloudy layers, $T_l = \exp(-m(\tau_a + \tau_c + k_n u_{wv}))$ where m is the optical air mass following Kasten and Young [1989]:

$$m = 1/(\mu_0 + 0.50572(96.07995 - (180/\pi) \times \text{acos}(\mu_0))^{-1.6364}) \quad (5.22)$$

where μ_0 is the azimuth angle. When the random overlapping assumption is considered for cloudiness, the reflection and transmission functions are weighted by cloud fraction Cf_l , as suggested by Morcrette and Fouquart [1986]: $T_l = Cf_l T_l^c + (1 - Cf_l) T_l^{nc}$ and $R_l = Cf_l R_l^c + (1 - Cf_l) R_l^{nc}$

To determine absorption in each vertical layer, the adding method is applied as described in LH74 and summarized below. It considers a discrete probability distribution of water vapour absorption coefficients, as described in Table A.4.

$k_n, n \in [1,8]$	$4 \cdot 10^{-6}$	$2 \cdot 10^{-6}$	0.0035	0.0377	0.195	0.94	4.46	19
$p(k_n)$	0.6470	0.0698	0.1443	0.0584	0.0335	0.0225	0.0158	0.0087

These coefficients are determined in order to have:

$$A_{wv}(y) = \frac{0.29}{(1 + 14.15y)^{0.635} + 0.5925y} \quad (5.23)$$

for $y=u_{wv}$ in kg m^{-2} .

The layer transmission and reflection functions going down and going up are added. The upward and downward global fluxes boundary between the layers 1,l and l, L+1 are determined by (the level L corresponds to the ground level):

for global radiation:

$$U_l = \frac{T_{1,l}R_{L+1,l}}{1 - R_{1,l}^*R_{L+1,l+1}}; D_l = \frac{T_{1,l}}{1 - R_{1,l}^*R_{L+1,l+1}} \quad (5.24)$$

for direct radiation :

$$U_l^d = 0; D_l^d = T_{1,l} \quad (5.25)$$

with $T_{1,1} = \exp(-mu_{wv}(11000, \infty))$ and $R_{1,1} = 0$ as an upper boundary condition for both global and direct radiations in order to take into account the absorption by water vapour above 11000 m and $R_{L+1}=R_g$ and $T_{L+1} = 0$ at the ground surface where R_g is the ground albedo. The fraction of the total incident flux absorbed in the upper composite layer is:

$$A_{1,l}(n) = p(k_n)[(1 - R_{1,L+1}(n)) + U_l(n) - D_l(n)] \quad (5.26)$$

and the total absorption in each layer l is found by differencing:

$$A_l(n) = A_{1,l}(n) - A_{1,l-1}(n) \quad (5.27)$$

The total absorption F_{abs}^{SIR} and the fluxes $F \downarrow_g^{SIR}$ (global downward), $F \uparrow_g^{SIR}$ (global upward), and direct downward $F \downarrow_d^{SIR}$ in each layer l are found by summing over the values of n:

$$F_{abs}^{SIR} = \mu_0 F \sum_{n=2}^{n=8} A_l(n), \quad (5.28)$$

$$F \downarrow_g^{SIR} = \mu_0 F \sum_{n=2}^{n=8} D_l(n)p(k_n), \quad (5.29)$$

$$F \uparrow_g^{SIR} = \mu_0 F \sum_{n=2}^{n=8} U_l(n)p(k_n), \quad (5.30)$$

$$F \downarrow_d^{SIR} = \mu_0 F \sum_{n=2}^{n=8} D_l^d(n)p(k_n) \quad (5.31)$$

Note that in this adding method for a homogeneous cloud or aerosol layer: $R_l^* = R_l$ and $T_l^* = T_l$ where the asterisk indicates illumination from below.

In the case where cloud fraction is taken into account with maximum overlapping, the adding method has to be done for cloudy atmosphere (c) and for atmosphere without clouds (nc) but with aerosols (in that case $\tau_c = 0$). The fluxes and the heating rate are weighted by the maximum of the cloud fraction C_f^{max} encountered between ∞ and the ground level L.

Solar radiation in the UV-vis band The multiple diffusion processes are directly modelled with the adding method but without the k-distribution method for ozone absorption, as it is relevant only in the upper layers of the atmosphere. Nevertheless, ozone absorption is taken into account after the adding method computation by adding its contribution to heating rate. The same adding method procedure as water vapour is applied, but by keeping only cloud and aerosol optical depth in the transmission and reflection functions. In that case, the boundary conditions at the top of the aerosol/cloud layer are: $T_{1,1} = 1$; $R_{1,1} = 0$ and at the ground $T_{L+1} = 0$; $R_{L+1} = R_g$.

The total absorption only due to aerosols and clouds in each layer l is found as for water vapour by:

$$F_{abs}^{UV-vis} = \mu_0 F (0.647 - A_{O_3}(x) - R_r(\mu_0)) (A_{1,l} - A_{1,l-1}) \quad (5.32)$$

The downward flux for global and direct radiation and the upward diffuse flux at the ground surface as described in Al Asmar et al. [2021a] are:

$$F \downarrow_g^{UV-vis} = \mu_0 F (0.647 - A_{O_3}(x) - R_r(\mu_0)) D_l \quad (5.33)$$

$$F \downarrow_d^{UV-vis} = \mu_0 F (0.647 - A_{O_3}(x) - R_r(\mu_0)) D_l^d \quad (5.34)$$

$$F \uparrow_g^{UV-vis} = \mu_0 F (0.647 - A_{O_3}(x) - R_r(\mu_0)) U_l \quad (5.35)$$

where A_{O_3} is the ozone absorption and $R_r(\mu_0) = 0.28 / (1 + 6.43\mu_0)$ the Rayleigh atmospheric albedo. A_{O_3} is parameterized as LH74 for both Chappuis and ultraviolet bands:

$$A_{O_3} = \frac{0.02118x}{1 + 0.042x + 0.000323x^2} + \frac{1.082x}{(1 + 138.6x)^{0.805}} + \frac{0.0658x}{1 + (103.6x)^3} \quad (5.36)$$

where $x = u_{O_3}(z)$ is the ozone amount in cm STP above the altitude z given by the well-known analytical function of Green (1964) $u_{O_3} = a(1 + \exp(-b/c)) / (1 + \exp((z-b)/c))$ with $a=0.4$ cm STP, $b=20$ km and $c=5$ km.

In the clear sky layers above the aerosol/cloud layers, the irradiances are computed as LH74 making the hypothesis of a pure absorbing layer on the top of a reflecting region. With this approximation, the solar heating rate due to ozone in the layer (l, l+1) is (LH74):

Above the aerosol layer when there is no cloud (nc)

$$F_{abs}^{UV-vis,nc} = \mu_0 F [A_{O_3}(x_{l+1}) - A_{O_3}(x_l - \bar{R}_a^{nc} A_{O_3}(x_{l+1}^* - A_{O_3}(x_l^*)))] \quad (5.37)$$

With $x = \mu_{O3}(\infty, z)$, $x^* = \mu_{O3}(\infty, 0) + \bar{m}(u_{O3}(\infty, 0) - u_{O3}(\infty, z))$ where $\bar{m} = 1.9$ is the optical air mass for diffuse irradiance.

R_a^{nc} is the composite albedo including aerosol diffusion effect and ground reflectivity,

$$R_a^{nc} = \bar{R}_a + \bar{T}_a R_g \bar{T}_a^* / (1 - \bar{R}_a^* R_g) \quad (5.38)$$

where \bar{T}_a and \bar{R}_a are calculated with equations (5.17) and (5.16) for the total optical aerosol depth τ_a^{tot} .

Above the aerosol/cloud layer in cloudy conditions (c):

$$F_{abs}^{UV-vis,c} = \mu_0 F [A_{o3}(x_{l+1} - A_{o3}(x_l - \bar{R}_c^c A_{o3}(x_{l+1}^* - A_{o3}(x_l^*)))] \quad (5.39)$$

R_c^c is determined as R_c^{nc} with equations (5.17) and (5.16) but for the total optical cloud depth τ_c^{tot}

$$R_c^c = \bar{R}_c + \bar{T}_c R_g \bar{T}_c^* / (1 - \bar{R}_c^* R_g) \quad (5.40)$$

The global and direct downward irradiances are equal for both cloud and no cloud situations:

$$F \downarrow_g^{UV-vis} = F \downarrow_u^{UV-vis} = \mu_0 F (0.647 - A_{o3}(x) - R_r(\mu_0)) \quad (5.41)$$

The upward irradiance:

$$F \uparrow_g^{UV-vis,nc} = \mu_0 F (0.647 - A_{o3}(x) - R_r(\mu_0)) (\bar{R}_a + U_{top}) \quad (5.42)$$

$$F \uparrow_g^{UV-vis,c} = \mu_0 F (0.647 - A_{o3}(x) - R_r(\mu_0)) (\bar{R}_c + U_{top}) \quad (5.43)$$

where U_{top} is the fraction of the upward flux at the top of the aerosol/cloud layer coming from the reflection by the earth surface through the aerosol/cloud layers. When maximum overlapping assumption is made for cloud fraction, as for SIR band, the fluxes and the heating rate are weighted by the maximum of the cloud fraction $C f^{max}$.

$$F \downarrow_g^{UV-vis} = C f^{max} F^c \downarrow_g^{UV-vis} + (1 - C f^{max}) F^{nc} \downarrow_g^{UV-vis} \quad (5.44)$$

$$F \downarrow_d^{UV-vis} = C f^{max} F^c \downarrow_d^{UV-vis} + (1 - C f^{max}) F^{nc} \downarrow_d^{UV-vis} \quad (5.45)$$

$$F \uparrow_g^{UV-vis} = C f^{max} F^c \uparrow_g^{UV-vis} + (1 - C f^{max}) F^{nc} \uparrow_g^{UV-vis} \quad (5.46)$$

$$F_{abs}^{UV-vis} = C f^{max} F_{abs}^{UV-vis,c} + (1 - C f^{max}) F_{abs}^{UV-vis,nc} \quad (5.47)$$

Total solar radiation The fluxes for global and direct radiations are the sum of the contribution of both UV-vis and SIR bands but multiplied by T_{mg} in order to consider the absorption by minor gases. The general transmittance function, T_i , for five minor atmospheric gases (CO_2 , CO , N_2O , CH_4 and O_2) is expressed by the following equation [Psiloglou et al., 2000]:

$$T_i = 1 - amu_i / ((1 + bmu_i)^c + dmu_i) \quad (5.48)$$

where m is the optical air mass, a , b , c , d are numerical coefficients that are given in the table given by Psiloglou et al. [2000].

The broadband transmittance function due to the total absorption by the uniformly mixed gases is then calculated by:

$$T_{mg} = T_{\text{CO}_2} T_{\text{CO}} T_{\text{N}_2\text{O}} T_{\text{CH}_4} T_{\text{O}_2} \quad (5.49)$$

The downward fluxes are equal to:

Global radiation

$$F \downarrow_g = T_{mg} (F \downarrow_g^{UV-vis} + F \downarrow_g^{SIR}) \quad (5.50)$$

Direct radiation

$$F \downarrow_d = T_{mg} (F \downarrow_d^{UV-vis} + F \downarrow_d^{SIR}) \quad (5.51)$$

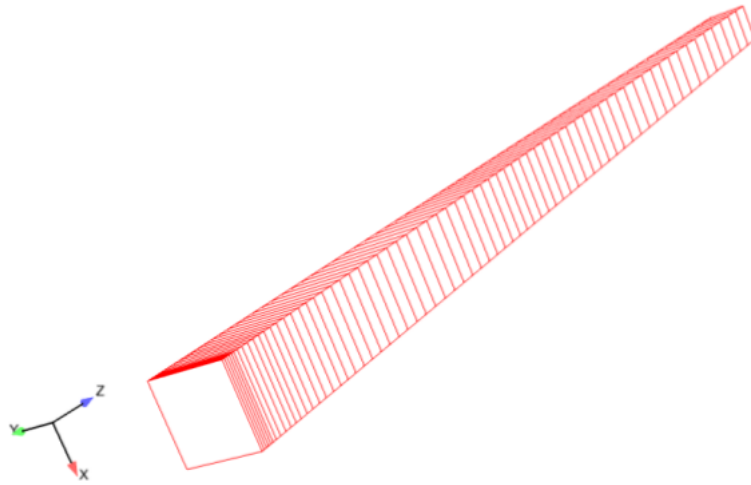


Figure 5.8: The simulated domain for the case ParisFog [Makké, 2015]

5.3 Complementary notes

As the simulated domain along with the detailed calculation of the BC fraction in cloud droplets are not presented in LA21-2, they are described in the following section.

5.3.1 The domain of the simulation

The simulated domain (figure 5.8) is a vertical column of 1 km x 1 km x 11 km with 78 cells logarithmic dispatched on the vertical, the first level above the ground surface is at 2 m height, and it goes up to 11 000 m.

The configuration of the simulation as well as the meteorological data used as input are detailed in LA21-2, XZ14 and in Makké [2015] and the simulation time-step is of 1 min.

5.3.2 Calculation of the Black Carbon Fraction in cloud droplets

BC or soot aerosols are generated from the incomplete combustion of fossil fuel and biomass burning. By serving as cloud condensation nuclei or becoming outside attachments to water droplets, they modify the SSA of clouds and play an important role in cloud absorption of solar irradiance. They are often neglected in SSA calculations (section 2.3.2.4) but, as we were interested to see how BC particles in cloud droplets would affect the fog dissipation, we used Chuang et al. [2002] parametrization of SSA that is dependent on the BC fraction, cloud droplet radii and the wavelength. As we didn't have Polyphemus simulations for the 18-19/02/2007 to provide information about BC, we needed to estimate the BC fraction in aerosols that served as condensation nuclei for the nucleation process. The Abdul-Razzak et al. [1998],

Composition	Sulfate	Nitrate	Soot	Organic
Percentage (%)	25	20	16.4	38.6

Table 5.2: Aerosol chemical composition, percentage representing the mass fraction of each compound contained in the aerosol (XZ14).

Abdul-Razzak and Ghan [2000] nucleation scheme is used in the Parisfog simulation to characterize aerosols. In this scheme, it is essentially the coarse mode particles that served as condensation nuclei. The aerosols size distribution follows a log normal distribution which standard deviation is σ_a , the number of particles is N_a and the dry radius is R_a . The OPC Wallace 200 instrument provided the number of cloud droplets. From table 5.1, for the coarse mode, the dry radius R_a is equal to $0.4 \mu\text{m}$, which gives us information about the dry diameter. From table 5.2, there is 16.4 % of soot in aerosols. It is the mass percentage measured by filters. If we assume that the density is constant and equal to 1.77×10^3 , we can consider that the volume fraction of BC in the dry aerosol is equal to its fractional mass: 0.164. Let's note that in literature, the BC density varies from 1.0×10^3 to 2.0×10^3 depending on the forming process of BC [Chýle et al., 1996]. If we assume that the dry aerosol radii is equal to $0.4 \mu\text{m}$ and that the fog cloud radii after nucleation is equal to $4 \mu\text{m}$, the volume BC fraction would be equal to $0.164 (\text{rad}/\text{rg})^3$ which gives $\nu_d = 1.6 \times 10^{-4}$. This hypothesis overestimate the BC fraction because we have to consider the wet radii in the estimation of the ν_d . Taking into consideration that the wet radii R_{aw} depends on the atmosphere humidity, following Zieger et al. [2010]:

$$\frac{R_{aw}}{R_a} = \left(1 + \kappa \frac{RH}{1 - RH}\right)^{\frac{1}{3}} \quad (5.52)$$

where κ is a coefficient representing the hygroscopy of aerosols and RH the ambient relative humidity. In this approach the Kelvin effect is neglected, but it is a good approximation for radii greater than $0.1 \mu\text{m}$. If we consider that, after nucleation, the radii of fog droplets contains 95 % of humidity then, it gives $\nu_d = \frac{1.610^{-4}}{19} = 8.6 \times 10^{-6}$. Both volume fraction of BC (1.6×10^{-4} and 8.6×10^{-6}) calculated are tested in our simulation and detailed in LA21-2 .

5.4 Summary

This chapter focused on the calculation of radiation fluxes and heating rates on the vertical and at the surface using the *multi-layered* method. The calculations of flux divergence on the vertical allowed us to better understand the contribution of aerosols to fog evolution, and results are presented in LA21-2. The *multi-layered 1D* radiative scheme is also useful for the *3D* radiative scheme that will be presented in the next chapter.

Chapter 6

General conclusion

This chapter concludes this thesis and presents the results in terms of the three objectives presented in chapter 1 before presenting some future prospects.

Contents

6.1 Overview on the chapters	120
6.2 Future prospects	122
6.3 Implementation of a 3D radiative scheme in code_saturne	123
6.3.1 Introduction	123
6.3.2 Resolution of the RTE in code_saturne 3D radiative model	124
6.3.3 Calculation of the absorption coefficients from the 1D model	127
6.3.4 Comparison 1D/3D	130
6.3.5 Work in progress	130
6.3.6 Conclusion	132

6.1 Overview on the chapters

Life on earth depends on energies; it is essential for economic and social development, however it poses an environmental challenge as it often increases the carbon footprint. Things need to change to avoid the catastrophic impact that climate change could have. Hence, renewable energies are a good alternative to reduce the emissions of greenhouse gases, moreover, they are promising solutions in many places where no other resources are possible, to allow the access to reliable and affordable energy. The work of this thesis lies in this general context and focuses on the development of solar energies. The different chapters are summarized here.

As mentioned in chapter 1, the sector of solar energies is expected to grow in the coming years and, in order to optimize the performance of PV farms, an accurate estimation of the amount of surface solar irradiance is necessary. As detailed in chapter 2, the sun produces a huge amount of energy, its electromagnetic spectrum spans in a range of wavelengths from gamma and x-rays, to ultraviolet (UV), visible, infrared (IR), and radio waves. We are then interested in short wave radiation ranging from the UV, visible to the near infrared (SIR) wavelength that Earth's atmosphere allows reaching the ground. As radiation gets closer to

the Earth's surface, it interacts with different atmospheric components like gas, molecules, aerosols and clouds and gets attenuated through different physical processes: on average half of extra terrestrial irradiance reaches the ground. In particular, ozone is responsible for most absorption at high altitudes in the [UV-vis](#) spectral band and water vapour absorbs solar flux in the troposphere in the [SIR](#) band. Furthermore, clouds are known to have a huge influence on solar radiation that reaches the ground. A wide variety of cloud types, structures and distributions exist and their three-dimensional characteristics as well as their high spatio-temporal variability makes it quite complicated to model the solar radiation transfer through them. In order to have a better understanding of the atmosphere processes and constituents, in-situ and remote sensing measurement techniques were developed and are also used to estimate the surface solar irradiance. Nevertheless, they aren't deployed everywhere on earth and often not for long periods, in consequences, numerical models are necessary for the estimation of the solar resource. These models can be based on statistical equations, satellite images or on the resolution of the [Radiative Transfer Equation \(RTE\)](#), the mathematical description of the propagation of radiation through a medium. An overview of some models is presented in chapter 3. This thesis focused on the use of the radiative model of the [CFD](#) code `code_saturne`, in its [1D](#) and [3D](#) versions, and was centred around three objectives:

Objective 1: *Improvement of the [1D](#) integral radiation model in a cloudy atmosphere using measurements and verification of its robustness on a long period.*

In the studies conducted in chapter 4, the integral method of the [1D](#) radiative model of `code_saturne` is used in order to estimate surface solar irradiance. In this method, the atmosphere is assumed to be made of one homogeneous layer with optical properties of atmospheric components integrated over the vertical axis. Special attention is given to the use of in-situ and remote sensing measurements: they allow us, on one hand, to improve the model, and on the other hand, to conduct sensitivity tests on the extracted cloud optical properties. We showed that, global irradiance modelling is improved by using measurements of [Cloud Optical Depth \(COD\)](#) only and measurements of cloud fraction are useful if the [COD](#) is well estimated. For the estimation of cloud fraction, pyranometers or sky imager measurements were more accurate than [LIDAR](#) or satellite measurements in our case. Moreover, an analytical model is developed to estimate the [COD](#) from [Liquid Water Path \(LWP\)](#) measurements only, and we showed that it is a good-enough proxy. Simulations ran on a period of a year in order to test the robustness of the model through different seasons. Satisfactory results were obtained and validated through on site measurements and comparison to the HelioSat model; the direct component was particularly well modelled, which is important for many solar energy applications. However, some discrepancies between model and measurements were detected and analysed to physically understand the cause of the persistent biases. No particular type of cloud specifically impacted the results. However, the error increased with the cloud fraction, which influenced more the direct component. Moreover, we show that the bias could be related to the fluctuations of the measurements at a timescale shorter than 1 hour, used as input to the model or for comparison purposes.

Objective 2: *Modelling the vertical profile of flux divergence using the [1D](#) multi-layered model and taking into account the contribution of aerosols to a fog evolution through their influence on*

solar radiation

In chapter 5, the multi-layered method of the 1D radiative model of code_saturne is used to estimate the vertical profiles of the downward and upward fluxes as well as the flux divergence. In this method, the atmosphere is assumed to be made of several homogeneous layers, each having its own optical properties. It is applied to a case of a radiative fog that evolves into a low stratus cloud. Different sensitivity tests are conducted in order to study the effect of aerosols and black carbon in cloud droplets on the dissipation of the fog. We showed that their impact is important on the heating rate in both spectral bands (UV-vis and SIR) as they can increase or decrease the heating in the layer and on fog dissipation. The contribution of the UV-vis band, where the absorption is mostly from ozone and usually considered as small in the lower atmosphere, becomes relatively important for high aerosols and BC concentration. Moreover, the effect of cloud droplet radius and the assumption taken for the cloud fraction is investigated, and we showed that taking a constant cloud droplet radius was a good approximation and the change in cloud fraction assumption had a very low impact in our case. Lastly, we showed that a simpler parametrization, the integral method applied to the UV-vis band, is indeed a good first approximation for the estimation of surface solar irradiances. However, the calculations on the vertical allowed us to better understand the effect of aerosols and particles and, more generally, is useful for applications in which the estimation of the heating rate of atmospheric layers has to be calculated.

6.2 Future prospects

Here are some suggestions for future research based on the work done in this thesis:

For the first study (presented in chapter 4), we may consider testing the model for the year 2014 using satellite measurements for the COPs which is expected to improve the comparison to the in-situ measurements and to the HelioClim database. Moreover, we could develop a more accurate model to calculate the COD from LWP measurements based on different intervals of LWP. The time-step of the simulation and measurements used as input might be reduced in order to have more accurate results. We may also consider running the simulation on different sites in order to test the robustness of the model.

For the second study (presented in chapter 5), we could try to use a more accurate distribution of aerosols on the vertical. Moreover, it would be good to evaluate the contribution of Black Carbon (BC) to fog dissipation with a more precise calculation of the BC fraction in cloud droplets.

Finally, as the objective of this thesis is the optimization of PV, it would be interesting to apply it to a case study of a PV farm taking advantage of the capacities offered by a CFD code. Thus, CFD simulations, coupling between radiative, dynamic and thermal processes, could allow estimating more accurately the energy production of the farm taking into account some important factors like panels temperature. Application to concentrated solar power could also be interesting, as it has been shown that the modelling presented in this thesis has the ability to improve the estimation of the direct component of the radiative flux.

In order to do so, we would need 3D modelling of irradiance that constitutes the last objective of this thesis, **Objective 3: Development of the 3D model and comparison to the 1D model in horizontal homogeneous conditions**. It is presented in section 6.3 where the model is described and comparisons to the 1D model are conducted. We first present the results under clear-sky conditions when only the absorption by ozone or water vapour is considered. Afterwards, we present the results when aerosols and clouds are taken into account. It is still a work in progress and preliminary results are good but yet to be validated.

6.3 Implementation of a 3D radiative scheme in code_saturne

6.3.1 Introduction

This section aims at developing the following objective of the thesis:

Objective 3: Development of the 3D model and comparison to the 1D model in horizontal homogeneous conditions

When studying atmospheric radiation, the question arises to adopt 1D or 3D approach to compute radiative transfers. An equilibrium between requirements, accuracy, and computer cost should be found. As mentioned earlier, for a better description of clouds and in order to consider the so-called 3D effect, 3D solving of the RTE is necessary. Moreover, for solar energy applications in urban zones with numerous obstacles like buildings, trees, ... the shadowing can decrease the amount of solar radiation. Indeed, when certain PV systems don't receive homogeneous incident radiation level, the cells having less irradiance absorb power instead of producing it [Veerapen and Huiqing, 2016]. In order to take into account the shadowing effect, a 3D approach may seem adequate to compute the radiative transfer.

For both infra-red and solar spectrum, various methods were developed to solve the RTE in a 3D medium. As detailed in section 3.4 the Monte-Carlo (MC) method for angular integration is a method commonly used for solar radiation. However, despite its accuracy, computational cost is expensive and interaction of radiation with the atmosphere is difficult to model using this method. In the aim of finding a good compromise between accuracy and computing cost in 3D simulations, Makké [2015] proposed to use the Discrete Ordinate Method for Radiative Transfer (DISORT) to solve the angular integration coupled with broadband emissivity for integration over wavelength for IR radiation. The advantages of this method include a reduced computational time and are largely discussed in Milliez [2006], Makké [2015]. A similar approach was then applied for solar radiation, for which it is simpler to solve the RTE because, in the solar domain, there is no proper emission in the atmospheric layers and the radiation source (the sun) is external to the atmosphere. This method consists in resolving the RTE using a DISORT method for a non-scattering medium and combining it with equivalent absorption coefficients taken from the 1D upward and downward fluxes. It does not allow treating diffusion processes, but some approximations can be used in order to take into account Rayleigh diffusion and eventually clouds extinction.

In code_saturne v-3, this method was used for the resolution of the 3D RTE in the solar domain without considering the effects of clouds and aerosols. However, code_saturne evolved from v-3 to v-7 and many changes were brought to the solver and to the radiative model as detailed earlier. The goal of this section is the integration of the 3D resolution of the RTE in

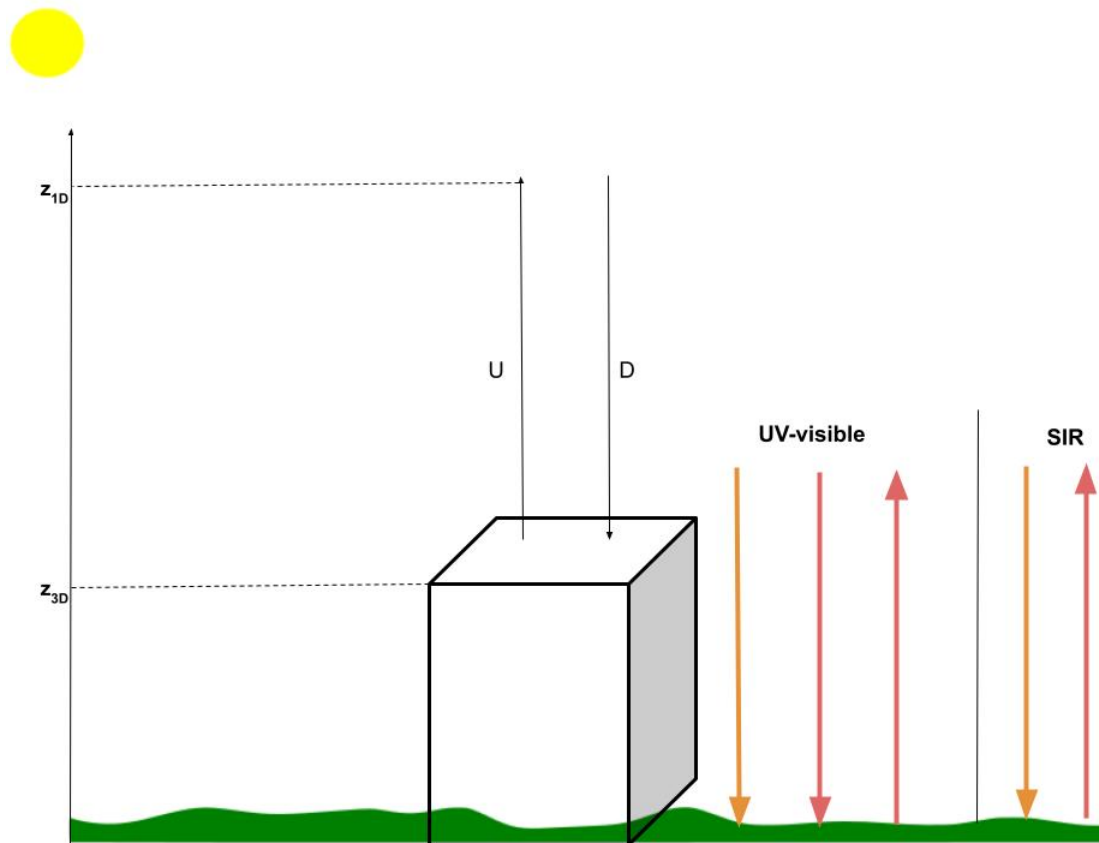


Figure 6.1: Schematic representation of the resolution of the RTE in code_saturne for a clear-sky atmosphere without aerosols or clouds. z_{1D} and z_{3D} are the altitudes until which the 1D and 3D equations are solved. U and D are, respectively, the upward and downward fluxes of the 1D model. The direct (—) and diffuse (—) components for both the UV-vis and SIR band are represented.

code_saturne v-7 and to provide comparisons with the 1D model. This section is organized as follows: the equations used for code_saturne 3D radiative scheme are presented in section 6.3.2, comparisons with the 1D model are presented in section 6.3.4 and the work in progress in section 6.3.5 before concluding in section 6.3.6.

6.3.2 Resolution of the RTE in code_saturne 3D radiative model

Figure 6.1 schematically represents the resolution of the RTE in code_saturne 3D radiative model: at first, the 1D calculation for the radiation fluxes runs using the multiple layered approach. From this resolution, the values of upward and downward radiation for each band and each component at z_{3D} (the altitude of the 3D domain) are stored and are then used for the top boundary conditions of the 3D model. Furthermore, the absorption coefficients for water vapour, ozone, aerosols and clouds are calculated. Then, the 3D model runs and uses

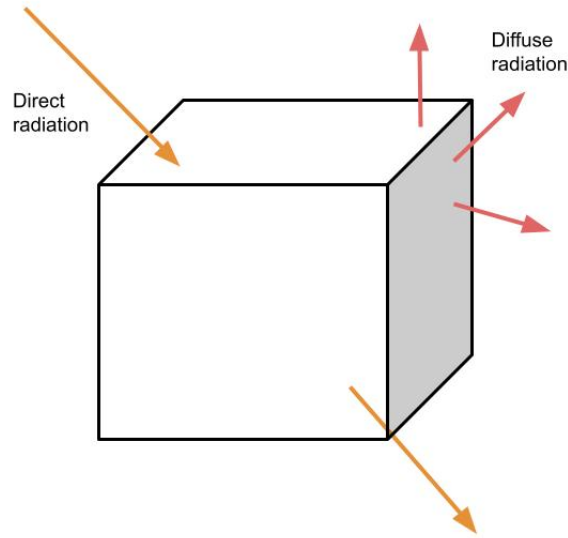


Figure 6.2: Schematic representation of the direct (—) and diffuse (—) radiation around one mesh cell of the 3D domain.

the stored values from the 1D model for top boundary conditions and periodic conditions at the side. The direct and diffuse radiation now have a direction (as shown in figure 6.2) and a DISORT model is used for the spatial and angular integration of the radiance in each 3D mesh cell. At the earth's surface, the irradiance fluxes are calculated from the radiance. As in the 1D model, the resolution is done for both the UV-vis and SIR band and for the upward and downward directions.

The spatial and angular integration of the RTE in a 3D domain are detailed in this section, as well as the boundary conditions, the calculation of the heating rate and the absorption coefficients from the 1D model for both clear-sky and cloudy-sky conditions.

Spatial and angular integration of the RTE in the 3D domain Equation 3.57 is solved in the 3D radiation scheme of code_saturne using the grey approximation. The grey approximation method is a simplification that considers that the absorption coefficient of matter in the atmosphere is constant on the wavelength of radiation. A spectral and angular integration are conducted on the RTE to solve it in order to have the radiative field at every point of the domain and to consider the variation of radiance's direction. The DISORT method is used for angular integration with a S_4 quadrature (24 directions). The spatial integration of the RTE is done using the finite volume method for the resolution of the Navier-Stokes equations: the discretization points of the RTE corresponds to the centre of the cell. Let's consider a control volume V_i occupied by a cell i and in which all variables are assumed to be constant. The integration of the RTE along the direction of the control volume V_i can be written:

$$\int_{V_i} (\mathbf{\Omega}_k \cdot \nabla) I_k(s, \mathbf{\Omega}_k) dV_i = \int_{V_i} -k(r) I_k(s, \mathbf{\Omega}_k) dV_i \quad (6.1)$$

Using the Green-Ostrogradski flux divergence theorem that relates the flux of a vector field through a closed surface to the divergence of the field in the volume enclosed, we can write:

$$\int_{S_i} I_k(s, \mathbf{\Omega}_k) \mathbf{\Omega}_k \cdot d\mathbf{n} = \int_{V_i} -k(r) I_k(s, \mathbf{\Omega}_k) dV_i \quad (6.2)$$

where $d\mathbf{n}$ is the normal vector to the surface S_i . Let's consider j as the index of the neighbouring volume to V_i , Γ_{ij} the surface between the cells i and j and \mathbf{n}_{ij} the vector normal to Γ_{ij} oriented from the surface i to surface j . By substituting the integral over the surface S_i by a discrete sum on the inner surfaces of the control volume, the RTE in finite volume becomes:

$$\sum_{j \in V_i} I_{ij}^k \mathbf{\Omega}_k \Gamma_{ij} \mathbf{n}_{ij} = |V_i| (-k_i I_i^k) \quad (6.3)$$

where $I^k = I(\mathbf{\Omega}_k)$ is the radiance in the direction $\mathbf{\Omega}_k$ in the volume V_i and I_{ij} is the radiance on the boundary between the volumes V_i and V_j that should be interpolated as a function of the radiance in the centre of each control volume. The upwind scheme is used for the interpolation of the radiance:

$$\mathbf{\Omega}_k \Gamma_{ij} \mathbf{n}_{ij} > 0 \Rightarrow I_{ij}^k = I_i^k \quad (6.4)$$

$$\mathbf{\Omega}_k \Gamma_{ij} \mathbf{n}_{ij} < 0 \Rightarrow I_{ij}^k = I_j^k \quad (6.5)$$

Equation 6.3 leads to a linear system which is solved using an iterative method (like, Gauss-Seidel, Jacobi,...) allowing the calculation of the radiance $I(s, \mathbf{\Omega}_k)$ at the centre of each cell.

Boundary conditions For the 3D simulations the domain is limited to z_{3D} and the top boundary condition for radiance is imposed by the 1D radiative model using:

$$I \downarrow (z_{3D}) = F \downarrow (z_{3D}) / \pi \quad (6.6)$$

Note that the 1D model gives the solution for the irradiance and the 3D model solves the equation for the radiance, the division by π allows us to go from the irradiance to the radiance. In that upper boundary condition, direct and diffuse radiations are treated separately. Direct radiation has a fixed direction in function of solar declination that is taken into account by dividing it by μ_0 and diffuse radiation is supposed to be isotropic (illustrated in figure 6.2). For lateral boundary conditions, the plane parallel assumption leads to set periodic boundary conditions in the x and y directions, which is often implemented for 3D radiative calculations. For simulations at height higher than z_{3D} , the 1D radiation model is used. Moreover, the 1D radiation model is used for the calculations of the absorption coefficients for the UV-vis and SIR bands as described below. Heating rate

The heating rate S_{rad} is deduced from equation 3.57 by:

$$S_{rad}(s) = \int_{4\pi} k(s) I(s, \mathbf{\Omega}) d\Omega \quad (6.7)$$

Its spectral and angular discretization leads to:

$$S_{rad,i} = \sum_{p=1}^{N_{dir}} k_i I_{p,i} \omega_p \quad (6.8)$$

where the subscripts i and p defines the cell and the discrete direction respectively.

6.3.3 Calculation of the absorption coefficients from the 1D model

The purpose of this section is to give an equivalent absorption coefficient for solar radiation that can be used in a 3D solver like code_saturne for the RTE using the DISORT method. We start from the two bands model (one for ozone and the other one for water vapour). For each band the equivalent absorption coefficient is deduced from the analytical absorption coefficient given in LH74. As for IR radiation in Makké [2015], where the expressions for these equivalent absorption coefficients are obtained by matching the upward and downward fluxes, but here by distinguishing direct and diffuse radiation fluxes. Thus, the equivalent absorption coefficients are directly linked to the analytical absorption coefficients used in LH74 to estimate the downward and upward fluxes in both water vapour and ozone band.

From equation 3.9 of a plane-parallel atmosphere applied to a homogeneous medium and using the system:

$$I^\uparrow(z_0, \mu) = I^\uparrow(0, \mu)\tau(0, z, \mu) \quad (6.9)$$

$$I^\downarrow(z_\infty, \mu) = I^\downarrow(z_\infty, \mu)\tau(z_\infty, z, \mu) \quad (6.10)$$

where $\tau(z_1, z_2, \mu)$ is the monochromatic transmissivity between z_1 and z_2 for the cosinus zenith angle μ :

$$\tau(z_1, z_2, \mu) = \exp\left(-\frac{1}{\mu} \int_{z_1}^{z_2} k(z') dz'\right) \quad (6.11)$$

Integration over the solid angle gives:

$$F^\uparrow(z) = 2\pi \int_0^1 I^\uparrow(0, \mu)\tau(0, z, \mu)\mu d\mu \quad (6.12)$$

$$F^\downarrow(z) = 2\pi \int_0^1 I^\downarrow(z_\infty, \mu)\tau(z_\infty, z, \mu)\mu d\mu \quad (6.13)$$

with:

$$I^\uparrow(z, \mu) = \frac{F^\uparrow(0)}{\pi} \quad (6.14)$$

$$I^\downarrow(z, \mu) = I \frac{F^\downarrow(z_\infty)}{\pi} \quad (6.15)$$

Thus,

$$F^\uparrow(z) = 2F^\uparrow(0) \int_0^1 \tau(0, z, \mu)\mu d\mu \quad (6.16)$$

$$F^\downarrow(z) = 2F^\downarrow(z_\infty) \int_0^1 \tau(z_\infty, z, \mu)\mu d\mu \quad (6.17)$$

To obtain the equations for fluxes, an integration over the zenith angle is necessary. The widely used hypothesis of the “diffusivity factor” [Elsasser, 1942] leads to eliminating the zenith angle

dependence in favour of a constant inclination, $\tilde{\mu}$ so that $\tilde{\mu} = 5/3$. It is similar to taking a zenith angle equal to zero, but an optical path expanded by a factor of 5/3. Therefore,

$$\frac{\delta F^\uparrow(z)}{\delta z} = \frac{-5}{3} k^\uparrow(z) F^\uparrow(z, \mu) \quad (6.18)$$

$$\frac{\delta F^\downarrow(z)}{\delta z} = \frac{5}{3} k^\downarrow(z) F^\downarrow(z, \mu) \quad (6.19)$$

Thus, we can calculate $k^\uparrow(z)$ and $k^\downarrow(z)$ from the fluxes and their derivative over z . They are valid for the diffuse components of solar irradiance. However, for the direct component, as the zenith direction is fixed, the “diffusivity factor” is not taken into account.

6.3.3.1 Estimations during clear-sky days of the equivalent absorption coefficient

The following equations are first derived for a clear-sky day without aerosols, then for clear sky with aerosols.

Clear-sky without aerosols As shown in figure 6.1, when only the absorption by gases is considered, in the **SIR** band the diffuse radiation is in the upward direction due to ground isotropic reflection and the direct radiation in the downward direction but in the **UV-vis** band, the diffuse radiation propagates in both the upward and downward directions and the direct radiation is in the downward direction only due to Rayleigh scattering in the **UV-vis** band that contributes in the downward diffuse component, but it is neglected in the **SIR** band. As the mathematical expression for the 1D and 3D are equivalent, the differences can be attributed to the difference of numerical discretization between 1D and 3D.

UV-vis band From equations 6.18 and 6.19 combined, respectively, to equations 4.29 and 4.16 (without the transmission functions for aerosols/ minor gases), we may determine the equivalent absorption coefficients in the **UV-vis** band.

Direct irradiance:

$$k_{UV-Vis, Ir}^\downarrow = \frac{-\frac{\delta A_{UV-Vis}(x^\downarrow(z))}{\delta z}}{(0.647 - R_{ray} - A_{UV-Vis}(x^\downarrow))} \quad (6.20)$$

The different components were defined in the previous chapters.

Diffuse irradiance: The diffuse irradiance is estimated by the difference between global and direct irradiances:

Downward diffuse flux

$$k_{UV-Vis, D}^\downarrow = -\frac{3}{5} \frac{\frac{\delta A_{UV-Vis}(x^\downarrow(z))}{\delta z}}{(0.647 - R_{ray} - A_{UV-Vis}(x^\downarrow))} \quad (6.21)$$

Upward diffuse flux

$$k_{UV-Vis, G}^\uparrow = k_{UV-Vis, D}^\uparrow = \frac{3}{5} \frac{\frac{\delta A_{UV-Vis}(x^\uparrow(z))}{\delta z}}{(0.647 - R_{ray} - A_{UV-Vis}(x^\uparrow))} \quad (6.22)$$

SIR band Similarly, we may determine the equivalent absorption coefficients in the SIR band:

For direct downward irradiance:

$$k_{SIR,Ir}^{\downarrow}(z) = \frac{-\delta A_{SIR}(y^{\downarrow}(z))}{\delta z} \frac{1}{(0.353 - A_{SIR}(y^{\downarrow}))} \quad (6.23)$$

For diffuse upward irradiance:

$$k_{SIR,D}^{\uparrow}(z) = \frac{3}{5} \frac{\delta A_{SIR}(x^{\uparrow}(z))}{\delta x} \frac{1}{(0.353 - A_{SIR}(x^{\uparrow}))} \quad (6.24)$$

Clear-sky with aerosols We are here interested in the case where aerosols are considered. For the direct irradiance, we can inject equation 4.29 for the UV-vis band and equation 4.31 for the SIR band into equation 6.18. Let's first consider the SIR band, after simplifying, we obtain:

$$k_{SIR/a,Ir}^{\downarrow}(z) = k_{SIR,Ir}^{\downarrow}(z) + \frac{\delta T_{a,SIR}}{T_{a,SIR} \delta z} \quad (6.25)$$

with $T_{a,SIR} = e^{-m\tau_{a,SIR}}$ and therefore:

$$k_{SIR/a,Ir}^{\downarrow}(z) = k_{SIR,Ir}^{\downarrow}(z) - m \frac{\delta \tau_{a,SIR}}{\delta z} \quad (6.26)$$

we may define the extinction coefficient for aerosols $k_{a,SIR} = -m \frac{\delta \tau_{a,SIR}}{\delta z}$. Similarly, for the UV-vis band:

$$k_{UV-vis/a,Ir}^{\downarrow}(z) = k_{UV-vis,Ir}^{\downarrow}(z) + k_{a,UV-vis} \quad (6.27)$$

and $k_{a,UV-vis} = -m \frac{\delta \tau_{a,UV-vis}}{\delta z}$. For the diffuse radiation, as we are considering a non-scattering but absorbing medium, we may add the impact of aerosols by summing the extinction coefficient for aerosols to the extinction gas coefficient as:

$$k_{UV-vis/a,D}^{\downarrow}(z) = k_{UV-vis,D}^{\downarrow}(z) + k_{a,UV-vis} \quad (6.28)$$

$$k_{UV-vis/a,D}^{\uparrow}(z) = k_{UV-vis,D}^{\uparrow}(z) + k_{a,UV-vis} \quad (6.29)$$

$$k_{SIR/a}^{\uparrow}(z) = k_{SIR}^{\uparrow}(z) + k_{a,SIR} \quad (6.30)$$

6.3.3.2 Estimations during cloudy-sky days of the equivalent absorption coefficient

In a cloudy atmosphere, the major effect of cloud droplet absorption is the increase of solar heating within the cloud. Even if cloud droplets are weakly absorbing, the heating in the cloud layers is enhanced by droplet scattering that increases the path of photons in the cloud. One way to simply parameterize this effect is to consider that cloud droplets are purely absorbing,

like in the IR spectral domain. This approximation can be easily used in our approach and allows the separation between gaseous and liquid water absorption. It has been applied in Makké [2015] for the IR domain and consists in considering cloud droplets as locally extinctive. Thus, we can define the equivalent absorption coefficient similarly to the one of aerosols as: $k_c = -m \frac{\delta \tau_c}{\delta z}$. It should be weighted following the cloud fraction. Moreover, k_c is multiplied to C_e , the cloud scattering efficiency, as we are not taking into account the scattering processes it can be considered in our case as an adjustable corrected factor that ranges between 0 and 1. It leads to

$$k_{UV-vis/a+c}^{\uparrow\downarrow}(z) = (1 - F_c)k_{UV-vis,a}^{\uparrow\downarrow}(z) + F_c k_{UV-vis,a}^{\uparrow\downarrow} k_c C_e \quad (6.31)$$

$$k_{SIR/a+c}^{\uparrow\downarrow}(z) = (1 - F_c)k_{SIR,a}^{\uparrow\downarrow}(z) F_c k_{SIR,a}^{\uparrow\downarrow} k_c C_e \quad (6.32)$$

where $k_{UV-vis,a}^{\downarrow}$ may be equal to $k_{UV-vis,aIr}^{\downarrow}$ or $k_{UV-vis,a,D}^{\downarrow}$.

6.3.4 Comparison 1D/3D

6.3.4.1 Clear sky - without aerosols

In order to verify the implementation of the 3D radiative scheme in the current version of code_saturne, the radiative fluxes obtained using this scheme have been compared to the fluxes computed with the 1D scheme (that is validated in chapter 5). We first consider the absorption by ozone and water vapour only during clear-sky days. The simulations ran on a 1D domain, the same as in chapter 5 (presented in section 5.3.1) and compared to the 1D model under the same conditions. However, due to its high computer cost, the 3D calculations are achieved every 15 min while the 1D model has a time step of 1 min. The same study case as chapter 5 is considered (ParisFog) but we are here interested in the clear-sky conditions only. The comparison for the downward and upward fluxes on the 18/02/2007 at 13 h and 15 h are presented in figures 6.3 and 6.4 and on the 19/02/2007 at 12 h (end of simulation) in figure 6.5. We see in those figures that the top boundary conditions for the downward fluxes are well respected: the values of 1D and 3D fluxes are exactly the same at $z_{3D}=2494$ m. Moreover, in the UV-vis band, as absorption by ozone is low in the low atmosphere, it explains why the fluxes are constant on the vertical. The 3D estimation of radiative fluxes compares well with the 1D model, despite the small differences obtained for the upward fluxes ($\sim 1 \text{ W m}^{-2}$). In the SIR band, where absorption by water vapour is more important in the low atmosphere, the 1D and 3D models compare well with differences of less than 2 W m^{-2} for upward fluxes and less than 4 W m^{-2} for downward fluxes. Despite the small discrepancies, this comparison allow us to verify the implementation of the 3D scheme in code_saturne.

6.3.5 Work in progress

The work in progress concerns the integration of aerosols and clouds in the 3-D model. In fact, for a better description of radiative fluxes in the 3D model, we should take into consideration the impact of aerosols and clouds. The following work couldn't be completed on time due to many technical problems in the 3D model.

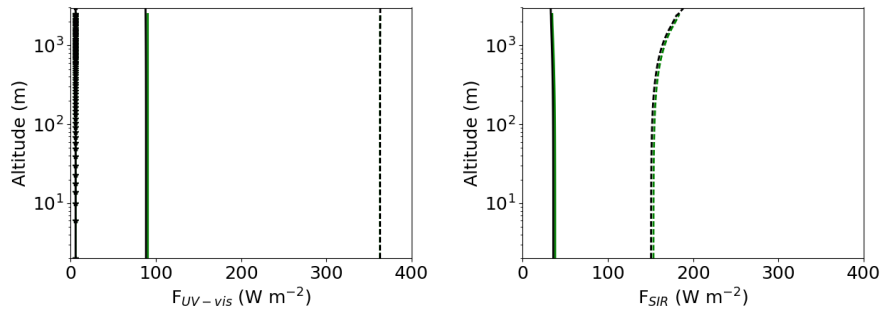


Figure 6.3: The vertical profiles of downward and upward fluxes in the **UV-vis** (left panel) and **SIR** (right panel) bands on 18/02/2007 at 13 h (in W m^{-2}) using the **1D** (represented in black) and **3D** (represented in green) models in a clear-sky without aerosols. $F^{\uparrow}_{diffuse}$ (—) F^{\downarrow}_{direct} (---) $F^{\downarrow}_{diffuse}$ (- * -).

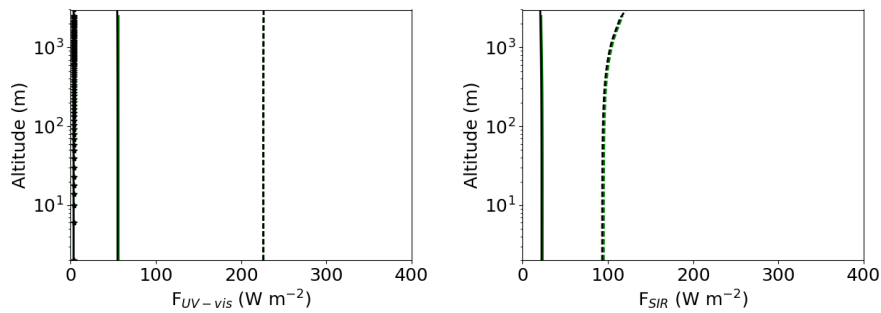


Figure 6.4: The vertical profiles of downward and upward fluxes in the **UV-vis** (left panel) and **SIR** (right panel) bands on 18/02/2007 at 15 h (in W m^{-2}) using the **1D** (represented in black) and **3D** (represented in green) models in a clear-sky without aerosols. $F^{\uparrow}_{diffuse}$ (—) F^{\downarrow}_{direct} (---) $F^{\downarrow}_{diffuse}$ (- * -).

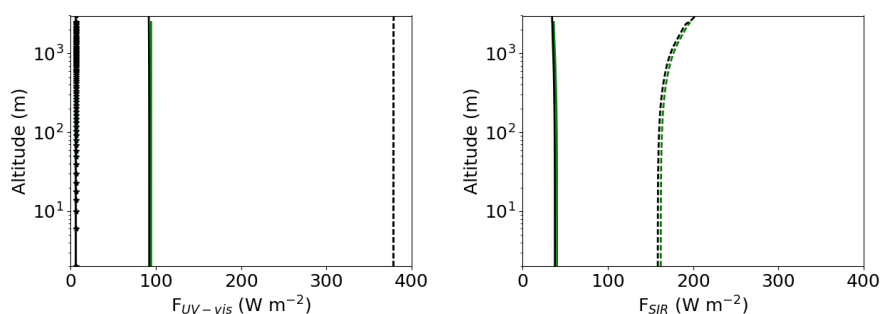


Figure 6.5: The vertical profiles of downward and upward fluxes in the UV-vis (left panel) and SIR (right panel) bands on 19/02/2007 at 12 h (in W m^{-2}) using the 1D (represented in black) and 3D (represented in green) models in a clear-sky without aerosols until 500 m. $F_{\uparrow}^{\text{diffuse}}$ (—) $F_{\downarrow}^{\text{direct}}$ (---) $F_{\downarrow}^{\text{diffuse}}$ (- * -).

The comparison between the 1D and 3D models of the vertical profiles of downward and upward fluxes in a clear-sky with aerosols distributed on the vertical until 500 m is shown in figure 6.6. The global component of the downward direction of the 3D model compares well with the 1D model (figure 6.8) above the aerosol layer, however, in the aerosol layer the 3D model overestimate the 1D model and therefore, absorption by aerosols is weaker in the 3D model. The overestimation may reach around 50 W m^{-2} at the surface. Moreover, the breakdown of the direct and diffuse components in the 3D model is unsatisfactory. This is because scattering is neglected and only the absorption by aerosols is considered in the 3D model. However, even for global fluxes, an important difference may be obtained at the surface, and contrarily to the case when aerosols were neglected, the difference is more important for the UV-Vis band and for the downward fluxes.

The comparison is then conducted at 8h am on the 19/02/2007 during the presence of the fog in order to test our configuration in a cloudy atmosphere and with a scattering coefficient equal to 10^{-3} . The fluxes are represented, for the 1D and 3D model, in figure 6.7. The reduction of the radiation in the fog is well taken into account in the downward fluxes of the 3D model, however the absorption is more important in the 3D model leading to an underestimation of fluxes. The underestimation at the surface is around 25 W m^{-2} in the UV-Vis band and 10 W m^{-2} in the SIR band. The distribution of the upward fluxes on the vertical is constant, showing that the absorption by fog might not have been considered and should be fixed for future works.

6.3.6 Conclusion

The 3D solving of the RTE is useful for many applications like a better representation of clouds or to consider the shadow effect in an urban canopy. In consequences, the 3D radiative model of code_saturne was developed and this study which aimed at presenting the model and implement it in the v7.0. The model is based on the DISORT algorithm for the angular inte-

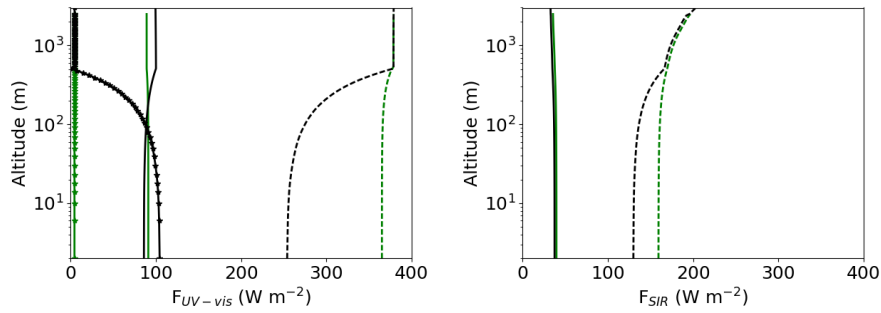


Figure 6.6: The vertical profiles of downward and upward fluxes in the **UV-vis** (left panel) and **SIR** (right panel) bands on 19/02/2007 at 12 h (in W m^{-2}) using the **1D** (represented in black) and **3D** (represented in green) models in a clear-sky with aerosols until 500 m. $F_{\uparrow}^{\text{diffuse}}$ (—) $F_{\downarrow}^{\text{direct}}$ (---) $F_{\downarrow}^{\text{diffuse}}$ (- * -).

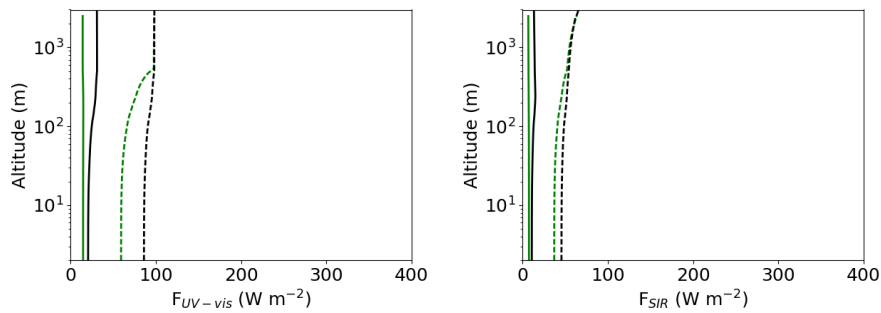


Figure 6.7: The vertical profiles of downward and upward global fluxes in the **UV-vis** (left panel) and **SIR** (right panel) bands on 19/02/2007 at 8 h (in W m^{-2}) using the **1D** (represented in black) and **3D** (represented in green) models in a cloudy-sky situation ($C_e=1$). $F_{\uparrow}^{\text{global}}$ (—) $F_{\downarrow}^{\text{global}}$ (---).

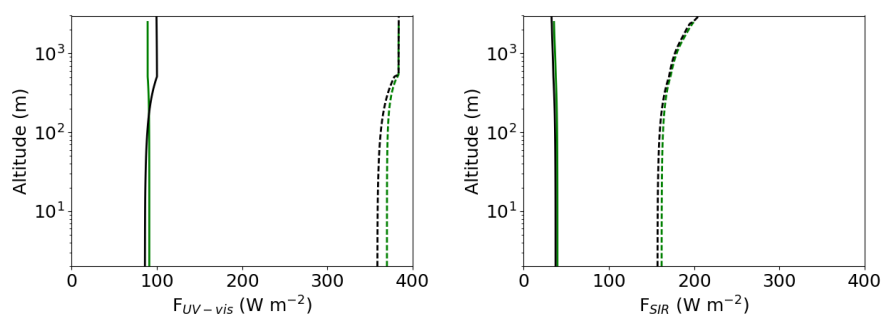


Figure 6.8: The vertical profiles of downward and upward global fluxes in the **UV-vis** (left panel) and **SIR** (right panel) bands on 19/02/2007 at 12 h (in W m^{-2}) using the **1D** (represented in black) and **3D** (represented in green) models in a clear-sky with aerosols until 500 m. $F_{\uparrow global}$ (—) $F_{\downarrow global}$ (---).

gration, and it is coupled to the absorption coefficient calculated using the **1D** model. We first focused on clear-sky situation, and acceptable comparison was obtained with the **1D** model when only the absorption by gas (ozone or water vapour) was considered.

This work is a first step in integrating the **3D** solar radiative scheme in code_saturne.

Some more work is required in order to validate the model. More particularly, the diffusion operator could be added to the **3D** radiative solving in order to have a better description of fluxes when aerosols are considered. Later on, we would like to consider a **3D** mesh of an urban area with buildings or a field of **PV** farm in order to evaluate the shadowing effect on **PV** energy production. It could also be interesting to run the **3D** model to simulate the radiation going through clouds in order to study the so-called **3D** cloud effect.

Appendix A

Supporting Material

This section details the equations used for the 1D radiative model of code_saturne (multi-layered method).

A.1 The 1D radiative scheme

In the present version, the aerosols are taken into account as absorbing and diffusive particles characterized by their optical properties: aerosol optical depth, single scattering albedo and asymmetry factor. To do that, the adding method for multiple scattering has been added in the [UV-vis](#) and [SIR](#) bands. Other improvements have been made for: the optical air mass, the Rayleigh diffusion and the direct radiation estimation. In addition, the absorption by minor gases has been introduced. The methodology followed for the improvement of the model is described in chapter 4.

A.1.1 Solar radiation at the upper limit of the atmosphere

The first step consists in the determination of astronomic factors linked to the earth-sun position.

Determination of the sun zenith angle and correction factors for the solar constant [Paltridge and Platt, 1976]

$$\mu_0 = \cos\theta = \sin\delta\sin\Phi + \cos\delta\cos\Phi\cos(t_h) \quad (\text{A.1})$$

where Φ is the latitude, δ the inclination which depends on the day of the year:

$$\delta = 0.006918 - 0.399912\cos\Theta_0 + 0.070257\sin\Theta_0 - 0.006758\cos(2\Theta_0) + 0.000907\sin(2\Theta_0) - 0.002697\cos(3\Theta_0) + 0.001480\sin(3\Theta_0) \text{ with } \Theta_0 = 2\pi J/365.$$

A correction for solar-earth distance is taken into account

$$F = F_0(1.00011 + 0.034221\cos(\Theta_0) + 0.001280\sin(\Theta_0) + 0.000719\cos(2\Theta_0) + 0.000077\sin(2\Theta_0)) \quad (\text{A.2})$$

with $F_0 = 1367 \text{ W m}^{-2}$.

In order to take into account earth curvature, a correcting term is added:

$$\mu_0 = \frac{r_1}{\sqrt{\mu_0^2 + r_1(r_1 + 2)}} - \mu_0 \quad (\text{A.3})$$

with $r_1 = \frac{H_{atmo}}{R_{earth}} = \frac{8km}{6371km}$

Appendix A Supporting Material

gas	a	b	c	d
CO_2	0.0721	377.89	0.5855	3.1709
CO	0.0062	243.67	0.4246	1.7222
N_2O	0.0326	107.413	0.5501	0.9093
CH_4	0.0192	166.095	0.4221	0.7186
O_2	0.0003	476.934	0.4892	0.2748

Table A.1: Numerical coefficients for the calculation of Tmg

A.1.2 Atmospheric parameters

m the optical air mass given by [Kasten and Young \[1989\]](#) :

$$m = \frac{1}{\mu_0 + 0.50572 * (96.07995 - \frac{180}{\pi \arccos(\mu_0)^{-1.6364}})} \quad (A.4)$$

The general transmittance function, T_i , for five minor atmospheric gases (CO_2 , CO, N_2O , CH_4 and O_2) can be expressed by the following equation [[Psiloglou et al., 2000](#)]:

$$T_i = 1 - amu_i / ((1 + bmu_i)^c + dmu_i) \quad (A.5)$$

where m is the optical air mass, a, b, c, d are numerical coefficients that are given in the table [A.1](#).

The broadband transmittance function due to the total absorption by the uniformly mixed gases can then be calculated by:

$$Tmg = T_{CO_2} T_{CO} T_{N_2O} T_{CH_4} T_{O_2} \quad (A.6)$$

A.1.2.1 Meshes

The atmosphere is divided in vertical layers. Two meshes are used in the code and are represented in figure [A.1](#).

The physical mesh represents the physical model: zray is the altitude of the domain and zaero is the altitude of the highest aerosol level. They are given as input to the code. The units are in meters.

The simulation mesh represents the indexes used in the code. k1 represent the index for ground level. kmray the number of vertical levels (index of zray). iaero the index of the top of the aerosol layer (index of zaero). itop the index of the highest cloud or aerosol layer.

A.1.3 Clouds and aerosol optical proprieties

Both cloud droplets and aerosols induce multiple diffusion. They are characterized by their optical properties: their optical thicknesses τ_C and τ_a , their single scattering albedos ω_C and ω_a and their asymmetry factors g_c and g_a .

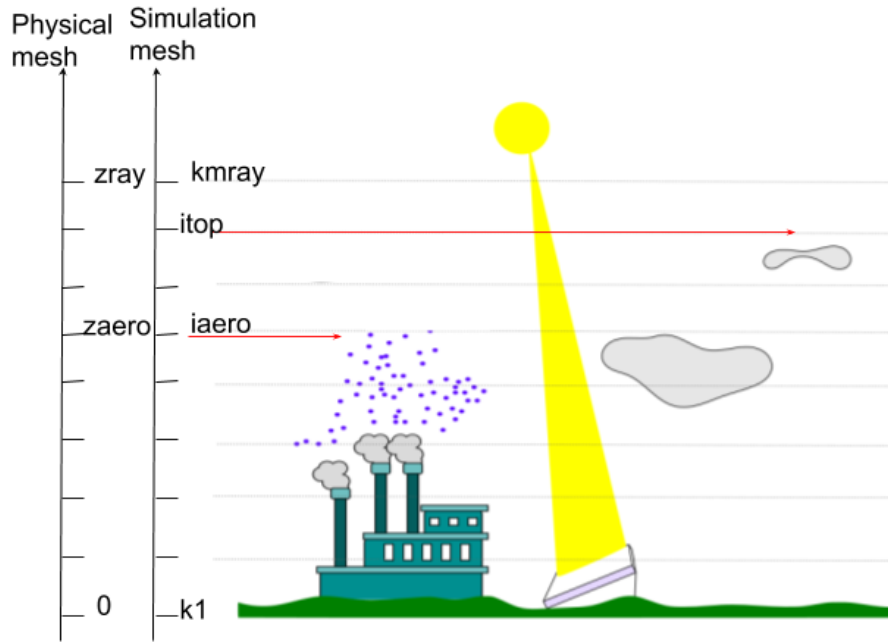


Figure A.1: Physical and simulation mesh

A.1.3.1 Parameterization of aerosols

The single scattering albedo ω_a and asymmetry factor g_a for the **UV-vis** and **SIR** band are given as input of the code.

Two options exist for the determination of the **Aerosol Optical Depth (AOD)**.

If the aerosol concentration at each vertical level C_a (in $\mu\text{g.m}^3$) is known, then **AOD** at each vertical level is given by:

$$\tau_a = \frac{3}{2} \frac{w_{aero}}{r_{ea}} \quad (\text{A.7})$$

with $w_{aero} = 10^3 \rho c_{aero} C_a$

ρ being the air density, $c_{aero} = 10^{-9}$ and r_{ea} equivalent radius of aerosol particles.

If the total aerosol optical depth is given as input of the code, then it is distributed linearly on the vertical until the aerosol highest level, z_{aero} (given as input). The aerosol optical thickness at each vertical level is given by:

$$\tau_a = \frac{\tau_{a-tot} \Delta z}{z_{aero}} \quad (\text{A.8})$$

Δz is the gap between two vertical levels. In this case, the **AOD** is defined in the **UV-vis** band and in the **SIR** band.

A.1.3.2 Parameterization of clouds

The calculation of cloud optical properties are detailed in this subsection. The **Cloud Optical Depth (COD)**, τ_C is calculated following [Stephens \[1984\]](#):

$$\tau_C = \frac{3 Lwc}{2 r_e} \quad (\text{A.9})$$

where r_e is the cloud droplet equivalent radius in μm and **Lwc** is the liquid water content in g/m^2 .

The calculations for the **Single Scattering Albedo (SSA)** and asymmetry factor are made separately in the **UV-vis** band and in the **SIR** band.

They are approximated following the formulations of [Nielsen et al. \[2014\]](#). They depend only on the equivalent cloud droplet's radius r_e , and are defined for different spectral bands: 250-440; 440-690 nm in the **UV-vis** domain and 690-1190; 1190-2380 nm in the **SIR** domain. The integration over the wavelength is made by weighting each formulation with the radiance energy contained in each band.

The **SSA** in the **UV-vis** and **SIR** bands (ω_0^{UV-Vis} and ω_0^{SIR}) are calculated with the following formulas:

$$\omega_0^{UV-Vis} = \omega_{0-1} \times 0.24 + \omega_{0-2} \times 0.76 \quad (\text{A.10})$$

where ω_0^{UV-Vis} is the **SSA** in the **UV-vis** band it is weighted by the **SSA** ω_{0-1} in the first spectral band (250-440 nm), which radiance energy is equal to 0.24 and the **SSA** ω_{0-2} in the second spectral band (440-690 nm) which radiance energy is equal to 0.76.

$$\omega_{0-1} = 1 - 3.3 \times 10^{-8} r_e \quad (\text{A.11})$$

$$\omega_{0-2} = 1 - 10^{-7} r_e \quad (\text{A.12})$$

In the **SIR** band the **SSA**, ω_0^{SIR} , is calculated with the following formula:

$$\omega_0^{SIR} = \omega_{0-3} \times 0.60 + \omega_{0-4} \times 0.40 \quad (\text{A.13})$$

where ω_0^{SIR} is weighted by the **SSA** in the **SIR** band it is to the **SSA** ω_{0-3} in the third spectral band (690-1190 nm), which radiance energy is equal to 0.6 and the **SSA** ω_{0-4} in the fourth spectral band (1190-2380 nm) which radiance energy is equal to 0.40.

$$\omega_{0-3} = 0.99 - 1.49 \times 10^{-5} r_e \quad (\text{A.14})$$

$$\omega_{0-4} = 0.9985 - 9.210^{-4} r_e \quad (\text{A.15})$$

In the **UV-vis** band, the cloud asymmetry, g_0^{UV-Vis} , is calculated with the following formula:

$$g_0^{UV-Vis} = \omega_{0-1} \times 0.24 \times g_1 + \omega_{0-2} \times 0.76 \times g_2 \quad (\text{A.16})$$

Appendix A Supporting Material

where g^{UV-Vis} is the SSA in the SIR band it is weighted by the SSA g_{0-1} in the first spectral band (250-440 nm), and the SSA g_{0-2} in the second spectral band (440-690 nm).

$$g_{0-1} = 0.868 + 1.4 \times 10^{-4}re - 6.1 \times 10^{-3}e^{-0.25re} \quad (\text{A.17})$$

$$g_{0-2} = 0.868 + 2.5 \times 10^{-4}re - 6.3 \times 10^{-3}e^{-0.25re} \quad (\text{A.18})$$

In the SIR band, the cloud asymmetry, g_0^{SIR} , is calculated with the following formula:

$$g^{SIR} = \omega_{0-3} \times 0.60 \times g_3 + \omega_{0-4} \times 0.40 \times g_4 \quad (\text{A.19})$$

where g^{SIR} is weighted by the SSA in the UV-vis band it is to the SSA ω_{0-3} in the third spectral band(690-1190 nm), and the SSA ω_{0-4} in the fourth spectral band (1190-2380 nm)

$$g_{0-3} = 0.867 + 3.1 \times 10^{-4}re - 7.8 \times 10^{-3}e^{-0.195re} \quad (\text{A.20})$$

$$g_{0-4} = 0.864 + 5.4 \times 10^{-4}re - 0.133e^{-0.194re} \quad (\text{A.21})$$

The SSA as calculated using the formulations of Nielsen et al. [2014] is used in the case with a negligible black carbon fraction in the cloud droplet (lower than $\epsilon = 1.10^{-8}$).

In the other case, it is calculated using the approximation of Chuang et al. [2002]. With this approach, the absorption of black carbon is considered. In fact, black carbon in the cloud droplets could be responsible for an increase in solar radiation absorption and heating of the atmosphere. The calculation from Chuang et al. [2002] depend on the mean cloud droplet diameter and on the fraction of black carbon in the cloud droplet. They are defined for different spectral band. The integration over the wavelength is made by weighting each formulation with the radiance energy contained in each band.

The SSA is equal to $\omega(\nu_d, d_o) = 1 - \bar{\omega}(\nu_d, d)$ where $\bar{\omega}(\nu_d, d)$ is the single scattering co-albedo of a drop/BC mixture with diameter d approximated by:

$$\bar{\omega}(\nu_d, d) = \frac{\frac{d}{d_o} \bar{\omega}(\nu_d, d_o)}{1 + 1.8 \bar{\omega}(\nu_d, d_o) [\frac{d}{d_o} - 1]} \quad (\text{A.22})$$

where

$$\bar{\omega}(\nu_d, d_o) = \bar{\omega}_o + \beta_1 [1 - e^{-\beta_3(\nu_d - \nu_o)}] + \beta_2 [1 - e^{-\beta_4(\nu_d - \nu_o)}] \quad (\text{A.23})$$

and $d_o = 20\mu m$; $\nu_o = 10^{-8}$; $\bar{\omega}_o$ is the single scattering co-albedo for a $20\mu m$; ν_d the black carbon fraction. The list of values of $\bar{\omega}_o$ and β are given in table A.2 and A.3.

A.1.4 Solar radiation modelling

The radiative transfer equation is applied to a plane-parallel model atmosphere (1D) using the two-stream approximation in a non-scattering medium with an external radiation source term (the sun). They are applied for the global radiation (direct + diffuse radiation).

The solar spectrum is divided in two bands: the ultraviolet (UV)-visible band (0.3-0.7 μm) where

Appendix A Supporting Material

λ (μm)	0.2985 - 0.3225	0.3225 - 0.3575	0.3575 - 0.4375	0.4375 - 0.4975	0.4975 - 0.6925
$\bar{\omega}_o$	6090293.d-12	3794524.d-12	1735499.d-12	1136807.d-12	2261422.d-12
β_1	0.2542476	0.2588392	0.2659081	0.2700860	0.2783093
β_2	0.2824498	0.2775943	0.2698008	0.265296	0.2564840
β_3	45.75322	42.43440	37.03823	32.32349	25.99426
β_4	448.3519	409.9063	348.9051	297.9909	233.7397
E_{UV-Vis}	0.029	0.045	0.168	0.1868	0.570

Table A.2: Coefficients of single Scattering co-albedo for a Drop/BC Mixture with $d=20 \mu m$ - in the UV-vis band - [Chuang et al., 2002]

λ (μm)	0.6925 - 0.8621	0.8621 - 2.2727	2.2727-3.84672
$\bar{\omega}_o$	1858815.d-11	5551822.d-9	2325124.d-7
β_1	0.2814346	0.2822860	0.1797007
β_2	0.2535739	0.2487382	0.1464709
β_3	20.05043	12.76966	3.843661
β_4	175.4385	112.8208	39.24047
E_{SIR}	0.27	0.68	0.044

Table A.3: Coefficients of single Scattering co-albedo for a Drop/BC Mixture with $d=20 \mu m$ - in the SIR band - [Chuang et al., 2002]

absorption by ozone occurs in the upper layers of the atmosphere, and the near infrared (SIR) domain (0.7-3 μm) where absorption by water vapour occurs in the lower part of the atmosphere.

The equations are defined depending on the spectral band.

A.1.4.1 UV-vis band (Absorption by ozone)

In the UV-vis band, the multiple diffusion processes are modelled using the adding method. The k distribution method is not used because ozone absorption is relevant only in the upper layers of the atmosphere. The adding method is applied only in the layers below the top of the cloud or in the aerosol layers.

Clear sky without aerosols In the layers above the top of the cloud, the absorption and the different fluxes are computed with the formulations from LH74 for the clear sky situation. Using these approximations, the heating rate due to ozone in the layer (l, l+1) is (LH74):

$$F_{o3} = \mu_0 F [A_{o3}(x_{l+1}) - A_{o3}(x_l) - \bar{R}(\mu_0)(A_{o3}x_{l+1}^* - A_{o3}x_l^*)] \quad (\text{A.24})$$

with $x = mu_{o3}(\infty, z)$, $x^* = mu_{o3}(\infty, z) + (\bar{M})(u_{o3}(\infty, 0) - u_{o3}(\infty, z))$ where $\bar{M} = 1.9$ and $m = 35/(1224\mu_0^2 + 1)^{1/2}$ x^* is the ozone path traversed by the diffuse radiation illuminating the lth layer.

$u_{o3}(\infty, 0)$ is the total ozone amount in a vertical path above the ground level.

$u_{o3}(\infty, z)$ is the ozone amount in a vertical column above the layer 'z'.

\bar{M} is the effective magnification factor for diffuse upward radiation.

$\bar{R}(\mu_0)$ is the composite albedo including Rayleigh diffusion from lower part of the atmosphere and ground albedo.

$$\bar{R}(\mu_0) = \bar{R}_a(\mu_0) + (1 - \bar{R}_a(\mu_0))(1 - \bar{R}_a^*)R_g/(1 - \bar{R}_a^*R_g)$$

$\bar{R}_a(\mu_0) = 0.213/(1 + 0.816\mu_0)$ Rayleigh's diffusion albedo for illumination from above and

$\bar{R}_a^* = 0.144$ for diffuse illumination from below.

The ozone absorption is parameterized as in LH74 for both Chappuis and ultraviolet bands:

$$A_{O3} = \frac{0.02118x}{1 + 0.042x + 0.000323x^2} + \frac{1.082x}{(1 + 138.6x)^{0.805}} + \frac{0.0658x}{1 + (103.6x)^3} \quad (\text{A.25})$$

where x is in cm NTP.

The global downward flux in the O3 band is:

$$F_g^{O3} \downarrow = \mu_0 F (0.647 - A_{O3}(x) - \bar{R}_r(\mu_0))/(1 - \bar{R}_r^*R_g) \quad (\text{A.26})$$

with Rayleigh atmosphere albedos from above $\bar{R}_r(\mu_0) = 0.28/(1 + 6.43\mu_0)$ and $\bar{R}_r^* = 0.0685$ and below . 0.647 corresponds to the fraction of solar energy present in the UV-vis band.

The direct downward flux is defined by:

$$F_d^{O3} \downarrow = \mu_0 F (0.647 - A_{O3}(x) - \bar{R}_r(\mu_0)) \quad (\text{A.27})$$

Cloudy/ Aerosol layers In the layers below the top of the cloud or the aerosol layer, the adding method is used. For each cloud and aerosol layer l , the optical thickness $\tau_{l,n}$, the single scattering albedo $\omega_{l,n}$ and the asymmetry factor g are equal to:

$$\tau'_l = \tau_c + \tau_a \quad (\text{A.28})$$

$$\omega'_l = \frac{\omega_c \tau_c + \omega_a \tau_a}{\tau'_l} \quad (\text{A.29})$$

$$g' = \frac{\omega_c \tau_c g_c + \omega_a \tau_a g_a}{\omega'_l \tau'_l} \quad (\text{A.30})$$

Joseph et al, 1976 corrections are applied in order to describe the highly forward scattering for cloud droplets and aerosol particles. Therefore,

$$\tau_l = \tau'_l (1 - f \omega'_l) \quad (\text{A.31})$$

$$\omega_l = \frac{\omega'_l (1 - f)}{(1 - f \tau'_l)} \quad (\text{A.32})$$

$$g = \frac{(g' - f)}{(1 - f)} \quad (\text{A.33})$$

Where $f = g'^2$ (Stephens, 1984). The transmission and reflection functions for global radiation used by LH74 correspond to the quadrature method in [Meador and Weaver \[1980\]](#):

$$R_l = \frac{\gamma_2 (e^{k\tau} - e^{-k\tau})}{(k + \gamma_1) e^{k\tau} + (k - \gamma_1) e^{-k\tau}} \quad (\text{A.34})$$

$$T_l = \frac{2k}{(k + \gamma_1) e^{k\tau} + (k - \gamma_1) e^{-k\tau}} \quad (\text{A.35})$$

with $\tau = \tau_{l,n}$ and $k = (\gamma_1^2 - \gamma_2^2)^{1/2}$. The values γ_1 and γ_2 depend on the two-stream approximation used:

Standard Eddington approximation [[Meador and Weaver, 1980](#), [Eddington, 1916](#)]

$$\gamma_1 = 1/4(7 - \omega_{l,n}(4 + 3g)) \quad (\text{A.36})$$

$$\gamma_2 = -1/4(1 - \omega_{l,n}(4 - 3g)) \quad (\text{A.37})$$

Two-stream quadrature approximation ([[Liou, 2002](#), [Meador and Weaver, 1980](#)])

$$\gamma_1 = 3^{1/2}(1 - \omega_{l,n}(1 + g))/2 \quad (\text{A.38})$$

$$\gamma_2 = 3^{1/2}\omega_{l,n}(1 - g)/2 \quad (\text{A.39})$$

Appendix A Supporting Material

The transmission function for direct solar radiation is $T_l = \exp(-M \tau_a)$ for the clear-sky layers and $T_l = \exp(-M(\tau_a + \tau_c))$ for the cloudy layers. The reflection and transmission functions are weighted by the cloud fraction F_C : $T_l = F_C T_{l,cloud} + (1 - F_C) T_{l,clear}$ and $R_l = F_C R_{l,cloud}$. The cloud fraction is taken into account in the code following the random overlap assumption. The following five steps are carried out:

1. R_l and T_l for $l = 1, L$ are computed for each layer
2. The layers are added, going down, to obtain $R_{1,l}$ and $T_{1,l}$ for global radiation as follows: $R_{1,l} = R_{1,l-1} + \frac{T_{1,l-1} R_l T_{1,l-1}^*}{1 - R_{1,l-1}^* R_l}$, $T_{1,l} = \frac{T_{1,l-1} T_{1,l-1}^*}{1 - R_{1,l-1}^* R_l}$ with similar expressions for R^* and T^* and for direct radiation $R_{1,l}^d = 0$, $T_{1,l}^d = T_{1,l-1} T_l$ with $T_{1,l} = \exp(-M \mu_{O_3}(itop, \infty))$ as boundary condition for both global and direct radiation. Similar expressions are defined for R^* and T^*
3. Layers are added one at a time, going up, to obtain $R_{L+1,l}$ and $T_{L+1,l}$ with $R_{L+1} = R_g$ and $T_{L+1} = 0$ at the ground level.
4. As two composite layers, say $l, l+1$ and $l+1, l+2$ are added, the upward and downward global fluxes boundary between the two layers are determined: $U = \frac{T_{1,l} R_{L+1,l}}{1 - R_{1,l}^* R_{L+1,l+1}}$, $D_l = \frac{T_{1,l}}{1 - R_{1,l}^* R_{L+1,l+1}}$ and for direct radiation $U_l^d = 0$, $D_l^d = T_{1,l}$ where the fraction of the total incident flux absorbed in the upper composite layer is: $A_{1,l} = (1 - R_{1,l+1}) + U_l - D_l$
5. The total absorption in each layer l is found by subtraction, e.g., $F_{abs}^{O_3'} = \mu_0 F (0.647 - A_{O_3}(x) - \bar{R}_r(\mu_0)) (A_{1,l} - A_{1,l-1})$ The absorption by ozone is added to aerosol and cloud absorption as a purely absorbing region:

$$F_{abs}^{O_3} = F_{abs}^{O_3'} + \mu_0 F [A_{O_3}(x_{l+1}) A_{O_3}(x_l) - \bar{R}(\mu_0) (A_{O_3}(x_{l+1}^*) A_{O_3}(x_l^*))] \quad (A.40)$$

The downward flux for global and direct radiation and the upward diffuse flux are:

$$F_g^{O_3} \downarrow = \mu_0 F (0.647 - A_{O_3}(x) - \bar{R}_r(\mu_0)) D_l \quad (A.41)$$

$$F_d^{O_3} \downarrow = \mu_0 F (0.647 - A_{O_3}(x) - \bar{R}_r(\mu_0)) D_l^d \quad (A.42)$$

$$F_d^{O_3} \uparrow = \mu_0 F (0.647 - A_{O_3}(x^*) - \bar{R}_r(\mu_0)) U_l \quad (A.43)$$

The level L corresponds to the ground level, x is the effective ozone amount from the ground level to the top of the cloud or the aerosol layer: $\mu_{O_3}(\infty, z(itop))$.

In order to take into account the upward flux transmitted by the cloud or aerosol layers in the clear-sky layers above the clouds or the aerosol, the following is done:

For the layers above the cloud top or aerosol layers:

$$F_d^{O_3} \uparrow = F_d^{O_3} \uparrow (z = itop) \times (1 - A_{O_3}(x^*)) \quad (A.44)$$

A.1.4.2 SIR band (Absorption by water vapor)

In the SIR spectral band, where water vapour absorption is dominant, the multiple diffusion processes are directly modelled using the adding method with a k-distribution method for overlapping between liquid and vapour water (LH74). In fact, the absorption by water vapour is highly frequency-dependant and accurate monochromatic values are not available for the entire spectrum. Plus, scattering and absorption can occur in the same part of the atmosphere and the absorption coefficient has a significant dependence on pressure. For clear skies, the effect of scattering is negligible, however for cloudy skies, the parameterization is based on a discrete probability distribution for the absorption coefficient derived from measured absorptivities. It allows treating correctly the overlapping between clouds and water vapour. The K-distribution method is expressed as follows:

$p(k)dk$ is the fraction of incident flux that is associated with an absorption coefficient between k and $k + dk$ and it is related to the absorptivity by

$$A_{wv}(y) = 1 - \int_0^{\infty} p(k)e^{-ky} dk \quad (\text{A.45})$$

We can do the following approximation:

$$\int p(k)e^{-ky} dk = \sum_{n=1}^N p(k_n)e^{-k_n y} \quad (\text{A.46})$$

Table A.4 gives the values of k_n and $p(k_n)$ for $N=8$.

The adding method is applied on every vertical level: from the ground to the highest vertical level.

For each cloud layer l in the frequency interval n , the optical thickness $\tau_{l,n}$, the single scattering albedo $\omega_{l,n}$ and the asymmetry factor g are:

$$\tau_{l,n} = \tau_c + \tau_a + k_n u_{H2O} \quad (\text{A.47})$$

$$\omega_{l,n} = (\omega_c \tau_c + \omega_a \tau_a) / \tau'_{l,n} \quad (\text{A.48})$$

$$g' = (\omega_c \tau_c g_c + \omega_a \tau_a g_a) / \tau'_{l,n} \omega'_{l,n} \quad (\text{A.49})$$

As for the ozone band, Joseph and Wiscombe [1976] correction and the Two-stream quadrature approximation [Liou, 2002, Meador and Weaver, 1980] are used.

The transmission function for direct solar radiation is $T_l = \exp(-m(\tau_a + k_n u_{H2O}))$ for the clear-sky layers and for the cloudy layers $T_l = \exp(-m(\tau_a + \tau_c + k_n u_{H2O}))$.

The reflection and transmission functions are weighted by the cloud fraction F_C : $T_l = F_C T_{l,cloud} + (1 - F_C) T_{l,clear}$ and $R_l = F_C R_{l,cloud}$

The same five steps as in the UV-vis band are carried out, but for each value of k_n which can yield significant absorption. e.g. $n=2, 8$ for the discrete distribution given in table A.4.

However, the total absorption in each layer l is found by summing over the values of n for

Appendix A Supporting Material

$k_n, n \in [1, 8]$	4.10^{-6}	2.10^{-6}	0.0035	0.0377	0.195	0.94	4.46	19
$p(k_n)$	0.6470	0.0698	0.1443	0.0584	0.0335	0.0225	0.0158	0.0087

Table A.4: Discrete distribution of p_{k_n}

which k_n is significant

$$F_{abs}^{H20} = \mu_0 F \sum_{n=2}^{n=8} A_l(n) \quad (\text{A.50})$$

The downward and upward fluxes for global radiation are:

$$F_g^{H20} \downarrow = \mu_0 F \sum_{n=2}^{n=8} D_l(n) p(k_n) \quad (\text{A.51})$$

$$F_g^{H20} \uparrow = \mu_0 F \sum_{n=2}^{n=8} U_l(n) p(k_n) \quad (\text{A.52})$$

The downward direct radiation is:

$$F_d^{H20} \downarrow = \mu_0 F \sum_{n=2}^{n=8} D_l^d(n) p(k_n) \quad (\text{A.53})$$

The level L corresponds to the ground level.

A.1.5 Total absorption and fluxes

The total absorption is the sum of water vapour and ozone band absorption.

The total fluxes for global and direct radiation are equal to the sum of the contribution of both ozone and water vapour bands. They are then multiplied by T_{mg} in order to take into account the absorption by minor gases. T_{mg} being the transmission function by minor gases (refer to section A.1.2).

The downward fluxes are:

Global radiation

$$F_g \downarrow = T_{mg} (F_g^{03} \downarrow + F_g^{H20} \downarrow) \quad (\text{A.54})$$

Direct radiation

$$F_d \downarrow = T_{mg} (F_d^{03} \downarrow + F_d^{H20} \downarrow) \quad (\text{A.55})$$

The diffuse irradiation is the difference between global and direct irradiation.

Bibliography

- H. Abdul-Razzak and S. Ghan. A parameterization of aerosol activation: 2. multiple aerosol types. *J. Geophys. Res.*, 105:6837–6844, 2000. doi: 10.1029/1999JD901161.
- H. Abdul-Razzak, S. Ghan, and C. Rivera-Carpio. A parameterization of aerosol activation: 1. single aerosol type. *J. Geophys. Res.*, 103:6123–6131, 1998. doi: 10.1029/97JD03735.
- L. Al Asmar, L. Musson Genon, E. Dupont, J-C. Dupont, and K. Sartelet. Improvement of irradiance modelling during cloudy sky days using measurements- soon to be published. *Sol. Energy*, 2021a.
- L. Al Asmar, L. Musson Genon, E. Dupont, M. Ferrand, and K. Sartelet. Modeling the contribution of aerosols to fog evolution through their influence on solar radiation - submitted. *J. Geophys. Res. Atmos.*, 2021b.
- K. Al-Jumaily, A. Al-Salihi, and O. Al-Taai. Evaluation of Meteosat-8 Measurements Using Daily Global Solar Radiation for Two Stations in Iraq. 1, January 2010.
- M. André, K. Sartelet, S. Moukhtar, J.M. André, and M. Redaelli. Diesel, petrol or electric vehicles: what choices to improve urban air quality in the ile-de-france region? a simulation platform and case study. *Atmos. Environ.*, (241):117752, 2020. doi: 10.1016/j.atmosenv.2020.117752.
- J. Angles, L. Ménard, O. Bauer, C. Rigollier, and L. Wald. *A climatological database of the Linke turbidity factor*, volume 1. ISES, Jerusalem, Israel, 1999.
- A. Angstrom. Solar and terrestrial radiation. report to the international commission for solar research on actinometric investigations of solar and atmospheric radiation. *Quart. J. Roy. Meteor. Soc.*, 50(210):121–126, 1924. ISSN 1477-870X. doi: 10.1002/qj.49705021008.
- A. Angstrom. Computation of global radiation from records of sunshine. *Ark. Geophys.*, 2:Paper 22, 1956.
- V. Badescu, editor. *Modeling Solar Radiation at the Earth's Surface: Recent Advances*. Springer-Verlag, 2008. ISBN 978-3-540-77454-9. doi: 10.1007/978-3-540-77455-6.
- B.A. Baum, P. Yang, A.J. Heymsfield, A. Bansemer, B.H. Cole, A. Merrelli, C. Schmitt, and C. Wang. Ice cloud single-scattering property models with the full phase matrix at wavelengths from 0.2 to 100 μ m. *J. Quant. Spectrosc. Radiat. Transf.*, 146:123 – 139, 2014. ISSN 0022-4073. doi: 10.1016/j.jqsrt.2014.02.029. Electromagnetic and Light Scattering by Non-spherical Particles XIV.

Bibliography

- C. Bertrand, G. Vanderveken, and M. Journée. Evaluation of decomposition models of various complexity to estimate the direct solar irradiance over Belgium. *Renew. Energy*, 74(C):618–626, 2015. doi: 10.1016/j.renene.2014.08.
- P. Blanc, B. Gschwind, M. Lefèvre, and L. Wald. The HelioClim Project: Surface Solar Irradiance Data for Climate Applications. *Remote Sens.*, 3(2):343–361, February 2011. ISSN 2072-4292. doi: 10.3390/rs3020343.
- P. Blanc, B. Espinar, and L. Wald. *17. La ressource solaire : importance et moyens de caractérisation. À découvrir.* CNRS Éditions, 2017. ISBN 978-2-271-11914-8. URL <http://books.openedition.org/editions-cnrs/11054>.
- E. Bouzereau, L. Musson-Genon, and B. Carissimo. On the definition of the cloud water content fluctuations and its effects on the computation of a second-order liquid water correlation. *J. Atmos. Sci.*, 64:665–669, 2007. doi: 10.1175/JAS3842.1.
- J.W. Boylan and A.G. Russell. Pm and light extinction model performance metrics, goals, and criteria for three-dimensional air quality models. *Atmos. Environ.*, 40(26):4946 – 4959, 2006. ISSN 1352-2310. doi: 10.1016/j.atmosenv.2005.09.087. Special issue on Model Evaluation: Evaluation of Urban and Regional Eulerian Air Quality Models.
- H. Breitkreuz, M. Schroedter-Homscheidt, T. Holzer-Popp, and S. Dech. Short-Range Direct and Diffuse Irradiance Forecasts for Solar Energy Applications Based on Aerosol Chemical Transport and Numerical Weather Modeling. *J. Appl. Meteorol. Climatol.*, 48(9):1766–1779, September 2009. ISSN 1558-8424. doi: 10.1175/2009JAMC2090.1.
- D. Cano, J. M. Monget, M. Albuissou, H. Guillard, N. Regas, and L. Wald. A method for the determination of the global solar radiation from meteorological satellite data. *Sol. Energy*, 37(1):31–39, 1986. ISSN 0038-092X. doi: 10.1016/0038-092X(86)90104-0.
- J. Cao and X. Lin. Application of the diagonal recurrent wavelet neural network to solar irradiation forecast assisted with fuzzy technique. *Eng. Appl. Artif. Intell.*, 21:1255–1263, December 2008. doi: 10.1016/j.engappai.2008.02.003.
- J. C. Cao and S. H. Cao. Study of forecasting solar irradiance using neural networks with preprocessing sample data by wavelet analysis. *Energies*, 31(15):3435–3445, 2006.
- S. Cao and J. Cao. Forecast of solar irradiance using recurrent neural networks combined with wavelet analysis. *Appl. Therm. Eng.*, 25:161–172, February 2005. doi: 10.1016/j.applthermaleng.2004.06.017.
- S. Chandrasekhar. *Radiative Transfer*. Oxford Univ. Press, 1950. ISBN 978-0-486-31845-5.
- C-T. Cheng, W-C. Wang, and J-P. Chen. A modeling study of aerosol impacts on cloud microphysics and radiative properties. *Quart. J. Roy. Meteor. Soc.*, 133:283–297, 2007. doi: 10.1002/qj.25.

Bibliography

- M. Chiriaco, J-C. Dupont, S. Bastin, J. Badosa, J. Lopez, M. Haeffelin, H. Chepfer, and R. Guzman. ReOBS: a new approach to synthesize long-term multi-variable dataset and application to the SIRTAs supersite. *Earth Syst. Sci. Data*, 10(2):919–940, May 2018. ISSN 1866-3508. doi: 10.5194/essd-10-919-2018.
- M-D. Chou. A Solar Radiation Model for Use in Climate Studies. *J. Atmos. Sci.*, 49(9):762–772, May 1992. doi: 10.1175/1520-0469(1992)049.
- C. C. Chuang, J. E. Penner, J. M. Prospero, K. E. Grant, G. H. Rau, and K. Kawamoto. Cloud susceptibility and the first aerosol indirect forcing: Sensitivity to black carbon and aerosol concentrations. *J. Geophys. Res. Atmos.*, 107:AAC 10–1–AAC 10–23, 2002. ISSN 2156-2202. doi: 10.1029/2000JD000215.
- P. Chýle, G.B. Lesins, G. Videen, J. G. D. Wong, R. G. Pinnick, D. Ngo, and J.D. Klett. Black carbon and absorption of solar radiation by clouds. *J. Geophys. Res. Atmos.*, 105:6837–6844, 1996. doi: 10.1029/96JD01901.
- S. Clough, M. Shephard, E.J. Mlawer, J.S. Delamere, M.J. Iacono, K. Cady-Pereira, S.-A. Boukhabara, and P. Brown. Atmospheric radiative transfer modeling: A summary of the aer codes. *J. Quant. Spectrosc. Radiat. Transf.*, 91:233–244, 03 2005. doi: 10.1016/j.jqsrt.2004.05.058.
- J. Cohard, J. Pinty, and C. Bedos. Extending twomey’s analytical estimate of nucleated cloud droplet concentrations from ccn spectra. *J. Atmos. Sci.*, 55:3348–3357, 1998.
- W. R. Cotton and R. A. Anthes. *Chapter 5 Radiative Transfer in a Cloudy Atmosphere and Its Parameterization*, volume 44 of *Storm and Cloud Dynamics*. Academic Press, 1992. doi: 10.1016/S0074-6142(08)60544-6.
- code_saturne. URL <https://www.code-saturne.org/cms/>.
- K.-F. Dagestad. Mean bias deviation of the Heliosat algorithm for varying cloud properties and sun-ground-satellite geometry. (79):215–224, 2004.
- V. De Hulst. *Multiple Light Scattering: Tables, Formulas and Applications*. Academic press, 1980.
- J. Delanoë, J. Protat, J-P. Vinson, W. Brett, C. Caudoux, F. Bertrand, J. Parent du Chatelet, R. Hallali, L. Barthes, M. Haeffelin, and J-C. Dupont. Basta: A 95-ghz fmcw doppler radar for cloud and fog studies. *J. Atmos. Ocean. Technol.*, 33(5):1023 – 1038, 2016. doi: 10.1175/JTECH-D-15-0104.1.
- M. Diagne, M. David, P. Lauret, J. Boland, and N. Schmutz. Review of solar irradiance forecasting methods and a proposition for small-scale insular grids. *Renewable and Sustainable Energy Reviews*, 27:65–76, November 2013. ISSN 13640321. doi: 10.1016/j.rser.2013.06.042.
- ECMWF. URL <https://www.ecmwf.int/>.
- A. S. Eddington. On the radiative equilibrium of the stars. *Mon. Notices Royal Astron. Soc.*, 77: 16–35, 1916. ISSN 0035-8711. doi: 10.1093/mnras/77.1.16.

Bibliography

- W. M. Elsasser. Heat transfer by infrared radiation in the atmosphere. *Wiley Online Library*, 6, 1942.
- B. Espinar, P. Blanc, B. Wald, L. and Gschwind, L.I Ménard, E. Wey, C. Thomas, and L. Saboret. *HelioClim-3: a near-real time and long-term surface solar irradiance database*. Risoe, Denmark, May 2012.
- F. Evans. The spherical harmonics discrete ordinate method for three-dimensional atmospheric radiative transfer. *J. Atmos. Sci.*, 55(3):429 – 446, 1998. doi: 10.1175/1520-0469(1998)055<0429:TSHDOM>2.0.CO;2.
- C. Gautier, G. Diak, and S. Masse. A simple physical model to estimate incident solar radiation at the surface from goes satellite data. *J. Applied Meteor.*, 19(8):1005–1012, 1980. ISSN 00218952, 2163534X. doi: 10.1175/1520-0450(1980)019<1005:ASPMTE>2.0.CO;2.
- E. Gregow, AV. Lindfors, SH. van der Veen, D. Schoenach, S. de Haan, and M. Lindskog. The use of satellite and surface observations for initializing clouds in the harmonie nwp model. *Meteorol. Appl.*, 27(e1965), 2020. doi: 10.1002/met.1965.
- G. Grell and D. Devenyi. A generalized approach to parameterizing convection combining ensemble and data assimilation techniques. *Geophys. Res. Lett.*, 29, 07 2002. doi: 10.1029/2002GL015311.
- G. Grell, S. Peckham, R. Schmitz, S. McKeen, G. Frost, W. Skamarock, and B. Eder. Fully coupled “online” chemistry within the WRF model. *Atmos. Environ.*, 39(37):6957–6975, December 2005. ISSN 1352-2310. doi: 10.1016/j.atmosenv.2005.04.027.
- C. Gueymard. REST2: High-performance solar radiation model for cloudless-sky irradiance, illuminance, and photosynthetically active radiation – Validation with a benchmark dataset. *Sol. Energy*, 82(3):272–285, March 2008. ISSN 0038-092X. doi: 10.1016/j.solener.2007.04.008.
- C. A. Gueymard and J.A. Ruiz-Arias. Validation of direct normal irradiance predictions under arid conditions: A review of radiative models and their turbidity-dependent performance. *Renew. Syst. Energ. Rev.*, 45(C):379–396, 2015. doi: 10.1016/j.rser.2015.01.06.
- V. Guimet and D. Laurence. *A Linearised turbulent production in the k- model for engineering applications*. Elsevier Science Ltd, Oxford, 2002. ISBN 978-0-08-044114-6. doi: <https://doi.org/10.1016/B978-008044114-6/50014-4>.
- M. Gul, Y. Kotak, and S. Muneer, T.and Ivanova. Enhancement of albedo for solar energy gain with particular emphasis on overcast skies. *Energies*, 11(11):2881, 2018. doi: 10.3390/en11112881. Number: 11 Publisher: Multidisciplinary Digital Publishing Institute.
- M. Haeffelin, L. Barthès, O. Bock, C. Boitel, S. Bony, D. Bouniol, H. Chepfer, M. Chiriaco, J. Cuesta, J. Delanoë, P. Drobinski, J.-L. Dufresne, C. Flamant, M. Grall, A. Hodzic, F. Hourdin, F. Lapouge, Y. Lemaître, A. Mathieu, Y. Morille, C. Naud, V. Noël, W. O’Hirok, J. Pelon, C. Pietras, A. Protat, B. Romand, G. Scialom, and R. Vautard. Sirta, a ground-based atmospheric observatory for cloud and aerosol research. *Annales Geophysicae*, 23(2):253–275, 2005. doi: 10.5194/angeo-23-253-2005.

Bibliography

- M. Haeffelin, T. Bergot, T. Elias, R. Tardif, D. Carrer, P. Chazette, M. Colomb, P. Drobin-ski, E. Dupont, J.-C. Dupont, L. Gomes, L. Musson-Genon, C. Pietras, Artemio Plana-Fattori, Alain Protat, J. Rangognio, Jean-Christophe Raut, S. Rémy, D. Richard, J. Sciare, and X. Zhang. PARISFOG: Shedding new light on fog physical processes. *Bull. Amer. Meteor. Soc.*, 91:767–783, 2010. doi: 10.1175/2009BAMS2671.1.
- J D. Hamilton. *Time series analysis*. 1994.
- J. E. Hansen. Multiple scattering of polarized light in planetary atmospheres. part i. the doubling method. *J. Atmos. Sci.*, 28(1):120–125, 1971. ISSN 0022-4928, 1520-0469. doi: 10.1175/1520-0469(1971)028<0120:MSOPLI>2.0.CO;2.
- J.M. Haynes, C. Jakob, W.B. Rossow, G. Tselioudis, and J. Brown. Major characteristics of southern ocean cloud regimes and their effects on the energy budget. *J. Climate*, 24(19): 5061 – 5080, 2011. doi: 10.1175/2011JCLI4052.1.
- M. Hess, P. Koepke, and T Schult. Optical properties of aerosols and clouds: The software package OPAC. *Bull. Amer. Meteor. Soc.*, 79:831–844, 1998.
- R. Hogan and A. Bozzo. Ecrad: A new radiation scheme for the ifs. *ECMWF*, (787), 2016. doi: 10.21957/whntqkfdz.
- R.J. Hogan and J.K.P. Shonk. Incorporating the effects of 3D radiative transfer in the presence of clouds into two-stream multilayer radiation schemes. *J. Atmos. Sci.*, 70(2):708 – 724, 2013. doi: 10.1175/JAS-D-12-041.1.
- B.N. Holben, T.F. Eck, I. Slutsker, D. Tanré, J.P. Buis, A. Setzer, E. Vermote, J.A. Reagan, Y.J. Kaufman, T. Nakajima, F. Lavenu, I. Jankowiak, and A. Smirnov. Aeronet—a federated instrument network and data archive for aerosol characterization. *Remote Sens. Environ.*, 66 (1):1 – 16, 1998. ISSN 0034-4257. doi: 10.1016/S0034-4257(98)00031-5.
- IEA. Renewables 2020, analysis and forecast to 2025, 2020. URL https://iea.blob.core.windows.net/assets/1a24f1fe-c971-4c25-964a-57d0f31eb97b/Renewables_2020-PDF.pdf.
- P. Ineichen. Comparison of eight clear sky broadband models against 16 independent data banks. *Sol. Energy*, 80:468–478, 04 2006. doi: 10.1016/j.solener.2005.04.018.
- P. Ineichen. A broadband simplified version of the solis clear sky model. *Sol. Energy*, 82(8): 758–762, 2008. ISSN 0038-092X. doi: 10.1016/j.solener.2008.02.009.
- IRENA. Renewable capacity highlights. URL https://www.irena.org/-/media/Files/IRENA/Agency/Publication/2021/Apr/IRENA_-RE_Capacity_Highlights_2021.pdf?la=en&hash=1E133689564BC40C2392E85026F71A0D7A9C0B91.

Bibliography

- M.-J. Isabelle, L. Laurent, M.-L. Gobinddass, and L. Wald. On the applicability of the Heliosat-2 method to assess surface solar irradiance in the Intertropical Convergence Zone, French Guiana. *Int. J. Remote Sens.*, 34(8):3012–3027, April 2013. ISSN 0143-1161. doi: 10.1080/01431161.2012.756598.
- P. A. Jimenez, J. P. Hacker, J. Dudhia, S. E. Haupt, J. A. Ruiz-Arias, C. A. Gueymard, G. Thompson, T. Eidhammer, and A. Deng. WRF-solar: Description and clear-sky assessment of an augmented NWP model for solar power prediction. *Bull. Amer. Meteor. Soc.*, 97(7):1249–1264, 2016a. ISSN 0003-0007, 1520-0477. doi: 10.1175/BAMS-D-14-00279.1.
- P. A. Jimenez, J. P. Hacker, J. Dudhia, S.E. Haupt, J. A. Ruiz-Arias, C. A. Gueymard, G. Thompson, T. Eidhammer, and A. Deng. WRF-Solar: Description and Clear-Sky Assessment of an Augmented NWP Model for Solar Power Prediction. *Bull. Amer. Meteor. Soc.*, 97(7):1249–1264, 2016b. ISSN 0003-0007. doi: 10.1175/BAMS-D-14-00279.1.
- J. Joseph and W. Wiscombe. The delta-eddington approximation for radiative flux transfer. *J. Atmos. Sci.*, 33:2452–2459, 1976.
- J. S. Kain and J. M. Fritsch. *Convective Parameterization for Mesoscale Models: The Kain-Fritsch Scheme*, pages 165–170. American Meteorological Society, Boston, MA, 1993. ISBN 978-1-935704-13-3. doi: 10.1007/978-1-935704-13-3_16.
- H. D. Kambezidis, B. E. Psiloglou, and B. M. Synodinou. Comparison between measurements and models for daily solar irradiation on tilted surfaces in athens, greece. *Renew. Energy*, 10(4):505–518, 1997. ISSN 0960-1481. doi: 10.1016/S0960-1481(96)00045-6.
- H.D. Kambezidis, B. E. Psiloglou, D. Karagiannis, U.C. Dumka, and D.G. Kaskaoutis. Recent improvements of the meteorological radiation model for solar irradiance estimates under all-sky conditions. *Renew. Energy*, 93:142–158, 2016. doi: 10.1016/j.renene.2016.02.
- M. Kasahara, R. Hôller, S. Tohno, Y. Onishi, and C.J. Ma. Application of pixe technique to studies on global warming/cooling effect on atmospheric aerosol. *Nucl. Instrum. Methods Phys. Res. A*, 189:204–208, 2002.
- F. Kasten and A.T. Young. Revised optical air mass tables and approximation formula. *Appl. Opt.*, 28(22):4735–4738, 1989. ISSN 2155-3165. doi: 10.1364/AO.28.004735.
- E. Kessler. On the continuity and distribution of water substance in atmospheric circulations. *Atmos. Res.*, 38(1):109 – 145, 1995. ISSN 0169-8095. doi: 10.1016/0169-8095(94)00090-Z.
- D. Koerner, J. Portsmouth, and W. Jakob. P_nmethod for multiple scattering in participating media. *Eurographics Symposium Proceedings*, 2018.
- P. Kostka, M. Weissmann, R. Buras, B. Mayer, and O. Stiller. Observation operator for visible and near-infrared satellite reflectances. *J. Atmos. Ocean. Technol.*, 31(6):1216–1233, 2014. ISSN 0739-0572, 1520-0426. doi: 10.1175/JTECH-D-13-00116.1.
- F. Kurzrock. Assimilation de données satellitaires géostationnaires dans des modèles atmosphériques à aire limitée pour la prévision du rayonnement solaire en région tropicale, 2019.

Bibliography

- F. Kurzrock, S. Cros, F. C. Ming, J. A. Otkin, L. Hutt, A. and Linguet, G.s Lajoie, and R. Potthast. A review of the use of geostationary satellite observations in regional-scale models for short-term cloud forecasting. *Meteorol. Z.*, 27(4):277–298, 11 2018. doi: 10.1127/metz/2018/0904.
- A. Lacis and J. Hansen. A Parameterization for the Absorption of Solar Radiation in the Earth's Atmosphere. *J. Atmos. Sci.*, 31(1):118–133, January 1974. ISSN 0022-4928. doi: 10.1175/1520-0469(1974)031<0118:APFTAO>2.0.CO;2.
- M. Lefèvre, A. Oumbe, P. Blanc, B. Espinar, B. Gschwind, Z. Qu, L. Wald, M. Schroedter-Homscheidt, C. Hoyer-Klick, A. Arola, A. Benedetti, J. W. Kaiser, and J.-J. Morcrette. McClear: A new model estimating downwelling solar radiation at ground level in clear-sky conditions. *Atmos. Meas. Tech.*, 6:2403–2418, 09 2013. doi: 10.5194/amt-6-2403-2013.
- M. Lefèvre, L. Wald, and L. Diabaté. Using reduced data sets ISCCP-B2 from the Meteosat satellites to assess surface solar irradiance. *Sol. Energy*, 81(2):240–253, February 2007. ISSN 0038-092X. doi: 10.1016/j.solener.2006.03.008.
- J. Lenoble. *Atmospheric radiative transfer*. A. Deepak Pub., 1993. ISBN 978-0-937194-21-8.
- K-N. Liou. A numerical experiment on Chandrasekhar's discrete-ordinate method for radiative transfer: Applications to cloudy and hazy atmospheres. *J. Atmos. Sci.*, 30(7):1303–1326, 1973. ISSN 0022-4928, 1520-0469. doi: 10.1175/1520-0469(1973)030<1303:ANE OCD>2.0.CO;2.
- K. N. Liou. *Radiation and Cloud Processes in the Atmosphere: Theory, Observation, and Modeling*. Oxford University Press; 1st edition, 1992.
- K.N. Liou. *An Introduction to Atmospheric Radiation*. ISSN. Elsevier Science, 2002. ISBN 9780080491677.
- B. Liu and R. Jordan. The interrelationship and characteristic distribution of direct, diffuse and total solar radiation. *Sol. Energy*, 4(3):1–19, 1960. ISSN 0038-092X. doi: 10.1016/0038-092X(60)90062-1.
- C. N. Long and J. J. DeLuisi. Development of an automated hemispheric sky imager for cloud fraction retrievals. *In Proceedings 10th Symposium on Meteorological Observations and Instrumentation, 11–16 January 1998, Phoenix, AZ, USA*, 1998.
- C. N. Long, T. P. Ackerman, K. L. Gaustad, and J. N. S. Cole. Estimation of fractional sky cover from broadband shortwave radiometer measurements. *J. Geophys. Res. Atmos.*, 111(D11), 2006. ISSN 2156-2202. doi: 10.1029/2005JD006475.
- E. Lorenz and D. Heinemann. Prediction of solar irradiance and photovoltaic power. *Comprehensive Renewable Energy*, 1:239–292, 2012. doi: 10.1016/B978-0-08-087872-0.00114-1.
- E. Lorenz, J. Hurka, D. Heinemann, and H. G. Beyer. Irradiance forecasting for the power prediction of grid-connected photovoltaic systems. *J Sel Top Appl Earth Obs Remote Sens.*, 2: 2 – 10, 04 2009. doi: 10.1109/JSTARS.2009.2020300.

Bibliography

- Qiao Lu, Chao Liu, Delong Zhao, Chen Zeng, Jing Li, Chunsong Lu, Jiandong Wang, and Bin Zhu. Atmospheric heating rate due to black carbon aerosols: Uncertainties and impact factors. *Atmos. Res.*, 240:104891, 2020. ISSN 0169-8095. doi: 10.1016/j.atmosres.2020.104891.
- L. Makké. Modélisation tridimensionnelle du rayonnement infrarouge atmosphérique utilisant l'approximation en émissivité : application à la formation du brouillard radiatif, 2015. URL <https://pastel.archives-ouvertes.fr/tel-01310337>.
- V. Mallet, D. Quélo, B. Sportisse, M. Ahmed De Biasi, I. Korsakissok, Edouard Debry, L. Wu, Y. Roustan, K. Sartelet, M. Tombette, and H. Foudhil. Technical note: The air quality modeling system polyphemus. *Atmos. Chem. Phys.*, 7(20):5487, 2007. doi: 10.5194/acp-7-5479-2007.
- T. Markvart, A. McEvoy, and L. Castaer. *Practical Handbook of Photovoltaics: Fundamentals and Applications*. Elsevier, 2003. ISBN 978-1-85617-390-2.
- B. Mayer. Radiative transfer in the cloudy atmosphere. *Eur. Phys. J. Conferences*, 1:75–99, 2009. ISSN 2100-014X. doi: 10.1140/epjconf/e2009-00912-1.
- B. Mayer and A. Kylling. Technical note: The libRadtran software package for radiative transfer calculations - description and examples of use. *Atmos. Chem. Phys.*, 5(7):1855–1877, 2005. ISSN 1680-7316. doi: 10.5194/acp-5-1855-2005.
- W. E. Meador and W. R. Weaver. Two-Stream Approximations to Radiative Transfer in Planetary Atmospheres: A Unified Description of Existing Methods and a New Improvement. *J. Atmos. Sci.*, 37(3):630–643, March 1980. ISSN 0022-4928. doi: 10.1175/1520-0469(1980)037<0630:TSATRT>2.0.CO;2.
- C. Meng. Surface albedo assimilation and its impact on surface radiation budget in beijing. *Advances in Meteorology*, 2020. doi: 10.1155/2020/8312451.
- Mie. Beiträge zur optik trüber medien, speziell kolloidaler metallösungen. *Annalen der Physik*, 1908.
- M. Milliez. *Modélisation micro-météorologique en milieu urbain : dispersion des polluants et prise en compte des effets radiatifs*. phdthesis, 2006. URL <http://www.theses.fr/2006ENPC0629>.
- T. Ming, R. Richter, W. Liu, and S. Caillol. Fighting global warming by climate engineering: Is the earth radiation management and the solar radiation management any option for fighting climate change? *Renew. Syst. Energ. Rev.*, 31:792–834, 2014. ISSN 1364-0321. doi: 10.1016/j.rser.2013.12.032.
- A. Moncada, W. Richardson, and . Vega-Avila. Deep learning to forecast solar irradiance using a six-month utsa skyimager dataset. *Energies*, 11:1988, 07 2018. doi: 10.3390/en11081988.
- I. Moradi, R. Mueller, B. Alijani, and G. A. Kamali. Evaluation of the Heliosat-II method using daily irradiation data for four stations in Iran. *Sol. Energy*, 83(2):150–156, February 2009. ISSN 0038-092X. doi: 10.1016/j.solener.2008.07.010.

Bibliography

- J.-J. Morcrette and Y. Fouquart. The overlapping of cloud layers in shortwave radiation parameterizations. *J. Atmos. Sci.*, 43(4):321–328, 1986. ISSN 0022-4928, 1520-0469. doi: 10.1175/1520-0469.
- J.-J. Morcrette and C. Jakob. The response of the ecmwf model to changes in the cloud overlap assumption. *Mon. Wea. Rev.*, 128(6):1707–1732, 2000. ISSN 1520-0493, 0027-0644. doi: 10.1175/1520-0493.
- J.-J. Morcrette, H. W. Barker, J. N. S. Cole, M. J. Iacono, and R. Pincus. Impact of a New Radiation Package, McRad, in the ECMWF Integrated Forecasting System. *Mon. Wea. Rev.*, 136(12): 4773–4798, December 2008. ISSN 0027-0644. doi: 10.1175/2008MWR2363.1.
- J.-J. Morcrette, O. Boucher, L. Jones, D. Salmond and P. Bechtold, A. Beljaars, A. Benedetti, A. Bonet, J. W. Kaiser, M. Razinger, M. Schulz, S. Serrar, A. J. Simmons, M. Sofiev, M. Suttie, A. M. Tompkins and, and A. Untch. Aerosol analysis and forecast in the european centre for medium-range weather forecasts integrated forecast system:forward modeling. *J. Geophys. Res.*, 114, 2009. doi: 10.1029/2008JD011235,2009.
- Jean-Jacques Morcrette. Radiation and cloud radiative properties in the european centre for medium range weather forecasts forecasting system. *J. Geophys. Res. Atmos.*, 96(D5):9121–9132, 1991. doi: 10.1029/89JD01597.
- Y. Morille, M. Haeffelin, P. Drobinski, and J. Pelon. STRAT: An Automated Algorithm to Retrieve the Vertical Structure of the Atmosphere from Single-Channel Lidar Data. *J. Atmos. Ocean. Technol.*, 24(5):761–775, May 2007. ISSN 0739-0572. doi: 10.1175/JTECH2008.1.
- G. Motos, J. Schmale, J. C. Corbin, M. Zanatta, U. Baltensperger, and M. Gysel-Beer. Droplet activation behaviour of atmospheric black carbon particles in fog as a function of their size and mixing state. *Atmos. Chem. Phys.*, 19:2183–2207, 2019.
- L. Musson-Genon. Comparison of different simple turbulence closures with a one-dimensional boundary layer model. *Mon. Wea. Rev.*, 123(1):163–180, 1995. ISSN 1520-0493, 0027-0644. doi: 10.1175/1520-0493(1995)123<0163:CODSTC>2.0.CO;2.
- L. Musson-Genon, E. Dupont, and D. Wendum. Reconstruction of the surface-layer vertical structure from measurements of wind, temperature and humidity at two levels. *Bound.-Layer Meteorol.*, 124(2):235–250, 2007. ISSN 1573-1472. doi: 10.1007/s10546-007-9178-5.
- D.R. Myers. *Solar Radiation: Practical Modeling for Renewable Energy Applications*. CRC Press, 2017. ISBN 978-1-351-83247-2.
- R. Müller, K-F. Dagestad, P. Ineichen, M. Schroedter-Homscheidt, S. Cros, D. Dumortier, R. Kuhlemann, J. Olseth, G.o Izquierdo, C. Reise, L. Wald, and D. Heinemann. Rethinking satellite-based solar irradiance modelling: The solis clear-sky module. *Remote Sens. Environ.*, pages 160–174, 05 2004. doi: 10.1016/j.rse.2004.02.009.
- C.M. Naud, A.D. Del Genio, M. Bauer, and W. Kovari. Cloud vertical distribution across warm and cold fronts in cloudsat–calipso data and a general circulation model. *J. Climate*, 23(12): 3397 – 3415, 15 Jun. 2010. doi: 10.1175/2010JCLI3282.1.

Bibliography

- A. Nenes and J Seinfeld. Parameterization of cloud droplet formation in global climate models. *J. Geophys. Res. Atmos.*, 108, 2003. doi: 10.1029/2002JD002911.
- K. P. Nielsen, E. Gleeson, and L. Rontu. Radiation sensitivity tests of the harmonie 37h1 nwp model. *Geosci. Model Dev.*, 7(4):1433–1449, 2014. doi: 10.5194/gmd-7-1433-2014.
- J. Nou, R. Chauvin, S. Thil, and S. Grieu. A new approach to the real-time assessment of the clear-sky direct normal irradiance. *Appl. Math. Model.*, 40, 2016. doi: 10.1016/j.apm.2016.03.022.
- L. Oreopoulos and M. Khairoutdinov. Overlap properties of clouds generated by a cloud-resolving model. *J. Geophys. Res. Atmos.*, 108(D15), 2003. ISSN 2156-2202. doi: 10.1029/2002JD003329.
- A. Oumbe, P. Blanc, T. Ranchin, M. Schroedter-Homscheidt, and L. Wald. *A new method for estimating solar energy resource*. 2009.
- W. O’Hirok and C. Gautier. A three-dimensional radiative transfer model to investigate the solar radiation within a cloudy atmosphere. part i: Spatial effects. *J. Atmos. Sci.*, 55(12):2162 – 2179, 1998. doi: 10.1175/1520-0469(1998)055<2162:ATDRTM>2.0.CO;2.
- A. Padovan, D. Del Col, V. Sabatelli, and D. Marano. Dni estimation procedures for the assessment of solar radiation availability in concentrating systems. *Energy Procedia*, 57, 12 2014. doi: 10.1016/j.egypro.2014.10.100.
- G. W. Paltridge and C. M. Platt. *Radiative processes in meteorology and climatology*. Elsevier Scientific Pub. C., 1976. ISBN 978-0-444-41444-1. doi: 10.1002/qj.49710343713.
- G. H. Peebles and M. S. Plesset. Transmission of gamma-rays through large thicknesses of heavy materials. *Phys. Rev.*, 81(3):430–439, 1951. doi: 10.1103/PhysRev.81.430.
- R. Polkinghorne and T. Vukicevic. Data assimilation of cloud-affected radiances in a cloud-resolving model. *Mon. Wea. Rev.*, 139(3):755–773, 2011. ISSN 1520-0493, 0027-0644. doi: 10.1175/2010MWR3360.1.
- R. Polkinghorne, T. Vukicevic, and K. F. Evans. Validation of cloud-resolving model background data for cloud data assimilation. *Mon. Wea. Rev.*, 138(3):781–795, 2010. ISSN 1520-0493, 0027-0644. doi: 10.1175/2009MWR3012.1.
- J. Polo, L. Pomares, and J. Vindel. Correcting satellite derived dni with systematic and seasonal deviations: Application to india. *Renew. Energy*, 80:238–243, 08 2015. doi: 10.1016/j.renene.2015.02.031.
- B. E. Psiloglou and H. D. Kambezidis. Performance of the meteorological radiation model during the solar eclipse of 29 March 2006. *Atmos. Chem. Phys.*, 7(23):6047–6059, December 2007. ISSN 1680-7316. doi: 10.5194/acp-7-6047-2007.

Bibliography

- B. E. Psiloglou, M. Santamouris, and D. N. Asimakopoulos. Predicting the spectral and broadband aerosol transmittance in the atmosphere for solar radiation modelling. *Renew. Energy*, 12(3):259–279, November 1997. ISSN 0960-1481. doi: 10.1016/S0960-1481(97)00044-X.
- B. E. Psiloglou, M. Santamouris, and D. N. Asimakopoulos. Atmospheric broadband model for computation of solar radiation at the earth's surface. application to mediterranean climate. *Pure appl. geophys.*, 157(5):829–860, 2000. ISSN 1420-9136. doi: 10.1007/PL00001120.
- F. Qiang. An accurate parameterization of the solar radiative properties of cirrus clouds for climate models. *J. Climate*, 9:2058–2082., 1996. doi: 10.1175/1520-0442(1996)009<2058: AAPOTS>2.0.CO;2.
- Z. Qu. La nouvelle méthode heliosat-4 pour l'évaluation du rayonnement solaire au sol, 2013. Issue: 2013ENMP0040.
- J. Rangognio. Impact des aérosols sur le cycle de vie du brouillard : de l'observation à la modélisation, 2009.
- A. Rap, C. Scott, D. Spracklen, N. Bellouin, P. M. Forster, K. S. Carslaw, A. Schmidt, and G. Mann. Natural aerosol direct and indirect radiative effects. *Geophys. Res. Lett.*, 40(12): 3297–3301, 2013. ISSN 1944-8007. doi: 10.1002/grl.50441.
- G. Reikard. Predicting solar radiation at high resolutions: A comparison of time series forecasts. *Sol. Energy*, 83(3):342–349, March 2009. ISSN 0038-092X. doi: 10.1016/j.solener.2008.08.007.
- C. Rigollier, O. Bauer, and L. Wald. On the clear sky model of the esra - european solar radiation atlas - with respect to the heliosat method. *Sol. Energy*, 68:33–48, 01 2000. doi: 10.1016/S0038-092X(99)00055-9.
- B. Ritter and J-F. Geleyn. A comprehensive radiation scheme for numerical weather prediction models with potential applications in climate simulations. *Mon. Wea. Rev.*, 120(2):303, 1992. doi: 10.1175/1520-0493(1992)120.
- R. Roebeling, Arnout Feijt, and Piet Stammes. Cloud property retrievals for climate monitoring: Implications of differences between SEVIRI on METEOSAT-8 and AVHRR on NOAA-17. *J. Geophys. Res.*, 111:D20210, January 2006.
- T. Rose, S. Crewell, U. Löhnert, and C. Simmer. A network suitable microwave radiometer for operational monitoring of the cloudy atmosphere. *Atmos. Res.*, 75(3):183 – 200, 2005. ISSN 0169-8095. doi: 10.1016/j.atmosres.2004.12.005. CLIWA-NET: Observation and Modelling of Liquid Water Clouds.
- G. Roy, S. Hayman, and W. Julian. Sky analysis from ccd images: cloud cover. *Light. Res. Technol.*, 33(4):211–221, 2001. doi: 10.1177/136578280103300402.
- P. Räisänen. Effective longwave cloud fraction and maximum-random overlap of clouds:a problem and a solution. *Mon. Wea. Rev.*, 126(12):3336–3340, 12 1998. ISSN 0027-0644. doi: 10.1175/1520-0493(1998)126<3336:ELCFAM>2.0.CO;2.

Bibliography

- I. Sandu, P. Tulet, and J. L. Brenguier. Parameterization of the cloud droplet single scattering albedo based on aerosol chemical composition for LES modelling of boundary layer clouds. *Geophys. Res. Lett.*, 32, 2005. doi: 10.1029/2005GL023994.
- Chandan Sarangi, Vijay P. Kanawade, Sachchida N. Tripathi, Abin Thomas, and Dilip Ganguly. Aerosol-induced intensification of cooling effect of clouds during indian summer monsoon. 9(1):3754, 2018. ISSN 2041-1723. doi: 10.1038/s41467-018-06015-5. URL <https://www.nature.com/articles/s41467-018-06015-5>. Number: 1 Publisher: Nature Publishing Group.
- K. Sartelet, C. Legorgeu, L. Lugon, Y. Maanane, and L. Musson-Genon. Representation of aerosol optical properties using a chemistry transport model to improve solar irradiance modelling. *Sol. Energy*, 176:439–452, December 2018a. ISSN 0038-092X. doi: 10.1016/j.solener.2018.10.017.
- K. Sartelet, S. Zhu, S. Moukhtar, M. André, V. Andre, J.M.and Gros, O. Favez, and M. Brasseur, A.and Redaelli. Emission of intermediate, semi and low volatile organic compounds from traffic and their impact on secondary organic aerosol concentrations over greater paris. *Atmos. Environ.*, (180):126–137, 2018b. doi: doi:10.1016/j.atmosenv.2018.02.031.
- K. N. Sartelet, E. Debry, K. Fahey, Y. Roustan, M. Tombette, and B. Sportisse. Simulation of aerosols and gas-phase species over Europe with the Polyphemus system: Part I—Model-to-data comparison for 2001. *Atmos. Environ.*, 41(29):6116–6131, September 2007. ISSN 1352-2310. doi: 10.1016/j.atmosenv.2007.04.024.
- E Schaller. A delta two stream approximation in radiative flux calculation. *Contrib. Atmos. Phys.*, 52:17–26, 1979.
- C. Schillings, H. Mannstein, and R. Meyer. Operational method for deriving high resolution direct normal irradiance from satellite data. *Sol. Energy*, 76(4):475 – 484, 2004. ISSN 0038-092X. doi: 10.1016/j.solener.2003.07.038.
- J. Seinfeld and S. Pandis. *Atmospheric Chemistry and Physics: From Air Pollution to Climate Change*, 3rd Edition | Wiley, 2016.
- J. H. Seinfeld and S. N. Pandis. *Atmospheric Chemistry and Physics from air pollution to climate change*. John Wiley and Sons, Incorporated. New York., 1998.
- W. Skamarock, J. Klemp, J. Dudhia, D. Gill, D. Barker, W. Wang, X-Y. Huang, and M. Duda. A description of the advanced research wrf version 3. page 1002 KB, 2008. doi: 10.5065/D68S4MVH.
- American Meteorology Society. Fog - glossary of meteorology. URL <https://glossary.ametsoc.org/wiki/Fog>.
- K. Stamnes and H. Dale. A new look at the discrete ordinate method for radiative transfer calculations in anisotropically scattering atmospheres. II: Intensity computations. *J. Atmos. Sci.*, 38(12):2696–2706, 1981. ISSN 0022-4928, 1520-0469. doi: 10.1175/1520-0469(1981)038<2696:ANLATD>2.0.CO;2.

Bibliography

- K. Stamnes and R. A. Swanson. A new look at the discrete ordinate method for radiative transfer calculations in anisotropically scattering atmospheres. *J. Atmos. Sci.*, 38(2):387–399, 1981. ISSN 0022-4928, 1520-0469. doi: 10.1175/1520-0469(1981)038<0387:ANLATD>2.0.CO;2.
- Knut Stamnes, S-Chee Tsay, Warren Wiscombe, and Kolf Jayaweera. Numerically stable algorithm for discrete-ordinate-method radiative transfer in multiple scattering and emitting layered media. *Appl. Opt.*, 27(12):2502–2509, Jun 1988. doi: 10.1364/AO.27.002502.
- G. L. Stephens. Radiation Profiles in Extended Water Clouds. I: Theory. *J. Atmos. Sci.*, 35(11): 2111–2122, November 1978a. doi: 10.1175/1520-0469(1978)035<2111:RPIEWC>2.0.CO;2>.
- G.L. Stephens. Radiation Profiles in Extended Water Clouds. II: Parameterization Schemes. *J. Atmos. Sci.*, 35,11:2123–2132, 1978b. doi: 10.1175/1520-0469(1978)035<2123:RPIEWC>2.0.CO;2.
- G.L. Stephens. Review: The parameterisation of radiation for numerical weather prediction and climate models. *Mon. Wea. Rev.*, 112:826–867, 1984. doi: 10.1175/1520-0493(1984)112<0826:TPORFN>2.0.CO;2.
- G. G. Stokes. IV. on the intensity of the light reflected from or transmitted through a pile of plates. *Proceedings of the Royal Society of London*, 11:545–556, 1862. doi: 10.1098/rspl.1860.0119.
- C. Stubenrauch, Rossow W., and Kinne S. Assessment of global cloud data sets from satellites. *WCRP report*, 2012.
- C.J. Stubenrauch. Assessment of Global Cloud Datasets from Satellites: Project and Database Initiated by the GEWEX Radiation Panel. *Bull. Amer. Meteor. Soc.*, 94:1031–1049, 2013. doi: 10.1175/BAMS-D-12-00117.1.
- L. Tian and J. Curry. Cloud overlap statistics. *J. Geophys. Res. Atmos.*, 94:9925–9935, 1989.
- G. Titos Vela. *Characterization of atmospheric aerosol particles using in-situ techniques: Optical, chemical and hygroscopic properties*. PhD thesis, 2014. URL <https://digibug.ugr.es/handle/10481/39637>. Accepted: 2016-01-27T13:37:10Z.
- S-C. Tsay, K. Stamnes, and K. Jayaweera. Radiative energy budget in the cloudy and hazy arctic. *J. Atmos. Sci.*, 46(7):1002 – 1018, 1989. doi: 10.1175/1520-0469(1989)046<1002:REBITC>2.0.CO;2.
- S. Veerapen and W. Huiqing. *Shadowing effect on the power output of a photovoltaic panel*. 2016. doi: 10.1109/IPEMC.2016.7512858.
- E. Wærsted. Phd thesis: Description of physical processes driving the life cycle of radiation fog and fog–stratus transitions based on conceptual models, 2018.

Bibliography

- M.A. Wahab, M. El-Metwally, R. Hassan, A. Lefèvre, M. and Oumbe, and L. Wald. Assessing surface solar irradiance and its long-term variations in the northern Africa desert climate using Meteosat images. *Int. J. Remote Sens.*, 31(1):261–280, January 2010. ISSN 0143-1161, 1366-5901. doi: 10.1080/01431160902882645.
- L. Wald and P. Blanc. The Performances of the HelioClim Databases in Mozambique. *ISES Solar World Congress 2011, Aug 2011, Kassel, Germany*, 2011.
- U. Wissmeier, R. Buras, and B. Mayer. paNTICA: A fast 3d radiative transfer scheme to calculate surface solar irradiance for NWP and LES models. *J. Appl. Meteorol. Climatol.*, 52(8): 1698–1715, 2013. ISSN 1558-8424, 1558-8432. doi: 10.1175/JAMC-D-12-0227.1.
- Y. Xie and M. Sengupta. A fast all-sky radiation model for solar applications with narrowband irradiances on tilted surfaces (FARMS-NIT): Part i. the clear-sky model. *Sol. Energy*, 174: 691–702, 2018. ISSN 0038-092X. doi: 10.1016/j.solener.2018.09.056.
- Y. Xie, M. Sengupta, and J. Dudhia. A fast all-sky radiation model for solar applications (farms): Algorithm and performance evaluation. *Sol. Energy*, 135:435–445, 06 2016. doi: 10.1016/j.solener.2016.06.003.
- Y. Xie, M. Sengupta, and C. Wang. A fast all-sky radiation model for solar applications with narrowband irradiances on tilted surfaces (FARMS-NIT): Part II. the cloudy-sky model. *Sol. Energy*, 188:799–812, 2019. ISSN 0038-092X. doi: 10.1016/j.solener.2019.06.058.
- Y. Xie, M. Sengupta, Y. Liu, H. Long, Q. Min, W. Liu, and A. Habte. A physics-based DNI model assessing all-sky circumsolar radiation. *iScience*, 23(3):100893, 2020. ISSN 2589-0042. doi: 10.1016/j.isci.2020.100893.
- X. Zhang. *Modélisation du brouillard durant la campagne ParisFog : approche prédictive et étude de l'effet des hétérogénéités spatiales*. phdthesis, 2010. URL <http://www.theses.fr/2010ENPC1007>.
- X. Zhang, L. Musson-Genon, E. Dupont, M. Milliez, and B. Carissimo. On the influence of a simple microphysics parametrization on radiation fog modelling: A case study during ParisFog. *Bound.-Layer Meteorol.*, 151(2):293–315, 2014. ISSN 1573-1472. doi: 10.1007/s10546-013-9894-y.
- Y. Zhu, C. Zhong, and K. Xu. Ray effect in rarefied flow simulation. *J. Comp. Phys.*, 422:109751, 2020. ISSN 00219991. doi: 10.1016/j.jcp.2020.109751.
- P. Zieger, R. Fierz-Schmidhauser, M. Gysel, J. Ström, S. Henne, K. E. Yttri, U. Baltensperger, and E. Weingartner. Effects of relative humidity on aerosol light scattering in the arctic. *Atmos. Chem. Phys.*, 10(8):3875–3890, 2010. ISSN 1680-7316. doi: 10.5194/acp-10-3875-2010.

List of Figures

1	Photo taken by the sky imager during my visit at the Bonn-Rhein-Sieg University	iii
1.1	Global renewable generation capacity by energy source (left panel) and power capacity growth (right panel) by IRENA.	2
1.2	Schematic representation of the direct, diffuse and ground-reflected irradiance.	3
2.1	Electromagnetic radiation spectrum	8
2.2	Illustration of the differential solid angle $d\Omega$ in polar coordinates and the zenith θ and azimuthal ϕ angles. [Liou, 2002]	9
2.3	Illustration of the solar zenith θ_0 and azimuthal ϕ_0 angles. [Nou et al., 2016]	9
2.4	Spectral energy curve outside the atmosphere and at sea level. The darkened areas represent gaseous absorption in the atmosphere (Lacis and Hansen [1974] (referred to as LH74)).	12
2.5	Vertical temperature profile [Liou, 2002]	13
2.6	Concentrations of permanent and variable gases in the atmosphere [Liou, 2002].	14
2.7	Schematic representation of the distribution of an atmospheric aerosol. Principal modes, sources, and particle formation and removal mechanisms are indicated [Seinfeld and Pandis, 1998]	16
2.8	Schematic representation of various clouds. Ci: cirrus, cc: cirrocumulus, Ac: altocumulus, Sc: stratocumulus, Cs: cirrostratus, At: altostratus, St: stratus, Ns: nimbostratus, Cb: cumulonimbus, Cu: cumulus. [Lenoble, 1993]	18
2.9	The physical processes which impact the liquid water of the fog layer by producing water (marked in blue) or reducing it (marked in red) [Wærsted, 2018]	19
2.10	Schematic representation of a pyranometer (left panel) for the measurement of the total global irradiance by integrating over all the directions of the hemisphere, a pyranometer with a shadow ring (middle panel) for the measurement of the total diffuse irradiance by integrating over all the directions of the hemisphere except a solid angle around the sun, a pyrliometer (right panel) for the measurement of the direct normal incident irradiance by integrating only over the solid angle around the sun [Blanc et al., 2017].	25
2.11	Satellite image of the Ecole Polytechnique campus, where the SIRTA observatory is situated. The two zones where instruments from which data are used in this thesis are shown.	27
3.1	Geometry of a plane parallel atmosphere where θ and ϕ are the solar zenith and azimuthal angles and s represents the sun [Liou, 2002].	35

List of Figures

3.2	Configuration of the adding method. For convenient illustration, the two layers (of optical depth τ_1 and τ_2) are illustrated like if they were physically separated.[Liou, 2002]	37
3.3	Illustrated diagram of the adding method for the computation of internal intensities U and D (defined in section 3.3.2.2) [Liou, 2002]	37
3.4	Schematic representation of the integral method (left) and multi-layered method (right) of the 1D solar radiation scheme of code_saturne.	41
3.5	Illustrated diagram of the discrete ordinate method for $N_{DOM}=8$, it is represented in 2D for simplification purposes.	43
4.1	Diurnal cycle of global (left panel) and direct (right panel) irradiances measured at the SIRTA during clear-sky days in August 2009 (---) and compared to simulated values computed with HelioClim (—), code_saturne (—), WRF solar (—), WRF-ref (—) from KS18 .	51
4.2	Diurnal cycle of global (left panel) and direct (right panel) irradiances measured at the SIRTA during cloudy-sky days in August 2009 (---) and compared to simulated values computed with HelioClim (—), code_saturne (—), WRF solar (—), WRF-ref (—) from KS18 .	51
4.3	Diurnal cycle of global (left panel) and direct (right panel) irradiances measured at the SIRTA during cloudy-sky days in August 2009 (---) and compared to simulated values computed with code_saturne as in KS18 (—) after improving the model and coupling it with satellite measurements for the COPs (—)	53
4.4	Ground albedo from WRF versus the one measured at SIRTA (left panel). Estimated ground albedo at SIRTA versus μ_0 (cosinus of the solar zenith angle) (right panel) during the period 08/01/2014-30/10/2014.	54
4.5	Topographic map of the main domain (W01 = Western Europe) showing the location of the two nested domains (W02 = France and W03 =Île-de-France). The SIRTA and Carpentras sites are located by a star. The domains simulated with Polyphemus/Polair3D are represented by the red quadrilaterals (P01 = Europe and P02 = France). (KS18)	55
4.6	Simulated versus observed AOD in 2014 at $\lambda=500$ nm (left panel) and $\lambda=1000$ nm (right panel)	57
4.7	Scheme representing the models chain used for our cases of studies of August 2009 and the year 2014.	62
4.8	Distribution of cloud fraction during August 2009 (a) and the comparison between the two available cloud fractions for year 2014 (b) at SIRTA.	66
4.9	The cloud fraction (PYR) at SIRTA during the four seasons of 2014.	67
4.10	Distribution of COPs in August 2009 and year 2014.	68
4.11	Distribution of LWP versus cloud fraction from PYR	69
4.12	COD versus LWP from 2005 to 2010 at SIRTA (*), the approximation of COD using the fitted model (linear model — + logarithmic model — and equation 4.1 with $r_e=12\mu\text{m}$ —).	70

List of Figures

4.13	Diurnal cycle of solar irradiances at SIRTA on clear-sky days in August 2009 (in $W m^{-2}$)	72
4.14	RMSEs (in $W m^{-2}$) between simulated and measured global (a) and direct (b) solar irradiances at SIRTA during cloudy-sky days in 2014. WRF evaluation: - - - Sim14.0. Sensitivity to cloud fraction/COD: * Sim14.1; * Sim14.2; * Sim14.4; - - - Sim14.3; - - - Sim14.5; - - - Sim14.6.	77
4.15	MBEs (in $W m^{-2}$) between simulated and measured global (a) and direct (b) solar irradiances at SIRTA during cloudy-sky days in 2014. WRF evaluation: - - - Sim14.0. Sensitivity to cloud fraction/COD: * Sim14.1; * Sim14.2; * Sim14.4; - - - Sim14.3; - - - Sim14.5; - - - Sim14.6.	77
4.16	NMB scores (in %) between simulated and measured global (a) and direct (b) solar irradiances at SIRTA during cloudy-sky days in 2014. WRF evaluation: - - - Sim14.0. Sensitivity to cloud fraction/COD: * Sim14.1; * Sim14.2; * Sim14.4; - - - Sim14.3; - - - Sim14.5; - - - Sim14.6.	78
4.17	Diurnal cycle of global irradiances measured at SIRTA during cloudy-sky days in August 2009 (- - -) and computed with HelioSat (-), code_saturne-Sim.09.3 (-)	87
4.18	Diurnal cycle of global (left panel) and direct (right panel) irradiances during cloudy sky days in May 2014 measured at SIRTA (- - -) and computed with HelioSat (-) and code_saturne-Sim.14.6 (-)	88
4.19	Diurnal cycle of global (left panel) and direct (right panel) irradiances during cloudy sky days in January 2014 measured at SIRTA (- - -) and computed with HelioSat (-) and code_saturne-Sim.14.6 (-)	88
4.20	MBE (in $W m^{-2}$) between SIRTA measurements of global (left panel) and direct (right panel) irradiances and simulations using HelioSat-v3 (*) and code_saturne-Sim.14.6 (*) for every month of year 2014.	89
4.21	RMSE (in $W m^{-2}$) between SIRTA measurements of global (left panel) and direct (right panel) irradiances and simulations using HelioSat-v3 (*) and code_saturne-Sim.14.6 (*) for every month of year 2014.	89
4.22	COD versus LWP from 2005 to 2010 at SIRTA (*), the approximation of COD using the fitted model (linear model — + logarithmic model —) and equation 4.1 with $r_e=12\mu m$ —) and Stephens [1978b] parametrization —.	91
4.23	Global (left panel) and direct (right panel) irradiances measured at the SIRTA and compared to simulated values computed with code_saturne (Sim. 14.3).	92
4.24	The proportion of low (blue), middle (red) and high (black) clouds at the SIRTA Observatory from 08/01/2014 to 30/10/2014 from ceilometer measurements.	92
4.25	Diagram showing the time evolution of LWP (in red, in $g m^{-2}$), Precipitation (in purple, in mm/hr), cloud fraction (in blue) and cloud base height (in green, in m) on the 08/09/2014 at the SIRTA Observatory. The horizontal black lines mark the separation between the low, middle and high clouds.	94
5.1	Temporal evolution of the simulated liquid water content in $g kg^{-1}$ with the solar scheme when surface parameters are deduced from observations.	103

List of Figures

5.2	Comparisons, at the earth surface, between observations and simulation of global solar (left) and direct solar (right) irradiances.	104
5.3	Heating rate in the atmospheric layers on 18/02/2007 at 1500 (UTC) for the UV-vis band (left) and for the SIR band (right) (in °C/day) — base case; - - - no aerosols in the modelling of irradiance fluxes; -v- aerosol boundary layer of 500 m.	104
5.4	Same as figure 5.2 but for a simulation without aerosols in the modelling of irradiance fluxes.	105
5.5	Vertical profile of the liquid water content (in g m ³) (left) and cloud fraction (right) at 0900 (UTC) on the 19 th February for the base case.	106
5.6	Downward global fluxes in the atmospheric layers at 0900 (UTC) on the 19 th of February for UV-vis band (left) and for SIR band (right) (— base case; +- constant cloud droplet's effective radius of 10μm).	107
5.7	Heating rate in the atmospheric layers at 0900 (UTC) on the 19 th of February for UV-vis band (left) and for SIR band (right) (for 'stationary case') (— base case, i.e. without BC; -.- V _{JBC} = 8.6 10 ⁻⁶ ; - - - V _{JBC} = 1.6 10 ⁻⁴).	109
5.8	The simulated domain for the case ParisFog [Makké, 2015]	118
6.1	Schematic representation of the resolution of the RTE in code_saturne for a clear-sky atmosphere without aerosols or clouds. z _{1D} and z _{3D} are the altitudes until which the 1D and 3D equations are solved. U and D are, respectively, the upward and downward fluxes of the 1D model. The direct (—) and diffuse (—) components for both the UV-vis and SIR band are represented.	124
6.2	Schematic representation of the direct (—) and diffuse (—) radiation around one mesh cell of the 3D domain.	125
6.3	The vertical profiles of downward and upward fluxes in the UV-vis (left panel) and SIR (right panel) bands on 18/02/2007 at 13 h (in W m ⁻²) using the 1D (represented in black) and 3D (represented in green) models in a clear-sky without aerosols. F ^{↑diffuse} (—) F ^{↓direct} (— — —) F ^{↓diffuse} (— * —).	131
6.4	The vertical profiles of downward and upward fluxes in the UV-vis (left panel) and SIR (right panel) bands on 18/02/2007 at 15 h (in W m ⁻²) using the 1D (represented in black) and 3D (represented in green) models in a clear-sky without aerosols. F ^{↑diffuse} (—) F ^{↓direct} (— — —) F ^{↓diffuse} (— * —).	131
6.5	The vertical profiles of downward and upward fluxes in the UV-vis (left panel) and SIR (right panel) bands on 19/02/2007 at 12 h (in W m ⁻²) using the 1D (represented in black) and 3D (represented in green) models in a clear-sky without aerosols until 500 m. F ^{↑diffuse} (—) F ^{↓direct} (— — —) F ^{↓diffuse} (— * —).	132
6.6	The vertical profiles of downward and upward fluxes in the UV-vis (left panel) and SIR (right panel) bands on 19/02/2007 at 12 h (in W m ⁻²) using the 1D (represented in black) and 3D (represented in green) models in a clear-sky with aerosols until 500 m. F ^{↑diffuse} (—) F ^{↓direct} (— — —) F ^{↓diffuse} (— * —).	133

List of Figures

6.7	The vertical profiles of downward and upward global fluxes in the UV-vis (left panel) and SIR (right panel) bands on 19/02/2007 at 8 h (in W m^{-2}) using the 1D (represented in black) and 3D (represented in green) models in a cloudy-sky situation ($C_e=1$). $F_{\uparrow global}$ (—) $F_{\downarrow global}$ (---).	133
6.8	The vertical profiles of downward and upward global fluxes in the UV-vis (left panel) and SIR (right panel) bands on 19/02/2007 at 12 h (in W m^{-2}) using the 1D (represented in black) and 3D (represented in green) models in a clear-sky with aerosols until 500 m. $F_{\uparrow global}$ (—) $F_{\downarrow global}$ (---).	134
A.1	Physical and simulation mesh	137

List of Tables

3.1	Coefficients in two-stream approximations (ω is the single scattering albedo, g the asymmetry factor, $\mu_0 = \cos\theta_0$, θ_0 the solar zenith angle, $\mu_1 = 1/\sqrt{3}$)	39
4.1	Comparison between simulated AOD from Polyphemus and observed AOD from SARTA ReObs at SARTA in 2014.	57
4.2	Instruments and parameters extracted from SARTA ReObs.	65
4.3	Number of clear-sky and cloudy-sky hours for each month of 2014 following the availability of cloud fraction from PYR and LWP from radiometric measurements.	70
4.4	Cloud parameters defining the different cases studied. F_C : cloud fraction; COD: cloud optical depth.	71
4.5	Comparison of simulated and measured direct and global solar irradiances at SARTA during cloudy days for the different cases studied. The RMSEs and MBEs are expressed in $W\ m^{-2}$	75
4.6	MBE of global (G) /direct (D) irradiance fluxes (in $W\ m^{-2}$) for different ranges of standard variation of measured global irradiance G_{obs} (in $W\ m^{-2}$)/liquid water path LWP in ($g\ m^{-2}$) / cloud fraction F_C in 2014.	78
4.7	Averaged standard variation of measured global irradiance G_{obs} (in $W\ m^{-2}$)/liquid water path LWP (in $g\ m^{-2}$) / cloud fraction F_C when measured global irradiance is underestimated or overestimated by code_saturne in 2014.	78
4.8	Mean absolute error (MBE) of global (G) and direct (D) irradiances and the ratio MBE over the averaged measured fluxes for different conditions on the cloud fraction (F_C) in 2014 (in $W\ m^{-2}$).	79
5.1	Aerosol size distribution characteristics at 2100 (UTC) during IOP 13 used in the control simulation. N_a is the number of particles, R_a their dry radius and σ_a the standard deviation of the log-normal distribution.	103
5.2	Aerosol chemical composition, percentage representing the mass fraction of each compound contained in the aerosol (XZ14).	119
A.1	Numerical coefficients for the calculation of T_{mg}	136
A.2	Coefficients of single Scattering co-albedo for a Drop/BC Mixture with $d=20\ \mu m$ - in the UV-vis band - [Chuang et al., 2002]	140
A.3	Coefficients of single Scattering co-albedo for a Drop/BC Mixture with $d=20\ \mu m$ - in the SIR band - [Chuang et al., 2002]	140
A.4	Discrete distribution of p_{kn}	145